Mechanisms and Functional Consequences of Impaired Keratin Network Formation in Genetic Skin Disorders

Von der Fakultät für Mathematik, Informatik und Naturwissenschaften
der RWTH Aachen University
zur Erlangung des akademischen Grades
eines Doktors der Naturwissenschaften genehmigte Dissertation
vorgelegt von

Sonja Maria Lehmann, M.Sc.
aus Aachen

Berichter: Universitätsprofessor Dr. rer. nat. Marc Spehr
Universitätsprofessor Dr. med. Rudolf Leube
Universitätsprofessor Dr. rer. nat. Geraldine Zimmer-Bensch

Tag der mündlichen Prüfung: 15. November 2022

Table of contents

Summary

One of the most important barriers of the body is the skin. Its outermost stratified layer, the epidermis, is mainly composed of differentiating keratinocytes. The integrity of the epidermis is to a large extent provided by structural elements such as the keratin intermediate filament cytoskeleton. The importance of keratin networks is emphasised by mutation-induced keratinopathies such as *Epidermolysis bullosa simplex* (EBS) or *Pachyonychia congenita* (PC), caused by mutations in keratins 5/14 and keratins 6/16/17, respectively. EBS is characterised by trauma-induced blister formation due to rupture of keratinocytes in the basal epidermal layer, which is caused by the disruption of the keratin filament network into granular structures. PC patients, on the other hand, display epidermal thickening with extreme hyperkeratosis in certain skin areas, such as the foot soles.

This work aimed to gain further insight into the different pathogeneses, in particular to apply novel image analysis tools to quantitatively describe mutant EBS keratin granules, and to investigate whether autophagy of mitochondria, representing an essential step of epidermal differentiation, is disturbed in PC.

Using live-cell microscopy of epithelial cells stably overexpressing fluorophore-tagged EBS-mutant keratins, an automated tracking routine was established. It allowed a detailed quantitative analysis of different parameters of mutant keratin granule dynamics. In particular, it was shown that the mutant granules are initially formed in the outermost lamellum of epithelial cells. Subsequently, they grow up to a plateau size, and are constitutively transported inwards with a velocity of approximately 0.5 µm/min. Most keratin granules display multiple fusion events with other granules during their lifetime before they rapidly disassemble at the boundary of the lamellum and the inner cytoplasm. Their transport highly resembles actin-dependent transport, and pharmacological inhibition of the actin motor protein non-muscle myosin II significantly reduced their dynamics. Fluorescence recovery after photobleaching experiments furthermore revealed that the granules rapidly exchange soluble keratins with the surrounding cytoplasm and within the granule itself. Thus, the formation of EBS-related keratin granules is based on liquid-liquid phase separation (LLPS). The kinase DYRK was investigated next, based on its ability to dissolve different LLPS condensates. Although a clear colocalisation of different overexpressed DYRK isoforms and mutant keratin granules was shown in patient-derived EBS keratinocytes, pharmacological inhibition of the kinases did not alter the percentage of granule-containing cells in keratinocyte cell clones stably overexpressing fluorophore-tagged mutant keratins.
In the second part of this work, functional consequences of mutant keratins on mitochondrial integrity were examined. First, the mitochondrial age was determined by a fluorescent reporter

in both EBS and PC keratinocytes. This revealed that PC cells contain increased amounts of overaged mitochondria, which was not the case for EBS. Furthermore, contact sites between mitochondria and the endoplasmic reticulum are reduced in PC. The expression of early mitophagy markers is not changed, but clearance of mitochondria is severely impaired in PC keratinocytes. Although they are able to form autolysosomes, these structures were shown to accumulate in PC. Assessment of lysosomal function revealed defective enzymatic capacity and the mitochondrial overaging phenotype could be mimicked by lysosomal pH modifications in healthy cells. Thus, it can be concluded that the process of autolysosomal recycling, which is essential for macroautophagy, is impaired in PC, which results in impaired mitophagy.

Overall, this work established new image analysis tools which allowed a detailed quantification of mutant keratin dynamics, and elucidated that mutant keratins modulate mitophagy and autolysosomal recycling in PC keratinocytes.

Publications

Publications

Growth, lifetime, directional movement and myosin-dependent motility of mutant keratin granules in cultured cells. Lehmann, S. M., Leube, R. E. & Windoffer, R. Sci Rep 11, 2379, doi:10.1038/s41598-021-81542-8 (2021).

Keratin 6a mutations lead to impaired mitochondrial quality control. Lehmann S, Leube RE, Schwarz N; Br J Dermatol. 2019 Apr 20. doi: 10.1111/bjd.18014.

Expression profile of pattern recognition receptors in skeletal muscle of SOD1((G93A)) amyotrophic lateral sclerosis (ALS) mice and sporadic ALS patients. Lehmann S, Esch E, Hartmann P, Goswami A, Nikolin S, Weis J, et al. Neuropathol Appl Neurobiol. 2018;44(6):606-27.

Conference Presentations

Mitochondria and lysosomes in PC pathogenesis (15 minutes presentation, invited talk). Lehmann, S. M., Leube, R. E. & Schwarz, N. 2021. 10th International *Pachyonychia Congenita* Consortium (IPCC) Symposium. Online.

Keratin 6a mutations lead to impaired mitophagy (10 minutes presentation). Lehmann, S. M., Leube, R. E. & Schwarz, N. 2019. 10th Anniversary of Targeting Mitochondria Congress. Berlin, Germany.

The challenge of keratin tracking: Keratin granules as an alternative? (15 minutes presentation). Lehmann, S. M., Leube, R. E. & Windoffer, R. 2018. Intermediate Filaments Gordon Research Seminar. Lucca (Barga), Italy.

Posters

Tracking mutant keratin granules: Common features & myosin-dependent motility. Lehmann, S. M., Leube, R. E. & Windoffer, R. 2021. Kármán Conference European Meeting on Intermediate Filaments. Aachen/Rolduc, Germany.

Keratin 6a mutations lead to impaired mitophagy. Lehmann, S. M., Leube, R. E. & Schwarz, N. 2019. 11th European Meeting on Intermediate Filaments. Turku, Finland.

Automated Tracking of Keratin Granules Reveals Effect of non-muscle Myosin II on Granule Motility. Lehmann, S. M., Leube, R. E. & Windoffer, R. 2018. Mechanobiology: Measuring and Modelling Cell Migration, Symposium. Aachen, Germany.

Automated Tracking of Keratin Granules Reveals Effect of non-muscle Myosin II on Granule Motility. Lehmann, S. M., Leube, R. E. & Windoffer, R. 2018. Intermediate Filaments Gordon Conference. Lucca (Barga), Italy.

Funding, prizes & scholarships

Since 07/2019: Associated Doctoral Student of the ME3T (Mechanobiology in Epithelial 3D Tissue Constructs) graduate school
Project: Consequences of keratin mutations on intraepidermal and epidermis-matrix adhesion

Mentee of the TANDEMpeerMed Programme. University hospital RwtH Aachen, Germany. 11/2019 – 12/2020.

Second Prize of the Image contest of the World Mitochondria Society on the occasion of the Targeting Mitochondria Congress. 2019.

I. Introduction

I.1 Orchestration of epidermal differentiation

The skin represents the first and one of the most important barriers of vertebrates and protects from mechanical stresses, chemicals, infections, radiation, and loss of water. In order to compensate for these stresses, continuous self-renewal takes place to constantly provide a functional barrier. To balance this dynamic turnover as well as to provide extreme stability, the outermost skin layer, the epidermis, has evolved a specialised stratification and a highly regulated differentiation process. Within this process, the integrity of the skin is to a large extent provided by structural cytoplasmic components, such as the keratin cytoskeleton. The crucial barrier function is maintained by the epidermis, which prevents virulent pathogens from entering the organism by providing a high content of lipids, hydrolytic enzymes and antimicrobial peptides[1] combined with a low water content and an acidic pH.[2]

I.1.1 Structure and composition of the epidermis

About 95% of the epidermal cells are keratinocytes, which are accompanied by melanocytes (pigment producing cells), Langerhans cells (dendritic immune cells) and Merkel cells (mechanoreceptor cells).[3] The human skin is composed of ~80 billion keratinocytes and is renewed on average every 60 days.[4,5] Although keratinocytes differentiate in a continuous manner, four histologically and functionally distinct layers can be distinguished in the epidermis (Fig. 1). They are characterised by differential expression certain proteins, among them keratins, which form the intermediate filament network of epithelial cells.[6] Keratin intermediate filaments provide mechanical integrity of epidermal cells and fulfil important regulatory functions, for example within intracellular signalling pathways.[6]

The *Stratum basale* is the innermost epidermal layer and contains a single-layer of proliferative keratinocytes which express keratins 5 and 14. These basal keratinocytes provide a constant supply of proliferating cells which presumably asymmetrically divide in the vertical direction. Thus, one fraction of the basal cells remains attached to the basement membrane, while the keratinocytes which loose contact to the basement membrane start to differentiate. This detachment is followed by extensive alterations of the gene expression profile of the henceforth non-proliferative cells.[7]

Triggered by not yet fully understood mechanisms, the keratinocytes migrate upwards into the multi-layered *Stratum spinosum*. Once they have reached this layer, the cells are no longer

capable of dividing. The differentiation process is initiated and accompanied by altered expression of keratins. The expression of certain structural proteins and enzymes is also increased by alterations within the epidermal differentiation complex (EDC), a specific gene region on chromosome 1q21.[8] These components later form the cornified envelope, a scaffold located underneath the plasma membrane composed of highly interconnected proteins and lipids.[4]

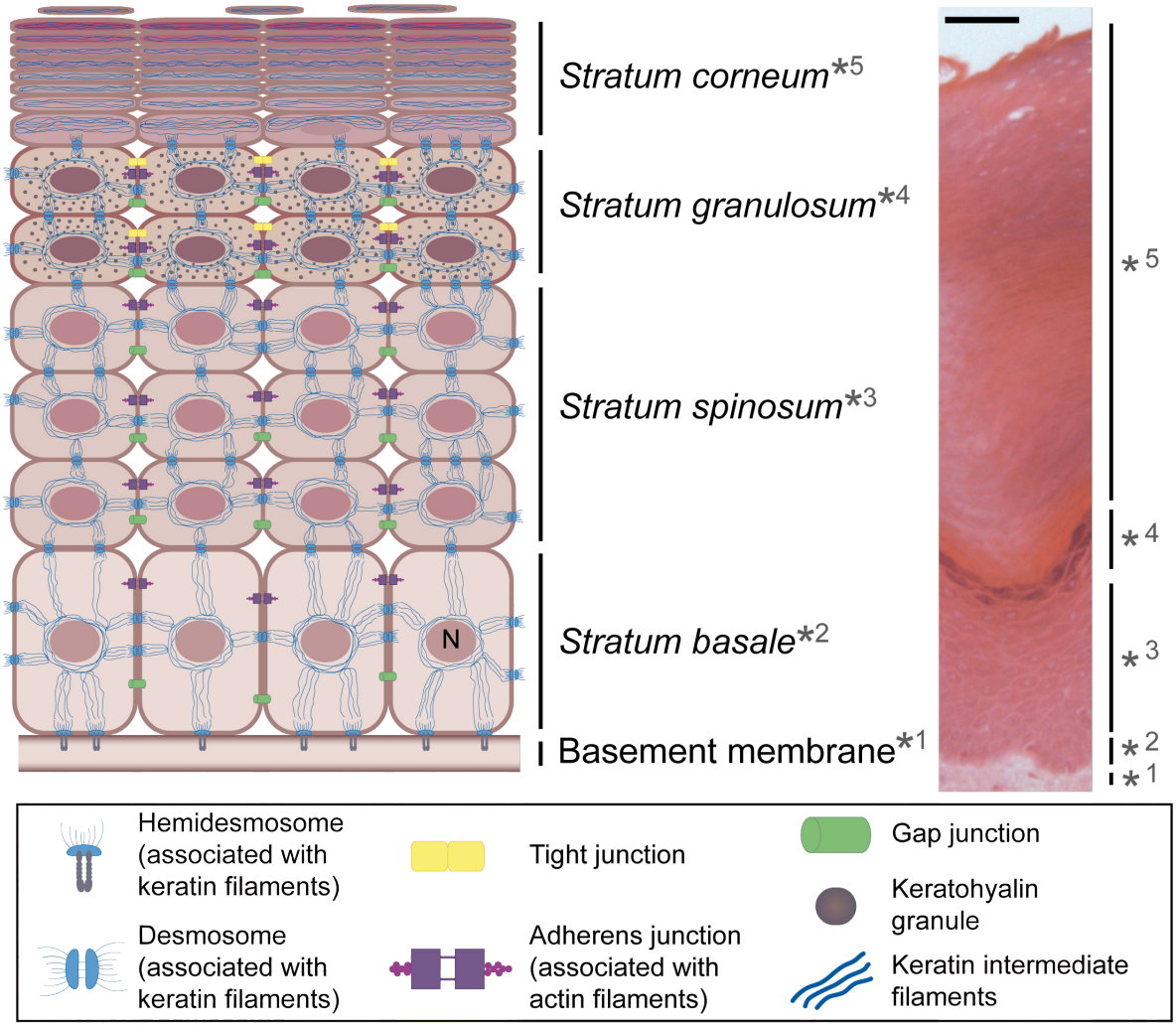

Figure 1 – The structure of the epidermis. Four distinct stratified layers build up the epidermis: *Stratum basale*, *Stratum spinosum*, *Stratum granulosum*, and *Stratum corneum*; shown schematically and as hematoxylin/eosin staining (scale bar = 50 µm). The proliferating keratinocytes of the *Str. basale* are connected to the basement membrane via hemidesmosomes. Different cell-cell junctions connect the cells to each other: adherens junctions, desmosomes, and gap junctions. The cells of the *Str. granulosum* additionally contain tight junctions and are characterised by prominent keratohyalin granules. During their differentiation, the cells lose their organelles, including the nucleus (N). In the outermost *Str. corneum* the keratinocytes have become dead corneocytes and are shed from the epidermis.

The subsequent layer is the *Stratum granulosum* which contains multiple cell layers of increasingly flattened and permeable keratinocytes. The most characteristic histological features are keratohyalin granules containing phosphorylated profilaggrin, one of the cornified envelope (CE) proteins.[9] Once matured into filaggrin, it binds to and aggregates the keratin filament network.[4] This process is suggested to cause the intermediate filament network to collapse, in turn resulting in flattened cells displaying keratin filaments aligned parallel to the outer surface of the epidermis.[9] A higher plasma membrane permeability results in increased influx of extracellular calcium, which activates epidermal transglutaminases.[10] These calcium-dependent enzymes are responsible for crosslinking the cornified envelope proteins into a primary scaffold by catalysing the formation of bonds between CE proteins.[9]
At the transition between granular and corneal layer, cell-cell adhesion is strongly increased by rearrangement of the constitution and morphology of desmosomes.[9] Once matured into corneodesmosomes, they represent much stronger desmosomal junctions than those of basal keratinocytes[9] and are being incorporated into the CE.[11] Furthermore, the cornified envelope is embedded in a intercellular lipid envelope which protects the cells from loss of water.[9]

The outermost *Stratum corneum* is formed by multiple layers of tightly compacted terminally differentiated, i.e. dead keratinocytes, which lack the nucleus and most other organelles and are thus incapable of conducting transcription and translation. At this stage, the cells are called corneocytes. They are closely sealed by lipids, and thus impermeable, insoluble and highly protective.[10] In order to shed from the epidermis, corneodesmosomal proteins must be cleaved by serine proteases to disintegrate the desmosomal plaques from the cornified envelope. The extent of desquamation is tightly regulated in order to maintain a consistent thickness of the epidermis.[4,12]

Basal and suprabasal keratinocytes are highly connected by different intercellular junctions (Fig. 1). Adherens junctions or *zonula adherens* are located at the lateral side of cell-cell connections.[4] They are composed of the canonical E- and P-cadherins as well as p120 catenin, ß- and α-catenin, and are highly connected to cortical actin.[4] Located sub-adjacent to these actin-associated junctions are desmosomes, which link the keratin networks of neighbouring cells across the plasma membranes by connecting desmosomal proteins of different cells across the extracellular space.[4] Gap junctions are responsible for direct electrical or chemical coupling between adjacent cells and are formed by connexins.[4] Tight junctions, also called *zonula occludens*, form a dense apical horizontal belt around the cells of the *Stratum granulosum* in order to specifically seal the epidermis from the environment.[13] They consist of claudins, occludins and junctional adhesion molecules and are scaffolded by *zonula occludens* proteins (ZOs) which link them to the actin cytoskeleton.[4]

I.1.3 Differentiation of epidermal keratinocytes

The cornification process is morphologically and biochemically distinct from canonical apoptosis, as it is much slower and sequentially regulated, and involves the tightly regulated autophagy of organelles that are no longer required.[14] The importance of autophagy in differentiating keratinocytes is supported by studies that found increased amounts of lysosome-like bodies accompanied by clearance of mitochondria, the Golgi apparatus, ribosomes, and endoplasmic reticulum.[7] However, the triggers and details of the intermediate stages of organelle removal are not fully elucidated yet. Nevertheless, several studies have shown that autophagy is crucial for functional differentiation of epidermal keratinocytes.[15-18]

Adequate differentiation of keratinocytes is crucial for the overall maintenance of the skin barrier. It is triggered by an increase of extracellular calcium which ultimately affects in a multitude of genomic and non-genomic pathways. These include expression of CE structural proteins and enzymes, formation, and reorganisation of cell-cell contacts and the cornified envelope, stabilisation of adhesion molecules, as well as cell shape changes. In order to ensure the consecutive cell architecture alterations, an outwardly increasing calcium gradient is present in the epidermis, which finally drops drastically in the *Stratum corneum*.[19-21] It is mainly sustained by intracellular calcium stores of ER and Golgi. Compared to the ER lumen or extracellular space, the cytosolic calcium concentration is approximately fourfold lower. To maintain the intracellular calcium concentration, calcium receptors in the plasma membrane are activated upon calcium binding. This induces the activation of phospholipase C, which then hydrolyses the lipid phosphatidyl inositol 4,5-biphosphate. Ultimately, second messengers are formed which bind to their respective receptors at the ER or Golgi, inducing calcium channel opening and release of calcium into the cytosol.
The importance of maintaining a physiological calcium supply is emphasised by mutations of calcium handling key players, which can lead to various genetic skin diseases. One example is Darier disease, caused by mutations in the ER calcium pump ATP2A2/SERCA2. It is characterised by loss of cell-cell adhesions or abnormal keratinisation patterns and manifests itchy, malodorous keratotic papules. Another related disorder is Hailey-Hailey disease, where mutations in the ATPase ATP2C1, which transports calcium into the Golgi, cause increased cytoplasmic calcium levels. Ultimately, this leads to a loss of responsiveness to extracellular calcium, resulting in reduced adhesion abilities of keratinocytes. The patients consequently suffer from painful erosions, scaly plaques, and vesicopustules.[5] Besides calcium handling defects, skin disorders can also be based on mutations in CE-related genes. They include transglutaminase-related defects like Lamellar ichthyosis, displaying collodion membranes (large, brown plate-like scales with random distribution) or Vohwinkel syndrome, in which patients display hyperkeratosis of palms and soles based on loricrin mutations.[9]

I.2 The many faces of epidermal keratinopathies

However, not only the disruption of calcium handling or the cornified envelope can cause severe skin disorders. The intermediate filament (IF) network of epithelial cells, composed of different cell type-specific keratins, is also a crucial element of skin integrity. Mutations of IF genes result in more than 80 human diseases.[22] The majority of these disorders are caused by keratin mutations, i.e. more than 60 different keratinopathies (www.interfil.org).[23] These skin disorders are in principle characterised by pathogenic tissue fragility, resulting in different symptoms depending on the keratin gene and the respective layer in which it is expressed.[24,25] The impact of disturbances of the keratin cytoskeleton in skin diseases is underlined by the fact that suprabasal keratins account for up to 85% of total protein mass of fully differentiated keratinocytes.[26] In this work, two exemplary keratinopathies were investigated, which are characterised by different symptoms.

I.2.1 *Epidermolysis bullosa simplex*

The first intermediate filament-related disorder to be discovered in 1991 is the blister-forming disease *Epidermolysis bullosa simplex* (EB *simplex*/EBS), and it is referred to as “the model keratin disorder”.[24,25] Besides EBS, accounting for ~70% of all EB cases, three other forms of *Epidermolysis bullosa* are classified which are based on mutations of junction-related proteins of other layers of the skin.[27]

The most prevalent EB subtype, EB *simplex*, is based on mutations in basal keratin 5 or 14, which account for more than 10% of the total protein in basal skin keratinocytes *in vivo*,[26] or mutations in genes of cytoskeleton-connecting proteins such as plakophilin-1, plectin or $\alpha 6\beta 4$ integrin.[28] A study by Vassar *et al*. provided the first evidence that mutant keratin 14 causes skin blistering upon mild physical trauma due to cytolysis within the basal epidermal layer of transgenic mice.[29] Trauma-induced blister formation also represents the main symptom of human EBS, and exemplary images of patients are shown in Fig. 2. EBS is based on fragility of basal keratinocytes that rupture when the epidermis is subjected to mechanical stress.[30] It has been shown in EBS skin and mouse models that this rupture often occurs in a specific area, particularly between hemidesmosomes and the nucleus.[25,31] Based on severity, distribution, and frequency of blisters, an international consortium agreed on three main types of EBS in 2008, thus ending a long period of inconsistent and non-specific nomenclature:

- Localised EBS, previously called Weber-Cockayne subtype, which displays mild and late-onset symptoms and blister formation localised to hands and feet.
- Other localised EBS, formerly called Koebner subtype, showing moderate generalised blistering at birth or early infancy.

- Generalised EBS, previously known as Dowling-Meara EBS, displaying severe blistering at several body sites already at birth.[28,30]

Occurring in approximately 1 of 25,000 live births, EB *simplex* is a rare disease, but one that has gained increased public interest in the last years by fundraising activities for so-called “butterfly children”, referring to the hypersensitive skin condition of EBS patients. It is mostly inherited in an autosomal dominant fashion and displays less severe symptoms than the other EB subtypes.[32-35]

Figure 2 – Symptoms of EBS patients. Representative pictures display the main symptoms of EBS, in particular blisters (A,) and resulting lesions (B, C). Photos were provided by the EB House Austria (http://www.eb-haus.org/startseite.html).

On the subcellular level, EBS is characterised by disruption of the keratin filament network and the occurrence of amorphous cytoplasmic aggregates positive for keratin 5 and 14.[29,30,36-38] Interestingly, these keratin granules are in dynamic equilibrium with soluble subunits in cultured cells[39] and are thus not as static and insoluble as canonical protein aggregates occurring in neurodegenerative diseases such as Alzheimer´s disease, amyotrophic lateral sclerosis or Parkinson´s disease.[40] Furthermore, EBS mutations alter dynamic and mechanical properties of the keratin network.[39] Although these cellular details are known and further studies are published every year, the molecular pathogenesis of blister formation is still not resolved. Future studies are required to dissect the molecular functions of keratins, apart from the textbook function of mediating mechanical resilience, in order to understand how keratin

mutations alter keratin functions in genetic skin disorders. Only a few formalised therapy trials have been performed which led to inconclusive results.[41] Thus, the limited standard therapy options include minimisation of trauma, prevention of infections in healing blisters, and treatment of itch and thus remain solely preventive and palliative.[30] However, a number of promising clinical studies have been performed in the last years (reviewed in [42]). They include cell-based therapies, which aim to improve symptoms by external addition of keratinocytes, fibroblasts, or other cell types to support natural skin processes.[42] Furthermore, several small molecules and repurposed drugs have been tested with mixed results, often aiming to diminish inflammation.[42] Particular focus is placed on gene therapies, either targeted to replace defective genes in recessive EB forms, or to silence genes mutated in dominant forms.[42] One novel phase I and II clinical trial has very recently shown remarkable success in ameliorating blisters in recessive dystrophic EB by topical administration of an engineered, non-replicating COL7A1-containing herpes simplex virus type 1 (HSV-1) vector. It was able to induce successful expression of collagen VII and wound healing of severe blisters within 3 months of treatment in most cases.[43] The emerging number of clinical trials is promising with regard to new therapeutic options to be available in the near future.

Besides EB *simplex*, three other forms of *Epidermolysis bullosa* exist. Dystrophic EB (DEB) is caused by collagen VII mutations,[33] which induces blistering inside the dermis.[27,44] Junctional EB (JEB) is based on mutations in hemidesmosomal proteins,[27] resulting in blister formation at the epidermal-dermal interface. Kindler EB was recently defined as the third subtype, caused by mutations in Fermitin family homolog 1 (Kindlin-1), a protein that is located at focal adhesions, resulting in variable blistering localisations.[27] In total, the number of patients suffering from all *Epidermolysis bullosa* subtypes is estimated at 500,000 worldwide.[42]

I.2.2. *Pachyonychia congenita*

Another rare genodermatosis called *Pachyonychia congenita* (PC) is based on autosomal dominant mutations in keratin 6 (isoforms a-c in humans), 16 or 17.[45] These keratins are not constantly present in the previously described epidermal layers, but are expressed in epithelial appendages or specifically produced in response to injury or environmental stresses.[45] The concrete prevalence of PC is extremely low, but not exactly known. However, the International PC Research Registry (IPCRR) comprised 1038 genetically confirmed patients in 53 countries in 2021.[46] PC patients show alterations of ectoderm-derived epithelial structures, such as palmoplantar keratoderma (PPK), nail dystrophies, or oral leukokeratosis (Fig. 3). PC patients suffer from severe plantar pain and a considerable impaired quality of life. Named after two scientists which were among the first ones to describe PC in 1906, one subtype was initially named Jadahsson-Lewandowsky PC, later on found to be caused by mutations in keratins 6

or 16.[47] The Jackson-Lawler form on the other hand is caused by Krt17 mutations and was named after the respective scientists, based on their publication from 1951.[48]

Figure 3 – *Pachyonychia congenita* symptoms. Representative photos display PC-characteristic keratoderma and hypertrophic nail dystrophy. Photos were provided the *Pachyonychia congenita* project (http://www.pachyonychia.org/).

The clinical PC phenotypes vary greatly, and a definitive diagnosis can only be made by genomic sequencing.[45] Based on the variety and inconsistency of symptoms, the nomenclature was recently altered and now only includes the gene that is mutated, in particular Krt6a , Krt6b, Krt6c, Krt16 or Krt17 PC subtype.[45] Palmoplantar keratoderma is the most frequent symptom, present in more than 90% of all PC patients.[49] Massive thickening of the epidermis, i.e. hyperkeratosis, is found mainly at pressure points in palmar and plantar regions.[50-53] In contrast to EBS, fragility of keratinocytes has not been observed.[25,30,34,36]

The standard palliative therapeutic option is the removal of the hyperkeratotic skin regions, followed by treatment with topical steroids or retinoids.[54] Most studies investigating the PC pathogenesis are based on transgenic mouse models, because no sophisticated *in vitro* cell culture models have been published yet.[55] One of these animal studies has shown that keratin

16 knock-out mice spontaneously develop footpad lesions, thus being the only model showing PPK-like symptoms yet.[56] Triple deletion of Krt6a , Krt6b and Krt17 in mice leads to severe cell lysis in the nail bed epithelium,[57] although deletion of only Krt17 causes morphologically normal nails and oral mucosa in mice, probably due to the expression of Krt17n (n stands for nail), which is mainly expressed in nail bed and matrix.[58]

Based on Krt16 null mice studies, three phases of PPK have been described. Active PPK as the first phase includes defects of paw skin to either maintain or return to normal tissue homeostasis, while the lesions arise mostly at areas of mechanical stress, but without showing keratinocyte fragility.[56,59] In the following onset stage, several features of oxidative stress are occurring.[60] The final pre-PPK stage is characterised by a selective defect in terminal differentiation of keratinocytes, for instance upregulation of differentiation markers, an altered nuclear aspect ratio of basal keratinocytes or an abnormal appearance of granular keratinocytes.[61] Furthermore, computational studies provide interesting hints that a link between Krt16, skin barrier genes and innate immunity effectors such as damage-associated molecular patterns (DAMPs) might exist.[59,62] One of these studies also shows that Krt16 expression is linked to expression of barrier homeostasis and inflammation genes in mouse tail skin.[62] Furthermore, Krt16 was identified as a member of barrier homeostasis genes, indicating that it might fine-tune the skin´s response to barrier-compromising stresses.[59]

While current PC therapeutic options remain preventive and palliative until now, the main future therapy of choice is genetic targeting of keratin alleles. For instance, one clinical trial on humans used siRNA to specifically target mutant Krt6aN171K and has shown promising results so far. Nevertheless, delivery was only possible by intradermal and thus painful injections.[63-65] Also drug-based approaches aiming at reducing keratin expression have been tested. They include for instance rapamycin, which has been shown to improve symptoms when taken orally, but also shows severe side effects.[66] Injections of botulinum toxin into plantar calluses have also been tested and shown to improve plantar blistering and pain, but they are expensive and can only be administered under anaesthesia.[67] Recent indications that keratinocyte differentiation may be impaired in PC have opened up another path of treatment options. Recent (pre-)clinical studies therefore investigated the possible targeting of stress response pathways[60,68,69] or methods to promote the restoration of normal epidermal differentiation.[45]

Overall, EBS and PC represent two genetic skin disorders which are both caused by mutations of epithelial keratins, but manifest in different epidermal responses, whose subcellular details are still not fully elucidated, and robust treatments are still lacking.

I.3 Dynamic properties of keratin networks in health and disease

I.3.1 Intermediate filaments as essential components of the cytoskeleton

With regard to cellular stability, the cytoskeleton represents the most relevant structural element. Eukaryotic cells contain three different cytoskeletal elements, each composed of different key proteins and associated molecules. The three classes are microtubules, actin filaments, and intermediate filaments. They are involved in mechanical stabilisation of cells to a different degree and fulfil a large variety of additional specific functions. A scheme of the complex interplay of the cytoskeletal components is illustrated in Fig. 4.

With a diameter of 20-27 nm, microtubules are the largest cytoskeletal structures and composed of globular tubulin monomers.[70,71] Microtubules possess a plus- and a minus-end and are thus polar structures. Consequently, they are able to mediate directed intracellular long-distance transport with the help of the molecular motor proteins kinesin and dynein.[72]

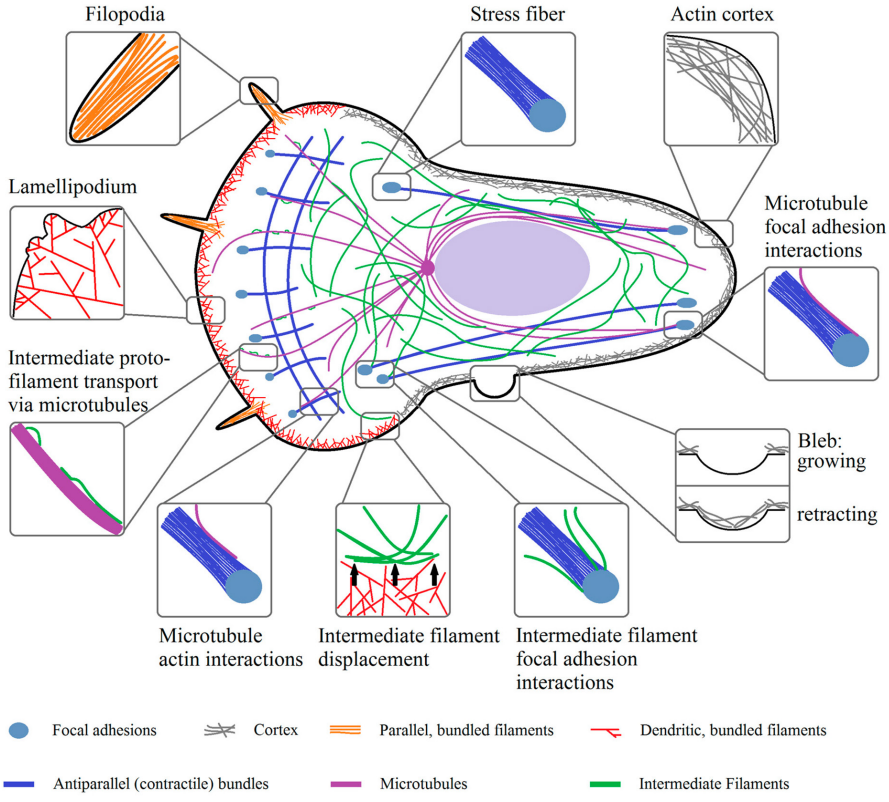

Figure 4 – Cytoskeletal organisation in mammalian cells. Morphologically and functionally distinct structures of the cytoskeletal elements actin, microtubules and intermediate filaments are shown. Notably, all three cytoskeletal proteins directly interact with each other. The figure was taken from [73].

The second cytoskeletal system is composed of actin, one of the most abundant and conserved proteins in eukaryotes. It was initially discovered as a main component of muscle cells in the 1940s where it forms highly contractile structures.[74] Non-muscle cells contain a morphologically distinct actin system, but both muscle and non-muscle actin filaments are

using myosin motorproteins in order to either contract or transport particles, respectively. Actin is a 42 kDa globular acidic protein and its structure is well-known at atomic resolution.[75] Globular actin monomers (G-actin) spontaneously polymerise into double-helical filaments (F-actin)[76,77] with a diameter of approximately 4-8 nm.[78]

Polymerisation and depolymerisation are highly dynamic and enable F-actin filaments to be key players in cell migration, wound healing, cancer cell invasion, cytokinesis, endo- and phagocytosis or immune responses.[79-83] These functions are based on the three main functions of actin: mediation of internal mechanical support, construction of tracks for short distance cargo transport, and provision of force to drive cell movements.[80] In order to fulfil the variety of different features, more than 100 actin-associated proteins are involved in the fine tuning of actin dynamics.[80] In contrast to microtubules, which are overall organised by the MTOC, actin filaments can form various structurally and functionally different structures.

In order to migrate, cells form lamellipodia, flat structures being formed by actin polymerisation at the cell front.[84,85] In combination with depolymerisation located further inside, a treadmilling effect is created which induces a retrograde flow in the cell periphery.[86,87] The second migration-related structure are filopodia. They form elongated cell protrusions composed of parallel actin bundles connected by formins, and are not required for all types of migration.[88]

Contractility and mechanical stability are however provided by stress fibres and the actin cortex. Stress fibres are bundles of either anti-parallel actin filaments containing myosin II, or parallel filaments[89] of each 10-30 single filaments and form at sites of mechanical stress or focal adhesions.[89-92] The cortex on the other hand forms a contractile structure close to the plasma membrane (less than 20 nm away[93]) and is built by filament-bundles and cross-linked filaments.[91] Composition and mechanical properties of the cortex are responsible for a cell´s response to external forces.[73] The different compositions and functions of different actin elements within the cell were discovered by utilisation of a large availability of small molecules and drugs. These can for example promote depolymerisation (Latrunculin, Cytochalasin D)[94,95], stabilise filaments (Phalloidin, Jasplakinolide)[96] or indirectly influence actin by binding actin-associated proteins.[97-100]

Intermediate filaments (IFs) represent the third and most diverse cytoskeletal group. IFs are highly abundant, but they are most probably absent in plants and fungi.[101-103] Six different protein groups can be distinguished in mammals based on cell type-specific expression.[104,105] More than 50 keratins make up the type I (more acidic) and type II (more basic) keratin intermediate filaments, with the epithelial keratins referred to as the “soft” and the hair and nail-forming as the “hard” keratins.

Type III intermediate filaments, for example vimentin or desmin, are expressed in different cell types, such as fibroblasts, muscle cells or glial cells. In contrast, expression of type IV

intermediate filaments, such as neurofilaments and synemin, are mainly expressed in neural cells.[101] The fact that IFs are expressed in a cell-type and differentiation-specific manner is extensively used in tumour diagnosis in different cancers.[106]

The function of intermediate filaments has been simplified for a long time as being plain structural proteins. However, research within the last years has led to the conclusion that IFs fulfil considerably more functions, for example in cell growth, migration, cellular architecture, stress-related signalling, and immunological processes.[107-112]
The importance of providing crucial structural support has been shown by tissue fragility diseases caused by IF mutations, together with the observation that lack of epithelial IFs leads to decreased mechanical stress resistance.[113,114] Furthermore, it has been shown that shear stress causes increased keratin solubility, aggregation and degradation.[115] This structural support is for example important in the skin, where disruption of keratins decreases mechanical stability, alters wound closure and decreases the epidermal barrier function.[116] Regarding the influence on stress protection, it has been shown that IFs are hyperphosphorylated upon stressful situations, thus altering protein solubility and total IF network morphology.[115,117] Hyperphosphorylation of IFs is suggested to act as a phosphate sink and thereby inhibit the phosphorylation of pro-apoptotic factors, thus protecting from apoptosis.[118,119] Reorganisation of the IF network furthermore impacts migration, wound healing and tissue remodelling.[120-122] Recent studies have also discovered that IFs play an important role in organelle localisation, influencing the positioning, shape, and function of various organelles.[107,123] Desmin knockout for example leads to mis-localisation, fragmentation and functional differences of mitochondria in the heart muscle.[124-126] Furthermore, vimentin knockout cells display a disturbed lysosome distribution.[127] These and further studies have shown that disruption of the cytoplasmic IFs causes several tissue-specific diseases. A re-occurring feature is the presence of cytoplasmic IF aggregates in skin disorders and muscle- and neuro-degenerative diseases.[30,128,129]

Compared to actin and microtubules, intermediate filaments are considerably different regarding certain properties.[104,130] They are much harder to solubilise, cannot conduct directed motor protein-driven transport due to their apolarity, and they assemble spontaneously without requiring any cofactors in appropriate buffers. IFs are flexible and tough, less rigid than actin at low strains, and less brittle than microtubules at high strains.[131] Furthermore, incorporation and dissociation of subunits can not only occur at the ends, but also along the entire filament length. IFs are also extremely stable compared to the other cytoskeletal elements, but can display a very dynamic behaviour on the other hand.[101] A similarity with the other cytoskeletal proteins is their interaction with associated proteins in order to connect IFs to each other and to other structures.

I.3.2 Keratin intermediate filament structure and assembly

All intermediate filaments share a common secondary structure, which is depicted in Fig. 5, with type V intermediate filaments containing an additional insertion in coil 1B plus a nuclear localisation signal. The highly conserved central alpha-helical rod domain, comprised of four alpha-helices (coils 1A, 1B, 2A, 2B), is connected by non-helical linkers (L1, L12, L2). The sequences at the beginning and end of the rod domain, called helix initiation and helix termination motif, respectively, are the evolutionary most conserved IF sequences and represent hotspots for various disease-causing mutations.

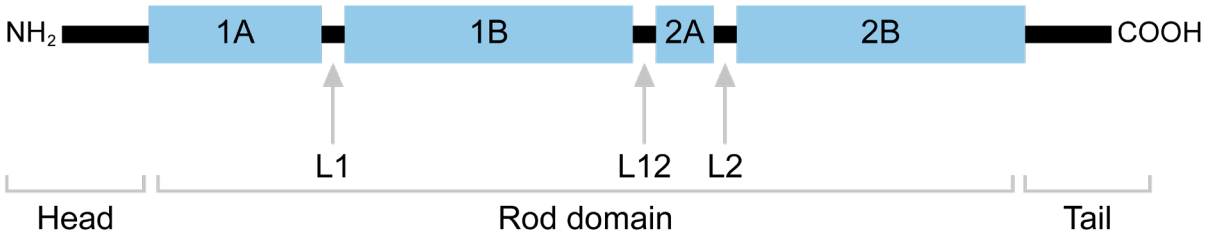

Figure 5 – Intermediate filament protein structure. All intermediate filament-forming proteins contain a central α-helical rod domain which is composed of segments 1A, 1B, 2A, and 2B that are connected by non-helical linker domains L1, L12, and L2. The rod domain is flanked by the highly variable N-terminal head (NH_2) and the C-terminal tail domain (COOH). The figure was adapted from [101].

The helical structure of the rod domain allows interaction with other IF proteins. The rod domain is flanked by non-helical head- and tail-domains, which differ considerably in size, sequence and secondary structure among intermediate filaments and are able to bind to other cytoplasmic elements. The head domain plays a role in regulating IF protein assembly, whereas the tail is dispensable and only affects filament stability.[105]

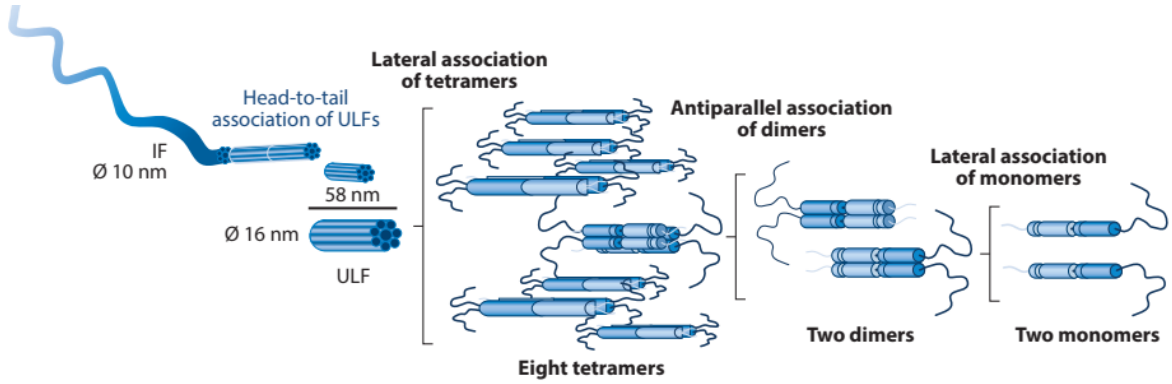

Figure 6 – Intermediate filament assembly. Four major stages of (keratin) intermediate filament assembly can be distinguished. The initial modules are IF monomers. They associate into polar obligatory heterodimers. Two of these dimers associate and form staggered, antiparallel and thus apolar tetramers. Lateral association of 8 tetramers results in 58 nm long unit-length filaments (ULFs), which in turn elongate longitudinally and are compacted into intermediate filaments with a diameter of 8-12 nm. The figure was taken from [103].

Parallel two-stranded coiled-coil dimers with strongly, but non-covalently bound alpha-helices, represent the basic structural module of intermediate filaments. Regarding the mode of assembly, three distinct groups can be distinguished. The type I and II keratins form the first group. Two keratins assemble into the obligatory heterodimer, and two such structures laterally associate into staggered tetramers, which consequently lack any polarity. Further lateral alignment of 6-10 tetramers results in short ~60 nm long unit-length filaments (ULFs) with a diameter of 8-16 nm. Subsequent longitudinal alignment and radial compaction take place, resulting in 8-12 nm mature IFs (IF bundles).[101] The assembly process is depicted in Fig. 6.

Compared to the other groups, keratin assembly is extremely fast and takes place spontaneously in physiological salt solutions without requiring any cofactors.[132,133] The other assembly groups differ by slower assembly rates, the number of subunits per filament, and the ability to form homodimers. [101]

I.3.3 The keratin intermediate filament cycle

During recent years, it has been shown that intermediate filaments fulfil more than structural functions, and that they are also more dynamic and less insoluble than it was suggested in the earlier days of IF research.[134-137] Several studies provided hints that initiation of filament assembly occurs in close proximity to the plasma membrane,[138] specifically in vicinity of focal adhesions,[139] desmosomes,[140] and hemidesmosomes,[141] and that keratins are rapidly incorporated into filaments.[142] Extensive imaging and careful analysis of fluorescently tagged keratins led to the now widely accepted concept of the keratin-filament cycle of assembly and disassembly (Fig. 7). According to this model, the cycle begins in the cell periphery with the nucleation of nascent keratins, which are called precursors. These precursors move inwards concurrently with actin with a velocity of 0.5 µm/min.[139] Elongation of these precursors by continuous integration of soluble oligomers can occur at either filament end or by mutual end-on fusion. Subsequent end-on integration of precursors into the peripheral network hampers further elongation and instead induces branching of filaments. Regulated either by IF-associated proteins or by intrinsic properties, lateral association of filaments or so-called bundling takes place, resulting in increased bundle thicknesses closer to the nucleus. Disassembly of keratin IFs can occur by degradation of filament polypeptides or by disassembly into reusable non-filamentous subunits. This cycle most likely applies to the majority of newly formed keratin filaments.[143]

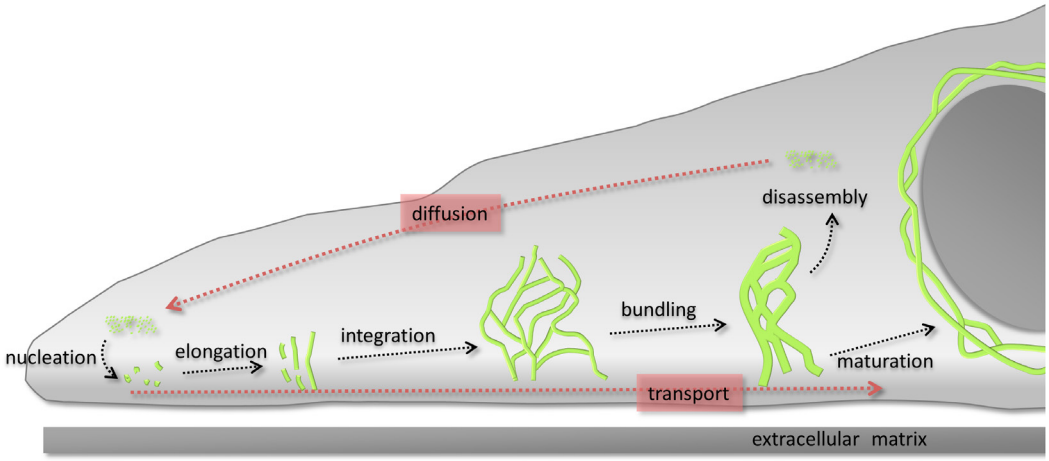

Figure 7 – The keratin cycle of assembly and disassembly. A starting point of the cycle is the assembly of soluble keratin particles in the cell periphery close to focal adhesions (nucleation). Growth (elongation) of these particles is combined with inward movement towards the cell centre, depending on actin (transport). Subsequent integration of these particles into the existing peripheral network (integration) takes place. Filament bundling occurs during centripetal translocation towards the nucleus (transport). Further dissociation of soluble subunits (disassembly) drives the recycling of keratins, which diffuse towards the cell periphery (diffusion) where *de novo* nucleation takes place. If not disassembled, bundled keratins are stabilised (maturation), thus forming for example the stable perinuclear cage. The figure was adapted from [144].

However, it is important to take into account that also thermal and mechanical stresses can result in keratin filament reorganisation. Although simple assembly of IFs can be reconstituted *in vitro* without additional factors, it is unlikely that the complex cycle of assembly and disassembly is functional without any modulating factors. Structurally intercalating IF-associated proteins have been studied in great detail, such as plakin family members, which link IFs to actin, microtubules, and adhesion complexes.[145] However, modulators with specific functions within the keratin cycle are very rare, for example epidermal growth factor (EGF) which enhances keratin dynamics.[146]

One aspect regarding the keratin cycle which is still not fully understood is the transport of keratins. During the last years, several studies have indicated that different intermediate filaments can be moved by motorprotein-driven transport either via actin or microtubules. For example, microtubule-driven, outwardly directed vimentin transport via kinesin or dynein was shown in several investigations.[147-154] In contrast, the limited number of studies on keratins has shown that they move inwards from the cell periphery to the nucleus.[155-157] Furthermore, interactions between the actomyosin system and focal adhesion-anchored vimentin have been shown and indicate actin-associated transport of intermediate filaments.[158] Also keratin was shown to associate with non-muscle myosin II.[159] Furthermore, it was recently shown that mature keratin filaments are transported by kinesin-1 along microtubules, which was suggested to represent a unified mechanism for intermediate filaments.[160] However, it has still not been resolved whether a direct binding to motorproteins or indirect binding via adaptor proteins is the mode of action, or if it differs between different IFs.

I.3.4 Mutant keratin granule dynamics

The previously described details of intermediate filament transport are based on studies of wild type proteins. However, some recent studies also focused on dynamics of EBS-associated mutant keratin granules. It has been shown that different cell lines expressing EBS-mutant Krt14R125C harbour prominent peripheral granules. These granules are highly dynamic, and their movement is energy-dependent, which was shown by ATP depletion experiments.[39] However, these granules are different from keratin granules that are formed in cells during mitosis regarding their distribution and origin, as mitotic granules are formed by controlled phosphorylation and cover the entire cytoplasm.[157]

A remaining perinuclear cage of mutant keratin filaments is still present in Krt14R125C-expressing cells, which appears to be morphologically similar to wild type keratin filaments, and is more stable and thus less mobile than the granules.[39] Other studies have shown that early assembly stages of Krt14R125H are functional.[133] Thus , filament formation of mutant keratins is not completely disturbed, but displays certain differences. Remarkably, the formation of mutant keratin granules goes hand in hand with a significant ~50% increase of mutant keratin in the soluble protein fraction.[39] Furthermore, if Krt14R125C, which alone only forms aggregates in preadipocytes, is co-expressed with keratin 8 and 18, it is incorporated into perinuclear filament bundles. Consequently, mutant keratin 14 impairs the formation of filaments with wild type keratins only in the absence of another type II keratin.[39]

An increased mobility of granules is often observed, but not always combined with a considerably higher velocity, as mutant Krt14R125C granules move with 0.6 µm/min if expressed in MCF-7 breast cancer cells[39] compared to wild type keratin precursors in mammary epithelium–derived EpH4 cells with a speed of 0.5 µm/min[139]. However, mutant keratin structures seem to be 6-10x faster than wild-type keratins in A431 and PtK2 cells.[155,156] Furthermore, it has been shown that mutant keratin granules display some of the typical features of the wild type keratin cycle (see I.7). The functional early stages of keratin assembly[133] can be observed as nucleation of round keratin precursors, which grow in diameter analogous to elongation of short wild type filaments.[39] Both wild type and mutant keratin precursors have been shown to be formed in close proximity to focal adhesions. Downregulation of the focal adhesion protein talin by shRNA depletes mutant keratin precursors in the periphery and causes retraction of the remaining keratin network in Krt14R125C-expressing cells.[139] Pharmacological inhibition of actin by Latrunculin B or Cytochalasin D reversibly prevents nearly all retrograde transport of mutant keratin granules, as well as formation of new keratin precursors close to the plasma membrane.[39] Disruption of microtubules by Nocodazole on the other hand does not block the formation or inward

movement of mutant keratin precursors, but might cause slightly increased bundling of remaining filaments.[39] The missing influence of microtubule-dependent transport of mutant keratin particles is in line with the observation that the granule dynamics are much slower than the microtubule-dependent zig-zag movement that was shown for wild type keratin 5.[161]

It is nowadays widely accepted that posttranslational modifications influence keratin organisation.[162] An example is keratin phosphorylation as a consequence of antagonistic kinase and phosphatase activities, which is suggested to influence keratin network dynamics.[163] Inhibition of p38 leads to disappearance of mutant keratin precursors in the cell periphery, immediate stop of granule motility and an increase of keratin granules in the central cytoplasm, all of which is reversible. However, after extended treatment granules are still present, are being stabilised, and dissolving of granules is inhibited. On the other hand, overexpression of p38 leads to granule formation in cells expressing wild type keratin 18.[164]
But not only alterations of phosphorylation affect mutant keratin granule disassembly. The ubiquitin-proteasome system also influences mutant keratin removal, indicated by studies showing that mutant keratin inclusions contain ubiquitin,[165] whereas wild type keratin 14 is not ubiquitinated in HaCaT cells.[166] It has been shown that occurrence of mutant Krt14R125C granules in MCF-7 cells is highly increased upon pharmacological proteasome inhibition. Furthermore, the stress-induced heat shock protein Hsp70 and the constitutively expressed Hsc70 are activated upon proteasome inhibition, and overexpression of their co-chaperone CHIP/STUB1 leads to a significant decrease of mutant keratin granules.[167] These results suggest that aggregation-prone keratins are targets of the chaperone machinery.
In line with these findings, pre-treatment of immortalised EBS cells with the chemical chaperones TMAO (trimethylamine N-oxide) and 4-PBA (4-phenylbutyrate) significantly reduces heat-induced keratin aggregate formation.[168]

I.4 The interplay of intermediate filaments and mitochondria

As already indicated in I.5.3, it has become evident in the past years that intermediate filaments are not only plain major mechanical cell components but fulfil a variety of other important functions. Among these is their ability to influence the shape and positioning of organelles, as well as to ensure the correct subcellular localisation of certain proteins.[107]

One of the organelles fine-tuned by intermediate filaments is the nucleus. Most obviously, nuclear intermediate filaments play the central role in affecting nuclear shape and function, which manifests in the large variety of known laminopathies.[169] However, also cytoplasmic IFs,

which span the cytoplasm from the plasma membrane to the nuclear envelope,[170] influence localisation and structure of the nucleus.[171-174]

In addition, it has been shown that IFs interact with the Golgi apparatus, which is a crucial organelle within the secretory pathway. The Golgi protein GM130 for example colocalises with vimentin filaments[175] and vimentin knockout causes impairment of glycolipid transport between endosomal/lysosomal compartments and the Golgi,[123,176] leading for example to changes in deposits of fat granules.[177]

Other organelles that were shown to associate with intermediate filaments are lysosomes. One of the most important findings regarding their interaction is the redistribution of lysosomes from a steady-state cytoplasmic localisation in wild type cells to a juxtanuclear position in vimentin-null cells.[178] The influence on lysosome positioning may be based on the binding of vimentin, peripherin and alpha-internexin to AP-3.[123,178] AP-3 is a heterotetrameric adaptor complex which is responsible for the transport of vesicles between endosomes and lysosomes and regulates the sorting of various subsets of lysosomes, such as melanosomes or synaptic vesicles.[179] IFs in turn control AP-3 positioning and thus possibly the localisation of late endosomal and lysosomal compartments. This is supported by the fact that both AP-3 and vimentin knockout result in similar phenotypes, including for example an accumulation of ionic zinc and defects in zinc uptake. AP-3-deficient fibroblasts furthermore display an increased lysosome pH.[180] Furthermore, the lysosomal membrane proteins CD63 & LAMP-1 also change their localisation from punctate-cytoplasmic to juxtanuclear upon vimentin knockout.

One example of a human disease which displays a link between IFs and organelles is Charcot-Marie-Tooth (CMT) disease, the most common hereditary peripheral neuropathy, characterised by progressive muscle degeneration.[181] Interestingly, CMT is caused by mutations of either kinesin1B,[182] intermediate filament subunits,[183,184] the mitochondrial membrane protein mitofusin 2[185] or the late endosome/lysosome GTPase Rab7. The various members of the Rab protein family, small GTPases, regulate the different steps of intracellular vesicular transport.[186] Several studies have shown that Rab proteins and intermediate filaments can associate at different stages of vesicular transport. For instance Rab4-vimentin[187,188] and Rab5-vimentin/desmin associations[189] take place in early endocytosis. Furthermore, vimentin is able to interact with Rab7a and Rab9 in late endocytic trafficking.[190,191] These hints support the hypothesis that IFs may play an important role in intracellular vesicle transport.[192]

I.4.1 The functional impact of intermediate filaments on mitochondria

One organelle being investigated with particular interest is the mitochondrium, which has shown to be modulated by various intermediate filaments. This modulation extends to many facets, including mitochondrial distribution, binding of intermediate filaments to mitochondria and modulation of mitochondrial function, and has been shown for different IF proteins from most of the cytoplasmic IF classes.

One of the facets which is easily detectable is the altered distribution of mitochondria in case of disturbed intermediate filament proteins that is presumably accompanied by an altered mitochondrial shape. The earliest study giving such hints from 1983 investigated rhodamine-stained mitochondria in comparison to the distribution patterns of all three cytoskeletal elements in various cell lines. Summerhayes *et al.* discovered that although actin filament localisation was not related to mitochondrial distribution, a good, but not absolute correlation was observed for mitochondria and both microtubules and vimentin intermediate filaments.[193] These results are in line with later studies that confirmed the intracellular transport of mitochondria along microtubules.[194-197] Furthermore, it was the first hint that intermediate filaments and mitochondria are located in close proximity. However, it took many years until the topic was revived. In 2008, Tang and colleagues showed that vimentin colocalises and interacts with mitochondria, even to a greater extent than actin and microtubules. They also demonstrated that knockdown of vimentin leads to mitochondrial fragmentation, swelling and disorganisation and suggested that vimentin might be involved in the mitochondrial association of microtubules.[198] Since then, several other studies supported the findings of colocalisation of mesenchymal vimentin filaments with mitochondria in several cell lines.[193,198-200] Furthermore, it was proven that vimentin is able to modulate both shape and motile behaviour of mitochondria.[201] The distribution of mitochondria was also shown to be altered upon disturbances of the muscle IF protein desmin, as desmin knockout mice display abnormal accumulations of sarcolemmal mitochondrial clumps.[126] Also the epithelial IF network-forming keratins were shown to influence mitochondrial distribution. Hepatocytes of keratin 8 knockout mice for example display abnormally distributed mitochondria, which are also smaller.[202] Investigations of the same keratin 8 knockout mice have shown that ß-cells also display mitochondrial defects, including an increased number of more fragmented mitochondria, which appear to be more round with diffuse cristae.[203] Furthermore it has been shown that EBS keratinocytes display mitochondria that are abnormally concentrated around the nucleus and retracted from the cell periphery.[204,205]

An altered mitochondrial distribution might be relevant because subcellular structures that require extensive energy supply might lose that very supply, resulting in functional defects. Furthermore, mitochondria are closely linked to the endoplasmic reticulum (ER) at so-called

mitochondria-associated membranes (MAMs), which are for example essential for lipid and calcium trafficking between the two organelles.[206-208] Disturbances of the mitochondrial distribution might alter the distance of ER and mitochondria[209] and thus cause disruption of MAM contact sites and their associated functions.

Another aspect which has shown to be influenced by intermediate filaments is the motility of mitochondria. Several studies have shown that vimentin influences the motile behaviour of mitochondria.[201,210,211] This is also the case in giant axonal neuropathy (GAN), a disease caused by mutations in gigaxonin, an E3 ligase adaptor which targets IFs for degradation. These mutations lead to large aggregates and bundles of vimentin. This in turn goes along with an altered distribution and decreased motility of mitochondria, with the authors describing the mitochondria behaving as if they were anchored to the disturbed vimentin.[212,213] The influence of IFs on mitochondrial motility was also shown in neuronal cells, which display a redistribution of mitochondria upon microinjection with excess neurofilaments.[214]

These studies indicate that intermediate filaments are able to influence the distribution and dynamics of mitochondria and implicate a colocalisation and potential physical connection between the two components. Although these studies prove that different IF proteins are located in close proximity to mitochondria, precise biochemical evidence of putative binding mechanisms remain to be investigated.

Despite missing potential binding mechanisms, it has been shown that IF disturbances affect mitochondrial function on different levels, such as mitochondrial signalling, energy production, calcium handling or lipid metabolism. Intermediate filament-formed aggregates in GAN for example increase energy demands in neuronal cells.[213] Also keratin network disruptions have been shown to lead to an altered ATP metabolism. However, the results of these investigations point either to increased cellular ATP levels, which were shown in keratin cluster knockout mice[215] or towards decreased ATP content in mitochondria of keratin 8 knockout ß-cells[202] which goes along with a strong decrease in mitochondrial membrane potential.[203]
Among the studies indicating impaired calcium handling upon IF disruption is a study from Fountoulakis and colleagues which used proteomic analysis and discovered perturbed calcium homeostasis in hearts of desmin knockout mice.[124] Furthermore, mice expressing an aggregation-prone desmin mutant not only show altered mitochondrial morphology, but also differences in calcium handling in both skeletal and cardiac muscle. In particular, these cells show an increased mitochondrial calcium uptake and reduced calcium release, resulting in an overload of mitochondrial calcium.[216] These results are contradictory to *in vitro* studies which demonstrated impaired calcium uptake in myotubes expressing aggregation-prone desmin

mutants.[217] Furthermore, knockout of desmin causes mitochondria to be more susceptible to high calcium levels.[218] The consequences of disturbed calcium handling might for instance have severe consequences on autophagy and apoptosis, as mitochondrial calcium overload promotes both processes, whereas only a slight increase boosts ATP production.[219,220]

Another interesting aspect is the influence of intermediate filaments on mitochondrial lipid metabolism, which has mainly been shown in epithelial cells. One of the important subcellular structures in this context are the mitochondria-associated membranes, which are crucial for functional calcium transfer between the two organelles.[221] As indicated earlier, an altered mitochondrial distribution can also alter the distance to the ER and might thus influence crucial MAM functions.[209] The putative keratin-binding protein trichoplein/mitostatin was suggested to play a role in ER-mitochondria tethering.[222,223] More explicit hints come from investigations of keratin cluster-knockout keratinocytes that display alterations of the lipid composition.[215] This includes the elevation of phosphatidyl ethanolamine and the mitochondrial non-bilayer-forming lipid cardiolipin,[215] whose precursors are imported from the ER into mitochondria via MAMs.[206,209,224] This in turn might explain why the absence of keratins causes disruption of mitochondrial lipid homeostasis and possibly also the structural and functional alterations of mitochondria.[215,225,226]

All of these studies have expanded knowledge of intermediate filament functions and shown that various intermediate filament-forming proteins affect mitochondrial morphology, spatial distribution, and function. However, the precise mechanisms of interaction between mitochondria and IFs still have to be elucidated.

I.4.2 Maintenance of mitochondrial integrity

The main function of mitochondria is to supply the cell with ATP, and they are thus known as the “powerhouse of the cell”. However, they fulfil a variety of other important functions, such as regulating calcium homeostasis, producing reactive oxygen species, influencing apoptosis and autophagy, and metabolising amino acids, lipids, and glucose.[227] As the organelles are inherited and cannot be produced *de novo,* a stringent quality control is required to maintain a healthy cellular pool of mitochondria. The biogenesis of mitochondrial mass is driven by proteins encoded by both mitochondrial DNA (mtDNA) and nuclear DNA (nDNA).

One of the mechanisms driving mitochondrial quality control is fusion of mitochondria. It allows exchange of mtDNA, proteins and metabolites between mitochondria of different health statuses and thus prevents accumulation of these contents in single mitochondria. As they are double-membrane-bound organelles, mitochondrial fusion of both the outer mitochondrial

membrane (OMM), controlled by mitofusins (MFN), and inner mitochondrial membrane (IMM), regulated by optic atrophy 1 (OPA1), has to take place.[228]

Complementary, mitochondrial fission is required for content transmission to daughter cells during mitosis, separation of damaged contents, or the fragmentation of mitochondria prior to their ultimate removal by autophagy. The main regulating protein is dynamin-related protein 1 (Drp1), a cytosolic GTPase, which is recruited to the OMM in order to build multimeric ring-like structures at mitochondrial fission sites, thus constricting and scissoring the organelles. The recruitment of Drp1 to mitochondria is mediated by different OMM-localised receptors.[228]

However, fusion and fission events are sometimes not sufficient to keep a healthy mitochondrial pool, because some damaged mitochondria produce reduced ATP levels and release high levels of reactive oxygen species (ROS) and must thus be permanently eliminated.[229] This process is a specialised form of macroautophagy, called mitophagy. As macroautophagy is essential to remove organelles of differentiating keratinocytes in order to become corneocytes,[17] alterations of this process might play a role in epidermal keratinopathies.

One of the best-studied mitophagy pathways relies on the serine/threonine kinase phosphatase and tensin homolog (PTEN)-induced kinase 1 (PINK1) and Parkin.[229] The key processes of this pathway are depicted in Fig. 8 and described in the following section.
A healthy mitochondrial state is characterised by an intact mitochondrial membrane potential. In this ground state, PINK1 is constitutively expressed at basal levels.[230] Immediately after translation, PINK1 is translocated to mitochondria due to its N-terminal mitochondrial targeting sequence (MTS). Subsequently, it is imported into mitochondria via the TOM (translocase of outer membrane)/TIM23 (translocase of inner membrane 23) complex and cleaved by presenilin-associated rhomboid-like protein (PARL). The cleaved protein is then released back into the cytosol and rapidly degraded by the proteasomal pathway.[231]
If depolarisation of the mitochondrial membrane potential occurs, the import of PINK1 via TIM23 at the inner mitochondrial membrane is blocked due to PINK1 autophosphorylation at serins 228 and 402.[232] This results in stabilisation of PINK1 at the OMM, representing the first cellular signal indicating damaged mitochondria.[233] PINK1 then catalyses the phosphorylation of ubiquitin which is constitutively present on certain OMM proteins, such as mitochondrial Rho GTPase 1 (RHOT1/Miro), mitofusin 2 or TNF Receptor Associated Protein (TRAP-1).[234] The accumulation of PINK1 on mitochondria furthermore drives the recruitment of the E3 ubiquitin ligase Parkin[235] and it was shown that PINK1 binds to[236-238] and phosphorylates Parkin.[239,240] However, the exact molecular mechanism of PINK1-driven Parkin recruitment is still not

elucidated.[231] As Parkin has a higher affinity to phospho-ubiquitin than to the non-phosphorylated version, it is retained to mitochondria[241] and its E3 ubiquitin ligase activity is increased with mitochondrial translocation.[242] Consequently, Parkin attaches ubiquitin moieties to OMM proteins[243] such as mitofusin 1 and 2 [244,245] and VDAC.[236]

The canonical feedback cycle of substrate ubiquitination finally results in poly-ubiquitin chains attached to different proteins of the mitochondrial surface.[241] Subsequently, the ubiquitin-binding adaptors p62 (Sequestosome 1),[236,246-250] optineurin and NDP52 (Nuclear domain 10 protein 52/CALCOCO2: Calcium-binding and coiled-coil domain-containing protein 2)[251-253] bind to the ubiquitinated proteins and accumulate on mitochondria. Another protein that is able to bind ubiquitinated substrates is the protein HDAC6 (histone deacetylase 6), which has been shown to accumulate on mitochondria during Parkin-dependent mitophagy.[231,250] The binding of the autophagosome adaptors to LC-3 (MAP1LC3B: Microtubule-associated proteins 1A/1B light chain 3B), a widely used autophagosome marker, then induces the formation of the autophagosomal membrane around damaged organelles.[246,250,252]

A group of genes involved in macroautophagy was initially discovered in yeast and named autophagy-related genes (ATGs)[254] with LC-3 representing the homologue of the yeast protein Atg8. Both versions are covalently attached to phosphatidylethanolamine during autophagosome biogenesis. This enables them to integrate into and modify the forming isolation membrane[255] as well as being involved in cargo recruitment.[256] The source of the autophagosomal membrane has been a contradicting issue for a long time, but several recent studies have shown that autophagosomes can originate from mitochondria-associated membranes.[257-261] Some of these studies have shown that the autophagosomal membranes are clearly derived from the ER, but that no ER markers are found within autophagosomes. Thus, they concluded that tubular ER derivates from a Ω-like-shaped structure which was therefore called omegasome. This structure is enriched in PI3P (phosphatidylinositol-3-phosphate) and the recently discovered PI3P-binding protein DFCP1.[257,258,261] Further supporting evidence includes the relocalisation of PINK1 and the pro-autophagic protein Beclin-1 at MAMs which enhances omegasome formation, as well as the accumulation of Parkin at MAM sites after mitophagy induction.[262] The engulfment of mitochondria itself can be extremely fast and occur within five minutes.[263]

After completion of the autophagosome formation, they are transported to lysosomes and form autolysosomes by fusing with each other. This fusion is required for organelle acidification and degradation of the autophagosomal cargo. Rab proteins are the key players of this fusion process in mammalian cells. Rab7 for example has been implicated in autolysosome maturation[264] and was also shown to interact with the intermediate filament protein vimentin.[190] After hydrolytic degradation of the mitochondrial cargo,[265] the lysosomal components of the autolysosomes are being recycled in order to reform functional lysosomes. This process is

called autophagic lysosome reformation (ALR). It involves the extrusion of tubules from the autolysosomes. These subsequently form proto-lysosomes that still lack lysosomal activity.[266] Lysosomal maturation includes re-acidification and the functional activity of Rab7, a vesicle transport regulator, and KIF5B, a member of the kinesin 1 family.[264,267]

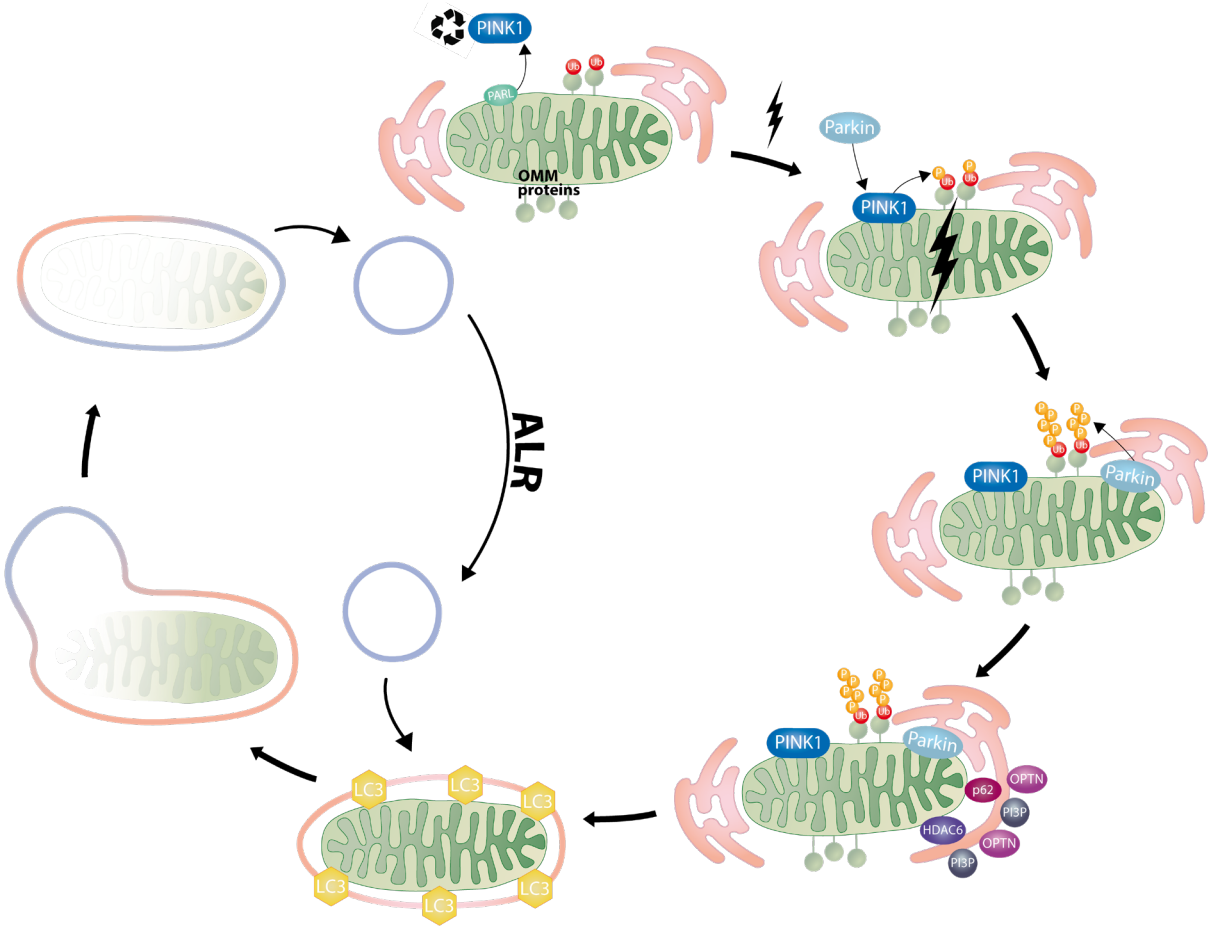

Figure 8 – The canonical PINK1/Parkin-dependent mitophagy pathway. During a healthy mitochondria state, PINK1 is imported into mitochondria, cleaved by PARL, and degraded via the proteasomal pathway. If mitochondria are severely damaged, i.e. the membrane potential being depolarised, the protein PINK1 is accumulating on the outer mitochondrial membrane. PINK1 then phosphorylates ubiquitin which is constitutively present on certain OMM proteins. Furthermore, recruitment of Parkin is induced, which then further ubiquitinates OMM proteins. Subsequently, ubiquitin-binding adaptor proteins such as p62, optineurin (OPTN), and HDAC6 are recruited. These adaptors bind to LC-3 and the formation of the omegasome is initiated, enriched in PI3P. Once autophagosomes fully engulf mitochondria, they fuse with lysosomes (blue circle) and form autolysosomes. The lysosomal components are recycled after completion of cargo degradation by autolysosomal reformation (ALR).

I.13 Objectives

The overall aim of this work was to gain a better understanding of the mechanisms of disturbed keratin network formation and its functional consequences in genetic skin disorders caused by keratin mutations. For this purpose, epithelial cells stably overexpressing mutant keratins and immortalised human keratinocytes derived from healthy subjects and *Epidermolysis bullosa simplex* and *Pachyonychia congenita* patients were used.

The first objective was to establish and apply advanced image analysis tools to quantitatively determine the dynamic properties of the pathognomonic keratin granules. To this end, high resolution time-lapse recordings of fluorophore-tagged keratin mutants were used to obtain numerical information on granule motility and turnover, and the contribution of potential modulators.

The second objective was to examine the functional consequences of keratin mutations, focusing on mitochondrial quality control. This goal was based on pilot experiments which suggested dysfunctional mitophagy in keratinopathies. To corroborate this hypothesis, mitochondrial overaging and the canonical mitophagy pathway were investigated using a combination of molecular, biochemical, and microscopy methods.

II. Material and methods

II.1 Material

II.1.1 Chemicals

Table 1: List of chemicals

Name	Source of supply
2-Mercaptoethanol	Carl Roth, Karlsruhe, Germany
Acetic acid	Carl Roth, Karlsruhe, Germany
Acetone	Carl Roth, Karlsruhe, Germany
Acrylamide/bisacrylamide 40%, mixing ratio 29:1	Carl Roth, Karlsruhe, Germany
Agar-Agar, Kobe I	Carl Roth, Karlsruhe, Germany
Agarose, high gelling	Sigma-Aldrich, St. Louis, MO, USA
Ammonium hydroxide 5N	Sigma-Aldrich, St. Louis, MO, USA
Ammonium persulfate (APS)	Sigma-Aldrich, St. Louis, MO, USA
Boric acid	Carl Roth, Karlsruhe, Germany
Bovine serum albumin - Fraction V (BSA)	Sigma-Aldrich, St. Louis, MO, USA
Bromophenol blue	SERVA Electrophoresis GmbH, Heidelberg, Germany
$CaCl_2$	Merck KGaA, Darmstadt, Germany
Copper(II) sulfate	Merck KGaA, Darmstadt, Germany
Dimethyl sulfoxide (DMSO)	Merck KGaA, Darmstadt, Germany
Dithiothreitol (DTT)	Merck KGaA, Darmstadt, Germany
Elvanol	Carl Roth, Karlsruhe, Germany
Ethanol	Carl Roth, Karlsruhe, Germany
Ethylene glycol tetraacetic acid (EGTA)	Sigma-Aldrich, St. Louis, MO, USA
Ethylenediaminetetraacetic acid (EDTA)	Sigma-Aldrich, St. Louis, MO, USA
Formaldehyde	Carl Roth, Karlsruhe, Germany
Gel loading dye purple (6x)	New England Biolabs (NEB), Ipswich, MA, USA
Glutaraldehyde	Merck KGaA, Darmstadt, Germany
Glycerol (99.5%)	Carl Roth, Karlsruhe, Germany
Glycine	Biomol GmbH, Hamburg, Germany
Hydrochloric acid 1N	Carl Roth, Karlsruhe, Germany
Hydrochloric acid 37%	Carl Roth, Karlsruhe, Germany
Isopropanol	Carl Roth, Karlsruhe, Germany
KCl	SERVA Electrophoresis GmbH, Heidelberg, Germany
Methanol	Carl Roth, Karlsruhe, Germany
Midori Green Advance	Nippon Genetics Europe (Düren, Germany)
$MnCl_2$	Sigma-Aldrich, St. Louis, MO, USA
MnCl24H2O	Merck KGaA, Darmstadt, Germany
N-acetyl-l-cysteine, ≥ 99% (TLC), powder	Sigma-Aldrich, St. Louis, MO, USA
NaCl	Carl Roth, Karlsruhe, Germany
NaOH	Carl Roth, Karlsruhe, Germany
PBS, without Ca2+/Mg2+	Sigma-Aldrich, St. Louis, MO, USA

Name	Source of supply
PBS, without Ca2+/Mg2+, powder	Biochrom, belongs to Merck KGaA, Darmstadt, Germany
Phos-tag™ solution	Wako Chemicals, Neuss, Germany
Pierce™ ECL Western blotting substrate	Thermo Fisher Scientific, Waltham, MA, USA
Ponceau S	Sigma-Aldrich, St. Louis, MO, USA
Powdered milk, blotting grade, low fat	Carl Roth, Karlsruhe, Germany
Roti®-Block Blocking Reagent	Carl Roth, Karlsruhe, Germany
Sodium bicarbonate	Carl Roth, Karlsruhe, Germany
Sodium dodecyl sulfate (SDS)	SERVA Electrophoresis GmbH, Heidelberg, Germany
Tetramethylethylenediamine (TEMED)	Carl Roth, Karlsruhe, Germany
Tris(hydroxymethyl)aminomethane (Tris base)	Biomol GmbH, Hamburg, Germany
Tris(hydroxymethyl)aminomethane hydrochloride (Tris HCl)	Life Technologies, Carlsbad, CA, USA
Triton-X 100	Sigma-Aldrich, St. Louis, MO, USA
Trypan blue	Sigma-Aldrich, St. Louis, MO, USA
Tryptone	Carl Roth, Karlsruhe, Germany
Tween-20	Merck KGaA, Darmstadt, Germany
Uranylacetate	EMS, Domat, Switzerland
Vaseline	Sigma-Aldrich, St. Louis, MO, USA
Yeast extract	Carl Roth, Karlsruhe, Germany

II.1.2 Buffers

Table 2: List and composition of buffers

Buffer	Composition
5X SDS denaturation buffer	83% (v/v) Glycerine, 7.5% (w/v) SDS, 16.6% (w/v), 16.6% (v/v) ß-Mercaptoethanol, 250 µg/ml bromphenolblue, dissolved in stacking gel buffer
LB agar plates	1% (w/v) Trypton, 0,5% (w/v) yeast extract, 86mM NaCl, 1,5% (w/v) agar-agar (autoclaved)
LB medium	1% (w/v) Trypton, 0,5% (w/v) yeast extract, 86 mM NaCl (autoclaved)
LB medium high salt	1% (w/v) Trypton, 0,5% (w/v) yeast extract, 171 mM NaCl (autoclaved)
Phosphate-buffered saline (PBS)	137 mM NaCl, 2,7 mM KCl, 8,1 mM Na2HPO4, 1,5 mM KH2PO4 (pH 7,4)
Phos-tag transfer buffer A	25 mM Tris-HCl, 190 mM glycine, 0.1% (v/v) SDS, 20% (v/v) Methanol, 1 mM EDTA
Phos-tag transfer buffer B	25 mM Tris-HCl, 190 mM glycine, 0.1% (v/v) SDS, 20% (v/v) Methanol
Resolving gel buffer	1.5 M Tris + 0.4% (v/v) SDS, pH 8.8
RIPA buffer	50 mM Tris-HCl, 150 mM NaCl, 1% (v/v) Triton X-100, 0.5% (v/v) DOC, 0.1% (v/v) SDS, pH 8.0, 1 tablet PhosSTOP + 1 tablet cOmplete™ ULTRA Mini added per 10 ml
SDS running buffer (10X)	250 mM Tris, 1.92 M glycine, 1% (v/v) SDS
SOC medium	0.5% (w/v) yeast extract, 2% (w/v) tryptone, 10 mM NaCl, 2.5 mM KCl, 10 mM $MgCl_2$, 10 mM $MgSO_4$, 20 mM glucose (autoclaved)
Stacking gel buffer	780 mM Tris + 0.4% (v/v) SDS, pH 6.8
Stripping buffer	100 mM glycine (pH 2)
TBE buffer	102 mM Tris, 89 mM H_3BO_3, 1,6 mM EDTA

Buffer	Composition
TBST	20 mM Tris, 150 mM NaCl, 0,1% (v/v) Tween-20 (pH 7.6)
Transfer buffer	192 mM glycine, 25 mM Tris, 20% (v/v) methanol

II.1.3 Molecular weight markers

Table 3: List of molecular weight markers

Name	Source of supply
GeneRuler 100 bp Plus (SM0321)	Thermo Fisher Scientific, Waltham, MA, USA
GeneRuler 1 kb DNA Ladder (SM0311)	Thermo Fisher Scientific, Waltham, MA, USA
GeneRuler DNA Ladder Mix	Thermo Fisher Scientific, Waltham, MA, USA
ProSieve QuadColor Protein Marker	Lonza, Basel, Switzerland

II.1.4 Kits

Table 4: List of kits

Name	Source of supply
AceGlow™ Chemiluminescence Substrate	PEQLAB Biotechnologie GmbH, Erlangen, Germany
DNeasy Blood&Tissue Kit	Qiagen, Venlo, The Netherlands
FastStart Essential DNA Green Master kit	Roche, Mannheim, Germany
KAPA HiFi Kit	KAPA Biosystems, Wilmington, MS, USA
Magic Red® Cathepsin B	ImmunoChemistry Technologies, Bloomington, USA
NucleoBond™ Xtra Maxi-Kits	Macherey-Nagel, Düren, Germany
QIAfilter Plasmid Maxi Kit	Qiagen, Venlo, The Netherlands
QIAprep Spin Miniprep Kit	Qiagen, Venlo, The Netherlands
QIAquick Gel Purification Kit	Qiagen, Venlo, The Netherlands
RNeasy Mini Kit	Qiagen, Venlo, The Netherlands
T4 DNA Ligase Kit	New England Biolabs (NEB), Ipswich, MS, USA
Transcriptor First Strand cDNA synthesis kit	Roche, Mannheim, Germany
Venor®GeM Mycoplasma Detection kit	Minerva Biolabs GmbH, Berlin, Germany
Xfect polymer + Xfect reaction buffer	TakaraBio, Shiga, Japan

II.1.5 Enzymes

Table 5: List of enzymes

Name	Source of supply
Alkaline phosphatase	Sigma-Aldrich, St. Louis, MO, USA
Pierce Universal Nuclease for Cell Lysis	Thermo Fisher Scientific, Waltham, MA, USA
Reverse transcriptase	Roche, Mannheim, Germany
rSAP (shrimp alkaline phosphatase)	New England Biolabs (NEB), Ipswich, MS, USA

Table 6: List of restriction endonucleases

Enzyme	Recognition site	Buffer	Source of supply
BamHI-HF	G*GATCC	cutsmart®	New England Biolabs (NEB), Ipswich, MS, USA
BsrGI-HF	T*GTACA	cutsmart®	New England Biolabs (NEB), Ipswich, MS, USA
XhoI	C*TCGAG	cutsmart®	New England Biolabs (NEB), Ipswich, MS, USA
AgeI-HF	A*CCGGT	cutsmart®	New England Biolabs (NEB), Ipswich, MS, USA
Bgl II	A*GATCT	cutsmart®	New England Biolabs (NEB), Ipswich, MS, USA

* *marks the restriction endonuclease cutting site*

II.1.6 Inhibitors

Table 7: List of inhibitors

Name	Source of supply
Bafilomycin A1	Sigma-Aldrich, St. Louis, MO, USA
cOmplete ULTRA tablets Mini EASYpack (Protease inhibitor)	Roche, Mannheim, Germany
Cyanide m-chlorophenylhydrazone (CCCP)	Abcam, Cambridge, MA, USA
Leucettine L41	Adipogen, Diego, USA
ML-7	Tocris Bioscience, Bristol, UK
Para-nitroblebbistatin	Optopharma, Budapest, Hungary
PhosSTOP EASYpack (Phosphatase inhibitor)	Roche, Mannheim, Germany

II.1.7 Cell culture media, matrix proteins, and antibiotics

Table 8: List of cell culture media, matrix proteins and antibiotics

Name	Source of supply
Accutase	PAA Laboratories, Pasching, Austria
Ampicillin sodium salt (used at 150 µg/ml)	Carl Roth, Karlsruhe, Germany
Antibiotic-Antimycotic (100X)	Sigma-Aldrich, St. Louis, MO, USA
Aqua B. Braun (distilled H2O)	B. Braun Melsungen AG, Melsungen, Germany
Collagen type I rat tail	Corning Incorporated, Corning, NY, USA
DPBS without Ca/Mg	Sigma-Aldrich, St. Louis, MO, USA
Dulbecco's Modified Eagle Medium (DMEM), high glucose	PAA Laboratories, belongs to General Electric, Fairfield, CT, USA
Dulbecco's Modified Eagle Medium (DMEM), high glucose, no glutamine, no phenol red (Gibco)	Life Technologies, Carlsbad, CA, USA
EpiLife medium (60 µM Calcium)	Thermo Fisher Scientific, Waltham, MA, USA
Sera Plus, EU approved regions, special processed FBS, 0.2 µm sterile filtered	Pan Biotech, Aidenbach, Germany
Human Keratinocyte Growth Supplement (HKGS)	Thermo Fisher Scientific, Waltham, MA, USA
Kanamycin sulphate (used at 60 µg/ml)	Carl Roth, Karlsruhe, Germany
Trypsin neutraliser	Thermo Fisher Scientific, Waltham, MA, USA
Trypsin, powder	Biochrom, belongs to Merck KGaA, Darmstadt, Germany

II.1.8 Antibodies

Table 9: List of primary antibodies

Antigen	Lab-internal number	Clonality	Species source	Lot nr.	Dilution immuno-cyto-chemistry	Dilution immuno-blot	Order number, source of supply
Beta-actin	rb123	Polyclonal	Rabbit	095M4765V, 018M4753V, 099M4864V	-	1:2000	A 2066, Sigma-Aldrich
Dyrk1B (H-6)	mc232	Monoclonal	Mouse	#G2817	1:200	-	sc-390417, Santa Cruz
Dyrk3 (H-11)	mc230	Monoclonal	Mouse	#J1016	1:200	-	sc-390532, Santa Cruz
GAPDH	Mc123	Monoclonal	Mouse	GR9686-1, GR286286-16	-	1:2000	ab9484, Abcam
Keratin 14	gp83	Antiserum	Guinea pig	-	1:2000	-	Provided by Lutz Langbein, DKFZ
Keratin 5	gp41	Polyclonal	Guinea pig	604141, 703281	1:100	-	GP-CK5, Progen
Non muscle Myosin Heavy Chain IIA	rb244	Polyclonal	Rabbit	B204023, B259821	1:200		90801, BioLegend
Non muscle Myosin Heavy Chain IIB	rb269	Polyclonal	Rabbit	B254282	1:500	-	19099, BioLegend
Optineurin	N/A; sample	Monoclonal	Rabbit	1	-	1:1000	D2L8S, Cell signaling
p62/sequesto-some	gp-87	Polyclonal	Guinea pig	FAK15149-01	-	1:1000	GP62-C, Progen
Pan-Keratin	mc192	Monoclonal	Mouse	#RA213618 9, VK3105871 B	1:200	-	MA5-13203, Thermo Fisher
PI3K p85	rb198	Polyclonal	Rabbit	4	-	1:1000	4292, Cell Signaling
PINK1	rb255	Polyclonal	Rabbit	GR1117074, GR2117078, GR111707-18, GR 3217577-1	-	1:1000	ab23707, Abcam
PTEN	rb230	Monoclonal	Rabbit	12	-	1:1000	9559, Cell Signaling
VDAC	rb201	Monoclonal	Rabbit	YJ091913S, GR219209-9	-	1:5000	ab154856, Abcam

Table 10: List of secondary antibodies

Antigen	Lab-internal number	Clonality	Species source	Lot nr.	Dilution immuno-cyto-chemistry	Dilution immuno-blot	Order number, source of supply
Goat anti-Guinea Pig IgG-Alexa555	Gp-B	Polyclonal	Goat	1666303	1:500	-	A-21435, Molecular probes
Goat anti-Guinea Pig IgG-Alexa488	Gp-E	Polyclonal	Goat	1841755, 2304259	1:1000	-	A-11073, Invitrogen
Goat anti-Mouse IgG-Alexa488	Mc-B	Polyclonal	Goat	1829920	1:500	-	A-11029, Invitrogen
Goat anti-Mouse IgG-Alexa647	Mc-M	Polyclonal	Goat	751096	1:200	-	A-21236, Invitrogen
Goat anti-Mouse IgG-Alexa555	Mc-P	Polyclonal	Goat	1040044, 2123594	1:1000	-	A-21424, Invitrogen
Donkey anti-Rat IgG-DyLight405	Rat-D	Polyclonal	Donkey	129503, 139541	1:250	-	712-476-153, Jackson/ Dianova
Anti-rabbit-HRP	Rb X	Polyclonal	Goat	20027913, 20023997	-	1:5000	P0448, DAKO
Goat F(ab)2 anti-Rabbit-Alexa488	Rb-C	Polyclonal	Goat	1705868, 1907301, 2018208	1:1000	-	A-11070, Invitrogen
Goat F(ab)2 anti-Rabbit-Alexa633	Rb-E	Polyclonal	Goat	1839600	1:1000	-	A-21072, Thermo Fisher
Donkey F(ab)2 anti-Rabbit-Alexa488	Rb-L	Polyclonal	Donkey	146640	1:1000	-	711-546-152, Jackson/Dianova
Donkey F(ab)2 anti-Rabbit-Alexa647	Rb-U	Polyclonal	Donkey	134897	1:200	-	711-606-152, Dianova
Donkey F(ab)2 anti-Rabbit-DyLight405	Rb-V	Polyclonal	Donkey	131876	1:200	-	711-476-152, Dianova

Table 11: List of fluorescent dyes

Dye	Dilution	Source of supply
MitoTracker Red CMXRos	100 nM/L	Thermo Fisher Scientific, Waltham, MA, USA
Phalloidin-Alexa488	1:500	A12379, Invitrogen, GmbH, Karlsruhe, Germany
Phalloidin-Alexa647	1:500	A30107, Invitrogen, GmbH, Karlsruhe, Germany

II.1.9 Labware

Table 12: List of labware

Name	Source of supply
10 ml serological pipette, sterile	Corning Incorporated, Corning, NY, USA
100 µl Bevelled, Filter Tip (Sterile)	STARLAB INTERNATIONAL GmbH, Hamburg, Germany
1000 µl, Filter Tip (Sterile)	STARLAB INTERNATIONAL GmbH, Hamburg, Germany
2 ml serological pipette, sterile	Greiner Bio-One GmbH, Frickenhausen, Germany
20 µl XL Graduated Filter Tip (Sterile)	STARLAB INTERNATIONAL GmbH, Hamburg, Germany
200 µl Graduated, Filter Tip (Sterile)	STARLAB INTERNATIONAL GmbH, Hamburg, Germany
25 ml serological pipette, sterile	Greiner Bio-One GmbH, Frickenhausen, Germany
5 ml serological pipette, sterile	Greiner Bio-One GmbH, Frickenhausen, Germany
50 ml Centrifuge Tubes with Screw Caps	VWR International, Radnor, PA, USA
96 well Tissue culture plates	SPL Life Sciences Co., Ltd., Korea
Amersham Hyperfilm ECL	GE Healthcare, Buckinghamshire, UK
Autoclaving band	Carl Roth, Karlsruhe, Germany
Bottle-Top-Filter, ZA92, 0.22 µm (500 ml)	A. Hartenstein Laborbedarf GmbH, Würzburg, Germany
CELLSTAR culture dishes, 100x20 mm	Greiner Bio-One GmbH, Frickenhausen, Germany
CELLSTAR culture dishes, 60x15 mm	Greiner Bio-One GmbH, Frickenhausen, Germany
Cloning cylinder ⌀8mm	Hilgenberg, Malsfeld, Germany
Cover slips, d=24 mm, #1.5	Gerhard Menzel GmbH, Braunschweig, Germany
CRYO.S, PP, with screw cap, sterile	Greiner Bio-One GmbH, Frickenhausen, Germany
Disposal boxes	SARSTEDT, Nümbrecht, Germany
Easy-Grip Cell Culture Dish, 35x10 mm	Becton Dickinson Labware, Franklin Lakes, NJ, USA
EU Classic Thin-wall 8-tube Stripe 0.2 ml	BIOplastics, Landgraaf, The Netherlands
EU Optical Semi-Domed Cap	BIOplastics, Landgraaf, The Netherlands
Filter-Tips, 1000 µl (4x32)	Qiagen, Venlo, The Netherlands
Glass bottom dishes, d=14 mm	MatTek Corporation, Ashland, MA, USA
Glass Pasteur Pipettes	Carl Roth, Karlsruhe, Germany
Immobilon-P Transfer Membrane	Merck Millipore, Darmstadt, Germany
Micro tube 1.5 ml	SARSTEDT, Nümbrecht, Germany
Micro tube 1.5 ml, green	SARSTEDT, Nümbrecht, Germany
Midwest TPP Cell Scraper 24CM 150/CS	Thermo Fisher Scientific, Waltham, MA, USA
Natural-rubber scraper	Sigma-Aldrich, St. Louis, MO, USA
Object slides, 76x26 mm	R. Langenbrinck, Emmendingen, Germany
Parafilm	Pechiney Plastic Packaging, Menasha, WI, USA
Pipette tip 200 µl, yellow	SARSTEDT, Nümbrecht, Germany

Name	Source of supply
Pipette tips Standard MIKRO, 0.1-10 µl PP	Carl Roth, Karlsruhe, Germany
SafeSeal micro tube 2 ml, PP	SARSTEDT, Nümbrecht, Germany
Secureline Lab Markers	Aspen Surgical, Southbelt Dr. SE, MI, USA
Syringe Filter Unit, 0.22 µm, Millex-GP	Merck Millipore, Darmstadt, Germany
Syringe filter, 0.45 µm, (surfactant-free)	Sigma-Aldrich, St. Louis, MO, USA
tips Crystal-E-0.5-10 µl	Ratiolab GmbH, Dreieich, Germany
Tissue culture flasks, 250 ml	Greiner Bio-One GmbH, Frickenhausen, Germany
Tissue culture flasks, 50 ml	Greiner Bio-One GmbH, Frickenhausen, Germany
Tube 15 ml, 120x17mm, PP, non-pyrogenic	SARSTEDT, Nümbrecht, Germany
Tube 50 ml, 114x28mm, PP, non-pyrogenic	SARSTEDT, Nümbrecht, Germany
Whatman®, Gel Blotting Papers	VWR International, Radnor, PA, USA

II.1.10 Laboratory equipment

Table 13: List of laboratory equipment

Name	Source of supply
Biometra OV-4 hybridisation oven	Biometra, GmbH Göttingen, Germany
Biometra Power Pack P25	Biometra GmbH, Göttingen, Germany
Centrifuge 5417C	Eppendorf, Hamburg, Germany
Centrifuge 5417R	Eppendorf, Hamburg, Germany
Centrifuge 5810	Eppendorf, Hamburg, Germany
Cloning Cylinder made of borosilicate glass 3.3, 8 mm height, outer diameter 8 mm	Hilgenberg, Malsfeld, Germany
Consort E455	Consort, Turnhout, Belgium
Ice machine B200	ZIEGRA Eismaschinen GmbH, Isernhagen, Germany
Electrophoresis Power Supply EPS 3500	Pharmacia Biotech, belongs to General Electric, Fairfield, CT, USA
Electrophoresis Power Supply EPS 3500XL	Pharmacia Biotech, belongs to General Electric, Fairfield, CT, USA
Electrophoresis Power Supply EPS 3501XL	Pharmacia Biotech, belongs to General Electric, Fairfield, CT, USA
Eppendorf research pipette (0.1-2.5 µl)	Eppendorf AG, Hamburg, Germany
Eppendorf research pipette plus (10 µl)	Eppendorf AG, Hamburg, Germany
Eppendorf research pipette (2-20 µl)	Eppendorf AG, Hamburg, Germany
Eppendorf research pipette (10-100 µl)	Eppendorf AG, Hamburg, Germany
Eppendorf research pipette (100-1000 µl)	Eppendorf AG, Hamburg, Germany
Fusion-Solo.WL.4M	Vilber Lourmat, France
GFL 3005 orbital shaker	GFL, Burgwedel, Germany
Heidolph 3002 magnetic stirring hotplate	Heidolph Instruments, Schwabach, Germany
Heidolph Reax 2000 shaker	Heidolph Instruments, Schwabach, Germany
HERACell™ 150i CO2 Incubator	Thermo Fisher Scientific, Waltham, MA, USA
Heraeus® CO2-Auto-Zero (incubator used for bacteria)	Thermo Fisher Scientific, Waltham, MA, USA
Heraeus™ BB15 CO2 Incubator	Thermo Fisher Scientific, Waltham, MA, USA
Heraeus™ Sepatech Megafuge™ 3.0R	Thermo Fisher Scientific, Waltham, MA, USA

Name	Source of supply
HLC Heating-ThermoMixer MHR 23	DITABIS Digital Biomedical Imaging Systems AG, Pforzheim, Germany
Incubator shaker series Innova® 42	New Brunswick Scientific, belongs to Eppendorf, Hamburg, Germany
Integra VACUBOY® - Vacuum Hand Operator	Integra LifeSciences, Plainsboro, NJ, USA
Mini-PROTEAN® 3 Cell System	Bio-Rad, Hercules, CA, USA
Mini-PROTEAN® Tetra Cell System	Bio-Rad, Hercules, CA, USA
Moulinex Micro-Chef FM 2515 (microwave oven)	Moulinex, belongs to Groupe SEB, Ecully, France
MR Hei-Mix L (magnetic stirring hotplate)	Heidolph, Schwabach, Germany
MSC-Advantage Class II Biological Safety Cabinet	Thermo Fisher Scientific, Waltham, MA, USA
Nalgene® Cryo 1°C 'Mr. Frosty' Freezing Container	Thermo Fisher Scientific, Waltham, MA, USA
Nanodrop™ 1000 (microvolume spectrometer)	Thermo Fisher Scientific, Waltham, MA, USA
peqSTAR 96 Universal (thermal cycler)	PEQLAB Biotechnologie GmbH, Erlangen, Germany
peqSTAR 96 Universal gradient (thermal cycler)	PEQLAB Biotechnologie GmbH, Erlangen, Germany
PerfectBlue™ Wide Gel System (40-2314)	PEQLAB Biotechnologie GmbH, Erlangen, Germany
pH211 Microprocessor pH Meter	Hanna Instruments, Woonsocket, USA
PP3000 Programmable High Voltage Power Supply	Biometra, Göttingen, Germany
Reverstir RS-8 (magnetic stirring plate)	Toyo Kagaku Sangyo Ltd., belongs to Advantec Toyo Kaisha Ltd., Tokyo, Japan
RH basic 2 IKAMAG (magnetic stirring hotplate)	IKA-Werke GmbH & Co. KG, Staufen, Germany
Roller mixer RS-TR05	Phoenix Instruments GmbH, Garbsen, Germany
Rotanta 460R	Hettich Zentrifugen, Tuttlingen, Germany
SM25 mechanical shaker	Edmund Bühler GmbH, Hechingen, Germany
Systec VX-150 autoclave	Systec, Wettenberg, Germany
Techne Dri-Block® Heater DB-1	Bibby Scientific Limited, Staffordshire, UK
TS-100, Thermo-Shaker	Biosan, Riga, Latvia
Ultramicrotome	Leica, Wetzlar, Germany
Variomag Electronicrührer mono (magnetic stirrer)	Thermo Fisher Scientific, Waltham, MA, USA
Wacom Bamboo Pen & Touch (graphic tablet)	Wacom, Kazo, Japan

II.1.11 Microscopes

Table 14: List of microscopes

Name/Component	Source of supply
Zeiss LSM 710 Duo	
Axio Observer.Z1	Carl Zeiss, Jena, Germany
Objective Plan-Apochromat 63x / 1.40 Oil DIC M27	Carl Zeiss, Jena, Germany
Laser module LGK 7872 ML8 (Ar: 458, 488, 514 nm)	Carl Zeiss, Jena, Germany
Laser module LGK 7786 P (HeNe: 543 nm)	Carl Zeiss, Jena, Germany
Laser module LGK 7628-1F (HeNe: 633nm)	Carl Zeiss, Jena, Germany
Laser cassette 405 cw (diode laser 405 nm)	Carl Zeiss, Jena, Germany
Sapphire 488-200 Optically Pumped Semiconductor Laser	Coherent, Santa Clara, CA, USA

Name/Component	Source of supply
Compass 215 Diode-Pumped Laser (532 nm)	Coherent, Santa Clara, CA, USA
Definite Focus	Carl Zeiss, Jena, Germany
HXP 120 Compact Light Source	Leistungselektronik JENA GmbH, Jena, Germany
Incubator XL LSM710 S1	Pecon GmbH, Erbach, Germany
Heating Unit XL S	Pecon GmbH, Erbach, Germany
CO2-Module S	Pecon GmbH, Erbach, Germany
IsoStation Vibration Isolated Workstation	Newport Corporation, Irvine, CA, USA
Zen system 2009 (Software)	Carl Zeiss, Jena, Germany
Zeiss Apotome 2	
ApoTome.2	Carl Zeiss, Jena, Germany
Axio Imager.M2	Carl Zeiss, Jena, Germany
AxioCam 305 (camera)	Carl Zeiss, Jena, Germany
AxioCam MRm (camera)	Carl Zeiss, Jena, Germany
AxioVision Rev. 8.42	Carl Zeiss, Jena, Germany
Filters.: 38, 46, 47, 49, 50, 43	Carl Zeiss, Jena, Germany
HXP 120 C	Carl Zeiss, Jena, Germany
Objective: Plan-Apochromat 20X/0.8 DIC	Carl Zeiss, Jena, Germany
Objective: Plan-Apochromat 63X/1.4 Oil DIC	Carl Zeiss, Jena, Germany
Zen Blue 3.0 (Software)	Carl Zeiss, Jena, Germany
Zeiss Axiovert 135	
Axiovert 135	Carl Zeiss, Jena, Germany
Objective: LD A-Plan 20X/0.3 Ph1Var1	Carl Zeiss, Jena, Germany
Objective: A-Plan 10X/0.25 Ph1Var1	Carl Zeiss, Jena, Germany
Objective: N-Achroplan 2,5X/0,07	Carl Zeiss, Jena, Germany
Zeiss Auto Arc HBO (light source)	Carl Zeiss, Jena, Germany
Zeiss EM-10	
Digital camera	Olympus Corporation, Shinjuku, Japan
iTEM software	Olympus Corporation, Shinjuku, Japan
Zeiss EM-10 transmission electron microscope	Carl Zeiss, Jena, Germany

II.1.12 Bacteria strains

Table 15: List of bacteria strains

Bacteria	Genotype	Source of supply
JM109	endA1 glnV44 thi-1 relA1 gyrA96 recA1 mcrB$^+$ Δ(lac-proAB) e14- [F' traD36 proAB$^+$ lacI^q lacZΔM15] hsdR17(r_K-$m_K$$^+$)	New England Biolabs (NEB), Ipswich, MS, USA
NEB® 5-alpha Competent E. coli	*fhuA2 Δ(argF-lacZ)U169 phoA glnV44 Φ80 Δ(lacZ)M15 gyrA96 recA1 relA1 endA1 thi-1 hsdR17*	New England Biolabs (NEB), Ipswich, MS, USA
DH5α	F$^-$ *endA1 glnV44 thi-1 recA1 relA1 gyrA96 deoR nupG purB20* φ80d*lacZ*ΔM15 Δ(*lacZYA-argF*)U169, hsdR17($r_K^-m_K^+$), λ$^-$	New England Biolabs (NEB), Ipswich, MS, USA

II.1.13 Primers

Table 16: List of primers

Primer	Sense/Antisense	Nucleotide sequence (5' → 3')
AGPAT5	sense	TGCGCTACGTGCTGAAAG
AGPAT5	antisense	TGGCACTGCGCTTTACATAG
HDAC6	sense	AGTTCACCTTCGACCAGGAC
HDAC6	antisense	GCCAGAACCTACCCTGCTC
Keratin 5	sense	GCAGATCAAGACCCTCAACAAT
Keratin 5	antisense	CCACTTGGTGTCCAGAACCT
p62/Sequestosome	sense	AGCTGCCTTGTACCCACATC
p62/Sequestosome	antisense	CAGAGAAGCCCATGGACAG
Parkin	sense	GGAGCTGAGGAATGACTGGA
Parkin	antisense	ACAATGTGAACAATGCTCTGCT
PARL	sense	GCTCACTGCGGTCCTAACC
PARL	antisense	CTGAATCCGCATTTTTGTTG
PINK1	sense	GCCATCAAGATGATGTGGAAC
PINK1	antisense	GACCAGCTCCTGGCTCATT
TBP	sense	GAACATCATGGATCAGAACAACA
TBP	antisense	ATAGGGATTCCGGGAGTCAT

II.1.14 Plasmids

Table 17: List of plasmids

Lab-internal nr.	Encoded construct	Source
2395	pEGFP-rDYRK1A: rat DYRK1A in pEGFP-C1	provided by Dr. Walter Becker, Aachen, Germany
2396	pEGFP-hDYRK2: human DYRK2 in pEGFP-C1	provided by Dr. Walter Becker, Aachen, Germany
2397	pEGFP-hDYRK3 : human DYRK3 in pEGFP-C1	provided by Dr. Walter Becker, Aachen, Germany
2349	MyosinIIB-mCherry-N18	Addgene plasmid #55107
350	pmCherry_N1	provided by Anne Kölsch, Aachen, Germany
383	pMitoTimer	Addgene plasmid #52659
2304	eGFP-Parkin	provided by Dr. Sven Geisler, Tübingen, Germany
2322	pftLC3	Addgene plasmid #21074
Plasmids cloned	**in this work**	
2383	Krt14R125C-eYFP_Cbh_T2A_Puro	Krt14R125C-eYFP provided by Dr. Thomas Magin, Leipzig, Germany
2400	Krt14R125C-mCerulean_Cbh_T2A_Puro	eYFP from 2383 replaced with mCerulean

II.1.15 Cell lines

The wild-type human keratinocyte cell line Krt6a wt and the *Epidermolysis bullosa simplex* cell lines K5R165G and Krt14R125C were obtained by immortalisation of normal human epidermal keratinocytes of healthy subjects and EBS patients, respectively, using the HPV E6/E7 method and was kindly provided by Dr Julia Reichelt, Dr Verena Wally and Dr Thomas Lettner (EB house Austria, Salzburg). The PC cell lines Krt6aN171K and Krt6aN171del were derived from *Pachyonychia congenita* patients also by immortalisation of epidermal keratinocytes with the HPV E6/E7 method. They were generously provided by Dr Leonard M. Milstone (Yale University, New Haven).

The MCF-7 cell lines were obtained from Dr. Thomas Magin and generated as previously described, either wild type cells or cell clones stably expressing Krt14-eYFP or Krt14R125C-eYFP.[39]

II.1.16 Software

Table 18: List of used software

Name	Source of supply
AxioVision	Carl Zeiss, Jena, Germany
Clone Manager 9 Professional	Scientific & Educational Software, Cary, NC, USA
FusionCapt Advance	Vilber Lourmat, France
GraphPad Prism 9	GraphPad Software, Inc., La Jolla, CA, USA
Handbrake	The HandBrake Team
Illustrator CS3	Adobe Systems Incorporated, San Jose, CA, USA
ImageJ (Fiji distribution)	National Institutes of Health, USA
Light Cycler Software 3	Roche, Mannheim, Germany
Microsoft Office Professional plus 2016	Microsoft, Redmond, WA, USA
NanoDrop 1000	Thermo Fisher Scientific, Waltham, MA, USA
Photoshop CS3	Adobe Systems Incorporated, San Jose, CA, USA
SnapGene® Viewer 3.3.3	GSL Biotech LLC, San Diego, USA
Windows 7 Professional (64 bit)	Microsoft, Redmond, WA, USA
Zen 2011 (black)	Carl Zeiss, Jena, Germany
Zen 3.3 2011 (blue)	Carl Zeiss, Jena, Germany

II.2 Methods

II.2.1 Molecular Biological Methods

Occasional steps of the following methods were performed by lab technician Laura Koenigs. *In silico* editing was performed using CloneManager and vector maps were illustrated using SnapGene® Viewer.

II.2.1.1 Isolation of genomic DNA

DNA was isolated using the DNeasy Blood and Tissue kit according to the manufacturer´s protocol from one well of a confluent 6-well per cell line for undifferentiated cells. DNA concentration was measured using the Nanodrop™ 1000.

II.2.1.2 Polymerase chain reaction (PCR)

PCR reactions which were used for further cloning of plasmids were performed using the KAPA HiFi Kit, as KAPA polymerase possesses a 3´→5´exonuclease activity that results in a reduced error rate. PCRs were performed according to the manufacturer's protocol with the following standard protocols for reaction mixtures and PCR cycler protocols, unless otherwise stated:

Table 19: Standard reaction mix for PCRs using KAPA Hifi Kit

Component	25 µl reaction	Final concentration
H_2O	X µl	-
5X KAPA HiFi buffer	5.0 µl	1X
KAPA dNTP mix (10 mM)	0.75 µl	0.3 mM
Forward primer (10 µM)	0.75 µl	0.3 mM
Reverse primer (10 µM)	0.75 µl	0.3 mM
KAPA polymerase (1 U/µl)	0.5 µl	0.5 U
DNA	X µl	0.2 ng/µl

Table 20: Standard PCR programme for PCRs using KAPA Hifi Kit

Step	Temperature	Duration	Cycles
Initial denaturation	95 °C	3 min	1
Denaturation	98°C	20 s	15-35**
Annealing	60-75°C*	15 s	
Extension	72°C	15-60 s/kb	
Final extension	72°C	1 min/kb	

* determined via annealing temperature gradient PCR
** highest fidelity: ≤25 cycles;
low template concentrations/low reaction efficiency: 30-35 cycles

II.2.1.3 Restriction digestion

Restriction enzymes were used to specifically cleave DNA. For restriction digestions, whose products were further used for ligation of new plasmids, 5 µg of plasmid DNA was incubated with 5 µl of the respective digestion buffer and 5U of restriction enzyme(s) and up to 50 µl nuclease-free water. Test restriction digestions were used to check for successful ligations. 1 µl plasmid DNA or 2 µl in case of concentrations below 300 ng/µl were incubated with 2 µl of the respective digestion buffer and 1U of restriction enzyme(s) and up to 20 µl nuclease-free water. A non-digested sample of the vector (0.5-1.0 µg DNA) was also investigated. In both cases, the mixture was incubated for 1 hour at 37°C and subsequently purified by Agarose gel electrophoresis. Conditions for digestions with two different enzymes were adjusted according to the following website: https://nebcloner.neb.com/#!/redigest.
To prevent re-ligation of linearised vectors, 1 µl rSAP (recombinant shrimp alkaline phosphatase) was optionally added to a 50 µl reaction mix after the restriction digestion and incubated for further 30 minutes at 37°C followed by 5 minutes heat inactivation at 65°C.

II.2.1.4 Agarose gel electrophoresis

Agarose gel electrophoresis was used to clean up PCR products, purify restriction digestion products and to control for the correct insertion of DNA fragments into plasmids after test restriction digestions. 1% (w/v) agarose was cooked in a microwave oven and when cooled to 60°C Midori Green DNA staining solution was added to a final concentration of 0.001% (v/v). The solution was poured into a gel casting chamber and a comb with the required number of pockets for samples was added. After 30-60 minutes the gel was removed from the casting chamber and inserted into the electrophoresis chamber. Following removal of the comb, the samples were supplemented with the respective amount of 6X gel loading dye and inserted into the pockets. As DNA size standards, the respective DNA ladder was added. Voltage and electrophoresis duration were adjusted to the required degree of separation.

II.2.1.5 PCR fragment purification via agarose gel electrophoresis

Purification of PCR products or restriction digestion products was performed with the QIAquick gel extraction kit according to the manufacturer's protocol with the exception that standardly the DNA was always eluted with 30 µl H_2O after 1 minute incubation.

II.2.1.6 Ligation of DNA fragments

Ligation of PCR products and digested vectors was performed using the T4 DNA Ligase Kit according to the manufacturer´s protocol. Ligation reaction mixes were used with a 3:1 vector/insert ratio, unless otherwise stated. They were prepared according to table 21:

Table 21: Standard ligation using T4 DNA Ligase Kit

Component	3:1 vector/insert ratio	Vector re-ligation control
Linear vector	50 ng	50 ng
Insert DNA	X ng*	-
T4 ligase buffer (10X)	2 µl (1X)	2 µl
T4 ligase	0.2 µl (1U)	0.2 µl
H_2O	Up to 20 µl	Up to 20 µl
Total volume	20 µl	20 µl

* calculated according to the following website: https://nebiocalculator.neb.com/#!/ligation

Ligations were incubated for 2 hours at room temperature and subsequently heat inactivated for 10 minutes at 65°C before transformation.

II.2.1.7 Transformation of competent bacteria

Competent bacteria were thawed on ice for 10 minutes. For standard transformations, JM109 were used and ultra-competent NEB® 5-alpha competent *E. coli* or DH5α strains in case of more complicated cloning procedures. LB agar plates supplemented with antibiotics encoded on the respective plasmid were pre-warmed at 37°C. The complete ligation mixture was added to the bacteria and resuspended. Bacteria were incubated for 30 minutes on ice, followed by 45 seconds of heat shock at 42°C in a water bath. After 10 minutes of incubation, 1 ml of LB (JM109) or 1 ml of SOC medium (NEB ® 5-alpha/ DH5α) was added. After resuspending, the bacteria were incubated at 200 rmp for 30-60 minutes (depending on the antibiotic) at 37°C on a heating block. Next, the samples were centrifuged for 5 minutes at 1000xg. The supernatant, except for 300 µl, was discarded and the pellet resuspended in the remaining medium. The bacteria suspension was evenly distributed with a sterilised spreader rod until it was absorbed. The plates were incubated at 37°C and 5% CO_2 in an incubator. On the next day, 1-5 single colonies were picked with pipette tips and incubated in 5 ml LB medium supplemented with the respective antibiotics in bacteria suspension falcons overnight at 37°C and 250 rpm in an incubator shaker. The bacteria plates were protected by Parafilm and stored at 4°C until the cloning process was completed. Test restriction digestions were performed to confirm the successful integration of the desired fragment into the vector. Optionally, sequencing was performed.

II.2.1.8 Isolation of plasmids & PCR fragments

Bacteria suspensions grown over night were used for plasmid Miniprep using the QIAprep spin miniprep kit according to the manufacturer´s protocol. If analysis of test restriction digestions and optional sequencing confirmed the correct insertion, DNA isolation was performed on a large scale by using NucleoBond™ Xtra Maxi or QIAfilter Plasmid Maxi Kit according to the manufacturers protocol. In both cases, plasmid DNA was stored at -20°C and successfully cloned new plasmids were given a specific lab-internal identification number.

II.2.1.9 Sequencing

DNA plasmids and genomic DNA amplified by PCR were optionally sequenced by Eurofins MWG Operon, Ebersberg, Germany. Custom primers or standard primers provided by Eurofins were used. 50-100 ng of plasmid DNA was sent to be sequenced, or purified PCR products depending on the fragment length:

- 1 ng/µl for 150-300 bp fragments
- 5 ng/µl for 300-1000 bp fragments
- 20 ng/µl for 1000-3000 bp fragments

The sequencing results were compared with *in silico*-created sequences using CloneManager software. In case of uncertainties, the provided chromatograms were additionally analysed to exclude misinterpretations.

II.2.1.10 Generation of plasmids

2383 Krt14R125C-eYFP_Cbh_T2A_Puro

The vector 2157 (Krt14R125C-pEYFP, provided by Dr. Thomas Magin, Leipzig, Germany) with a pEYFP-N1 backbone was digested using the restriction enzymes XhoI and BsrGI. The resulting 2161 bp fragment (Krt14R125C-eYFP) was purified by agarose gel electrophoresis. The vector 2371 (Paxillin-eGFP_Cbh, provided by Dr. Marcin Moch, Aachen, Germany) was also digested using the restriction enzymes XhoI and BsrGI and the 4496 bp fragment purified by agarose gel electrophoresis. Both fragments were ligated, resulting in the 6657bp vector 2383.

2400 Krt14R125C-mCerulean_Cbh_T2A_Puro

The vector 2383 (Krt14R125C-eYFP_Cbh_T2A_Puro) was digested using the restriction enzymes BamHI and BsrGI. The resulting 5929 bp fragment was purified by agarose gel electrophoresis. The vector 2275 (Krt14-mCerulean, pEYFP-N1 backbone, provided by Dr. Marcin Moch, Aachen, Germany[140]) was also digested using the restriction enzymes BamHI

and BsrGI. The 716 bp fragment (mCerulean) was purified by agarose gel electrophoresis. Both fragments were ligated, resulting in the 6645 bp vector 2400.

II.2.1.11 Isolation of RNA

RNA was isolated using the RNeasy Mini Kit according to the manufacturer´s protocol from one confluent well of a 6-well per cell line for either undifferentiated or differentiated (3 days 1.2 mM calcium) cells. RNA concentration was measured using the Nanodrop™ 1000.

II.2.1.12 Reverse transcription of mRNA

Reverse transcription into cDNA was performed using 1 µg RNA which were incubated with random hexamer primers at 65 °C for 10 minutes. After adding 5X reaction buffer, RNase inhibitor, deoxynucleotide mix and reverse transcriptase, the samples were incubated in a cycler for 10 minutes at 25°C, 50 minutes at 50°C and 5 minutes at 85°C and kept at -20°C for long term storage.

II.2.1.13 Quantitative real time polymerase chain reaction (qRT-PCR)

Quantitative real time PCR was performed using the FastStart Essential DNA Green Master kit and primers which were diluted to 10 pm. The cDNA was diluted 1:5 in H_2O and a standard was prepared by pooling cDNA of every sample and a dilution series was generated (1:2, 1:4, 1:8, 1:16, 1:32). The PCR programme is depicted in table 22.

Table 22: Quantitative real-time PCR programme

Step	Temperature	Duration
Preincubation	95°C	600 s
3-step amplification (40 cycles)	95°C	15 s
	60°C	15s
	72°C	30 s
Melting	95°C	10 s
	60°C	60s
	97°C	1 s
Cooling	37°C	30 s

II.2.2 Biochemical Methods

III.2.2.2 Cell lysate preparation

Cell lysate preparation with SDS denaturation buffer

For standard immunoblot, cell lysates were prepared with SDS preparation buffer. Fully confluent cells were washed once with PBS and scraped off with a rubber scraper in 100 µl 2X SDS denaturation buffer per well of a 6-well on ice. To reduce viscosity of lysates, Pierce universal nuclease was added at a final concentration of 25U to each sample. After 15 minutes of incubation at room temperature, the samples were stored at -20°C. Cell lysate samples of HaCaT keratinocytes were provided by Dr. Marcin Moch.

Cell lysate preparation with RIPA buffer

For PhosTag blot, cell lysates were prepared with RIPA buffer. Fully confluent cells were washed once with PBS and scraped off with a rubber scraper in 100 µl RIPA buffer with freshly added PhoSTOP and cOmplete ultra tablets per well of a 6-well on ice. The samples were stored at -20°C and denatured directly before immunoblotting in 5X SDS buffer.

II.2.2.3 SDS polyacrylamide gel electrophoresis (SDS-PAGE)

The frozen cell lysates were thawed on ice, and aliquots were subsequently denatured at 95°C for 5-10 minutes and shortly centrifuged. Proteins were separated by 8-12% discontinuous SDS-polyacrylamide gel electrophoresis. Resolving and stacking gels with a thickness of 1 mm were prepared according to the recipes in table 23 and 24, respectively, in gel casting frames. The resolving gel was prepared, and polymerisation started with addition of APS and TEMED. The gel was inserted into the casting frame, overlaid with isopropanol, and polymerised for 60 minutes. Subsequently, the isopropanol was removed. Next, the stacking gel was prepared, and its polymerisation was started with APS and TEMED. It was loaded above the resolving gel and a comb with 10 or 15 pockets for protein samples was inserted. The gel was polymerised for another 30 minutes and then either used directly, or stored until the next day coated with humid paper tissues in a plastic bag at 4°C.

Table 23: Resolving gel composition

Chemical	8% Acrylamide (1 Gel)	10% Acrylamide (1 Gel)	12% Acrylamide (1 Gel)
Water	3.6 ml	3.0 ml	2.7 ml
40% Acrylamide	0.9 ml	1.5 ml	1.4 ml
Resolving gel buffer	1.5 ml	1.5 ml	1.5 ml
TEMED	6 µl	6 µl	6 µl
10% APS	60 µl	60 µl	60 µl

Resolving gel buffer = 1.5 M Tris + 0.4% (v/v) SDS, pH 8.8

Table 24: Stacking gel composition

Chemical	4.8% (1 gel)
Water	0.8 ml
40% Acrylamide	156 µl
Stacking gel buffer	312.5 µl
TEMED	1.25 µl
10% APS	12.5 µl

Stacking gel buffer = 780 mM Tris + 0.4% (v/v) SDS, pH 6.8

After polymerisation, the gel was inserted into the gel electrophoresis chamber system and the denatured samples, and a protein ladder were inserted into the gel pockets. The electrophoresis was started at 60-80 V until the protein ladder did start to show separated bands. Next, the voltage was increased to 100-120 V for 1-2 hours. The stacking gel part was removed and only the separation gel part used for further analysis.

II.2.2.4 Protein immunoblot

Protein transfer onto polyvinylidene difluoride (PVDF) membrane, which was activated in methanol, was performed in the presence of transfer buffer at 100 V for 1 hour. After transfer, the PVDF membrane was briefly washed in TBST, before blocking with 10% Roti®-Block reagent or 5% (w/v) dried milk powder for 1-2 hours at room temperature. Next, the membrane was incubated with the primary antibody in the respective blocking solution over night at 4°C in a hybridisation oven. Subsequently, the membrane was washed three times for 10 minutes with TBS-T at room temperature, followed by incubation with the HRP-coupled secondary antibody diluted in the respective blocking solution for 1 hour at room temperature with agitation. After another three washing steps in TBS-T, the membrane was covered evenly with 800 µl Pierce™ ECL Western blotting substrate for 1 minute. After removal of the Luminol substrate, chemiluminescence was visualised using Fusion-Solo.WL.4M CCD-camera and recorded with the FusionCapt Advance software.
In order to strip the bound antibody, the membrane was incubated with stripping buffer three times 20 minutes each at room temperature with agitation. Optionally, transfer of proteins onto the membrane was analysed by staining with Ponceau S solution for 5 minutes and subsequent removal of unspecific staining by washing in H_2O until protein bands became visible. To remove the staining, the membrane was incubated in TBS-T. Densitometric evaluation was performed using the “Gel Analyser” function of Fiji.

II.2.2.5 PhosTag SDS-PAGE and immunoblot

PhosTag blot was performed in order to detect alterations of PINK1 phosphorylation. The SDS-PAGE procedure was in principle the same as the standard procedure, with the following alterations:

- Protein sample preparation with RIPA buffer
- Resolving gel recipe adjusted (table 25)
- Incubation of the gel after SDS-PAGE and before immunoblotting for three times 10 minutes in PhosTag transfer buffer A and subsequently 10 minutes in PhosTag transfer buffer B
- Blotting at 100 V for 70 minutes
- Blocking only in 10% Roti®-Block

Table 25: Resolving gel (PhosTag) composition

Chemical	8% Acrylamide (1 Gel)
Water	3.15 ml
40% Acrylamide	1.2 ml
Resolving gel buffer	1.5 ml
$MnCl_2$ x $4H_2O$	120 µl
Phospho-Tag	60 µl
TEMED	17.5 µl
10% APS	85 µl

Resolving gel buffer = 1.5 M Tris + 0.4% (v/v) SDS, pH 8.8

II.2.3 Cell culture & Specific assays

II.2.3.1 Mycoplasma test

Cells were tested for mycoplasma bacteria one time per month using the Venor®GeM Mycoplasma Detection kit according to the manufacturer´s protocol by Nadieh Kuijpers, Sungjun Yoon, and Anna Stermberg. Contaminations with mycoplasma bacteria did not occur during this work.

II.2.3.2 Human keratinocyte cell lines

All keratinocyte cell lines were grown in EpiLife Medium supplemented with 1% (v/v) Antibiotic-Antimycotic solution and 1% (v/v) human keratinocyte growth factor in a 5% CO_2 humidified atmosphere at 37°C. They were grown in uncoated cell culture flasks or on glass coverslips

coated with rat tail collagen I at a final concentration of 5 µg/cm^2. The cell lines were passaged once or twice per week at a ratio of 1:2 - 1:5. For passaging, cells were washed with and incubated for 15 min in PBS without Ca^{2+}/Mg^{2+} and thereafter incubated for ~10 min with accutase and resuspended in trypsin neutraliser solution. After centrifugation at 83xg for 4 minutes, cells were seeded for further passaging or experiments. For experiments under differentiation conditions, cells were switched from standard culture medium (60 µM calcium) to 1.2 mM Ca^{2+} medium (high calcium) for three days.

II.2.3.3 MCF-7 cell lines

MCF-7 cell lines stably transfected with K14-eYFP or Krt14R125C-eYFP were used. They were grown in uncoated flasks or glass bottom dishes in DMEM supplemented with 10% (v/v) FBS in a 5% CO_2 humidified atmosphere at 37°C. The cell lines were passaged once a week at a ratio of 1:10 or 1:20, or if seeded for live cell imaging 1:30 - 1:40. For passaging, cells were washed and incubated for 10 min in PBS without Ca^{2+}/Mg^{2+} and thereafter incubated for ~10 min with accutase and resuspended in trypsin neutraliser solution. After centrifugation at 83xg for 3 minutes, cells were seeded for further passaging or experiments.

II.2.3.4 Freeze-stock preparation and revival of cell lines

Cells were grown until ~80% confluence and then incubated with DPBS and Accutase and centrifuged as previously described. Subsequently, they were resuspended in ice-cold freezing medium containing 10% DMSO, 45% Medium (DMEM + 10% (v/v) FBS or EpiLife + 1% (v/v) HKGS), and 45% FBS. Subsequently, the cell suspension was aliquoted as 1,5 ml of ~1/2 of a 25 cm^2 cell culture flask per cryo-tube and chilled in a Nalgene freezing container filled with 250 ml isopropanol at -80°C overnight. Next, the tubes were shifted into liquid nitrogen for long term storage.

Frozen tubes were partly thawed and the pellet was subsequently resuspended in 5 ml of warm medium. After centrifugation, the cells were seeded on 25 cm^2 cell culture flasks.

II.2.3.5 Collagen I matrix coating

0.05 mg of Collagen was diluted in 1 ml of 0.02 N acetic acid and added to glass bottom dishes or dishes with coverslips at a final concentration of 5 µg/cm^2. The plates were incubated at 37°C for 30 minutes and subsequently washed three times with DPBS. Subsequently, cells were seeded onto the coated plates.

II.2.3.6 Transfection of cell lines

Transfections were performed using the Xfect™ transfection reagent protocol. Cells were grown to approximately 50% confluence before transfection and unless otherwise stated used for experiments 48 h post transfection. For 6-well plates, ⌀3,5 cm dishes or glass bottom dishes 5 µg of plasmid DNA was added to 100 µl of Xfect™ reaction buffer per well/dish and vortexed for 10 seconds. Subsequently, 1.5 µl of Xfect™ polymer was added and the solution was vortexed for another 10 seconds. After 10 minutes of incubation at room temperature, the transfection mix was added to the cells. The medium was changed one day after transfection.

II.2.3.7 Generation of stable cell lines

Cells were seeded onto 6-well plates and transfected with the respective construct(s) at approximately 50% confluence. Medium was exchanged one day after transfection, and after two to three days, the medium was exchanged with antibiotic-supplemented medium which was henceforth used throughout the procedure. Medium was exchanged two to three times per week until the remaining colonies reached approximately 7 mm in diameter. The wells were then washed with DPBS and after removing the solution, ⌀8 mm cloning cylinders were dipped in sterile Vaseline and then carefully positioned around the cell colonies. 100 µl of DPBS was added to each cloning cylinder and incubated for 20 minutes at 37°C. Subsequently, the DPBS was aspirated with a pipet tip, and 50 µl of accutase was added. After a minimal incubation time of 15 minutes at 37°C, the plates were checked under a brightfield microscope if the cells were detached. If the cells were not yet detached, the volume inside the cloning cylinder was gently resuspended and further incubated, until the cells were detached. After detachment, 100 µl of Trypsin Neutraliser was added and the cell suspension inside the cloning cylinder was repeatedly resuspended in pre-heated, antibiotic-supplemented medium and then seeded in 12-well plates. The medium was exchanged the following day to remove any remaining accutase. After reaching 60-80% confluence, the cells were transferred to 6-well plates containing an ⌀8 mm coverslip. The coverslip was fixed for 15 minutes in 4% paraformaldehyde (PFA) at 37°C when at least 30% confluence was reached. If microscopic evaluation confirmed the expected fluorescent signal for ~100% of the cells, the cell clone was further propagated, frozen in liquid nitrogen and further examined.

II.2.3.8 Live-cell myosin II inhibitor treatments

MCF-7 cells were seeded on day 0 on glass-bottom dishes and were imaged one day after seeding in DMEM including 4-(2-hydroxyethyl)-1-piperazineethanesulfonic acid (HEPES) and without phenol red supplemented with 2% FBS. Live cell imaging was performed on a Zeiss

LSM710 Duo microscope at 37°C. The 488 nm line of an argon/krypton laser was used for fluorescence recording with a 63 × /1.40-N.A. DIC M27 oil immersion objective. The emitted light was monitored between 500 and 540 nm (green signal), with a pinhole set at 1–2 AU (airy unit) and a laser intensity of 0.2%. Cells were initially imaged in control medium. Subsequently, the medium was aspirated using a vacuum pump. It was replaced by adding medium supplemented with the respective inhibitor with a construction of a syringe and a tube that was attached to the dish prior to imaging, so imaging took place without interruption of recording. Para-nitroblebbistatin concentrations of 5, 10, 20 and 50 µM were tested. While 5 µM inhibited keratin granule motility only mildly, 50 µM showed signs of toxicity, completely inhibiting intracellular motility and dynamics. Based on the test results and the recommendation of the manufacturer to not exceed 20 µM because of unspecific side effects, the reported efficient inhibition of myosin 2 function in cultured cells using 10–20 µM para-nitroblebbistatin[268], the limited solubility of blebbistatin (4–25 µM in aqueous solution containing 0.1–2% DMSO for blebbistatin[268,269]), and the concern for toxicity of high para-nitroblebbistatin concentrations we decided to use 20 µM as the standard concentration.
ML-7 was used at a standard concentration of 20 µM which has been shown to inhibit MLCK efficiently in MCF-7 cells and is known to avoid unspecific inhibition of protein kinase A and C[270,271].

II.2.3.9 MitoTimer experiments

The keratinocyte cell lines were seeded on day 0 on collagen I-coated glass-bottom dishes. After two days, cells were transfected with the pMitoTimer plasmid, medium was exchanged on day 3, and imaging took place four days after seeding. Live cell imaging was done on a Zeiss LSM710 Duo microscope at 37°C. The 488 nm line of an argon/krypton laser was used for fluorescence recording via a 63×/1.40-N.A. DIC M27 oil immersion objective. The emitted light was monitored between 500-540 nm (green signal) and 580-640 nm (red signal) with a pinhole set at 1–2 AU and a laser intensity of 0.2%. Using Fiji, green and red channels were thresholded (Otsu algorithm) and a mask of regions of interest was calculated that shows signal positive in either channel. Fluorescence intensity mean values were determined for every region of interest. Three replicates per experiment were performed with 30 cells each per condition. Cell culture and microscopy was performed by myself and the image analysis by Dr. Nicole Schwarz.

II.2.3.10 Induction of mitophagy

The keratinocyte cell lines were seeded on collagen I-coated coverslips on day 0 and transfected with a Parkin-eGFP construct on day 1 using Xfect. On day 2, the cells were

incubated with 10 µM CCCP at 37°C for 2 or 18 hours, or with DMSO only for 18 hours as a control. After 2x 15 minutes washing with medium at 37°C, cells were stained with 100 nM MitoTracker Red CMXRos for 30 minutes at 37°C. After fixation with 4% warm paraformaldehyde for 25 minutes at room temperature, nuclei were stained with Hoechst 33342 and the coverslips were mounted with Elvanol. Using the ApoTome.2 microscope, ≥ 48 cells per condition were imaged at 63x magnification using the 63×/1.40-N.A. DIC M27 oil immersion objective. Imaging of one replicate was performed on the same day, with equal exposure times for interference contrast, MitoTracker and Parkin-eGFP. Using Fiji, the mitochondrial area per cell was determined for Parkin-positive cells after background subtraction (rolling ball set to 5). Parkin distribution was scored as cytoplasmic or dotted. Three replicates per experiment were performed. Statistical analysis used one-way ANOVA with Dunnett's post-test.

II.2.3.11 LC3 Assay

The keratinocyte cell lines were seeded at day 0 on collagen I-coated coverslips. They were transfected on day 3 with the pftLC3 plasmid[272]. On day 4, the low calcium medium was replaced by high calcium medium (1.2 mM Ca^{2+}) and cells were further propagated for three days prior to fixation with 4% paraformaldehyde for 25 minutes at 37°C. Nuclei were stained with Hoechst33342, and the coverslips were mounted with Elvanol. Using the ApoTome.2 microscope, ≥ 16 transfected cells per treatment were imaged with an 63×/1.40-N.A. DIC M27 oil immersion objective with equal exposure times for interference contrast, green and red channels. Using Fiji, LC3-positive puncta were automatically determined in the green and red channels with the help of the "analyse particles" function (size 5-50 Px) after background subtraction (rolling ball set to 20). Particles positive in only one channel were scored as either green or red and particles positive in both channels were scored as yellow. Three replicates per experiment were performed. Statistical analysis used one-way ANOVA with Bonferroni post-test. Cell culture and microscopy was performed by myself and the image analysis by Dr. Nicole Schwarz.

II.2.3.12 Magic Red Cathepsin B assay

The keratinocyte cell lines were seeded on day 0 on collagen I-coated coverslips. The low calcium medium was replaced by high calcium medium (1.2 mM Ca^{2+}) or low calcium medium for control condition on day 4. The cells were differentiated for 3 days and on day 7 incubated for 60 minutes at 37°C with Magic Red® cathepsin B substrate, which was dissolved in DMSO according to the manufacturer´s protocol. Subsequently, cells were washed once with medium

and fixed with 4% paraformaldehyde for 25 minutes at 37°C. Nuclei were stained with Hoechst33342, and the coverslips were mounted with Elvanol. Using the ApoTome.2 microscope equipped with an 63×/1.40-N.A. DIC M27 oil immersion objective, 10 images per condition were taken, resulting in >216 cells per condition for three independent experiments. Images of one replicate were taken on the same day with equal exposure times for the red channel (Magic Red® fluorescence). Images were analysed using Fiji, using default settings for brightness and contrast. For this purpose, single cells were encircled and regions of interest were set. The Magic Red® signal was thresholded using the Otsu setting, and the percent area per cell was measured. For each replicate, the values were normalised to the wt cells. Four replicates per experiment were performed. Statistical analysis used one-way ANOVA with Holm Šidák post-test. Cell culture and microscopy was performed by myself and the image analysis by Dr. Nicole Schwarz.

II.2.3.13 Bafilomycin A1 treatment and MitoTimer analysis

The keratinocyte cell lines were seeded at day 0 on collagen I-coated coverslips. The cells were transfected on day 2 with the pMitoTimer plasmid in the morning. Approximately 6 hours after transfection, the cells were incubated in medium containing either 1 nM of Bafilomycin A1 dissolved in DMSO or DMSO only. After 48 hours of Bafilomycin A1 treatment, the cells were washed with warm medium and subsequently fixed for 15 minutes with 4% paraformaldehyde at 37°C. Imaging was performed on a Zeiss LSM710 Duo microscope at 37°C. The 488 nm line of an argon/krypton laser was used for fluorescence recording via a 63×/1.40-N.A. DIC M27 oil immersion objective. The emitted light was monitored between 500-540 nm (green signal) and 580-640 nm (red signal) with a pinhole set at 1–2 AU and a laser intensity of 0.2%. Using Fiji, green and red channels were thresholded (Otsu algorithm) and a mask of regions of interest was calculated that shows signal positive in either channel. Fluorescence intensity mean values were determined for every region of interest. Three replicates per experiment were performed with 20 cells per condition. Statistical analysis used one-way ANOVA with Dunnett's post-test. Cell culture and microscopy was performed by myself and the image analysis by Dr. Nicole Schwarz.

II.2.3.14 DYRK inhibitor assay

The four different wt keratinocyte cell clones (clone A-D) overexpressing mutant Krt14R125C-eYFP (construct Krt14R125C-eYFP_Cbh_T2A_Puro) were seeded on day 0 on collagen I-coated coverslips. On day 2, the medium was switched to either DMSO control only or 1 µM or 3 µM Leucettine L1-containing medium. The cells were incubated for 2 hours at 37°C,

subsequently washed with medium and fixed for 15 minutes with 4% paraformaldehyde at 37°C. Nuclei were stained with Hoechst33342. Using the ApoTome.2 microscope, 7 images per condition were taken using the Plan-Apochromat 20X/0.8 DIC objective. Using Fiji, the images were converted to an inverse representation and the contrast was manually set in a way that the keratin cytoskeleton could unambiguously be scored as either solely filamentous or containing granules. Scoring of cells was performed using the Cell Counter plugin. Subsequently, the percentage of cells containing a solely filamentous or granular keratin cytoskeleton was calculated for three replicates. Statistical analysis used one-way ANOVA with Dunnett's post-test.

II.2.4 Histological Methods

II.2.4.8 Methanol/acetone and paraformaldehyde fixation of cells

Methanol/acetone fixation:

The coverslips were transferred to a teflon coverslip rack and immediately permeabilised and fixed in -20°C cold methanol for 3 minutes. Subsequently, they were transferred to acetone for 20 seconds at the same temperature. Next, three washing steps with PBS were conducted, before either using the cells immediately for immunocytochemistry, or stored for a short time in PBS or in dried form at 4°C.

Paraformaldehyde fixation:

The medium was aspirated from the 6-well plates, and immediately 4% paraformaldehyde pre-warmed to 37°C was added. The cells were fixed for 15-25 minutes at 37°C. After three washing steps, the cells were either used immediately for immunocytochemistry, or stored on short-term in PBS at 4°C. For permeabilisation, the cells were either incubated for 3 minutes in 0.1% Triton-X-100 or 20 seconds in -20°C cold acetone, followed by three additional washing steps in PBS.

II.2.4.9 Immunocytochemistry

Fixed and permeabilised cells grown on glass coverslips were blocked in 5% (w/v) bovine serum albumin (BSA) in PBS for 30 minutes. Subsequently, the primary antibody, diluted in 1% (w/v) BSA in PBS, was incubated for 60 minutes. After three washing steps in PBS, cells were incubated for another 60 minutes in fluorophore-coupled secondary antibody diluted in 1% (w/v) BSA in PBS in the dark. In case of additional nuclei staining, Hoechst 33342 was added to the secondary antibody solution at a final concentration of 1 µg/µl. After three washing

steps in PBS, the samples were mounted with Elvanol on microscopy slides and dried overnight at 4°C. All incubation steps were performed at room temperature.

II.2.5 Microscopy

II.2.5.1 Electron microscopy

Pelleted proliferating cells were fixed in 4% formaldehyde/1% glutaraldehyde for 2 hours and in 1% Osmium tetroxide (OsO_4) for 1 hour. Fixed samples were treated with 0.5% uranyl acetate in 0.05 M sodium maleate buffer, pH 5.2, for 2 hours in the dark and thereafter dehydrated and embedded in araldite using acetone as the intermedium. Polymerisation was performed at 60°C for 48 hours. Semi- and ultrathin sections were prepared with an ultramicrotome using a diamond knife. To enhance contrast, sections were treated with 3% uranyl acetate for 5 minutes and with 0.08 M lead citrate solution for 3 minutes. Images were taken on an EM10 with a digital camera using iTEM software. Analyses were done on 50000x magnification images. Cell culture procedures and analysis were performed by myself. Fixation, embedding and microscopy procedure was performed by lab technician Sabine Eisner.
Using Fiji, ≥50 mitochondria per cell line were encircled to calculate their circumference. Close endoplasmic reticulum membranes were defined as no more than 15 pixels away from the mitochondrial membrane and their length was determined to calculate the ratio of ER-covered mitochondrial circumference vs. whole mitochondrial circumference.

II.2.5.2 Structured illumination microscopy

The Zeiss ApoTome 2 was used for structured illumination microscopy of fixed samples, calculating optical sections from three images with different grid positions. This results in the elimination of out-of-focus light and the focal plane being the only one being calculated, therefore reaching comparable results to confocal microscopy. In case of single images which were not used for quantitative analysis, optimal exposure settings were chosen for each image. If image series were created for quantitative analyses, the optimal exposure times were determined for each channel by calculating the mean exposure time of ~5 test images per condition/cell line, which was then used for the complete image series, except for DIC channel.

II.2.5.3 Confocal laser scanning microscopy

Live-cell imaging and high-quality imaging of fixed cells was performed using the Zeiss LSM 710 Duo microscope. All images were recorded at 16 bit grey-scale resolution. Unidirectional

or bidirectional scanning was used depending on the experiment conditions. If higher acquisition speed was required, bidirectional scanning was preferred. In case one fluorophore was used with overlapping emission spectra, the detection was adjusted for the specific signal. The illumination density was always chosen not to cause unspecific detection. When more than one fluorophore was detected, two different scans were performed to exclude signal bleaching.

In case of live-cell experiments, the incubation chamber of the microscope was preheated to 37°C at least 10 hours before experiments started. Cells were either switched to DMEM without phenol red in case of MCF-7 cells or remained in EpiLife in case of human keratinocyte cell lines. If imaging of one sample exceeded 120 minutes, 5% CO_2 humidified atmosphere was additionally used.

II.2.5.4 Automated image analysis of mutant keratin granules

For best comparison high quality recordings of isolated cells were selected that had a comparable overall cell morphology (round shape, flat cell body). Image sequences were either recorded over a long period (between 270 and 365 frames per movie with 3 frames/minute) allowing the analysis of complete tracks, or in a before–after fashion to study the impact of modulators. In both instances, the analysis followed the following scheme.

First, granules were tracked with the help of the Fiji plugin TrackMate[273]. For segmentation, the LoG detector was applied with the following parameters: blob diameter = 1 µm; threshold = 33 (in some experiments 1, due to different recording settings); no mean filtering; and sub-pixel localisation active. For tracking, the LAP tracker was used with the following parameters: Frame to frame linking = 1 µm; track segment gap closing with maximal distance of 1 µm and maximal frame gap of 2; track segment splitting disabled; track segment merging 1 µm. After initial track calculation, the tracks were filtered for mean quality set to "auto". For further inspection numerical data (track-IDs; x, y, t; fluorescence) were exported and MATLAB custom scripts were used. Since merging of tracks occurred regularly, tracks which did not merge were automatically classified as solo tracks and merging tracks that were subdivided into main tracks and sub tracks. Mean local track speed, local advance speed and fluorescence of granules were calculated for the different track types. To consider local changes of speed, a gliding mean of speed was calculated by computing the local track and advance speeds for each time point taking 8 image recordings from t − 3 to t + 4 into account. To further examine the motion properties of granules, mean square displacement (MSD) analysis was performed using the MATLAB class @msdanalyzer[274]. The coefficient alpha was determined in the following way: The MSD function was calculated for each individual trajectory and its log–log representation was fitted with a linear function such that if the MSD curve could be modelled by

$\rho(r) = \langle r2 \rangle = \Gamma t^{\alpha}$, then

$log(\langle r2 \rangle) = f(log(t))$ was fitted with $\Gamma + \alpha\ log(t)$.

Individual MSD curves were fitted and discarded those for which the R2 coefficient, reflecting the quality of the fit, was < 0.8[274]. For MSD analysis along or perpendicular to the track direction, tracks were rotated in a way that start- and end-point were located horizontally. In that instance, x values reflect back and forth movements while y-values reflect up and down movements, i.e. movements perpendicular to the track axis. MSD analysis then was performed for x and y values separately. To test significance of before and after parameters the signrank function applying the Wilcoxon matched-pairs signed-ranks test[275] was used. Graphs were prepared using GraphPadPrism v7 Software. Values are given with standard deviation of the mean, i.e. ± SD. Significance with a $p \leq 0.001$ was labelled ***, $p \leq 0.01$ was labelled ** and $p \leq 0.05$ was labelled *.

Acquisition and visualisation of the movies was performed by myself and the automated image analysis was performed by Dr. Reinhard Windoffer. The generated automated image analysis protocols are available in the following GitHub repository:
https://github.com/rwindoffer/KER_TRACK.

II.2.5.5 Fluorescence recovery after photobleaching (FRAP)

Fluorescence recovery after photobleaching was used to determine the turnover of eYFP-tagged mutant keratin granules, using the standard live-cell imaging conditions. An overview of a complete cell was imaged with 3-4 z planes. Next, one section of the cell (zoom 6.0) was chosen, and the position noted. A short test recording of 10 frames with a 10 second interval was imaged to assess granule movement. If it was evaluated to be similar to the granules analysed in the automated image analysis, single granules in this section were bleached. The definite focus function was used and unidirectional scanning at 512x512 pixels was performed. A pixel dwell time of 1.58 µs was used and the pinhole was set to ~93 µm (=1 AU).

After one frame in unbleached condition, the 488 nm laser was used at 100% intensity with 10 iterations, which was previously tested to remove nearly all fluorescent signal. 29 further images were taken with an interval of 10 seconds.

A single focal plane of MCF-7-Krt14R125C-eYFP cells was imaged, including most of the keratin granule signal, and it was aimed to image 3 regions per cell with 3 granules per region. Unidirectional or bidirectional scanning was performed for bleaching of complete granules. Bleaching of half granules of MCF-7-Krt14R125C-eYFP cells was performed with unidirectional scanning at 512x256 pixels. A pixel dwell time of 1.58 µs was used and the pinhole was set to 2.16 airy units.

FRAP analysis was performed using a customised Fiji macro, which was created by Dr. Reinhard Windoffer and myself. It used a rectangular area within the image to align the slices. Next, the region of interest of the bleached granule was manually selected and the slices were once more aligned. Next, a circular area in the middle of the granulum was selected as region of interest, and the mean fluorescence intensity was measured. The same procedure was repeated for an unbleached granulum, which was chosen to display comparable dynamics and size as the bleached granule. The fluorescence intensity values and ROIs were automatically saved. Normalisation to frame 1 or 2 was performed, indicated specifically for the different experiments. Single timepoints were compared using t-test.

II.2.5.6 Image editing and analysis

Original images acquired using both ApoTome 2 and LSM 710 were saved in Carl Zeiss proprietary data formats (lsm5, czi) and further edited and analysed using Fiji software, unless otherwise stated. Maximum intensity projections of three-dimensional data were created for visualisation if indicated. Fiji software was furthermore used to adjust greyscale/colour range, create composite images, add of scale bars, and time stamps and concatenate movies. Images were saved in Tag Image File Format (TIFF) file format; movies were saved as Audio Video Interleaved (AVI) format and compressed to MP4 format using HandBrake software.

II.2.6 Statistical analysis

Each experiment was performed at least 3 times, unless otherwise stated. The number of analysed cells are indicated for each experiment. Differences between groups were evaluated using GraphPad Prism 5.0® using one-way ANOVA with either Dunnett's or Bonferroni post-test, unless otherwise stated. Data are summarised and presented as mean ± SD. Differences were considered significant when $p \leq 0.05$.

II.2.7 Movies

Movies were created with Fiji software and saved in TIFF and AVI data format. Scale bars, time stamps, and captions were added using Fiji if required. Final conversion to MP4 data format was performed with Handbrake software. The movies are listed in IX. and are available on the following websites:

https://www.nature.com/articles/s41598-021-81542-8
https://www.moca.rwth-aachen.de/gallery36.html

III. Results

III.1 Lifecycle parameters of mutant keratin granules can be quantitatively assessed by novel automated tracking tools

III.1.1 Standardised automated tracking routines allow quantitative analyses of mutant keratin granule dynamics

As summarised in I.9, it has already been shown by various studies that mutant keratin granules are not static protein aggregates but show remarkable dynamics. Consequently, imaging routines and automated image analysis tools were established to gain quantitative measures of mutant keratin granule dynamics.

For this purpose, a standard protocol for confocal live cell imaging and subsequent automated image analysis was developed. Single round and flat MCF-7-Krt14R125C cells were chosen and imaged for >1h at 20-25 s intervals. Maximum intensity projections (comprising the entire keratin granule signal) of the resulting movies were used for subsequent analysis, as shown in Fig. 9a. Segmentation and follow-up of tracks over time was performed by a Fiji/WEKA plugin and trackmate software, as depicted in Fig. 9b-c (movie 02).

The dynamic nature of mutant keratin granules was already visible in time-lapse movies (movie 01), showing certain similarities to the normal keratin filament cycle. Their dynamics included nucleation of nascent granules in the periphery, growth of granules as well as fusion with other granules, inward movement, and disassembly of granules. The disassembly represents the main difference compared to healthy keratin filaments, which are either being incorporated into the existing network, or being recycled for re-assembly (see I.7). Granule disassembly was observed in a circular region at the transition of the flat lamellum to the thicker inner cytoplasm, shortly after granules reached their maximum size. Inside of this border and much closer to the nucleus, another fraction of granules was observed. They were smaller than the “canonical” granules present in the lamellum and moved much faster, sometimes appearing and disappearing within two imaging frames. Consequently, analysis of this granule fraction was not possible, and they were excluded from further analysis.

The observed characteristics are in line with a study by Werner *et al*., which investigated mutant keratin granules by time-lapse microscopy and showed basically the same characteristics as seen in our investigations.[39]

One movie was used to test and optimise the initially established protocol (movie 01; Fig. 9). “Canonical” peripheral granules whose entire lifetime was within the time-lapse recording were analysed with regard to the following parameters:

- Appearance, growth, and disappearance
- Motility (III.2)
- Fusion (III.3.1)

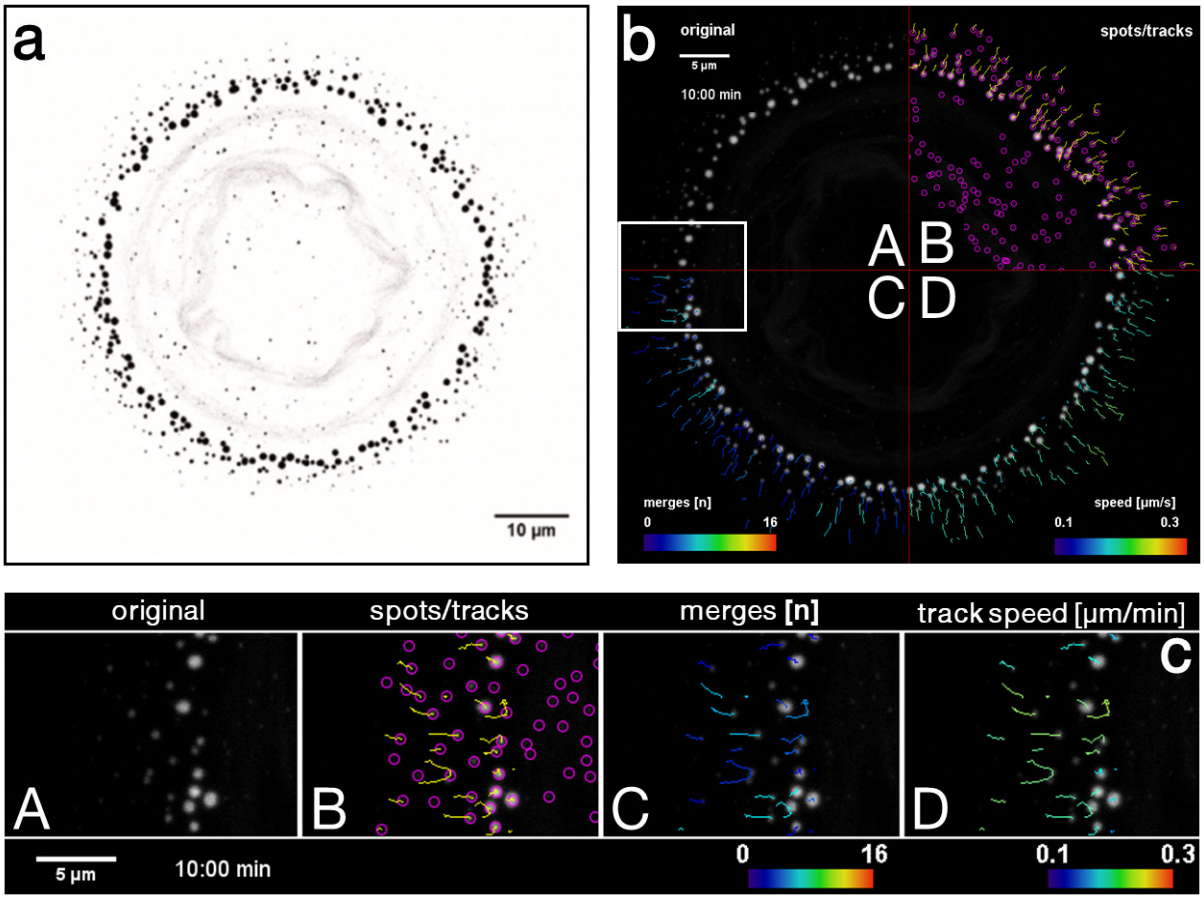

Figure 9 – Live cell imaging and automated tracking of keratin granules. Single, round MCF-7-Krt14R125C cells were recorded for >1h at 20-25s intervals. An example of a maximum intensity projection with enhanced contrast is shown in (a) in reverse representation. A weak perinuclear keratin cage is visible, as well as prominent keratin granules in the periphery that have a larger diameter with increased distance from the cell border. The Fiji/WEKA plugin and trackmate software were used for segmentation of granules as spots and tracks over time and to determine merges and track speed (b, c). The boxed region from (b) is shown enlarged in (c), showing the respective intermediate analysis steps (A-D). The figure was adapted from [276].

III.1.2 Nascent mutant keratin precursors appear frequently in the cell periphery

The initial characteristic step of the keratin cycle of assembly and disassembly is the appearance of precursors in the outermost cell periphery. Exemplary appearance events are shown in Fig. 10 (inset from movie 01), with each newly-forming precursor being encircled in a different colour. Within 3:20 minutes, 7 precursors were formed. Their intensity increased as they formed initial circular precursors.

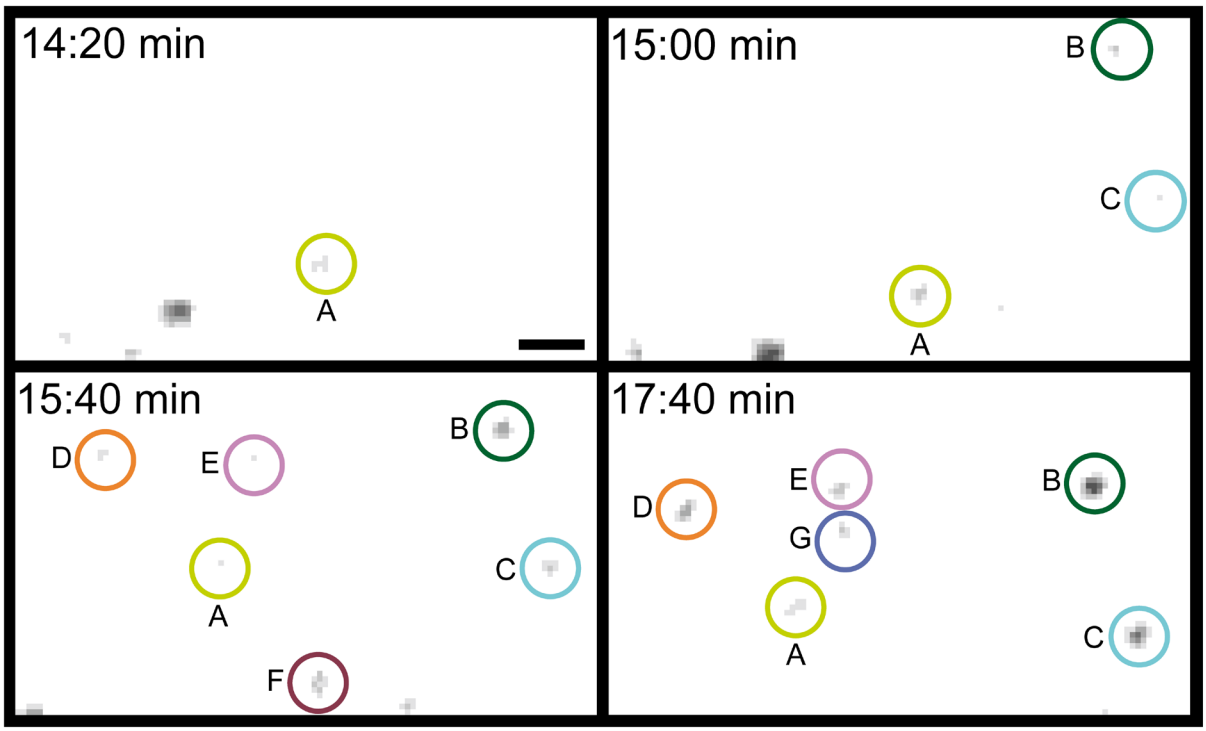

Figure 10 – Nucleation of mutant keratin precursors in the cell periphery. Representative images depict nucleation events of multiple nascent keratin particles in the cell periphery within 3 minutes. Each nascent particle is encircled in a different colour (A-G). The cell border is located at the left micrograph margin, the cell centre lies towards the right margin. Scale bar = 1 µm.

III.1.3 Mutant keratin granules increase in size during retrograde movement

Nearly all mutant keratin granules moved retrogradly towards the nucleus (example in movie 03). A representative montage of one granule shown in Fig. 11.

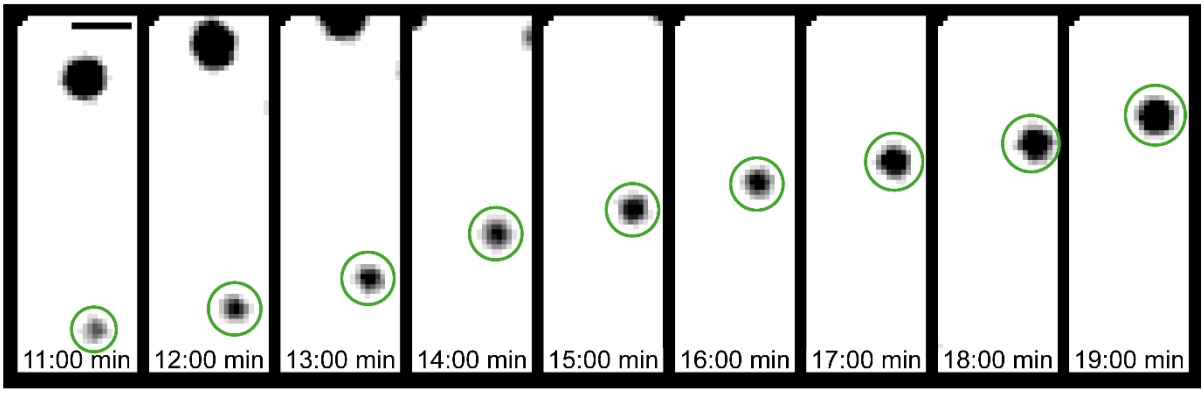

Figure 11 – Retrograde of mutant keratin granules. Representative images of a single mutant keratin granule which moves ~3.5 µm towards the centre of the cell within 8 minutes while growing in size. The cell border is located at the bottom micrograph margin, the cell centre lies towards the upper margin. Scale bar = 1 µm.

The granule travelled approximately 3.5 µm inwards within 8 minutes. The moving granule grew (Fig. 11) without displaying fusion with other granules (III.3.1). An increase in size can be observed during most of the granules´ lifetime.

III.1.4 Disappearance of granules takes place at a circular border region

Close to the distinct region where granules disappeared, they began to decrease in size before disappearing. The possibility of granules moving out of the imaging focus was excluded due to the fact that all granule signal was included in the z projections. An exemplary inset of movie 01 is shown in Fig. 12, being located at the disassembly region. 6 granules, encircled in different colours, rapidly decreased in size, and subsequently disappeared.

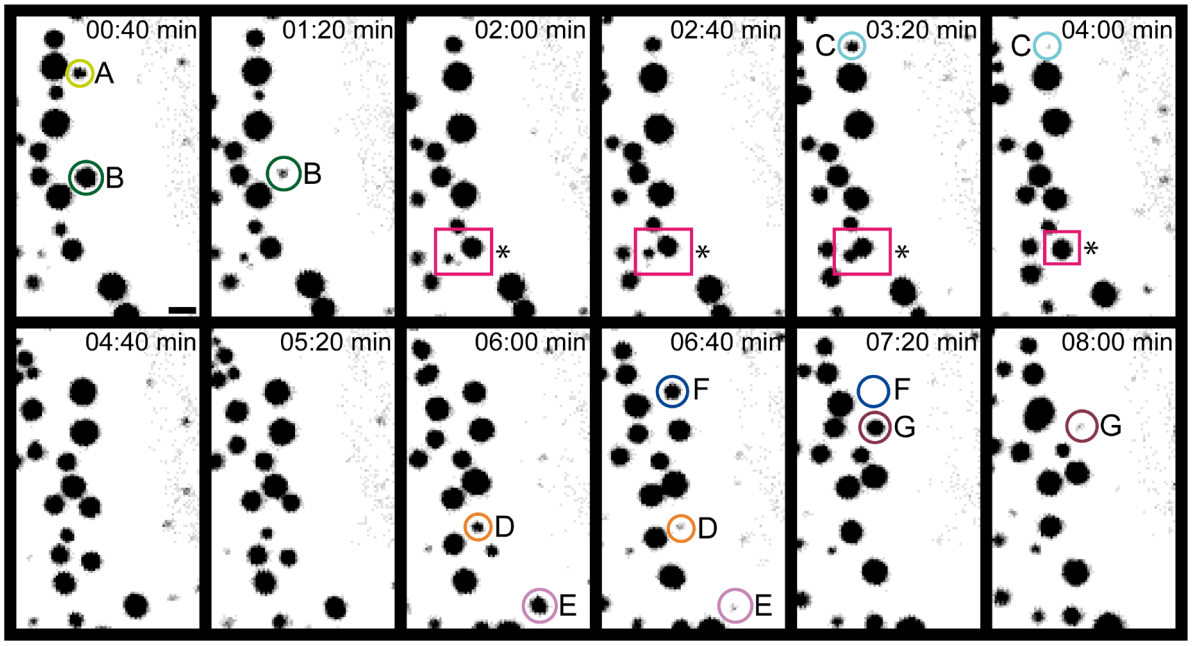

Figure 12 – Dissolving of mutant keratin granules at the transition zone. Representative images of several granules, which disappear at the transition zone within 7:20 minutes. Each granule is encircled in a different colour (A-G). Note that fusion of granules is also observed, marked in red box with asterisk. The cell border is located at the left micrograph margin, the cell centre lies towards the right margin. Scale bar = 1 µm.

Besides growth of granules taking place without fusion with other granules, a large proportion of keratin granules was also observed to merge with other granules once or multiple times during their lifetime (Fig. 12 boxed region; III.3.1). In order to distinguish between the two behaviours, the tracks of mutant keratin granules were classified according to Fig. 13. Granules which did not fuse with any other granules during their entire lifetime were classified as “solo tracks” (see movie 03) . Granules which underwent one or multiple fusions with other granules (see movie 04), were divided into different “sub tracks”. The “main track” represented the longest one. Further analyses of granules of the merging type took only the main track into account.

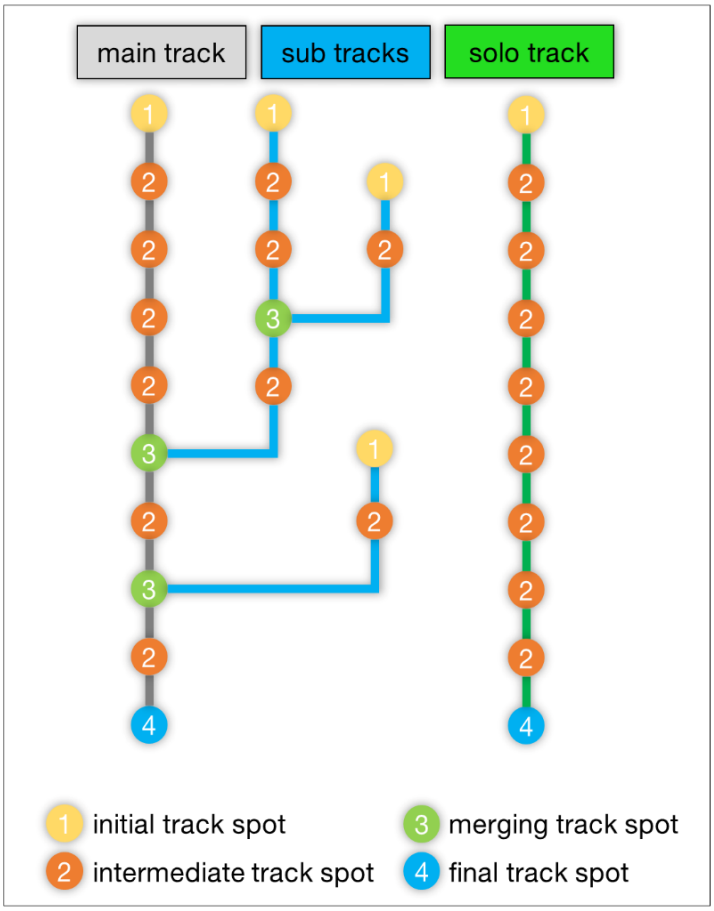

Figure 13 – Schematic overview the classification of different track types. The different positions classified for mutant keratin granules are initial track spot position (1), representing the time point of their first detection, the final track spot (4) as in the last detected time frame, and intermediate track spots (2), representing the positions in between (1) and (2). Merging track spots represent time points when two merging granules are detected as one spot (3). Granules of the merging type are distinguished into the main track, which is the longest sub track, and other sub tracks. Non-merging tracks are referred as solo tracks. The figure was adapted from [276].

III.1.5 Mutant keratin granules display a limited lifetime with a slow growth and a rapid dissolution phase

Next, a detailed quantitative analysis of mutant keratin granule lifetime was performed using the established tracking tools.

The overall lifetime of all granules of one representative time-lapse recording (movie 01) was measured, distinguishing solo and main tracks. The average lifetime of non-merging granules (solo tracks, Fig 14a) amounted to 18.49 ± 5.92 min and was thus a few minutes shorter than that of fusing granules (main tracks, 25.82 ± 6.34 min, Fig 14b). A possible explanation might be that the merging process of granules takes some time to complete.

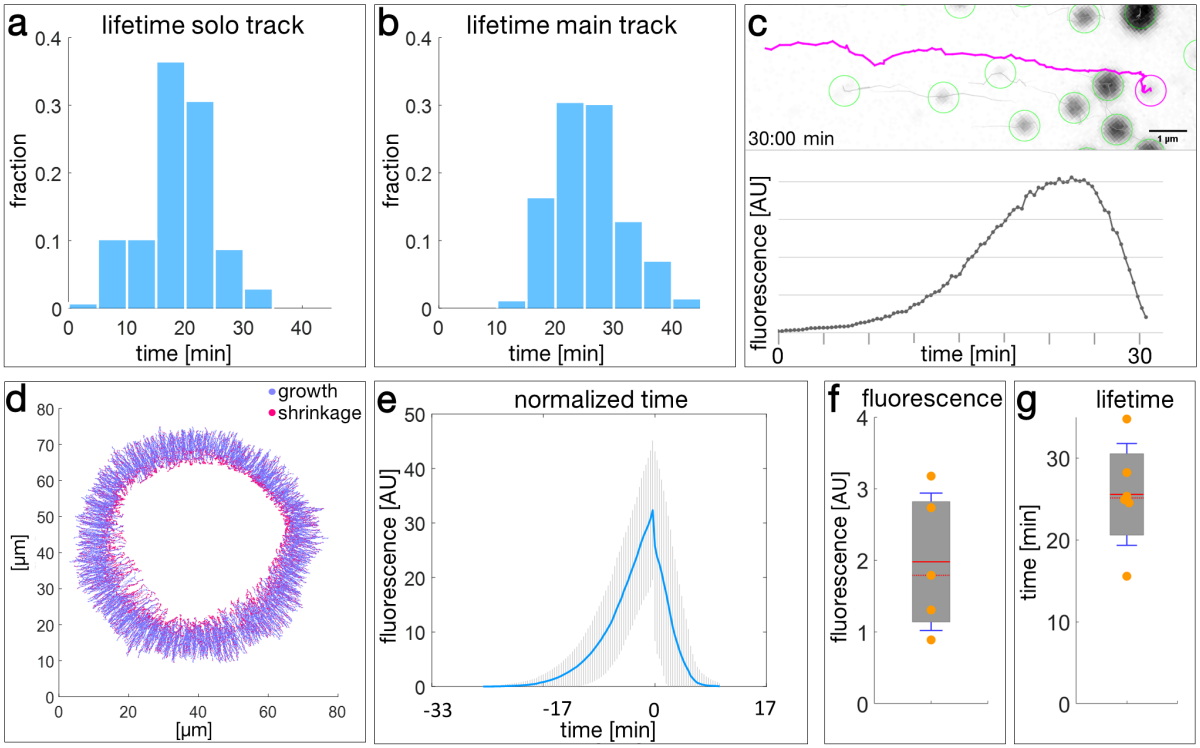

Figure 14 – Signet features of mutant keratin lifetime, growth, and disassembly. Lifetime of mutant keratin granules is depicted for granules which are either not fusing with any other granules during their lifetime (a, n=137; solo tracks) or merging with other granules (b; n=341; only main tracks analysed). The track of a representative granule (pink line) is shown in (c), projected onto a detail view of a fluorescence still image, together with the respective changes of fluorescence over time. The illustration represents the tracks of all analysed granules of Fig. 9a. By comparing fluorescence changes between each time point, each granule´s track is defined as growing (blue dots) or shrinking (pink dots) for each time point (d). The relative changes in fluorescence over time for non-fusing granules (solo tracks) are shown in (e; n=137). (a-e) represent data from the same representative cell. Multiple cells were analysed to obtain the mean maximum fluorescence (f; n=5 cells) and mean lifetime (g; n=6 cells), taking only complete tracks (from initial to final track spot) into account. The figure was adapted from [276].

Fig. 14c displays an exemplary non-fusing granule and illustrates the growth kinetics independently of fusion (movie 05). Increase or decrease in fluorescence corresponds in each case with the granule size and was thus used as a measure of granule growth. Initially, a slow growth phase of the granules took place, followed by exponential growth and a short plateau phase, before rapid, almost linear, disassembly. The changes in fluorescence were further analysed for 137 solo tracks, with the time point of strongest fluorescence being normalised to 0 (Fig. 14e). The results resemble those of the single granule from Fig. 14c. Visualisation of all spatial positions of granules classified as either growing or shrinking illustrated that both events are in principle spatially separated, with growth in the peripheral 2/3 of the granule-containing zone and shrinkage in the inner third (Fig. 14d).

Multiple cells were further analysed with regard to the average granule fluorescence, which varied by a factor of 3 (Fig. 14f). The mean granule lifetime, measured for 6 cells, amounts to 25.56 ± 6.22 min (Fig. 14g), in line with the mean of the representative cell from Fig. 14b.

III.2 Non-muscle myosin II contributes to the motility of mutant keratin granules

III.2.1 The velocity of mutant keratin granules decreases during their growth

The novel automated image analysis tools allowed detailed quantitative analysis of the motility of EBS-mutant keratin granules. Its accuracy allowed to detect alterations of different motility parameters if cells were treated with pharmacological agents (III.2.4).

The first parameter which was analysed is the velocity of mutant keratin granules. According to Fig. 15, two different track velocities were measured. The local track speed represents the values calculated as the track length (blue line) from t_{-3} to t_{+4} divided by time (t_{+4} - t_{-3}), as in distance travelled per time along the track in µm/min for 8 imaging frames at any given time point. The local advance speed was used as a measure for the persistence of movement, defined for the shortest distance between first and last position of each 8-frame window.

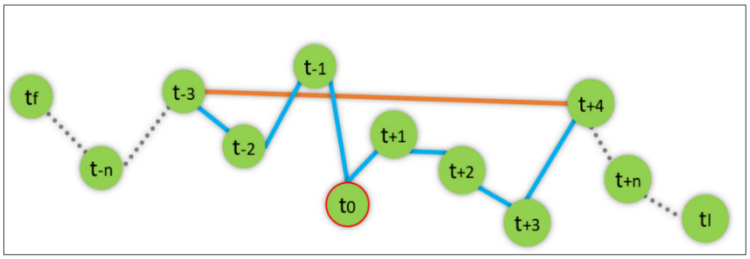

Figure 15 - Schematic overview of different track velocities. For velocity analyses, two different values were calculated. Positions of an exemplary granule are shown in green with t_f as the initial track spot and t_l as the final track spot. The local track speed is defined as the track length (blue line) from t_{-3} to t_{+4} divided by time (t_{+4} - t_{-3}). The local advance speed is defined as the distance covered between t_{-3} and t_{+4} divided by the evolved time. The figure was adapted from [276].

One exemplary cell was analysed in detail. It revealed that the average local track speed of mutant keratin granules amounted to 0.46 ± 0.06 µm/min in case of solo tracks and 0.44 ± 0.08 µm/min for main tracks (Fig 16a-b, respectively). The respective average local advance speed values were 0.35 ± 0.07 µm/min for solo tracks and 0.39 ± 0.09 µm/min for main tracks (Fig 16c-d, respectively).

The same values were further determined for recordings of 6 different cells (Fig. 16e). Mean local track speed (solo tracks: 0.39 ± 0.09 µm/min; main tracks: 0.39 ± 0.08 µm/min) was higher than mean local advance speed (solo tracks: 0.28 ± 0.12 µm/min; main tracks: 0.27 ± 0.09 µm/min). This was accompanied by considerable heterogeneity between different cells, with one group with fast- and another group with slow-moving granules. The local track speed and local advance speed were further illustrated as colour-coded tracks for one exemplary cell. Both values are high during most of the granules lifetime but are considerably reduced at the

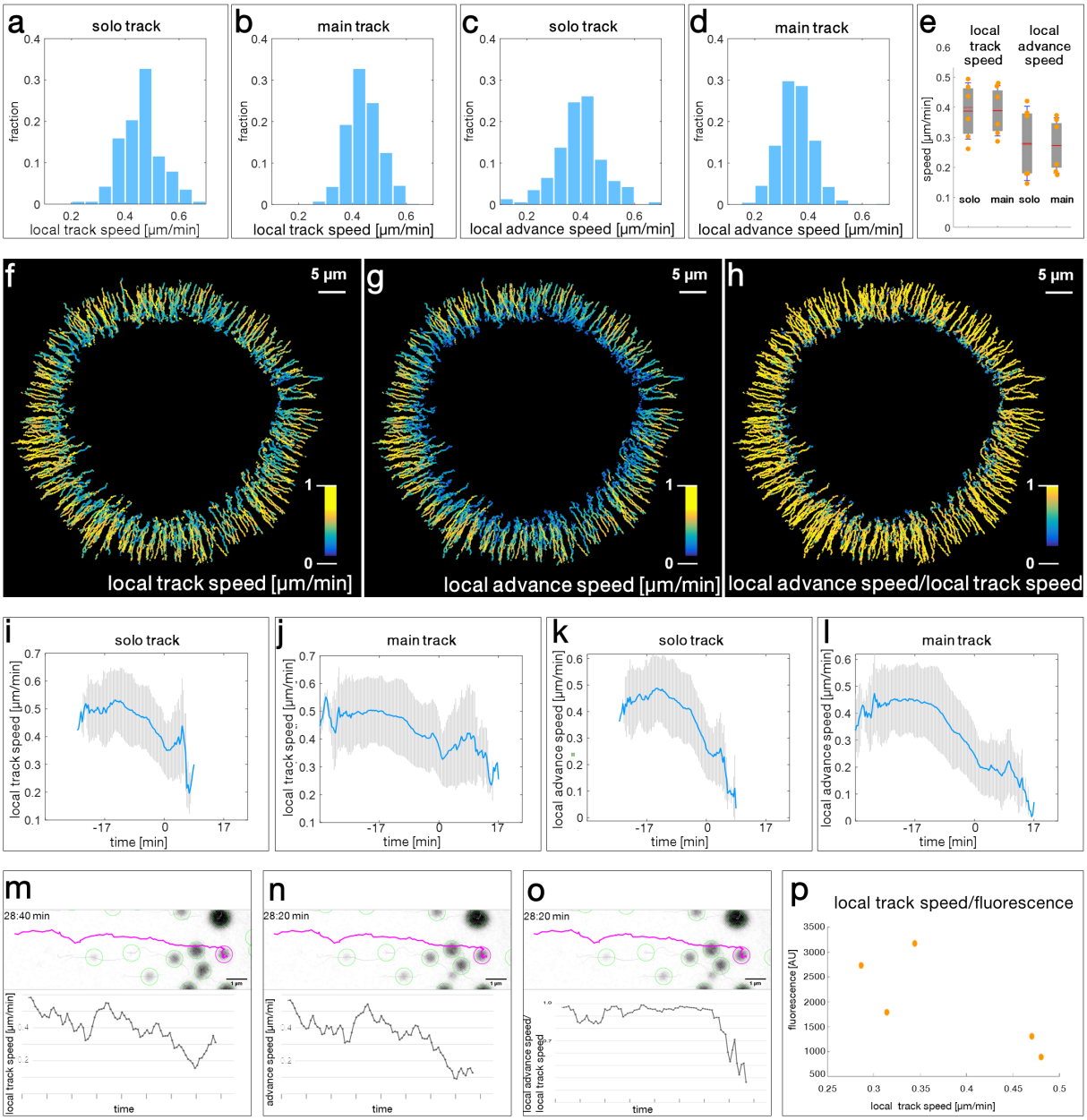

Figure 16 – Mobility of mutant keratin granules. The histograms show the local track speed of non-fusing (a; n=137) and fusing granules (b; n= 341), as well as the respective advance speed (c, d) of all analysed granules of one exemplary cell. The local track speed is defined according to Fig. 15 as the displacement [µm] per minute for an 8-frame window at a given time point. It amounts to 0.46 ± 0.06 µm/min for solo tracks (a) and 0.44 ± 0.08 µm/min for main tracks (b). The advance speed, being defined as the shortest distance travelled for an 8-frame window at a given time point, amounts to 0.35 ± 0.07 µm/min for solo tracks (c) and 0.39 ± 0.09 µm/min for main tracks (d). Local track speed and advance speed were also determined for 6 time-lapse fluorescence recordings (e). Mean speed of solo tracks amounts to 0.39 ± 0.09 µm/min, and 0.39 ± 0.08 µm/min for main tracks. The advance speed of solo tracks is 0.28 ± 0.12 µm/min, and 0.27 ± 0.09 µm/min for main tracks. The local track speed (f), advance speed (g), and ratios of local advance and local track speed of individual keratin granules of the same representative time-lapse recording are shown in a colour-coded way (h). The graphs (i-l) show the changes in local track and advance speed for non-fusing (solo track) and fusing (main track) single keratin granules, with curves being normalised with respect to time by setting the time point 0 minutes to the point of maximum granule fluorescence (Blue lines: mean; grey bars: SD). The track of the same non-merging granule is shown with the respective diagrams for local track speed (m), local advance speed (n), and ratio of local advance speed/local track speed (o) over time. The ratio of local track speed and granule fluorescence is shown for 5 different time-lapse recordings (p). The figure was adapted from [276].

end of their lifetime, with the local advance speed slowing down before the local track speed (Fig. 16f-g). Accordingly, the ratios of both values are consistent during most of the granules lifetime and decrease shortly before their disassembly (Fig. 16h). This phenomenon also becomes clear in graphs of exemplary granules, in which the fluorescence was normalised to the time point of strongest fluorescence for the two velocity values and both solo and main tracks (Fig. 16i-l).

The local track (Fig. 16m) and advance speed (Fig. 16n), as well as their ratio (Fig. 16o) is further shown for an exemplary granule, highlighting a decreased velocity at the end of its lifetime, coinciding with a less directed movement (see movie 06). The relation between local track speed and granule fluorescence is further illustrated in Fig. 16p, presenting the average values for 5 different cells.

These observations revealed that mutant keratin granules move with a similar velocity as healthy keratin filament precursors in a retrograde manner but show erratic and decreased movement just prior to their disassembly at the inner lamellum.

III.2.2 Mutant keratin granules move via directed transport

The results of the velocity analyses indicated a coordinated movement of nascent mutant keratin granules towards the cell centre. Mean square displacement (MSD) analysis was therefore performed to assess the mode of transport. The MSD analysis-derived alpha (α) coefficient indicates free diffusion if it equals 1, movement by active transport if α>1, or motion constrained in space if α<1.[277] MSD analysis of the exemplary time-lapse recording from movie 01 was performed. The alpha value for each time point of each granule is projected onto the respective spatial position in a colour-coded fashion in Fig. 17.

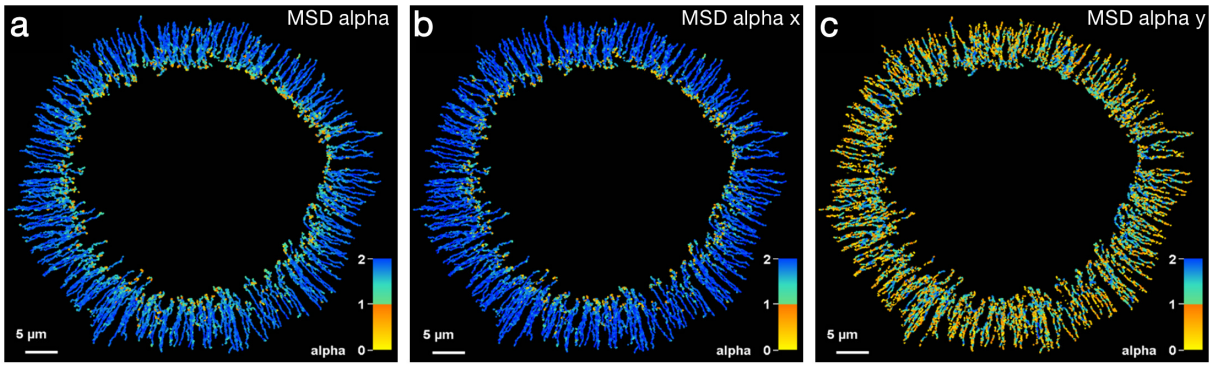

Figure 17 – Consistent retrograde directed transport of mutant keratin granules. To assess the transport mode of mutant keratin granules, mean square displacement analysis was performed. The resulting alpha value indicates directed transport if >1, free Brownian motion if =0, and restricted motion if <1. Color-coded tracks are shown for the overall alpha value (a), and only in x (b) and y direction (c). The alpha value stays >1 for most of the granule´s lifetime only in x and overall, being reduced <1 at the end of the lifetime. The movement along the y axis remains mostly <1 for the whole lifetime. The figure was adapted from [276].

The overall alpha value was above 1 for all granules at nearly all time points during the majority of their lifetime, which indicates consistent directed transport. Only at the very end of their lifetime, mutant keratin granules show decreased alpha values below 1, as in restricted diffusion for the last frames before disassembly (Fig. 17a).
In order to differentiate between inward movement along the x-axis (defined as axis between start- and end point of each track) and perpendicular to the x-axis (defined as y-axis), the alpha values were further calculated separately. The colour-coded representation of alpha along the x-axis is similar to the overall presentation, with values above 1 for most of the granules lifetime and a decrease below 1 for the last few frames (Fig. 17b). On the contrary, the alpha values along the y-axis are mostly below 1 for all granules during the entire lifetime (Fig. 17c), indicating a non-directed left- and right-movement of granules.

In summary, a consistent, directed retrograde movement can be observed, which points to specific transport machineries being involved in mutant keratin granule dynamics.

III.2.3 Retrograde mutant keratin granule movement is coupled to actin

Based on the observed mutant keratin granule dynamics and the fact that healthy wt keratin filament precursors are transported along actin,[139] a potential link between actin and mutant keratin granules was investigated next.

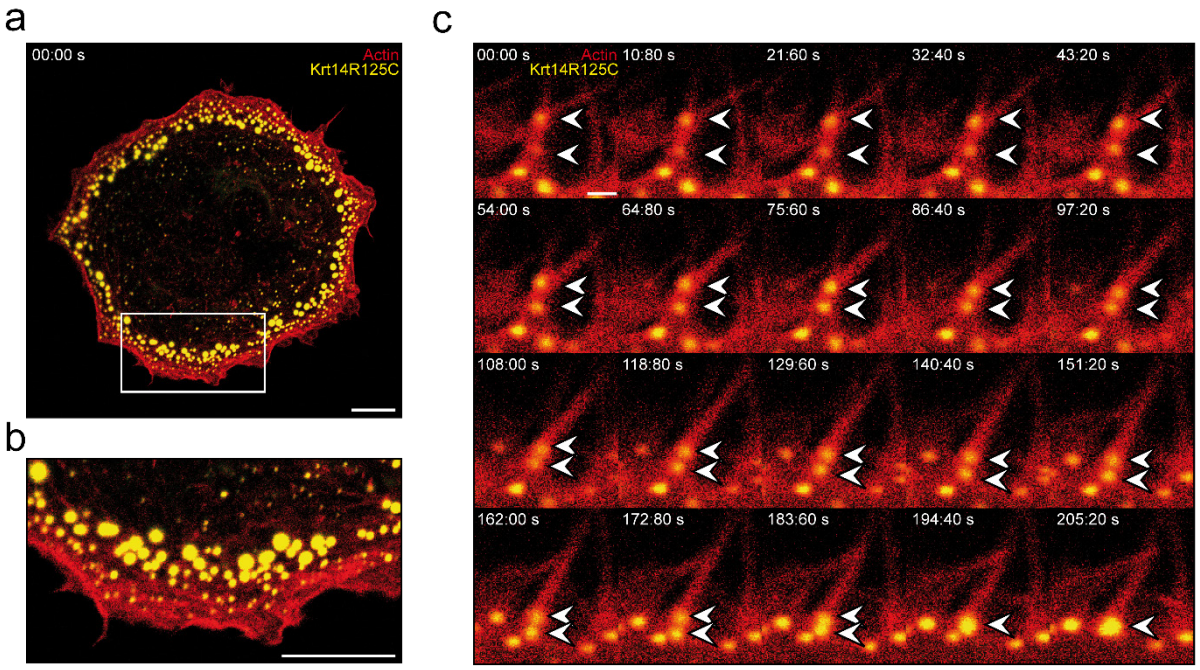

Figure 18 – Retrograde movement of mutant keratin granules along filopodia-like actin structures. MCF-7 Krt14R125C-eYFP cells were co-transfected with actin, which locates at the cell periphery, with most keratin granules being located closer to the cell centre (a), a magnification of the boxed area is shown in (b). Exemplary retrograde movement along a filopodium-like actin structure is shown for two keratin granules within a time frame of 3:40 minutes, indicated by white arrowheads (c).

At the base of the filopodium-like structure, the two granules fuse with each other. The cell membrane is located at the upper margin. Scale bars (a, b) = 10 µm; (c) = 1 µm.

For this purpose, MCF-7-Krt14R125C-eYFP cells were co-transfected with LifeAct-RFP and subjected to live-cell imaging. As shown in the maximum intensity projection of an exemplary time-lapse recording (Fig. 18a; enlarged view of the inset in Fig. 18b), LifeAct displays a cortical localisation. The small keratin granule precursors colocalised with the lamellipodium-localised actin. The inner keratin granule-bearing region, containing larger granules, reached a few micrometres further inwards than the main actin signal.

An inset from another time-point of the time-lapse recording is shown in Fig. 18c. It displays a filopodia-like actin structure which co-localises with two keratin granules. Within several minutes, both granules moved inwards along the filopodia-like actin structure, and ultimately fused with each other at the filopodia base (time point 194:40 s).

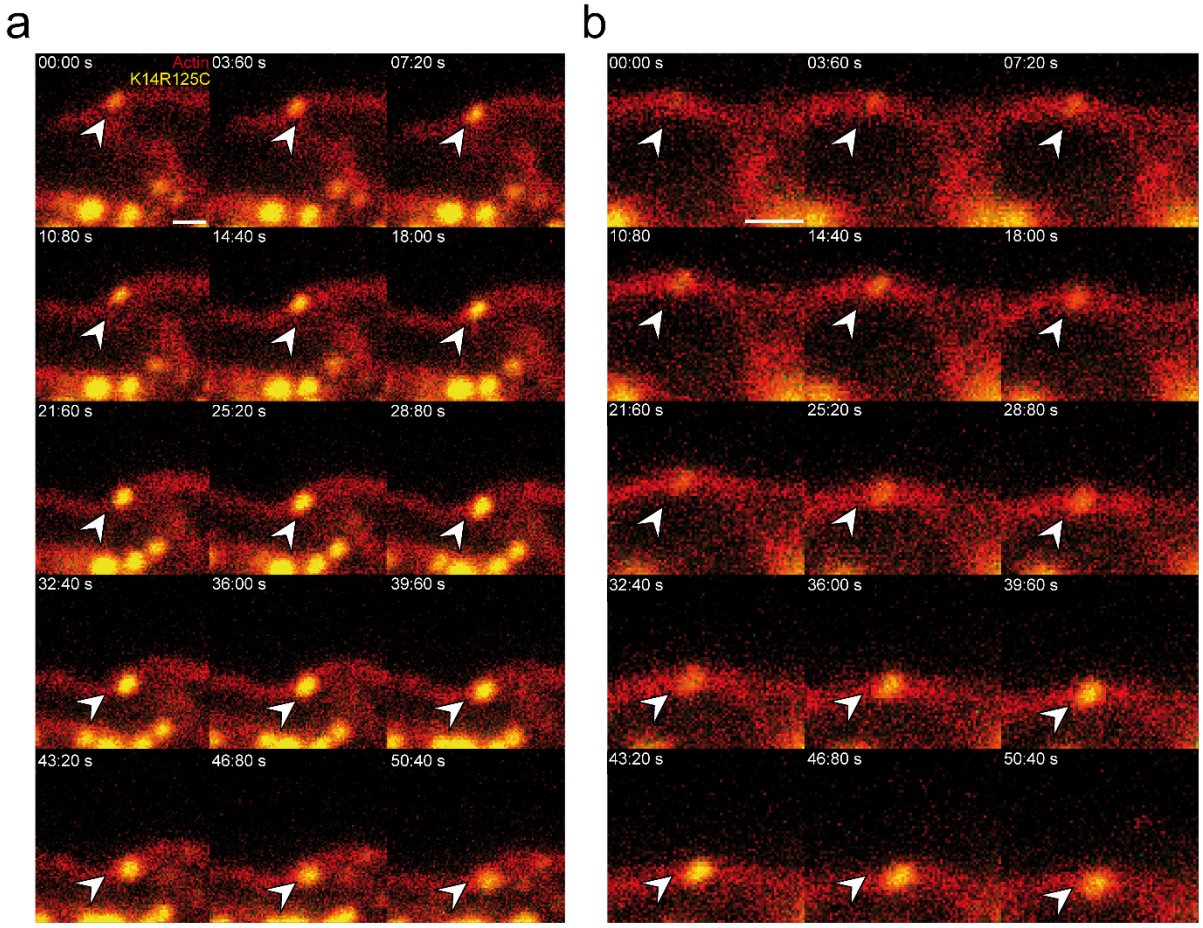

Figure 19 – Retrograde movement of mutant keratin granules along peripheral actin fibres. MCF-7 Krt14R125C cells were co-transfected with actin, which locates at the outermost cell periphery. Two examples of keratin granules which move inwards within ~50 s colocalising with cortical actin that is parallel to the cell membrane are shown in (a, b). Keratin granules are indicated with white arrowheads. The cell membrane is located at the upper margin. Scale bar = 1 µm.

Besides filopodia-like structures, actin fibres aligned parallel to the cell membrane are present. As shown in Fig. 19a-b (insets of Fig. 18a), keratin granules also moved along these actin fibres in a retrograde fashion. Fig. 19b depicts a nascent granule which colocalises with an actin fibre. It simultaneously grew and moved inwards together with the same actin fibre.

These experiments demonstrated that mutant keratin granules and actin structures colocalise and move inwards together with the same speed in the outer lamellum in MCF-7-Krt14R125C cells.

III.2.4 Myosin II inhibition reduces keratin granule dynamics

It has been shown that mutant keratin granules are actively transported, thereby being coupled to actin. A contribution of the actin motor protein non-muscle myosin (nm myosin) II on this transport has not been studied yet. Thus, pharmacological inhibition of myosin was performed. Pilot live cell experiments were performed in order to determine the most effective concentration of para-nitroblebbistatin, a non-phototoxic and non-cytotoxic variant of the specific non-muscle myosin II inhibitor blebbistatin.[268,269] A concentration of 20 µM was shown to not be harmful for the cells, based on assessment of their morphology in brightfield images, and to be most effective. Using the previously established automated image analysis protocol, multiple single round MCF-7-Krt14R125C cells were imaged one day after seeding for 30 frames with 20 s intervals in normal medium. Subsequently, the medium was aspirated using a vacuum pump without interrupting the recording. It was replaced with medium supplemented with 20 µM para-nitroblebbistatin and the cells were further imaged for 50 frames with 20 s intervals (exemplary movie 7). Neither striking morphological differences of the cells could be observed in all movies according to the respective brightfield images (not shown), nor general differences in the morphology or localisation of keratin granules.
Subsequent automated analysis of the movies used the solo tracks of single granules imaged throughout their entire lifespan during recordings. As shown for an exemplary cell in Fig. 20, the tracks of untreated granules (30 frames; Fig. 20a) were much longer than those of para-nitroblebbistatin-treated granules (50 frames; Fig. 20b). Further automated analysis accordingly revealed that granule velocity was significantly reduced from 0.332 ± 0.086 µm/min to 0.224 ± 0.086 µm/min when nm myosin II was inhibited (n=17 cells), whereas no speed changes were observed for DMSO-treated controls (Fig. 20c; n= 11 cells). The persistence was also significantly reduced in blebbistatin-treated cells from 0.739 ± 0.165 to 0.664 ± 0.103, but not in DMSO controls (Fig. 20d). The averaged MSD curves of an exemplary cell are shown before (Fig. 20e) and after the addition of para-nitroblebbistatin (Fig. 20f) and both individual and weighted curves are markedly flattened upon pharmacological myosin inhibition, pointing

towards a total granule motility decrease. Analysis of the overall alpha coefficient on the other hand showed no significant differences when myosin II was inhibited (Fig. 20g), whereas the alpha value perpendicular to the x-axis was slightly decreased upon myosin inhibition (Fig. 20h). These results suggest that although velocity and persistence of mutant keratin granules are reduced upon myosin II inhibition, the mode of motion is not altered.

Overall, these experiments revealed that keratin granules are either directly or indirectly transported along the actomyosin system, and that nm myosin II is involved in this process.

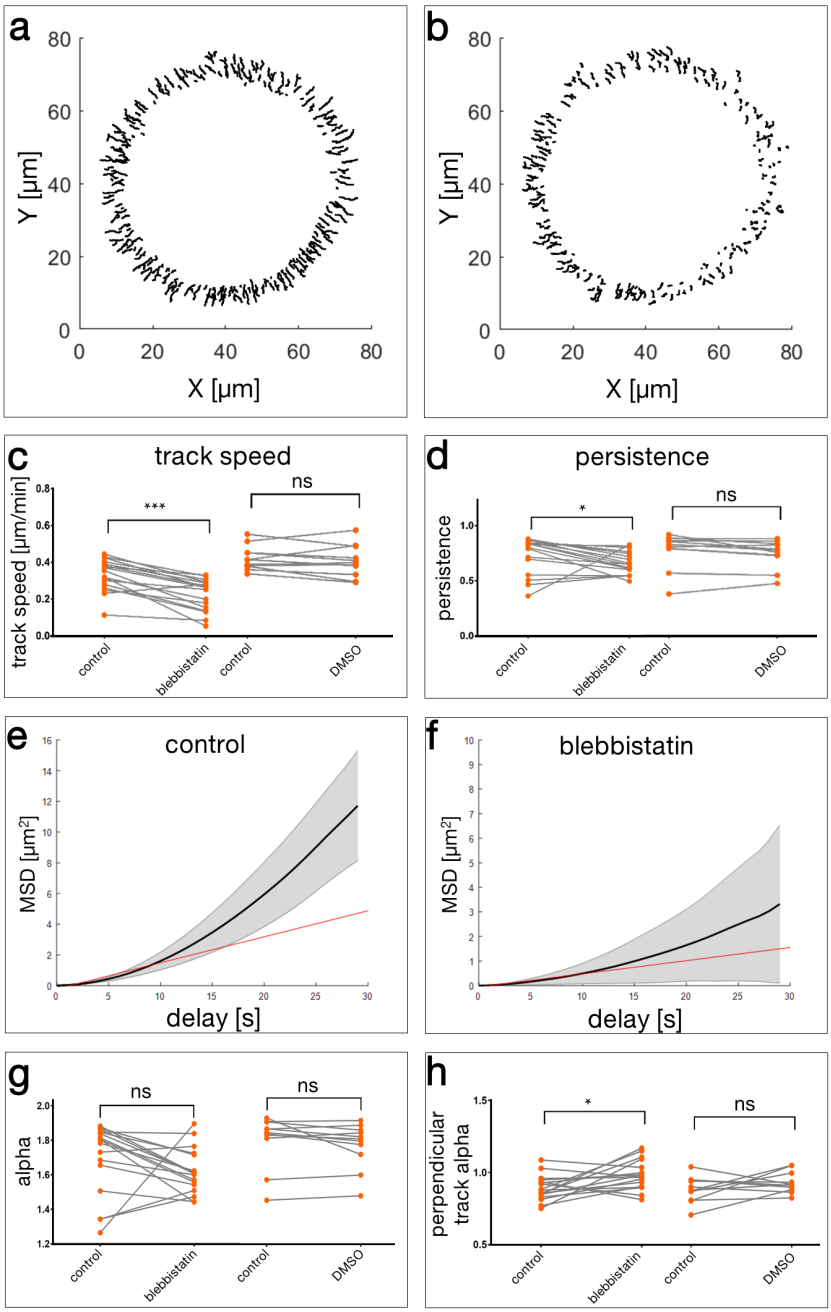

Figure 20 – Non-muscle myosin II inhibition by para-nitroblebbistatin results in alterations of mutant keratin granule motility. Representative images of the tracks of mutant keratin granules were retrieved from a live recording (only non-merging tracks), shown are tracks before (a) and after (b) the addition of 20 µM para-nitroblebbistatin. The overall track speed of mutant keratin granules is shown in (c) for untreated cells (control) and either blebbistatin- or DMSO-treated cells. For the blebbistatin

experiment 17 cells were analysed yielding 900 tracks before and 989 tracks after drug addition. Note the decrease in speed from 0.332 ± 0.086 µm/min to 0.224 ± 0.086 µm/min (p = 0.000076). Adding DMSO does not affect speed of keratin granule movement (n = 11; 0.396 ± 0.062 µm/min vs. 0.380 ± 0.081 µm/min; p = 0.320). The persistence, as in shortest distance between start and end point of a track divided by the actual distance travelled, of keratin motility is significantly reduced from 0.739 ± 0.165 to 0.664 ± 0.103 (p = 0.015) by para-nitroblebbistatin treatment, but not by DMSO (0.729 ± 0.152 vs. 0.696 ± 0.119; p = 0.083) (d). Averaged MSD curves with greyed areas, representing the weighted standard deviation over all MSD curves and the black line being the weighted average over all MSD curves, are shown for control (e) and blebbistatin (f) conditions. Fitting the first 50% of the mean curve yields the average diffusion coefficients D (red line) for both situations. Significant alpha coefficient changes are neither seen for blebbistatin- (1.699 ± 0.206 vs. 1.619 ± 0.131; p=0.057) nor DMSO treated-cells (710 ± 0.152 vs. 1.676 ± 0.140; p=0.102) (g). Alpha =0 indicates free Brownian motion, while values >1 indicate directed transport, values <1 indicate confined motion. Adding para-nitroblebbistatin significantly increases the perpendicular track alpha from 0.890 ± 0.086 to 0.981 ± 0.102 (p = 0.020), addition of DMSO does not (0.883 ± 0.090 vs. 0.931 ± 0.073; p = 0.320) (h). The figure was adapted from [276].

In order to validate the results obtained from the para-nitroblebbistatin inhibition experiments, another myosin inhibitor was used. ML-7, a selective myosin light chain kinase inhibitor, is mostly used for ATP-competitive inhibition of calcium-calmodulin-dependent and -independent smooth muscle myosin light chain kinases but is also used for non-muscle myosins.[278] A titration of the optimal concentration was performed similarly to that described for para-nitroblebbistatin and a concentration of 20 µM was chosen for the following experiments. The live cell inhibitor experiments were performed using the same setup as for the blebbistatin assay. Fig. 21 shows the track speed analysis results from n=8 cells before and after addition of ML-7. Inhibition of the myosin II light chain kinase significantly reduced the velocity of mutant keratin granules from 0.284±0.129 µm/min to 0.171±0.122 µm/min.

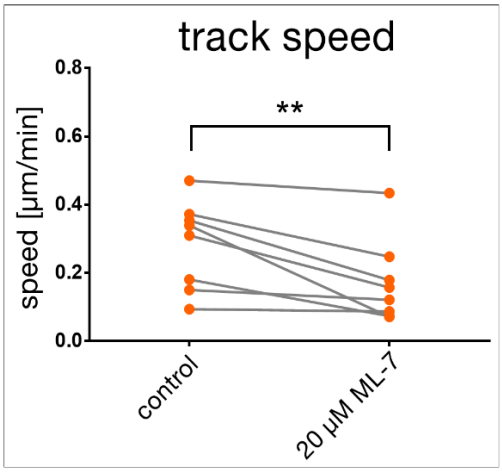

Figure 21 – Non-muscle myosin II inhibition by ML-7 reduced the track speed of mutant keratin granules. The track speed of mutant keratin granules was determined before (control) and after addition of 20 µM ML-7, a selective myosin light-chain kinase inhibitor. 8 cells were analysed, yielding 616 tracks before and 929 tracks after drug addition. The decrease in overall speed from 0.284±0.129 µm/min to 0.171±0.122 µm/min is significant (p=0.008). The figure was adapted from [276].

To further validate the influence of nm myosin II on granule dynamics, MCF-7-Krt14R125C-eYFP cells were transfected with mCherry-tagged nm myosin IIB (Fig. 22 a-b) and live-cell imaging was performed to assess the dynamic localisation of both structures under control and blebbistatin conditions. Non-muscle myosin IIB colocalised with the granule-bearing zone, with the innermost keratin granules being located slightly closer to the nucleus than myosin. Time-lapse recordings showed that myosin constantly moved inwards, corresponding with the retrograde keratin granule flow (movie 09).

Upon para-nitroblebbistatin treatment, performed without interruption of recording as previously described, the retrograde motility of both proteins was equally affected (Fig. 22 b; movie 09). However, residual inward-directed motility persisted upon pharmacological nm myosin II inhibition.

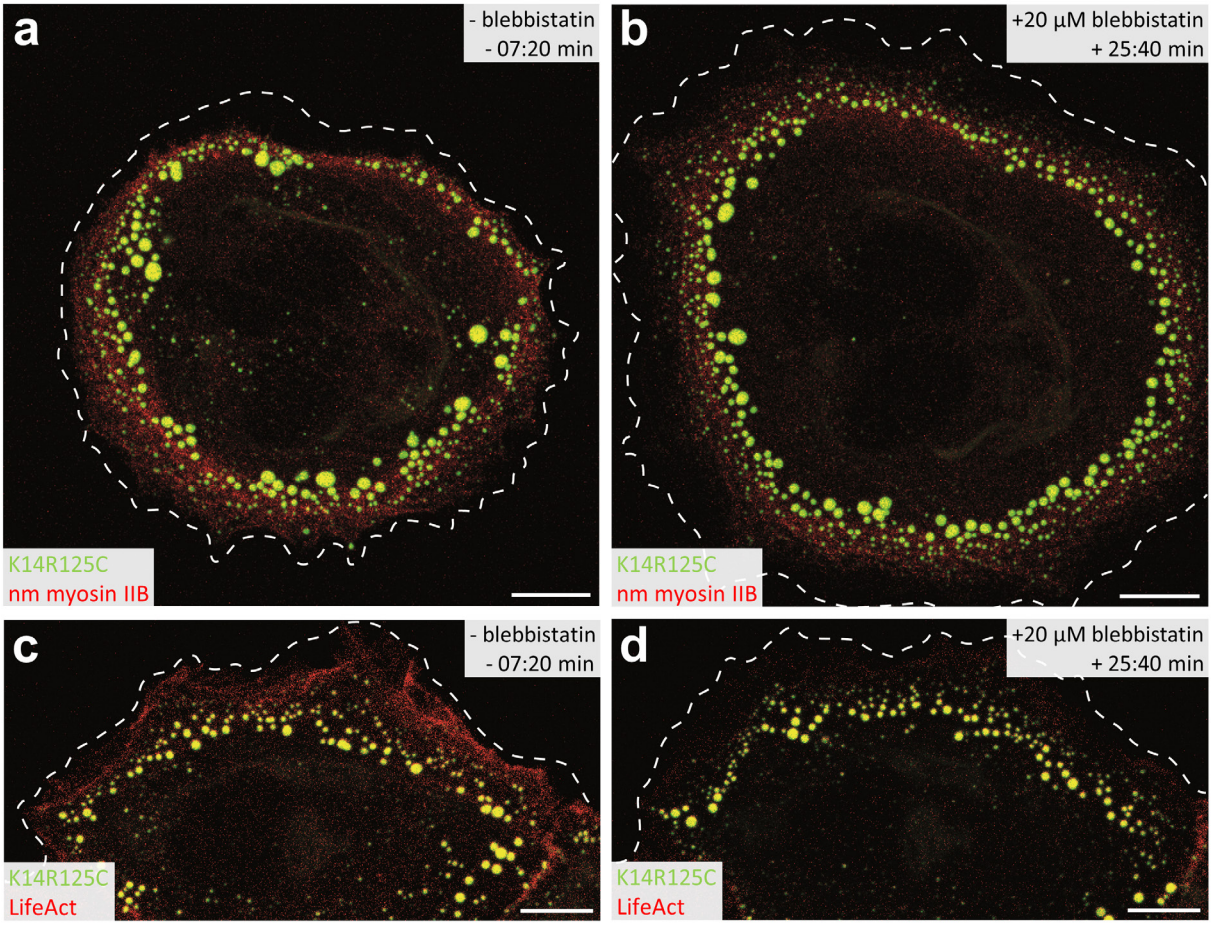

Figure 22 – Live-cell imaging reveals interconnected retrograde movement of mutant keratin granules and cortical actomyosin. Shown are maximum projection views of MCF-7-Krt14R125C cells transfected with mCherry-nm myosin IIB (a, b) or LifeAct-RFP (c, d), either before (a, c) or 25:40 minutes after the addition of para-nitroblebbistatin (b, d). Note the spatial proximity of mutant keratin granules and the dotted, ring-like myosin signal in the cell periphery (a, b). Live-cell recordings show a coordinated movement of both keratin granules and myosin towards the cell centre (movies 09-10). Blebbistatin induced the relaxation of the cell cortex and accompanied enlargement of the cells (b, d). Actin co-distributes with nascent mutant keratin granules in the outer lamellum (c). Actin signal is reduced upon myosin II inhibition (d). Dashed lines (derived from respective brightfield images) indicate the cell membrane. Scale bars = 10 µm. The figure was adapted from [276].

Consequently, MCF-7-Krt14R125C-eYFP cells were transiently transfected with LifeAct-RFP and also subjected to para-nitroblebbistatin treatment (Fig. 22 c-d). Untreated cells displayed correlating actin and keratin granule retrograde movement (Fig. 22 c; movie 10). Para-nitroblebbistatin treatment dissolved actin transverse arcs but did not completely inhibit the retrograde actin flow (Fig. 22 d; movie 10), which may explain the incomplete inhibition of granule movement under myosin inhibition.

In conclusion, pharmacological inhibition of non-muscle myosin II reduces the dynamics of mutant keratin granules and the close association with actin indicates either active transport of keratin granules as myosin cargo or passive transport driven by the continuous retrograde actomyosin flow.

III.3 Mutant keratin granules display characteristics of liquid-liquid phase separation

The results from the automated image analysis of this work clearly demonstrate that EBS-mutant keratin granules are not comparable to static protein aggregates but are instead highly dynamic and short-lived structures. Based on these findings, the remarkable intrinsic dynamics of keratin granules were investigated as a second main characteristic. Specifically, it was examined if formation of mutant keratin granules can be explained with the biochemical concept of liquid-liquid phase separation (LLPS).
The basic idea of this concept implies that liquid droplets, which are not surrounded by a lipid bilayer membrane, coexist within the cytoplasm and are able to exchange material with it.[279] Hyman et *al*. have compiled the main characteristics of cellular LLPS granules, based on the findings from the first study identifying *C. elegans* P granules as LLPS structures. They state that LLPS condensates: [280]

- fuse with each other and regain a spherical shape
- deform in shear flows
- exchange material with the surrounding cytoplasm while keeping a spherical shape
- rearrange internally

III.3.1 Mutant keratin granule fuse frequently with each other

The first feature of LLPS condensates is their ability to fuse after touching, and to regain a spherical shape after fusion.[279,280] An exemplary fusion event is shown in Fig. 23 (inset of movie

01), which displays two round granules getting in close contact, before they merge with each other to form a sphere once more over a course of 6 minutes. This behaviour was seen for a large proportion of granules in a cell (movie 04).

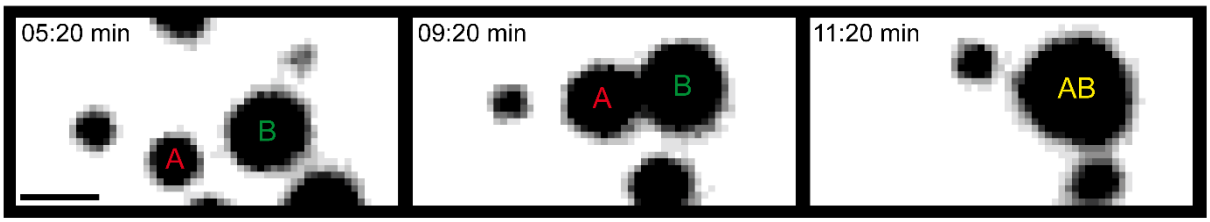

Figure 23 – Merging of mutant keratin granules. Exemplary merging event of two mutant Krt14R125C granules observed within 6 minutes. Two small granules (A, B) closely converge in approximately 4 minutes. Subsequently, they fuse with each other within the next two minutes and regain a spherical shape (AB). The cell border is located at the left micrograph margin, the cell centre lies towards the right margin. Scale bar = 1 µm.

The quantification of merging events based on the automated image analysis protocol shown in Fig. 9 is depicted in Fig. 24.

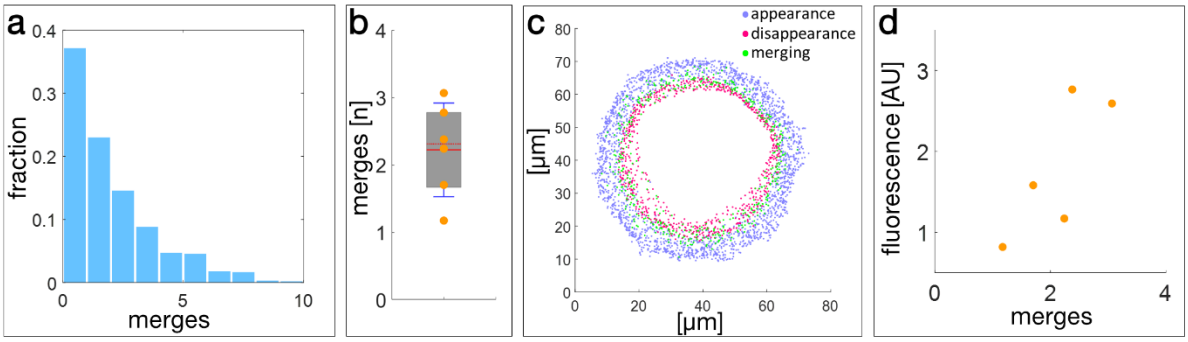

Figure 24 – Quantification of merging events of mutant keratin granules. The number of merging events for every newly formed granule (820 tracks from one exemplary cell) is shown in a histogram (a). The whisker box plot depicts the number of merging events of 6 time-lapse recordings (b). The positions of appearance (blue dots), merging (green dots) and disappearance (pink dots) of mutant keratin granules of one exemplary cell are shown in (c). The number of merging events versus fluorescence (in arbitrary units, AU) was determined for five independent time-lapse recordings (d). The figure was adapted from [276].

The histogram in Fig. 24 a shows that the major fraction (62.68%) of 820 tracks from one cell does not show any merging events. The other fractions show merging events from one to 10 events per track with a descending trend. Mean merging events per granule were calculated for 6 different cells (Fig. 24 b) and amount to a mean fusion rate of 2.22 ± 0.69 per track. Initial and final track spots of the 820 granules from (a) are depicted in (c) at their respective spatial positions, as well as merging track spots. It illustrates that fusion of granules mainly occurs in the middle of the other two regions, with a trend to the middle and inner granule-bearing region. As seen in (d), cells with a high overall fluorescence, i.e. these with a large number of large

granules, showed a high rate of merges. This observation may simply be because of a higher probability of granule approximation.

Overall, the frequent fusion of mutant keratin granules, which always regained a round shape, implicated that the first LLPS condensate criterium is valid in case of EBS granules.

III.3.2 Deformation of mutant keratin granules occurs spontaneously

A second characteristic property of LLPS condensates is their deformation in shear flows.[279,280] Targeted induction of shear flows was not part of this work, but spontaneous deformation of keratin granules was observed, which was different than the sole morphological changes during fusion (Fig. 25).

These findings indicate that mutant keratin granules randomly show a deformation similar to that of liquid droplets, and hint that the second LLPS criterium is likely also fulfilled.

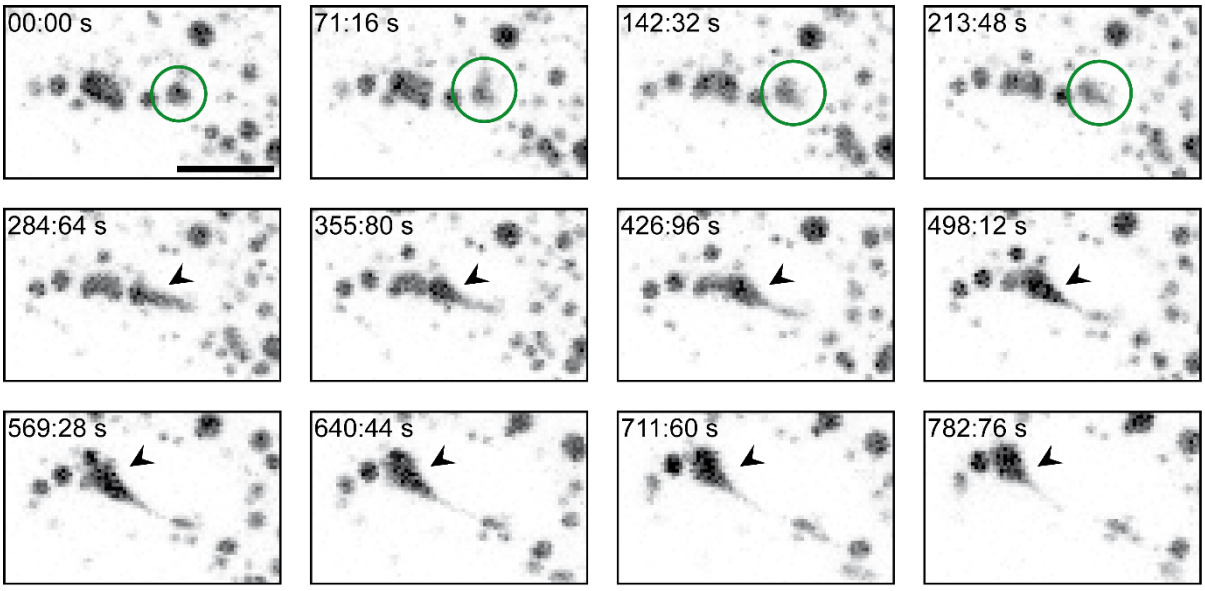

Figure 25 - Spontaneous deformation of mutant keratin granules. Deformation of mutant granules was occasionally observed in time-lapse microscopy of MCF-7-Krt14R125C-eYFP cells. An exemplary round granule (see time point 00:00 s) begins to deform (see time point 284:64 s) while it moves towards the left margin, before starting to regain a round structure (end of time-lapse recording after time point 782:76 s). The cell centre lies towards the upper right margin. Scale bar = 5 µm.

III.3.2 Mutant keratin granules show an intrinsic fluctuation and high turnover

The third feature defining LLPS condensates is their ability to exchange material with the cytoplasm while keeping a spherical shape, driven by surface tension.[279,280] Evidence of this process can be obtained by fluorescence recovery after photobleaching (FRAP) experiments.

A FRAP imaging setup was thus established, in which complete granules of MCF-7-Krt14-R125C-eYFP cells were photobleached after one imaging frame and fluorescence recovery was monitored for 04:40 minutes after bleaching with an interval of 10 seconds. Each photobleached granule was normalised to an unbleached control, which was chosen according to similar size, fluorescence intensity, and dynamics. The result of these experiments are shown in Fig. 26.

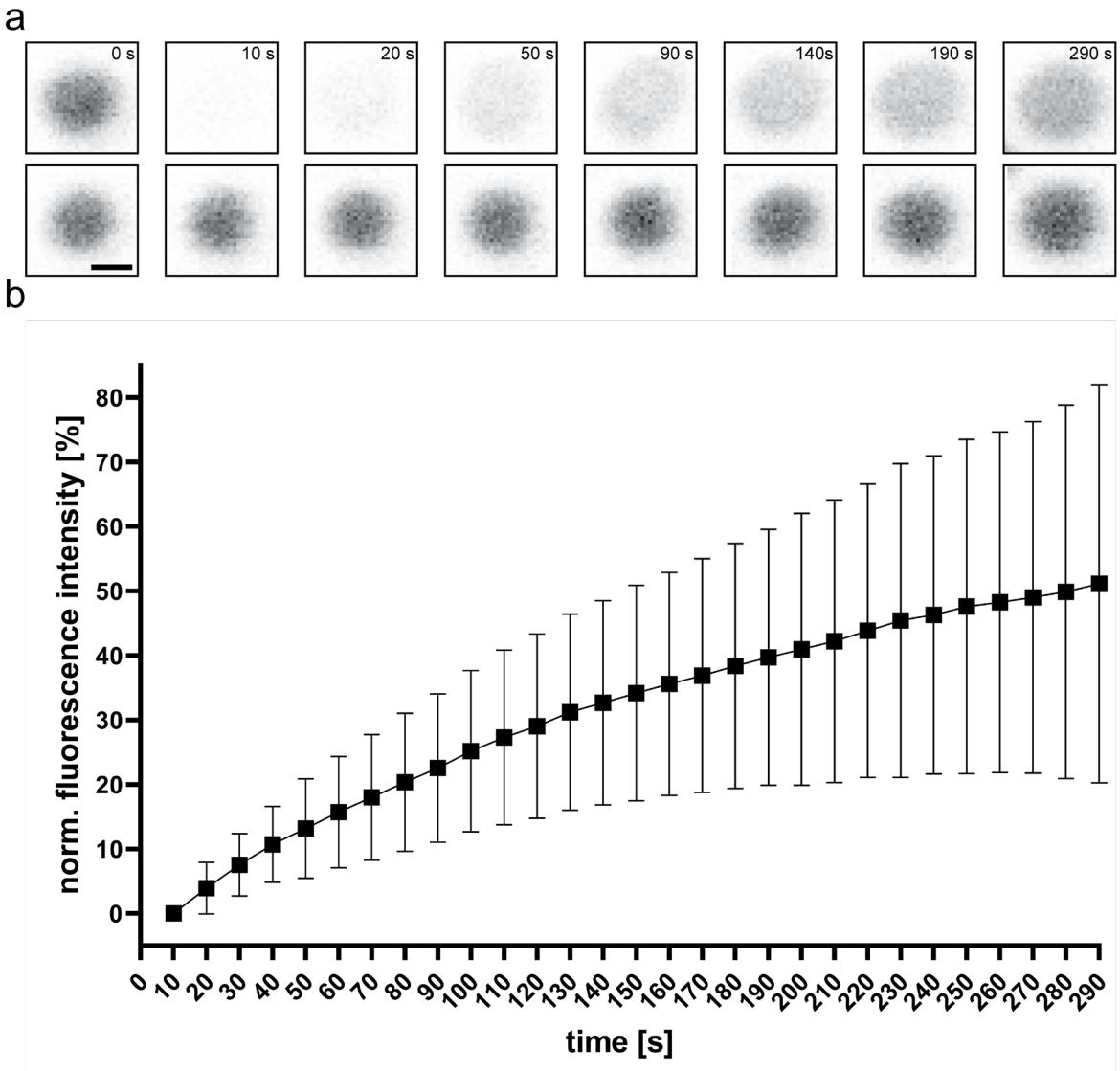

Figure 26 - Mutant keratin granules exchange material with the cytoplasm at a high turnover rate. Fluorescence recovery after photobleaching (FRAP) analysis was performed in MCF-7-Krt14R125-eYFP cells. (a) displays different timepoints before and after bleaching of a completely photobleached granule (upper row) and a non-bleached control granule (lower row). Repeated measurements of n=70 granules from different 14 cells (n=3 replicates) are shown. Each granule was normalised to the frame after bleaching (time point 10 s) and further normalised to a non-bleached granule. The normalised fluorescence intensity values ±SD are shown in (b). Scale bar = 500 nm.

Still images of a completely photobleached granule are shown in Fig. 26a (upper row), depicting different time points before and after bleaching, compared to a non-bleached granule

(lower row). It became evident that bleached granules displayed a rapid fluorescence recovery. Quantitative analysis of fluorescence intensity (normalised to the frame after bleaching at time point 00:10 s) revealed a high turnover rate over 4:50 minutes. However, a high heterogeneity between individual granules (Fig. 26b) was observed. Mutant Krt14R125C granules displayed an overall fluorescence recovery of 50.60±30.57% after 4:50 minutes.

These results clearly show that mutant keratin granules exhibit a high exchange rate with soluble cytoplasmic keratin while retaining their specific spherical morphology, thus giving evidence that the third LLPS condensate criterium is also valid for of EBS granules.

The fourth LLPS condensate-specific characteristic is their internal rearrangement, which can be verified by photobleaching of half condensates.[279,280] Consequently, the previously established protocol for FRAP of whole granules was used for MCF-7-Krt14R125C-eYFP cells, with the exception that only one half of a granule was photobleached. Each photobleached granule was normalised to an unbleached control granule, which was chosen according to similar size, fluorescence intensity, and dynamic behaviour. As seen in Fig. 27a, bleaching of half granules was technically feasible, and bleached granule halves displayed a high recovery. Only 5 imaging frames (10 s interval) were taken into account for quantitative analysis, as rotation and rearrangement of granules compromised the analysis during longer recordings.

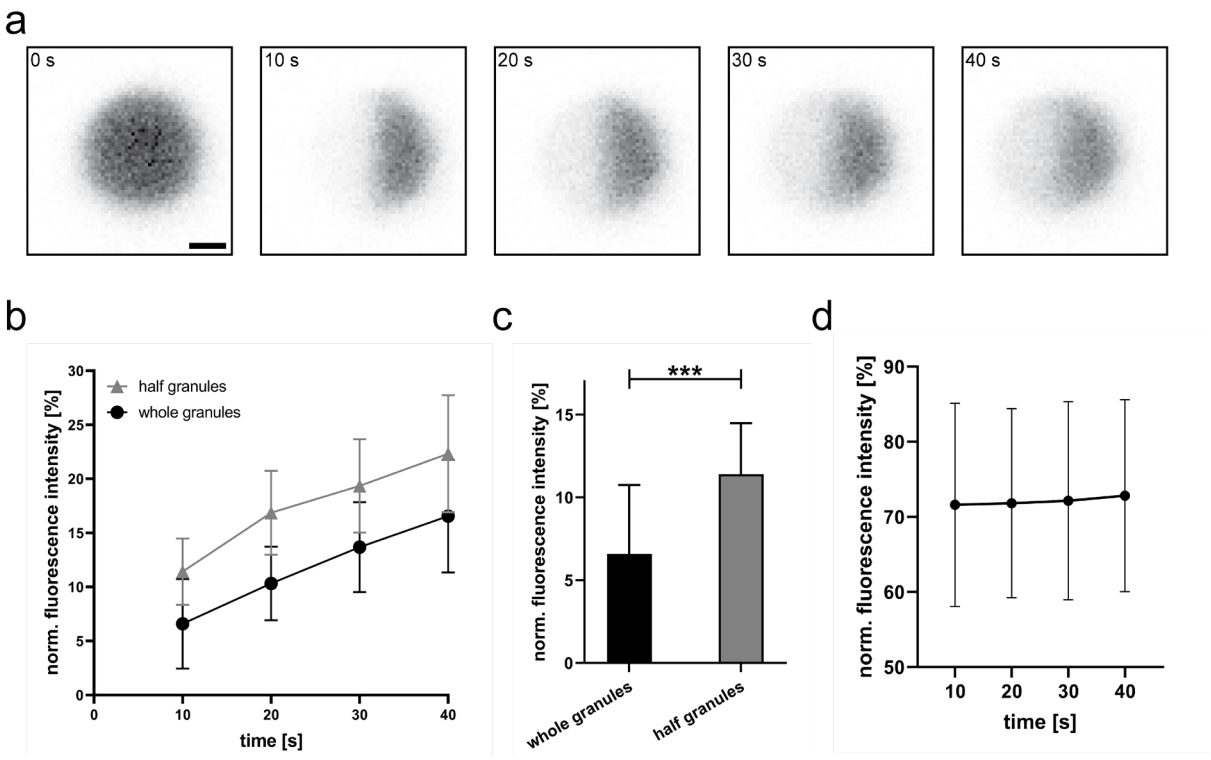

Figure 27 - Rapid internal turnover of mutant keratin granules. Shown are images of a granule of which only the left half was bleached after time point 0 seconds (a). Due to the high internal dynamics, the fluorescence intensity was analysed until time point 40 seconds only. The fluorescence intensity was measured for n=62 granules in 9 cells (n=4 replicates). The fluorescent signal of both the bleached granule half and the non-bleached half was normalised to the first frame (time point 0 seconds) and each granule was further normalised to a non-bleached granule. The recovery of the bleached half is

shown in comparison to the data of completely bleached granules from Fig. 26a (b) and statistical analysis (unpaired t-test with Welch´s correction; $p<0.0001$) shows that the two data sets are statistically different from each other at time point 10 seconds, with the recovery percentage of half granules being approximately twice as high at the indicated time point (c). Analysis of the fluorescence intensity of the non-bleached half of the data set shows a reduction of the signal from 100% at time point 0 seconds to 71.60±13.51% (mean ± SD), which minimally increases to 72.81±12.78 (mean ± SD) at time point 40 seconds (d). Scale bar = 500 nm.

As shown in Fig. 27a, fluorescence recovery of bleached granule halves was already visible after 40 seconds. Quantitative analysis of the fluorescence intensity normalised to frame 1 (time point 00:00 minutes, pre-bleaching) shows that half bleached mutant keratin granules displayed a high fluorescence recovery of 22.31±5.419% within 40 seconds after photobleaching (Fig. 27b). This recovery was ~6% higher than the recovery of completely bleached granules (normalised to frame 1) which amounts to only 16.55±5.218% after 40 seconds. The recovery after 10 seconds was compared to each other (6.59±4.15% for completely bleached vs. 11.41±3.07% for half bleached granules) and was shown to be significantly different (Fig. 27c).

Furthermore, the fluorescence intensity was measured in the non-bleached half and normalised to frame 1 (Fig. 27d). It shows a reduction from 100% to 71.60±13.51% at time point 10 seconds and increases minimally up to 72.81±12.78% at time point 40 seconds. This phenomenon can be explained by two different scenarios: On the one hand, although the photobleaching did in principle only target the intended half of the granule, the other half could also be unspecifically bleached to some extent. On the other hand, it can be hypothesised that soluble keratin might translocate from the non-bleached to the bleached half during the intervals of the 10 iterations of photobleaching. The latter hypothesis is supported by the fact that the fluorescence intensity in the non-bleached half does not considerably increase during the 40 seconds of imaging, although soluble keratin from the cytoplasm should lead to a net increase. Consequently, it is likely that approximately the amount of soluble keratin, which enters the non-bleached half from the cytoplasm, is transferred to the bleached half, before the first measurement after bleaching takes place.

In conclusion, the experiments of FRAP of half granules prove that an internal rearrangement takes place in addition to the exchange with the cytoplasm, thus substantiating that the fourth LLPS condensate criterium is fulfilled by EBS mutant granules.

Overall, the different experiments give evidence of all 4 features that define liquid-liquid phase separation. Consequently, EBS-mutant keratin granules should be considered as LLPS condensates, representing a novel and hitherto unknown biochemical state.

III.3.2 DYRK kinases potentially influence mutant keratin granule dynamics

III.3.2.1 Overexpressed DYRK kinases and keratin granules colocalise in EBS patient cells

Based on the previously described findings, a literature search revealed a study by Rai et *al*., which demonstrated that the dual-specificity kinase DYRK3 is able to induce dissolution of membraneless condensates during mitosis.[281] Consequently, a first pilot experiment was performed to determine if a close localisation of DYRK kinases and keratins could be observed. For this purpose, fluorescently tagged keratins were not required, and thus the cell culture system was switched to immortalised keratinocyte cell lines which also represent a more physiological system than MCF-7 cells. They are derived from healthy subjects (wt) and patients of both *Epidermolysis bullosa simplex* and *Pachyonychia congenita* patients, carrying the following genotypes:

Table 26 - Genotypes of immortalised keratinocyte cell lines.

Origin	Genotype
Healthy subject	Krt 6a/5/14 wild type
Epidermolysis bullosa simplex patient A	Krt5R165G
Epidermolysis bullosa simplex patient *B*	Krt14R125C
Pachyonychia congenita patient A	Krt6aN171K
Pachyonychia congenita patient *B*	Krt6aN171del

To assess the keratin network morphology of these cell lines, they were immunostained with a pan-keratin antibody (Fig. 28). Wild type keratinocytes contain a filamentous, cytoplasm-spanning keratin network, including a prominent perinuclear cage, granules were not observed (Fig. 28a). Most of the Krt5R165G cells also display a filamentous keratin network similar to wt cells (Fig. 28b), although individual granule-containing cells were observed.

On the other hand, the majority of Krt14R125C keratinocytes show a filamentous keratin staining only in the perinuclear region, and prominent keratin granules in the cell periphery (Fig. 28c). Both PC keratinocytes show in principle a similar keratin morphology as wt cells (Fig. 28d-e), although individual cells containing peripheral cytoplasmic keratin granules were observed.

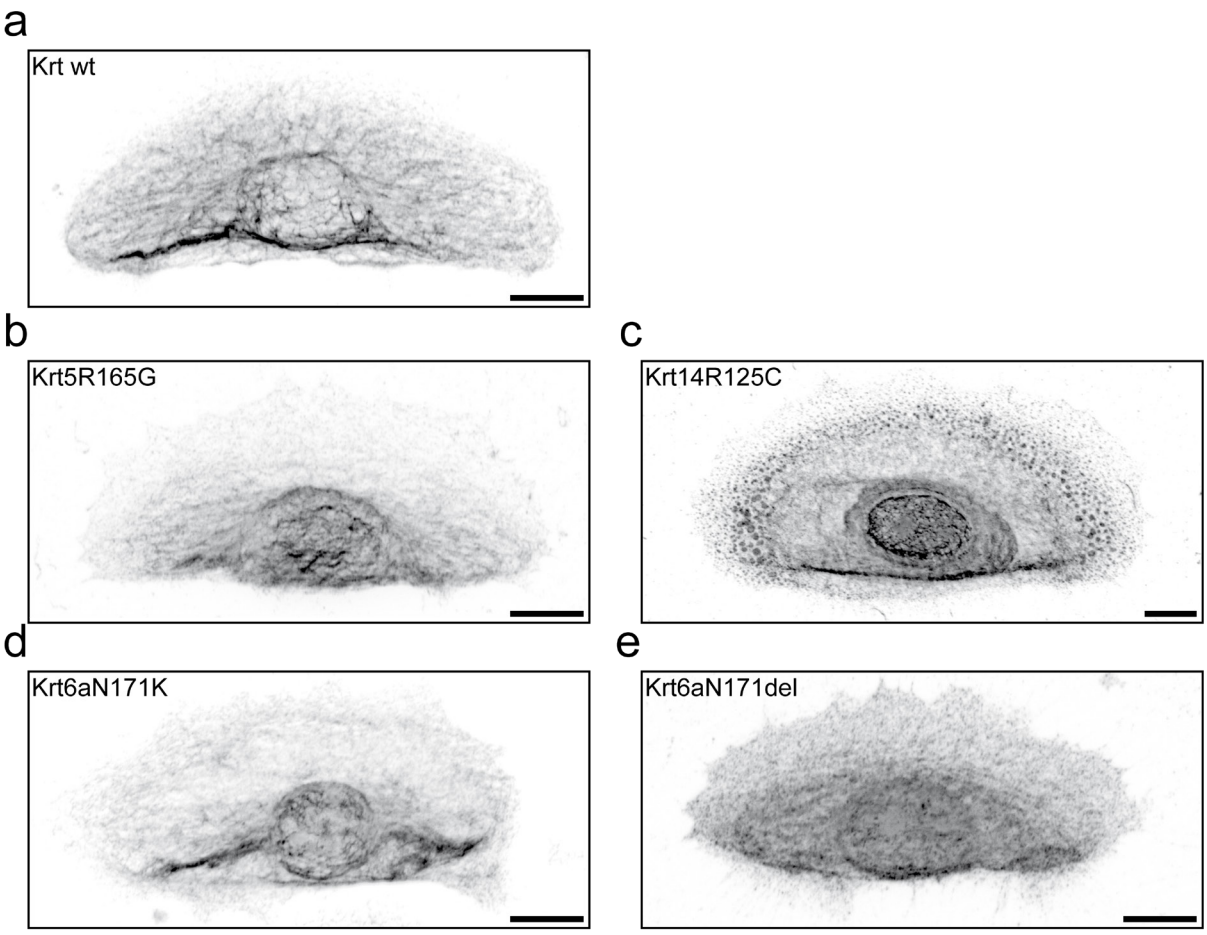

Figure 28 – Keratin network morphology of wild type and mutant keratinocytes. Images of immunofluorescence staining using a pan-keratin antibody (recognising keratins 4, 5, 6, 7, 8, 10, 13, 14, 18 and 19) are shown for wild type (a), Krt5R165G (b), Krt14R125C (c), Krt6aN171K (d) and Krt6aN171del (e) keratinocyte cell lines. A cytoplasm-spanning keratin network with a prominent perinuclear cage is observed in all cell lines. In addition, prominent granules are visible in the cell periphery of most Krt14R125C cells (c). Scale bars = 10 µm.

A first pilot experiment aimed to assess a potential correlation between mutant keratin granules and DYRK kinases by transient expression of 3 different isoforms of eGFP-tagged DYRK kinases in wt and EBS keratinocyte cell lines. As displayed in Fig. 29b-d, all isoforms tested (DYRK1A, DYRK2, DYRK3) showed a marked localisation in peripheral granules that highly resemble the mutant keratin granules of Krt14R125C cells. In contrast, a cytoplasmic DYRK localisation was found in wt cells that contain a pure filamentous keratin network (Fig.29a), indicating that a potential colocalisation of the two proteins would only be present in cells containing mutant keratin granules. As a consequence, the following experiments took only the Krt14R125C keratinocytes into account.

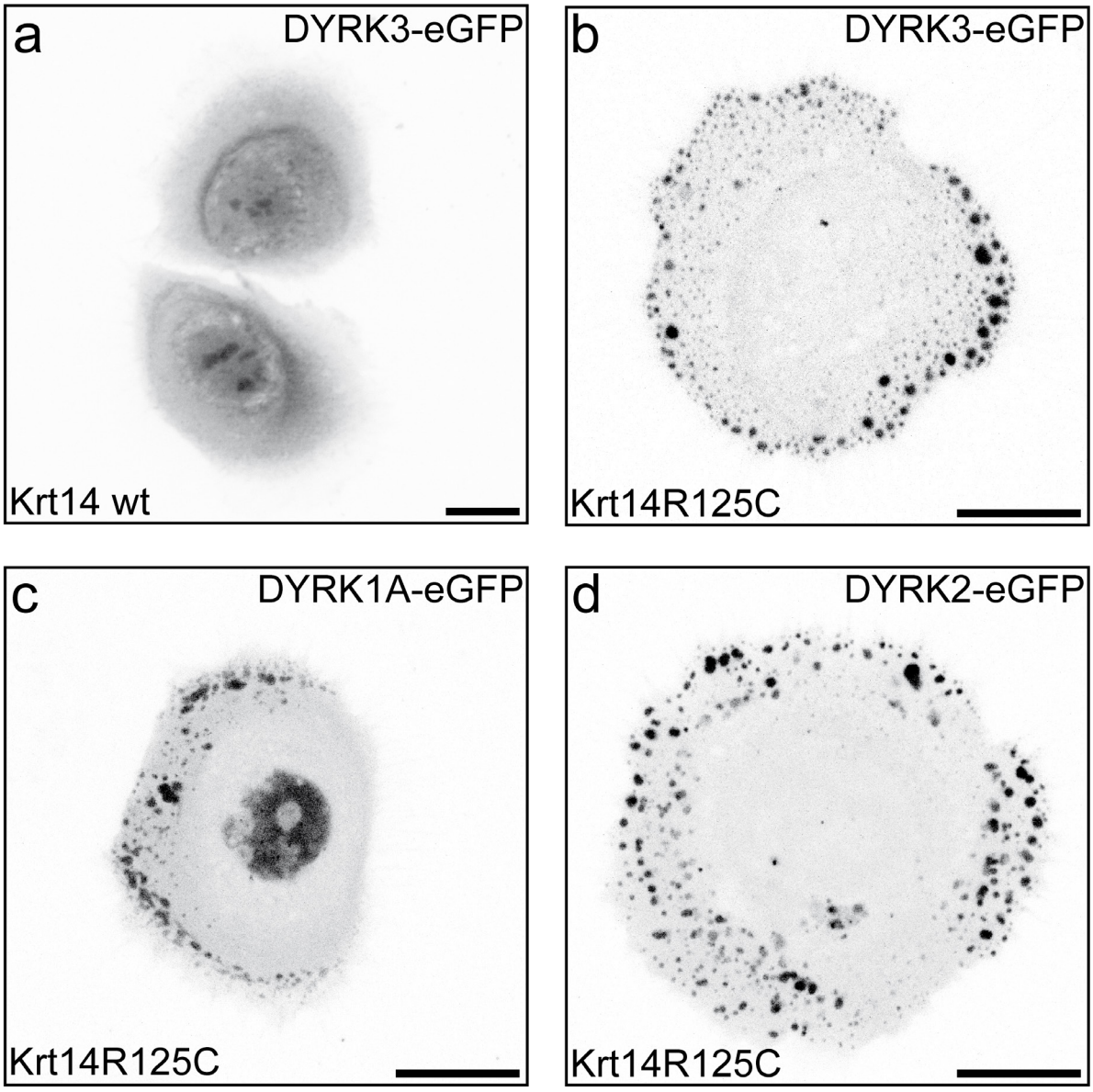

Figure 29 - Different fluorescence-tagged DYRK isoforms show a granular localisation similar to mutant keratin granules in mutant Krt14 keratinocytes. eGFP-tagged plasmids of three different DYRK isoforms were transiently expressed in wt and Krt14R125C keratinocytes; both cell lines did not produce any other fluorescently tagged protein. Note the cytoplasmic localisation of DYRK3-eGFP in wt cells (a), whereas the three isoforms DYRK3-eGFP (b) DYRK1A-eGFP (c), DYRK2-eGFP (d) show a show a clear granular staining in the outer lamellum, similar to the pattern of mutant keratin granules, but without any signal located at perinuclear keratin filaments. The DYRK1A protein furthermore shows a nuclear staining, as it is predicted for this isoform. Scale bars = 10 µm.

Next, transiently DYRK-transfected Krt14R125C cells were subjected to time-lapse confocal microscopy to examine if they displayed similar dynamics as mutant keratin granules. Exemplary still images of a recording of DYRK3-eGFP are shown in Fig. 30. It was revealed that DYRK granules share the same characteristic features as mutant keratin granules: growth, fusion, and disassembly, all with similar timeframes. The same granule dynamics were also seen in DYRK1A- and DYRK2-overexpressing cells (not shown).

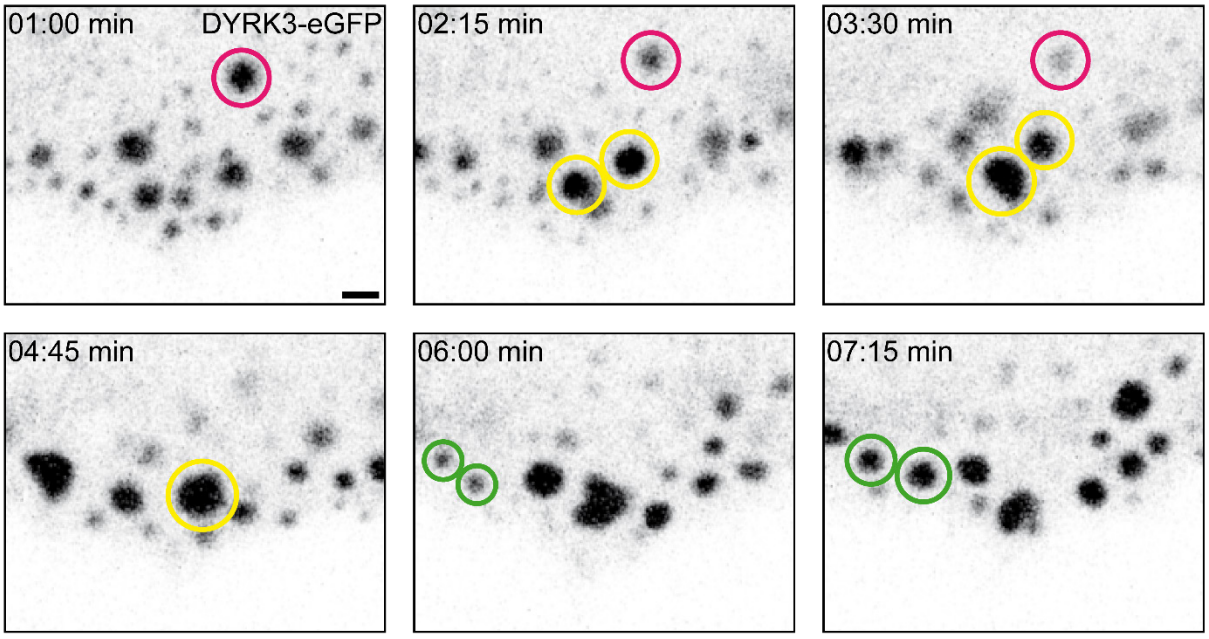

Figure 30 - Overexpressed DYRK granules display similar dynamics as mutant keratin granules. The three DYRK isoform constructs transiently transfected into Krt14R125C keratinocytes (see Fig.29) were also analysed by time-lapse microscopy. Depicted are still images of a 07:15 minute maximum projection view movie of a DYRK3-eGFP-transfected cell. The DYRK3-eGFP granules display very similar dynamics as mutant keratin granules, such as growth (green circles), fusion (yellow circles), or disassembly (pink circles). The cell membrane is located at the lower margin. The DYRK1A and DYRK2-tagged proteins showed similar motility. Scale bar = 1 µm.

Next, EBS cells carrying the Krt14R125C mutation were transiently transfected with DYRK3-eGFP and immunostained for keratin 14 after fixation. Fig. 31 shows that the peripheral keratin granules colocalise with the overexpressed DYRK3-eGFP granules. The keratin staining also detects the collapsed perinuclear keratin cage, but DYRK3 does not localise at this region.

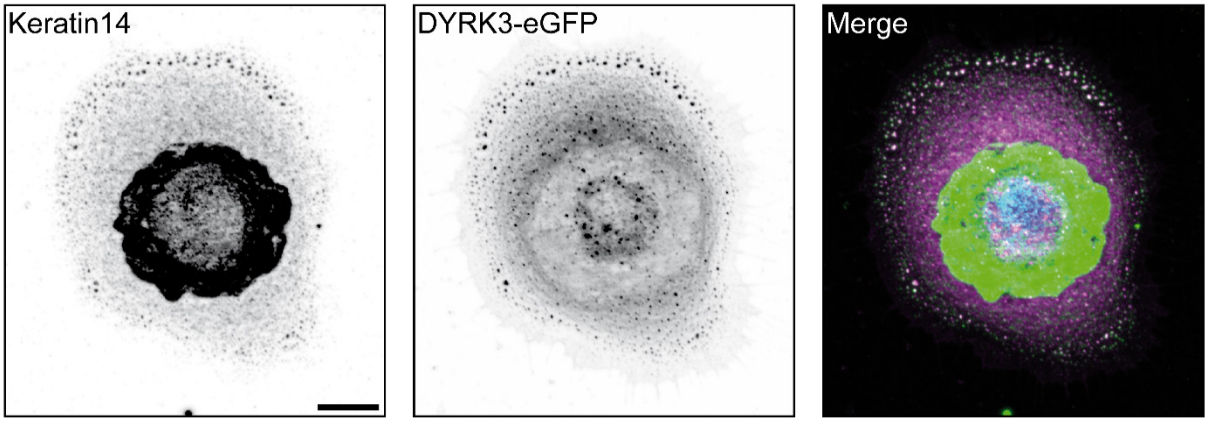

Figure 31 - Overexpressed DYRK granules colocalise with mutant keratin granules. DYRK3-eGFP was transiently transfected into EBS keratinocytes harbouring the Krt14R125C mutation and immunostained with a keratin 14 antibody. Note the staining of keratin-positive granules and the inner collapsed keratin filament network, which has a much higher fluorescence intensity than the granules (increased contrast used to visualise keratin granules). DYRK3-eGFP colocalises with the keratin granules in the outer lamellum (white colour in merge), but not with the remaining keratin filament network. Scale bar = 10 µm.

Detection of endogenous DYRK proteins with antibodies was unsuccessful since none of the antibodies tested produced an immunofluorescent signal.

III.3.2.2 Mutant keratin overexpressing keratinocyte cell clones display different granule patterns

Following the strong indications of colocalisation of DYRK kinases and mutant keratin granules, the potential functional influence of DYRK was investigated by pharmacological inhibition of DYRK. It was hypothesised that the kinase is able to dissolve mutant keratin granules. Thus, the percentage of cells with or without keratin granules was chosen as the analysis output.

In order to obtain these results, a modified construct encoding Krt14R125C-eYFP was cloned and transfected into wild type keratinocytes. Next, 4 single cell clones stably expressing the new construct were established. A first assessment indicated that the different clones displayed varying percentages of granule-containing cells. Consequently, three replicates of microscopic analysis of the cell clones were performed, with cells grown under proliferating (low calcium) conditions for 3 days prior to fixation. The z projection images were transformed into inverse representations with intensified contrast and the percentage of granule-containing cells was calculated as described in II.2.3.13. The results are shown in Fig. 32.

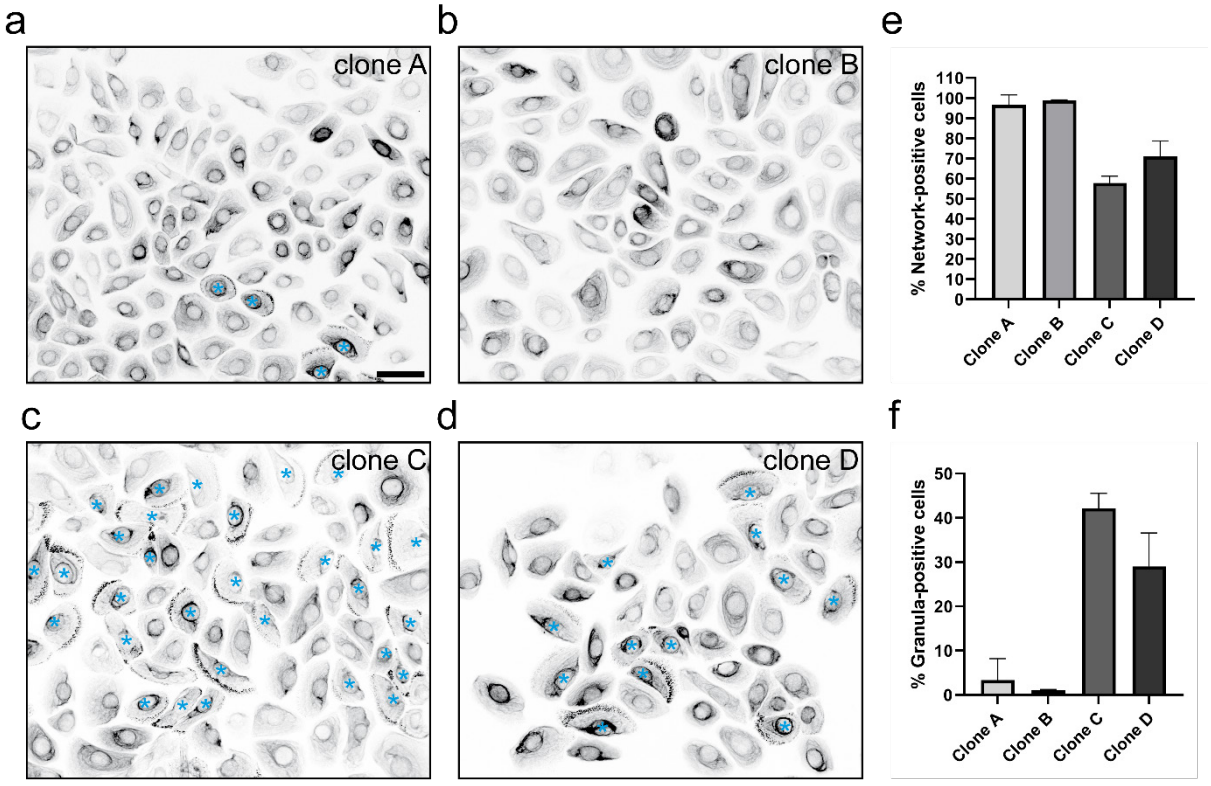

Figure 32 – Keratin network morphology of different keratinocyte cell clones overexpressing mutant Krt14R125C. Shown are 20x projection views (inverse representation) of four different single cell clones stably overexpressing Krt14R125C-eYFP (a-d); cells containing granules are marked with

blue asterisks. Quantification of the percentage of cells with (f) or without granules (e) was performed for n=3 (total cell numbers analysed: n=1362 for clone A; n=1525 for clone B; n=904 for clone C; n=788 for clone D). Scale bar = 50 µm.

As seen in the representative pictures of the 4 different cell clones (Fig. 32a-d), cell clones A and B only contained a low percentage of granule-containing cells, whereas clones C and D displayed higher percentages. The quantification of the percentage of network- and granule-positive cells is shown in Fig.32e and f, respectively. These values were stable over the course of several passages. Clone A shows 3.35±4.84% (mean±SD) of granule-positive cells and clone B 1.06±0.17%, both representing a dominant filamentous keratin network, despite overexpressing the mutant Krt14R125C construct. The other clones show a much higher prevalence of granule-positive cells, with 42.17±3.35% in clone C and 29.01±7.61% in clone D. In contrast, the native EBS patient-derived keratinocytes carrying the Krt14R125C mutation display granules in most cells. It is therefore likely that other factors except the sole genetic mutation are responsible for granule formation.

To test this hypothesis, one specific situation was investigated which requires dynamic alterations of keratin, i.e. spontaneous migration of keratinocytes. During the complex process of migration, the cells form flat protrusions at the leading edge, lamellipodium and filopodium.[282,283] In EBS, cell migration is especially important during closure of wounds caused by epidermal blistering. Exemplary images of a migrating cell of clone B (lowest baseline percentage of granule-positive cells) are shown in Fig. 33.

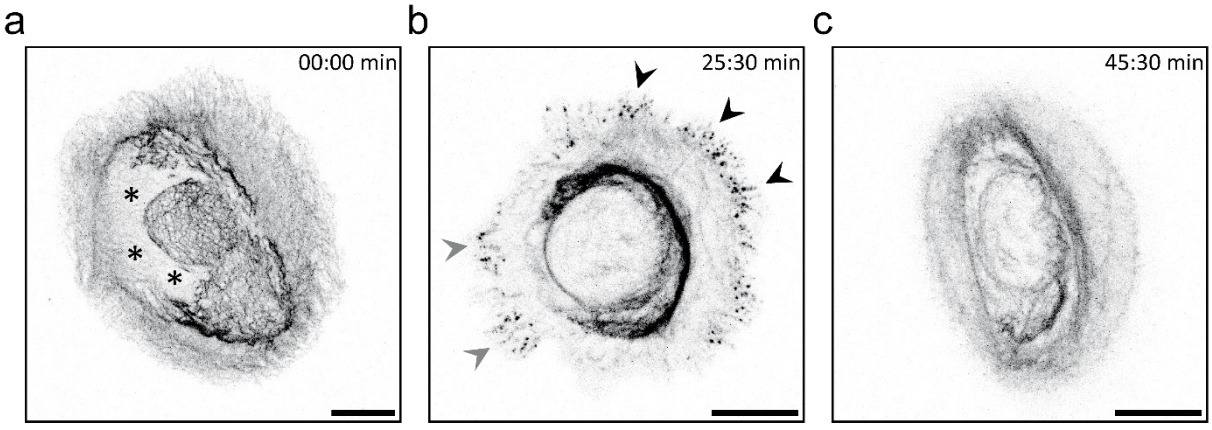

Figure 33 - Spontaneous formation of keratin granules during cellular reorientation in migrating keratinocytes expressing mutant Krt14R125C. Shown are maximum projection still images (inverse representation) of clone B of Krt14R125C-eYFP-expressing keratinocytes during migration towards the right margin. Note the filamentous keratin network at time point 00:00 min, which is very similar to that of wt keratinocytes, without any visible granules (a; region marked with asterisks lies outside the recording area of 1 µm in z). As the cell is reorienting, keratin granules rapidly appear at the front (black arrowheads) and rear (grey arrowheads) of the cell at time point 25:30 min (b). As the cell has finished its reorientation, it is once more migrating towards the right margin at time point 45:30 min, the keratin granules have disappeared, and a solely filamentous keratin network is observed (c; weaker fluorescence due to bleaching). Scale bars = 10 µm.

A completely filamentous keratin network is visible at time point 00:00 minutes, when the cell is migrating into the upper right direction for several minutes (Fig. 33a). Around time point 25:30 minutes, the cell pauses its directed movement and is reorienting. Interestingly, during this reorientation, prominent keratin granules rapidly appear at the cell front and rear (see arrowheads in Fig. 33b). After a few minutes, the cell polarises once again and continues to migrate towards the upper right corner. As soon as this directed movement starts once more, the keratin granules disappear, and a pure filamentous network is again present (Fig. 33c).
These results support the remarkable dynamics of the keratin cytoskeleton during migration and the hypothesis that formation of granules might occur in specific transient situations. It is likely that the formation of membraneless LLPS keratin granules is rapidly regulated by posttranslational or comparable modifications in these specific situations.

III.3.2.3 DYRK inhibition does not alter the percentage of mutant keratin granules

Due to the colocalisation of DYRK kinases with mutant keratin granules, a functional influence was strongly indicated. Thus, the previously described Krt14R125C-eYFP overexpressing keratinocyte cell clones were used to test if pharmacological inhibition of DYRK alters their granular content.
Based on pilot titration experiments, the cells were incubated with the DYRK1A inhibitor Leucettine L41 for 2 hours, either at 1 or 3 µM concentration. 1 µM is described to be specific against DYRK1A only, but it is suggested that a concentration of 3 µM inhibits further isoforms of DYRK and was thus additionally used.
Representative images of all 4 cell clones are shown for DMSO control and the two different Leucettine L41 concentrations in Fig. 34a-d. The quantification of granule-containing cells was performed as described in II.2.3.13 and as already established for quantification of the baseline granule percentages of the cell clones in III.2.2. As shown in the graphs for network-positive (Fig. 34e) and granule-positive-cells (Fig. 34f), the pharmacological inhibition with Leucettine L41 did not result in any significant alterations, except a minor reduction of granule-positive cells in clone D in DMSO control vs. 3 µM treatment. In parallel, a second pharmacological inhibitor of DYRK1B (AZ191) was tested in one experiment and did also not result in any considerable alterations of the percentage of granule-positive cells (not shown).

Consequently, despite the colocalisation of overexpressed DYRK kinases and keratins, a functional influence of DYRK proteins on mutant keratin dynamics could not be verified by using pharmacological DYRK inhibition in this work.

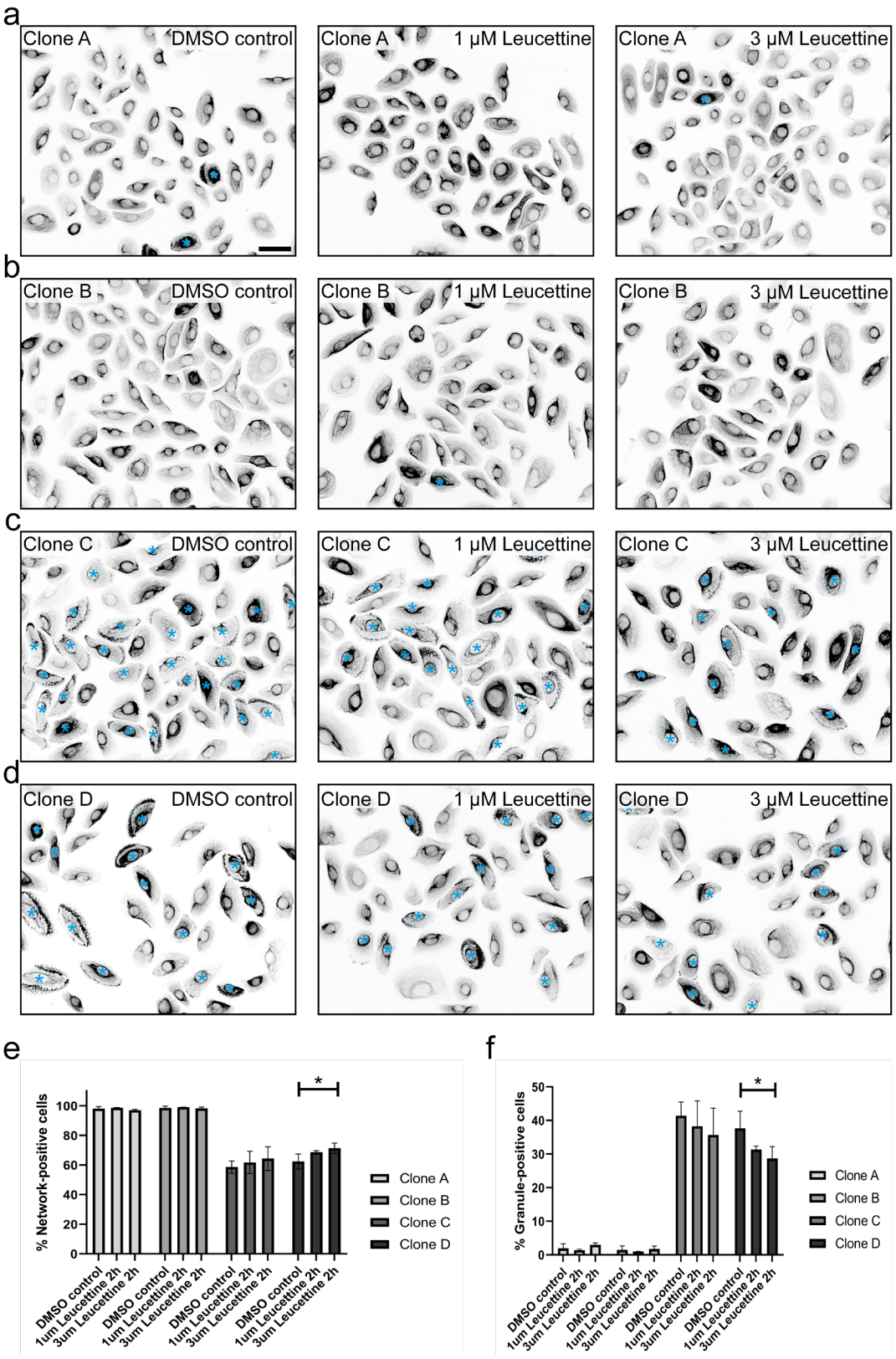

Figure 34 - Pharmacological inhibition of DYRK does not alter the percentage of granule-positive cell clones. The four different wt keratinocyte single cell clones A-D overexpressing Krt14R125C-eYFP (representative inverse representation projection views) were incubated for 2 hours with either DMSO solvent only (first lane), 1 µM (second lane), or 3 µM Leucettine L41 (third lane). The percentage of network- and granule-positive cells was quantified from n=3 replicates (e, f, respectively). Granule-positive cells are marked with blue asterisks. Total cell numbers (n1-n3) for DMSO control, 1 µM L41, 3 µM L41, respectively: clone A (1499; 1452; 1607), clone B (1290; 1363; 1425), clone C (1499; 644; 648), clone D (718; 649; 647). Scale bar = 50 µM.

III.3 The functional influence of keratin mutations on mitochondrial quality control

The following part of this work focused on the functional influence of keratin intermediate filaments on mitochondrial quality control, in particular it was investigated if skin disorder-causing keratin mutations alter mitophagy in patient-derived keratinocytes.

III.3.1 *Pachyonychia congenita*, but not *Epidermolysis bullosa simplex* keratinocytes contain increased amounts of overaged mitochondria

The aim of the initial experiment was to assess if mitochondrial quality control was in general impaired in keratinopathies. Thus, mitochondrial turnover was monitored by transfection of MitoTimer into wt and patient cells. MitoTimer is a mitochondria-targeted dsRed derivative whose fluorescence shifts from green to red as the protein matures.[284] The fluorescence transition of MitoTimer takes ~48 hours upon its expression and was measured by fluorescence microscopy. The results of the analysis are shown for EBS vs. wt in Fig. 35a-c.

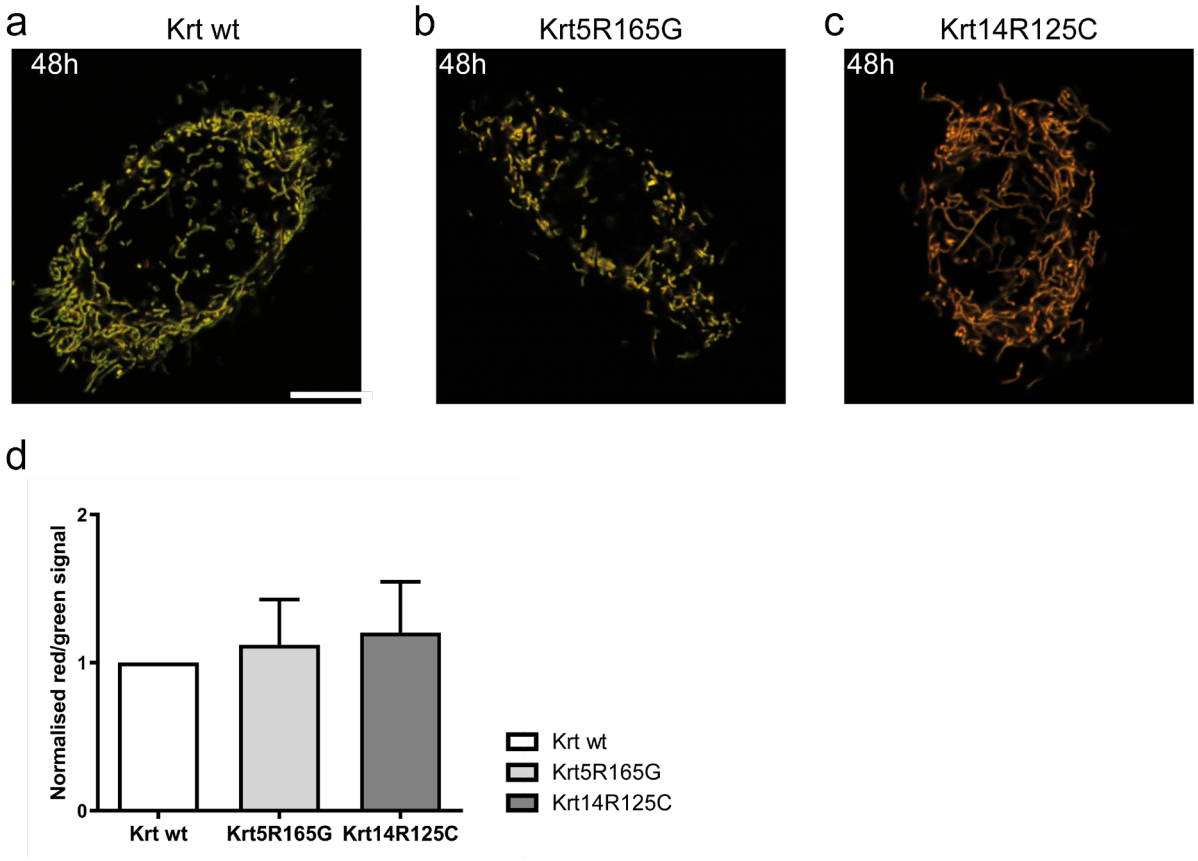

Figure 35 – *Epidermolysis bullosa simplex* keratinocytes do not contain overaged mitochondria. Cells were transfected with MitoTimer encoding a mitochondria-targeted dsRed derivative whose fluorescence shifts from green to red with increasing time after synthesis. Fluorescence images were recorded 48 hours after transfection. (a-c) show fluorescence micrographs taken from wild type Krt and mutant Krt5R165G and Krt14R125C keratinocytes. Each micrograph depicts an overlay of the green

and red channel. The histogram shows the ratiometric quantification of three independent experiments of 30 cells per cell line each (d). Ratios were normalised to control Krt wt cells. MitoTimer changes its colour from green to red over the course of 48 hours. No significant differences were observed for Krt wt cells compared to Krt5R165G and Krt14R125C cell lines 48h after transfection (d). Scale bar = 10 µm.

Overlayed signals of the red and green MitoTimer channels depict a distinct mitochondrial signal, which was yellow in case of wild type and Krt5R165G keratinocytes, and slightly orange in case of Krt14R125C. Quantification of the red-to-green ratio 48 hours after transfection revealed that no significant changes were present in wt vs. both EBS cell lines (Fig. 35d). Thus, it was concluded that mitochondrial quality control defects are unlikely to be present in EBS keratinocytes, and they were not further investigated in this part.

In contrast to the blistering phenotype of EBS patients, the main symptom of PC is epidermal thickening. This hyperkeratosis could be in line with defects within the skin differentiation process, during which macroautophagy is a crucial process.[17] Consequently, the MitoTimer ratio was also determined for the two PC patient-derived cell lines.

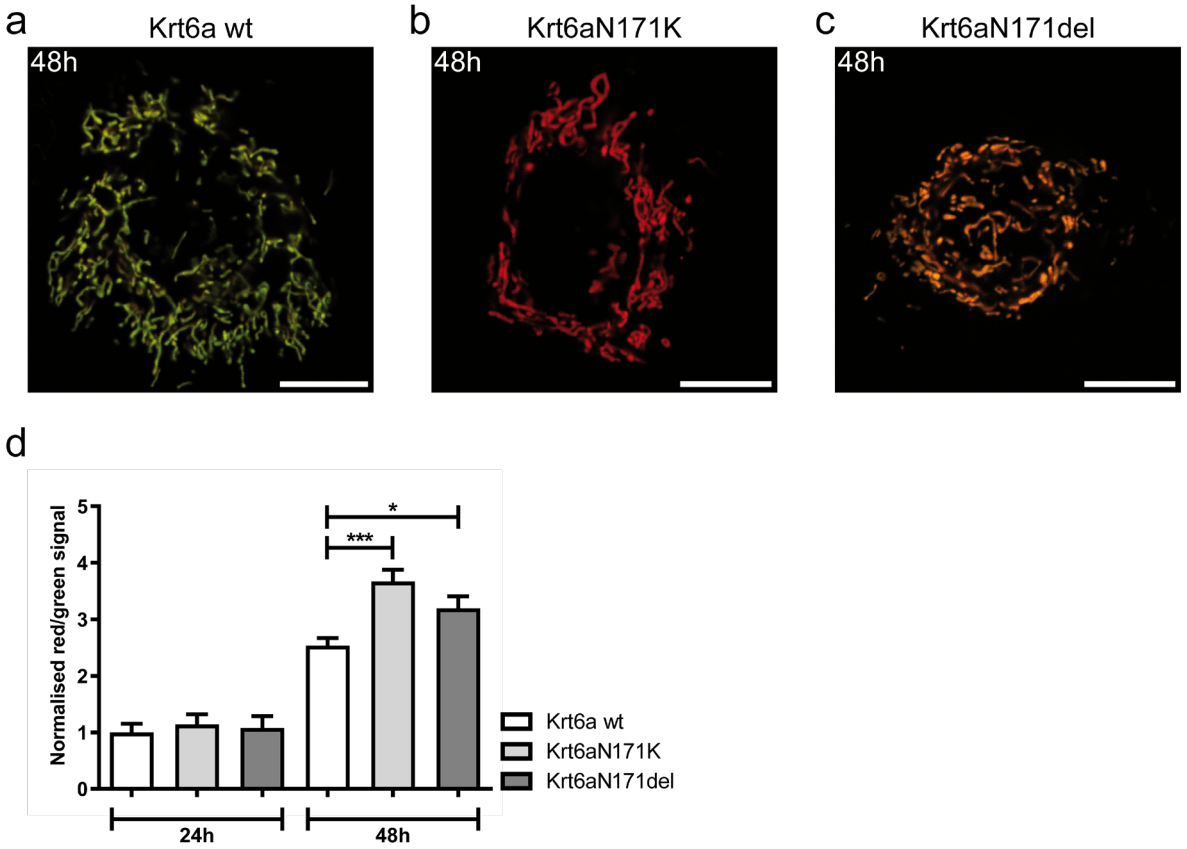

Figure 36 - Old mitochondria accumulate in *Pachyonychia congenita* keratinocytes. Cells were transfected with MitoTimer encoding a mitochondria-targeted dsRed derivative whose fluorescence shifts from green to red with increasing time after synthesis. Fluorescence images were recorded 24 and 48 hours after transfection. (a-c) show fluorescence micrographs taken from wild type Krt6a and mutant Krt6aN171K and Krt6aN171del keratinocytes 48h after transfection. Each micrograph depicts an overlay of the green and red channel. The histogram shows the ratiometric quantification of three independent experiments of 30 cells per cell line each (d). Ratios were normalised to control Krt6a wt cells 24 hours after transfection. MitoTimer changes its colour from green to red over the course of 48

hours. No differences in red/green ratios could be observed 24 hours after transfection. In contrast, after 48 hours Krt6aN171K and Krt6aN171del keratinocytes display a significantly increased red/green ratio of fluorescence intensity compared to Krt6a wt cells (d). Scale bars = 10 µm. Comparisons Krt6a wt cells were performed using one-way ANOVA with Dunnett's post-test. * p<0.05, *** p<0.001. The figure was adapted from [285].

In contrast to EBS, both Krt6aN171K and Krt6aN171del cell lines showed a significant shift towards red fluorescence compared to wt 48 hours after transfection (Fig. 36a-d). To exclude unspecific maturation of the MitoTimer protein, the red-to-green ratio was also analysed 24 hours after transfection. It did not reveal any statistical differences between wild type and PC cell lines (Fig. 36d).

It can therefore be concluded that mitochondria of *Pachyonychia congenita* keratinocytes show a pathological overaging phenotype, which could lead to various subsequent problems, for example in cell metabolism or proliferation. The following experiments aimed to determine why PC mitochondria show the overaged phenotype. Since the maintenance of a healthy mitochondrial pool depends on the elimination of dysfunctional organelles via mitophagy, the sequential steps of this process were subsequently investigated.

III.3.3 Mitochondria-ER contacts are disturbed in *Pachyonychia congenita* keratinocytes

As described in I.11 and I.12, mitochondria-associated membranes (MAMs) might play an important role in mitophagy, as they represent a putative source of autophagosomal membranes. Electron microscopy of wt and PC-mutant cell lines was performed to investigate mitochondrial ultrastructure. A first qualitative analysis revealed no major alterations of mitochondrial morphology (Fig. 37b-d). Thus, quantitative analysis of the contact sites between mitochondria and the surrounding endoplasmic reticulum was performed. Striking differences regarding the percentage of mitochondria closely surrounded with ER were observed. While 22.9% of the circumference of wt mitochondria possessed close contact sites with the ER, only 9.8% and 8% of these sites were present in Krt6aN171K and Krt6aN171del cells, respectively (Fig. 37a).

This indicates that MAM contacts are disturbed in PC keratinocytes, which in turn may have severe consequences regarding lipid metabolism or mitophagy.

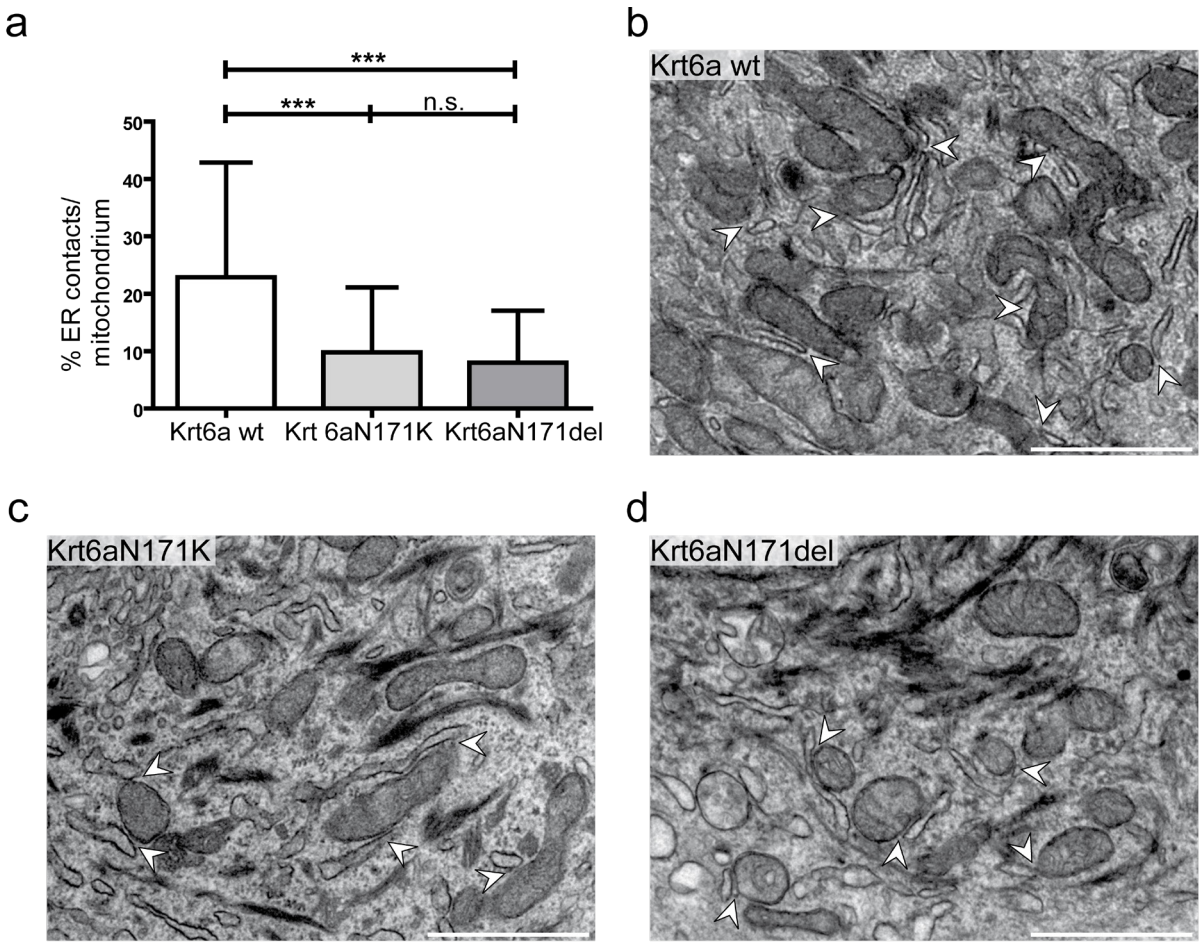

Figure 37 - Mitochondria-ER contacts are reduced in *Pachyonychia congenita* keratinocytes. The spatial relationship between mitochondria and ER was assessed by electron microscopy. (a) shows the quantitative analysis of close ER-mitochondria contacts in Krt6aN171K, Krt6aN171del and wt cells (n ≥ 50 mitochondria per cell line). Note the significant reduction of contact sites in the mutant cells. Representative electron micrographs depict mitochondria-ER contact sites in Krt6a wt (b), Krt6aN171K (c) and Krt6aN171del (d) keratinocytes (white arrowheads). Scale bars = 100 nm. Comparisons between groups were performed using one-way ANOVA with Bonferroni post-test. *** $p<0.001$. The figure was adapted from [285].

III.3.4 *Pachyonychia congenita* keratin mutations do not affect expression levels of early mitophagy key players

As stated in I.3, the physiological condition of suprabasal keratinocytes is a calcium-dependent differentiating state, in contrast to the proliferating *Stratum basale* cells. Consequently, induction of a differentiating state was compared to the proliferating state in most following experiments. It was induced by elevation of extracellular calcium from 0.06 mM to 1.2 mM for three days. Fig. 38 depicts morphological and gene expression-related differences between proliferating and differentiating condition. The cellular morphology was assessed by brightfield images obtained before and during differentiation.

They illustrate that wt keratinocytes displayed a rather homogenous morphology in both proliferating and differentiating state, whereas mutant PC cells varied to a higher extent regarding cell size, morphology, and monolayer alignment.

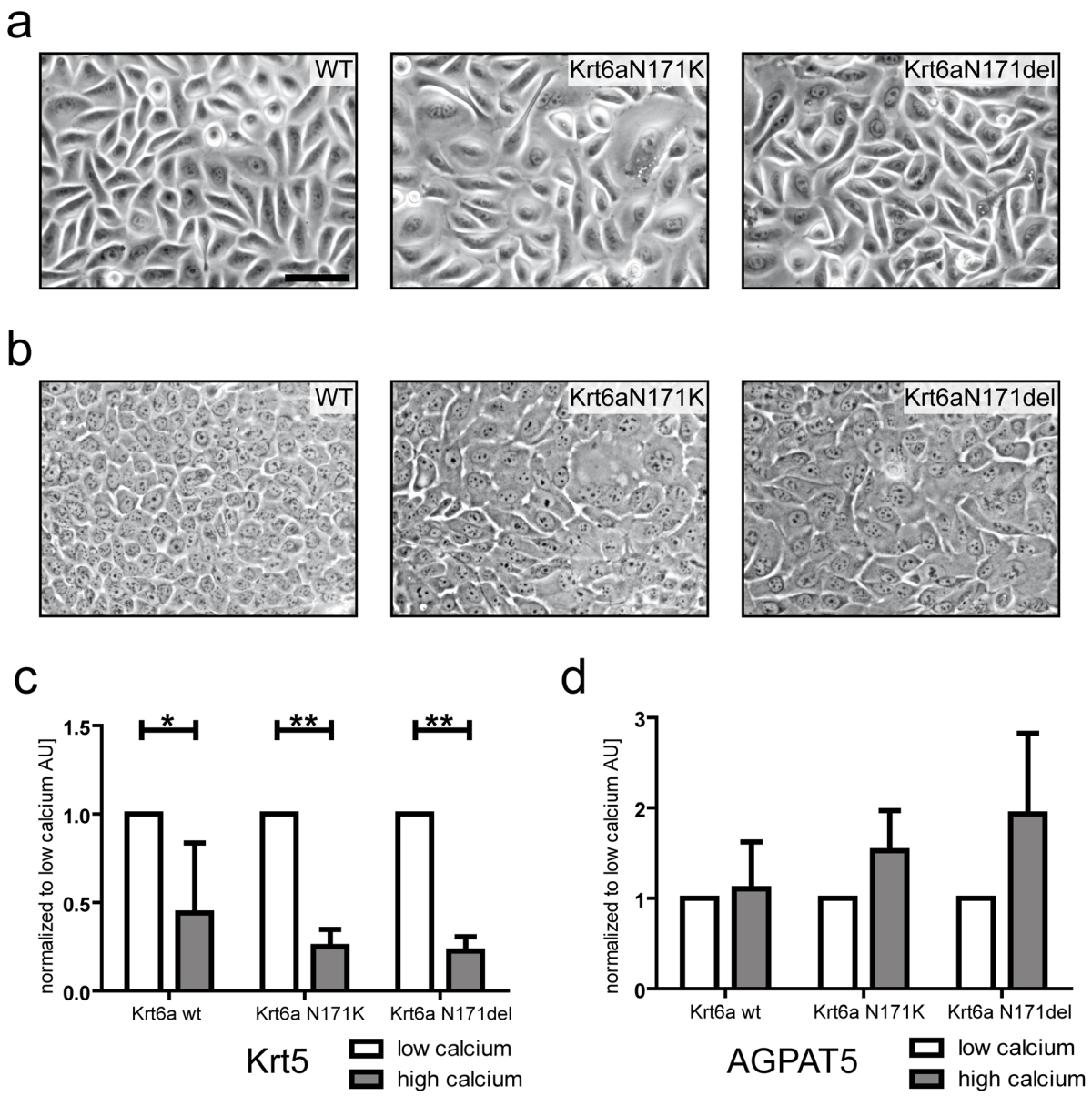

Figure 38 – Differentiation of wild type and PC-mutant keratinocytes. Immortalised wt and PC keratinocyte cell lines were grown in either low-calcium (a; 60 µM calcium) or high-calcium medium (b; 1.2 mM calcium) for three days. Representative images of transmitted light illumination after three days are depicted. High-calcium treatment induced visible alterations indicating differentiation, such as increased alignment and cobblestone-like shape, seen for all cell types, but most clearly for wt. mRNA expression of the differentiation markers keratin 5 (c) and AGPAT5 (d) was determined by quantitative real time PCR, using TBP as housekeeper, for wild type and both PC cell lines. Keratin 5 is significantly downregulated during differentiation in all cell types (c), whereas AGPAT5 is upregulated in all cell types (d). The qPCR graphs represent means ± SD of three independent replicates, the differentiating values thereby being compared to untreated cells of each cell line. Comparisons between groups were performed using one-way ANOVA with Bonferroni post-test. * $p<0.05$. Scale bar = 10 µm.

However, induction of differentiation induced increased alignment, and all keratinocyte cell lines displayed the typical cobblestone-like shape of differentiating skin cells, indicating that differentiation is in principle functional.
To examine characteristic gene expression changes, quantitative PCR was performed for the differentiation markers keratin 5 and AGPAT 5 for PC cell lines. As expected, keratin 5 expression was significantly reduced upon calcium elevation in wt and PC cell lines (Fig. 38c), as it is mainly expressed in basal proliferating cells[286]. The second differentiation marker, AGPAT5, was upregulated in all three cell lines in high calcium conditions, as it is typical for differentiating skin cells (Fig. 38d). These results demonstrate the efficiency of the differentiation protocol used in this work and supports the basic functionality of keratinocyte differentiation in *in vitro* monolayers of wt and PC-mutant cells.

Based on the initial result that PC keratinocytes contain overaged mitochondria, mRNA, and protein expression of early mitophagy key players was investigated for proliferating (low calcium) and differentiating (high calcium) cells. The initial step of mitophagy is the accumulation of PTEN-induced kinase 1 (PINK1) on the outer membrane of dysfunctional mitochondria. It is followed by recruitment of the ubiquitin-ligase Parkin. Under normal conditions, PINK is imported into mitochondria and cleaved by presenilin-associated rhomboid-like protein (PARL). However, upon mitochondrial uncoupling, PINK1 is autophosphorylated on two known phosphorylation sites. This prevents the import into mitochondria and induces PINK1 accumulation on the outer mitochondrial membrane instead.
Thus, quantitative real-time PCR and immunoblot were performed for early mitophagy key players. It revealed that neither PINK1, PARL nor Parkin were differentially expressed in low and high calcium conditions (Fig. 39a-c). Similarly, PINK1 protein levels were unaltered (Fig. 39d), while PTEN and its counterpart PI3K protein levels were slightly reduced independently of calcium addition (Fig. 39e-f). However, their ratios were not altered in both conditions (not shown) and a functional consequence of the minor expression changes not considered.
As the phosphorylation state of PINK1 is crucial for functional mitophagy, PhosTag immunoblot of electrophoretically separated protein samples of wt and PC cell lines was performed next. As a control for unphosphorylated PINK1, low calcium samples were treated with alkaline phosphatase (AP) prior to SDS-PAGE. Only phosphorylated PINK1 was present in proliferating and differentiating cells independently of the cell type. Levels of once phosphorylated PINK1 were not altered in both PC lines compared to control. The twice phosphorylated protein was slightly increased in Krt6a wt cells grown in low versus high calcium, whereas the phosphorylation status did not differ in both mutant K6 cell lines (Fig. 39g). However, these slight changes were not consistent in the other two replicates of PhosTag blot (not shown), indicating that PINK1 phosphorylation is not functionally affected in PC cells.

Overall, these results suggest that recognition and labelling of dysfunctional mitochondria for further mitophagy steps are functional.

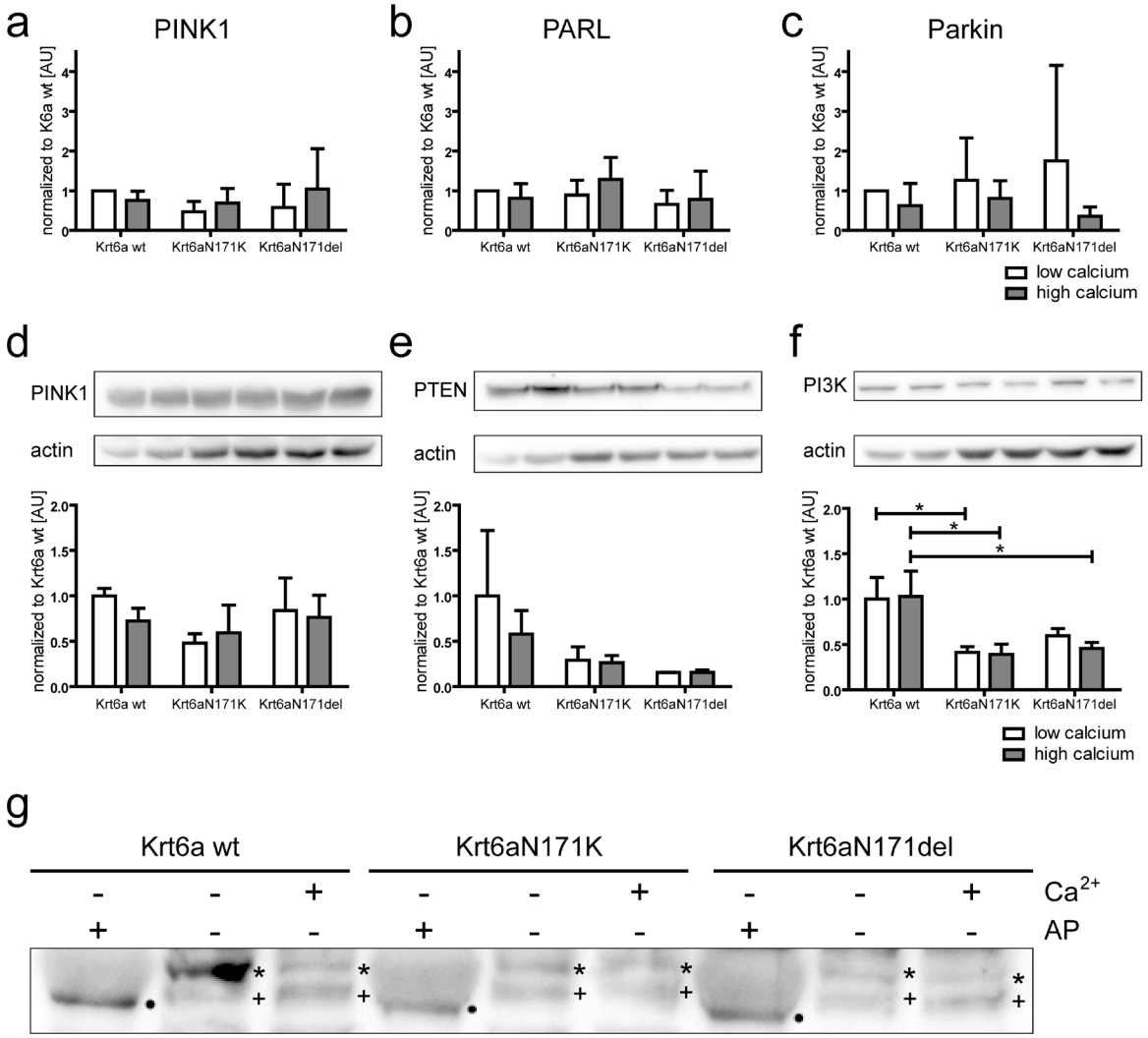

Figure 39 - Expression levels of early mitophagy markers are not affected by Krt6a mutations. Shown are qPCR results (n=3 each; mean±SD) determining mRNA levels of PINK1 (a), PINK1-cleaving protease PARL (b), and Parkin (c) in Krt6a wt and mutant Krt6aN171K and Krt6aN171del keratinocytes grown under low and high calcium conditions. No significant alterations are detectable. (d-f) Results of immunoblot analysis; top: examples of immunoblot images; bottom: histograms depicting quantitative analysis of three replicates; mean±SD. PINK1 protein levels are not significantly altered (d), but its inductor PTEN is slightly decreased (e) and the PTEN antagonist PI3K significantly decreased in Krt6aN171K cells under low and high calcium conditions and in Krt6aN171del keratinocytes under high calcium conditions compared to Krt6a wt (f). A representative PhosTag immunoblot of PINK1 wild-type and mutant Krt6a keratinocytes grown in low (-) and high calcium conditions (+) is shown in (g) (n=3 replicates). As a control, low calcium samples were treated with alkaline phosphatase (AP) prior to immunoblotting. Non-phosphorylated PINK1 is marked by filled circles. Note that PINK1 is always phosphorylated in low and high calcium. Levels of once phosphorylated PINK1, indicated by crosses, are not altered in both PC cell lines compared to Krt6a wt. The twice phosphorylated version of PINK1, demarcated by asterisks, is slightly increased in Krt6a wt keratinocytes grown in low versus high calcium. In contrast, the PINK1 phosphorylation status does not differ between low and high calcium in Krt6aN171K and Krt6aN171del. Comparisons between groups were performed using one-way ANOVA with Bonferroni post-test. * $p<0.05$. The figure was adapted from [285].

III.3.5 Mitophagy is severely impaired in *Pachyonychia congenita* keratinocytes

Despite the fact that early mitophagy key players are normally expressed, mitochondria are ultimately overaged in PC cells, which are presumably not properly recycled or disposed of. Consequently, the next mitophagy steps were investigated by fluorescence microscopy. Mitochondrial translocation of Parkin, representing a key process of early mitophagy, was monitored by transfection with fluorophore-labelled Parkin. Mitochondria were labelled with MitoTracker. Furthermore, mitophagy was induced by addition of the mitochondrial uncoupler carbonyl cyanide m-chlorophenyl hydrazine (CCCP). The sequential process of mitophagy was monitored by imaging mitochondrial and Parkin signal after 18 hours of DMSO control, and 2 and 18 hours after mitophagy induction. In the control state, Parkin showed a cytoplasmic pattern in all cell lines, without specifically localising to any cytosolic structures (100% of control cells, 99.35% of Krt6aN171K PC cells, and 100% Krt6aN171del PC cells) (Fig. 40a-c, upper panels). Two hours after mitochondrial uncoupling, it drastically changed its localisation and displayed a dotted pattern in 93.77% of control cells and 95.33% of Krt6aN171K and 94.60% of Krt6aN171del cells. The parkin signal colocalised with the MitoTracker staining (Fig. 40a-c, middle panels, quantification in 40d). These results prove that Parkin recruitment to depolarised mitochondria is functional in PC cells.

Furthermore, mitochondria re-localised towards the nucleus after 2 hours of CCCP treatment in all cell lines. Respectively, the mitochondrial area was significantly reduced in wt and Krt6aN171K cells compared to the respective DMSO controls, but not in Krt6aN171del (Fig. 40a-c, middle panels; quantification in 40e). This indicates functional fragmentation of dysfunctional mitochondria, which precedes further mitophagy.

A significant reduction of mitochondrial area from DMSO control and 2 hours compared to 18 hours treatment shows that mitochondria were successfully eliminated in wt cells (Fig. 40a, quantification in 40e). However, neither Krt6aN171K nor Krt6aN171del cells displayed a significant reduction of mitochondrial area from 2 to 18 hours. Furthermore, they contained significantly larger amounts of mitochondria than wild type cells after 18 hours CCCP treatment (Fig. 40a-c, quantification in 40e). Regarding Parkin localisation, a cytoplasmic pattern was restored in 72.62% of control cells after 18 hours of CCCP treatment, whereas only 9.33% of Krt6aN171K and 9.8% of Krt6aN171del PC cells were able to restore this cytoplasmic pattern.

In conclusion, dysfunctional mitochondria can still be labelled for subsequent mitophagy with Parkin in PC keratinocytes. However, subsequent mitophagy is disturbed in *Pachyonychia congenita*, resulting in a significant accumulation of mitochondria.

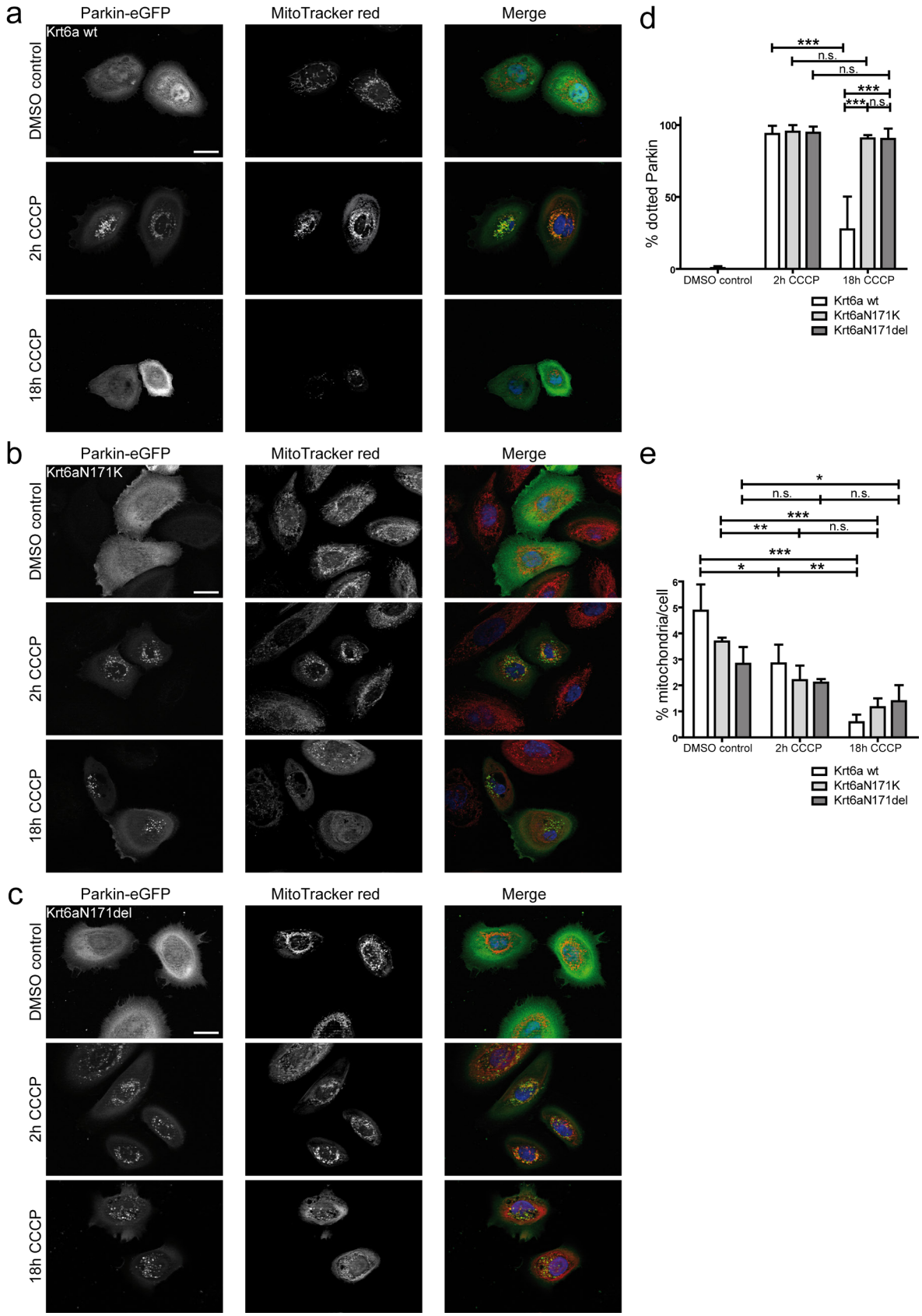

Figure 40 - Mitophagy is severely impaired in *Pachyonychia congenita* keratinocytes. Keratinocytes were transfected with a fluorescent Parkin reporter (Parkin-eGFP) one day after seeding and treated with the mitophagy inducer CCCP (10 µM) for 2 h and 18 h or with DMSO as a control for 18 h, stained with MitoTracker and subsequently fixed. (a-c) show representative fluorescence micrographs of three independent experiments with at least 48 cells per condition each. (d) shows a histogram of the percentage (mean ± SD) of cells displaying either dotted or diffuse cytoplasmic Parkin.

All cell lines display an even cytoplasmic Parkin distribution under control conditions (a-c; d), shifting to dotted, i.e. mitochondrial-targeted Parkin after two hours of CCCP treatment as expected for dysfunctional mitochondria. After 18 h of CCCP treatment, however, only 72.61% of Krt6a wt keratinocytes display a cytoplasmic Parkin distribution again (a, e), whereas 90.67% of Krt6aN171K and 90.2% of Krt6aN171del cells still display dotted Parkin (b, c, e). (e) The histogram depicts the percentage (mean ± SD) of the cell area covered by mitochondria. Note that mitochondrial area is significantly reduced in Krt6a wt cells by CCCP (4.87% in untreated cells, 2.84% after 2 h of CCCP, 0.58% after 18 h of CCCP) but that mitochondrial area in PC cell lines only changes within 2 h of CCCP treatment but not further after 18 h CCCP treatment. Scale bars = 20 µm. Comparisons between groups were performed using one-way ANOVA with Bonferroni post-test. * p<0.05, ** p<0.01, *** p<0.001. The figure was adapted from [285].

III.3.6 *Pachyonychia congenita* keratin mutations do not affect expression levels of late mitophagy and autophagosome formation key players

As shown in III.3.5, mitophagy is severely impaired in PC keratinocytes. Thus, the expression of late mitophagy and autophagosome formation markers was analysed next to evaluate if differential expression of these proteins may be the underlying cause. During late mitophagy and autophagosome formation, mitochondria-localised Parkin ubiquitinates various outer mitochondrial membrane proteins. This is recognised by the ubiquitin-binding deacetylase 6 (HDAC6) and the autophagy receptors SQSTM1/p62 and optineurin. Subsequently, aggregation of dysfunctional mitochondria is mediated by p62 which directly binds to the autophagic effector proteins LC3A and LC3B.[246,250] Furthermore, optineurin is recruited to damaged mitochondria, thus marking the initial site of autophagosome formation.[252] HDAC6 further drives autophagy by mediating the attachment of autophagosomes to dynein motors in order to deliver them to lysosomes.[287] Subsequent autophagosome-lysosome fusion is driven by cortactin-dependent actin remodelling mediated by HDAC6.[288]
Quantitative real-time PCR of the stated key players revealed that mRNA expression of optineurin, HDAC6 and p62 was not altered in wt and PC cells in both proliferating and differentiating condition (Fig. 41a-c). In line with these results, protein expression of optineurin and p62 was also not significantly changed in both conditions (Fig. 41d-e).

In conclusion, late mitophagy and autophagosome formation key players are not differentially expressed in *Pachyonychia congenita* keratinocytes and probably are thus not the cause of dysfunctional mitophagy.

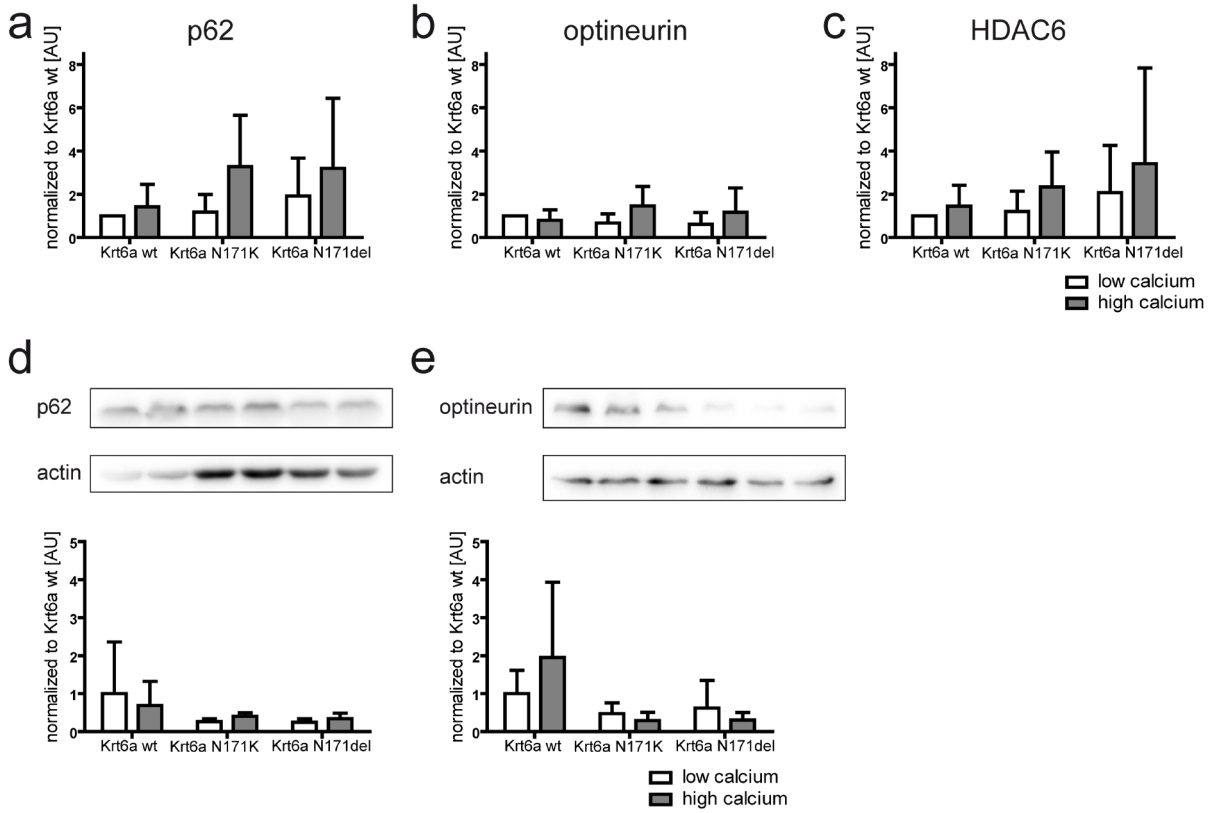

Figure 41 - Expression levels of markers for autophagosome formation are not affected by Krt6a mutations. (a-c) Histograms of autophagosomal mRNA levels (mean ± SD) were prepared from qPCR analyses of three independent experiments from cells grown at low and high calcium conditions. Neither p62 (a) nor optineurin (b) or HDAC6 (c) show significant alterations of mRNA levels in mutant Krt6aN171K and Krt6aN171del compared to Krt6a wt keratinocytes. (d-e) Immunoblot analyses of cell lysates from the same cell lines further demonstrate that p62 (d) and optineurin (e) protein levels are also not significantly altered in the mutant cell lines. Corresponding histograms of the protein levels (mean ±SD; three independent experiments) are shown below. Comparisons between groups were performed using one-way ANOVA with Bonferroni post-test. The figure was adapted from [285].

III.3.7 *Pachyonychia congenita* keratinocytes accumulate autolysosomal structures

As expression of early and late mitophagy key players was shown to be functional in PC, the next experiment assessed if the impaired mitochondrial removal is based on malfunction of autolysosome formation. Wild type and PC cells were transfected with an mRFP-GFP LC3 tandem fluorophore, which specifically localises to autophagic membranes, i.e. both autophagosomes and autolysosomes.[289] Under steady-state conditions, the protein fluoresces both green and red. Upon fusion of autophagosomes with lysosomes the green fluorescence is lost due to the acidic and degradative conditions of the lysosome.[272]

Quantification of green and/or red LC3 puncta was performed to compare the number of autolysosomes, i.e. only red puncta. The total number of autolysosomes (red puncta) was not altered in wt keratinocytes, comparing proliferating and differentiating state (61.99 autolysosomes/cell in low calcium vs. 69.65 autolysosomes/cell in high calcium) (Fig. 42a, d).

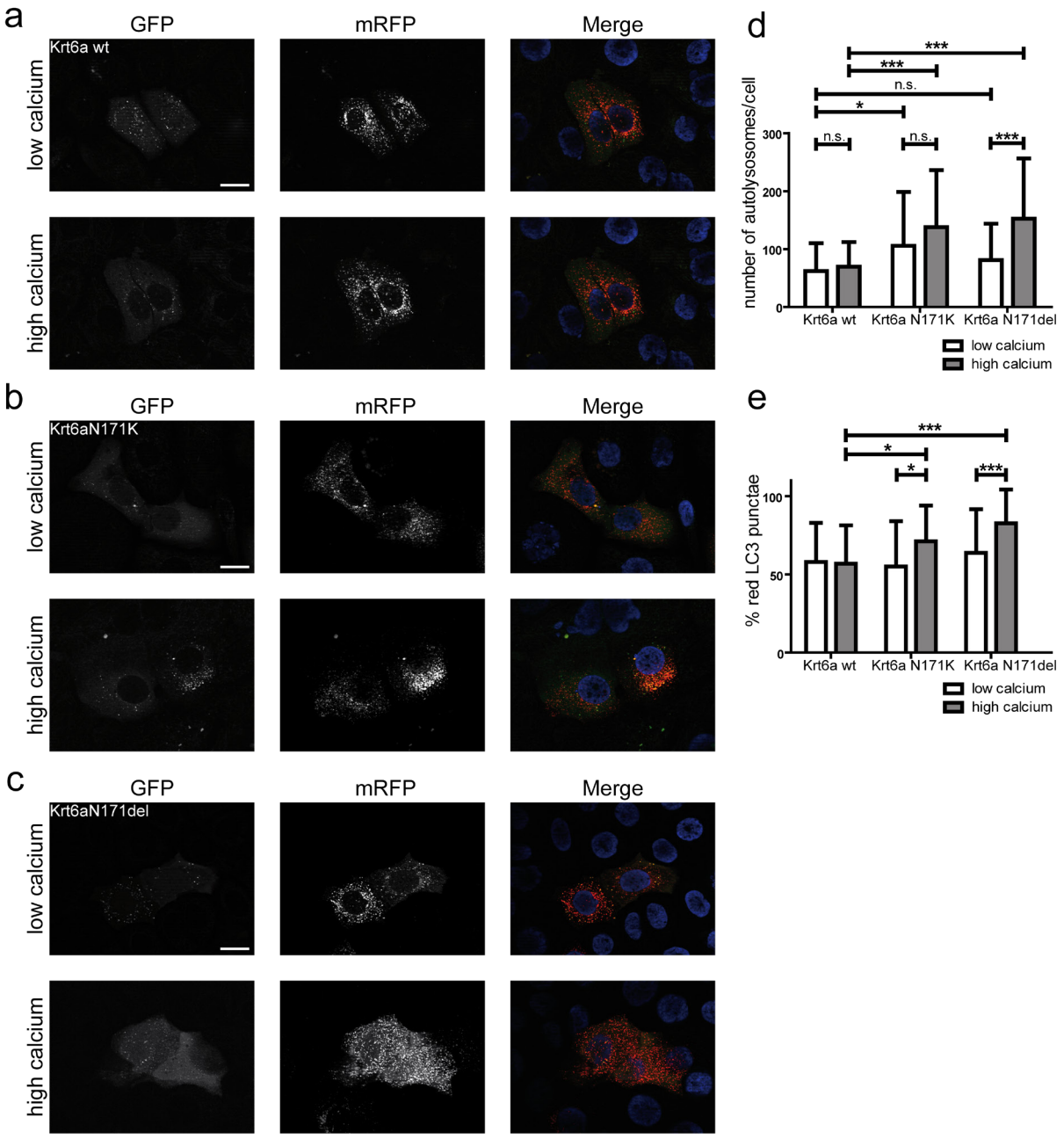

Figure 42 - Krt6a mutations lead to impaired autolysosome maturation/recycling. To monitor autophagosome and autolysosome formation, cells were transfected with a LC3 tandem fluorophore. Autophagosomes are represented by green and red puncta (single channels represented in white-black representation), whereas autolysosomes show only red fluorescence. (a-c) The representative fluorescence micrographs (three independent experiments of n≥16 cells per condition each) taken from cells grown at low and high calcium conditions show that the total number of red puncta (autolysosomes) is significantly increased in PC cell lines compared to Krt6a wt cells grown at high calcium (histogram in d). Furthermore, the percentage of only red puncta is significantly increased at high calcium compared to low calcium conditions in both mutant cell lines but not in wt Krt6a keratinocytes (quantification in e). Scale bars = 20 µm. Comparisons between groups were performed using one-way ANOVA with Bonferroni post-test. * $p<0.05$, ** $p<0.01$, *** $p<0.001$. The figure was adapted from [285].

On the other hand, the total number of autolysosomes per cell was already increased in both PC cell lines under proliferating conditions compared to wt keratinocytes (61.99 autolysosomes/cell in wt, 105.6 autolysosomes/cell in Krt6aN171K cells, and 80.88 autolysosomes/cell in Krt6aN171del cells) (Fig. 42a-c upper panels; quantification in Fig. 42e). Furthermore, induction of differentiation further elevated the total number of autolysosomes in both PC cell lines (69.65 autolysosomes/cell in wt cells, 138.00 autolysosomes/cell in Krt6aN171K cells, and 152.5 autolysosomes/cell in Krt6aN171del cells) (Fig. 42a-c lower panels; quantification in Fig. 42e).
The percentage of autolysosomes (red puncta) was not altered in low calcium compared to high calcium in wt cells. However, the elevation of extracellular calcium led to a significantly increased percentage of autolysosomes in both PC cell lines (57.86% vs. 56.82% in wt cells, 55.09% vs. 71.13% in Krt6aN171K, and 63.8% vs. 82.6% in Krt6aN171del) (Fig. 42d).

These results strongly indicate that while formation of autolysosomes itself is not affected by keratin 6a mutations, the autolysosomal maturation or recycling process is disturbed in PC keratinocytes, leading to an accumulation of these organelles.

III.3.8 Lysosomal function is disturbed *in Pachyonychia congenita* cells

To examine whether lysosomal dysfunction is present in PC keratinocytes, the lysosomal activity was assessed using a Magic Red® Cathepsin B assay. It provides a substrate for the lysosomal cysteine protease cathepsin B, i.e. a modified version of the photostable red fluorophore cresyl violet. It is non-fluorescent in the unprocessed state which changes upon enzymatic cleavage, resulting in red fluorescence.

Its fluorescent signal was measured as area percentage per cell. Fig. 43 shows that cathepsin B activity is significantly reduced in both PC cell lines compared to wt, in Krt6aN171K cells from 100.00 to 36.22±16.5, and in Krt6aN171del cells to 71.10±11.17 (mean±SD), all measured under differentiating conditions (Fig. 43a).

Thus, it can be concluded that lysosomal enzymatic functionality is disturbed in *Pachyonychia congenita* keratinocyte cell lines.

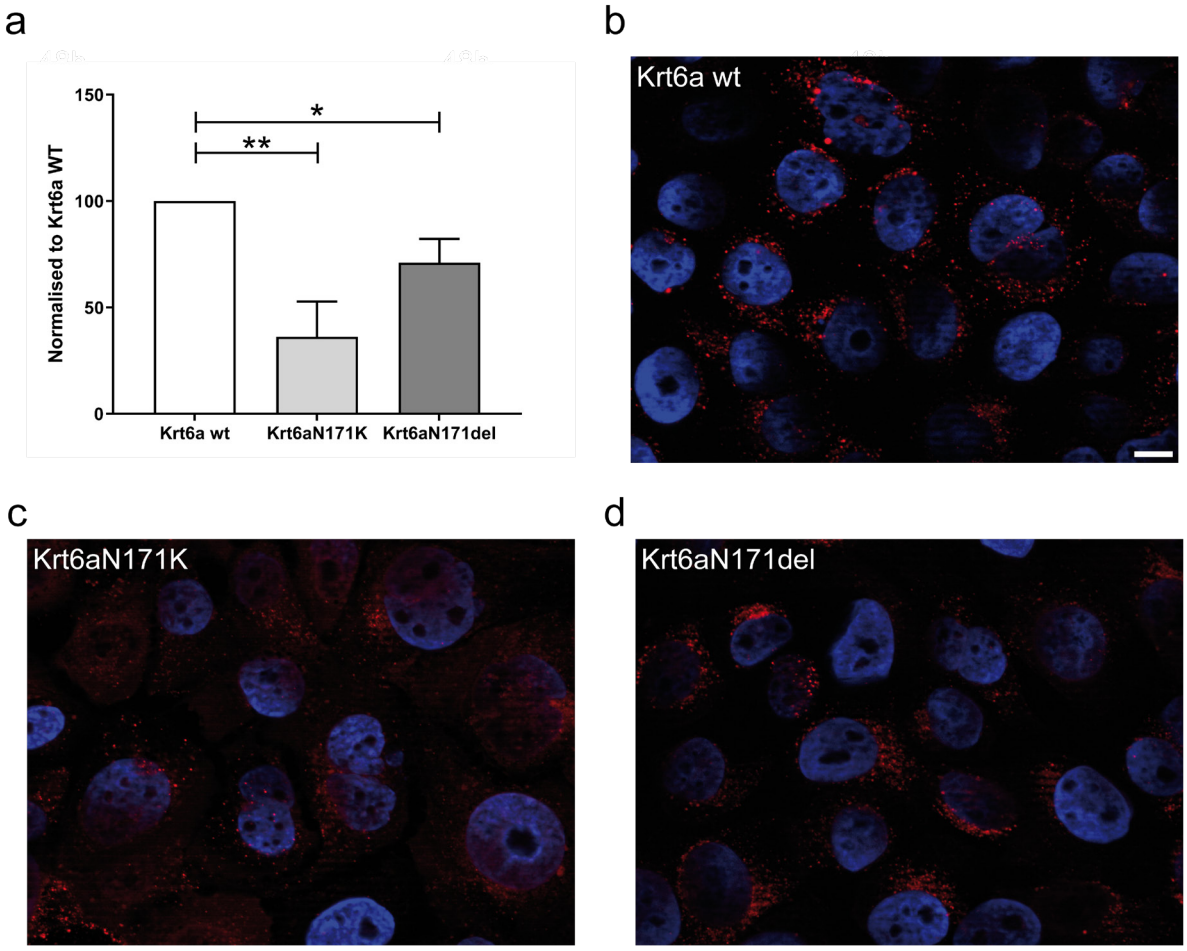

Figure 43- Lysosomal function is reduced in *Pachyonychia congenita* keratinocytes. To assess lysosomal function in terms of cathepsin B function, the cells were incubated for 60 minutes with Magic Red® Cathepsin B substrate. Differentiated wt (b), Krt6aN171K (c) and Krt6aN171del (d) cells display a red fluorescence signal in lysosomes (contrast was equally set for images taken on the same day, i.e. both PC mutants). Three independent experiments with n=327 (wt), n=216 (Krt6aN171K), and n=241 (Krt6aN171del) were performed. The red fluorescence signal was measured as area percentage per cell, and the values were normalised to wt cells for each replicate. Note the significantly reduced fluorescent signal in both PC cell lines (a). Scale bar = 10 µm. Comparisons between groups were performed using one-way ANOVA with Holm Šidák post-test. * $p<0.05$, ** $p<0.01$.

In order to determine if altering the lysosomal pH influence the activity of lysosomes, cells were next treated with Bafilomycin A1, a specific inhibitor of vacuolar type H^+-ATPase (V-ATPase). It induces an increase of lysosomal pH. Cells were first transfected with the MitoTimer construct, and subsequently treated with 1 nM Bafilomycin A1 for 48 hours. The red-to-green ration of MitoTimer was determined as an indirect readout for lysosomal activity, as reduced lysosomal activity is assumed to impair mitophagy and result in overaged mitochondria.

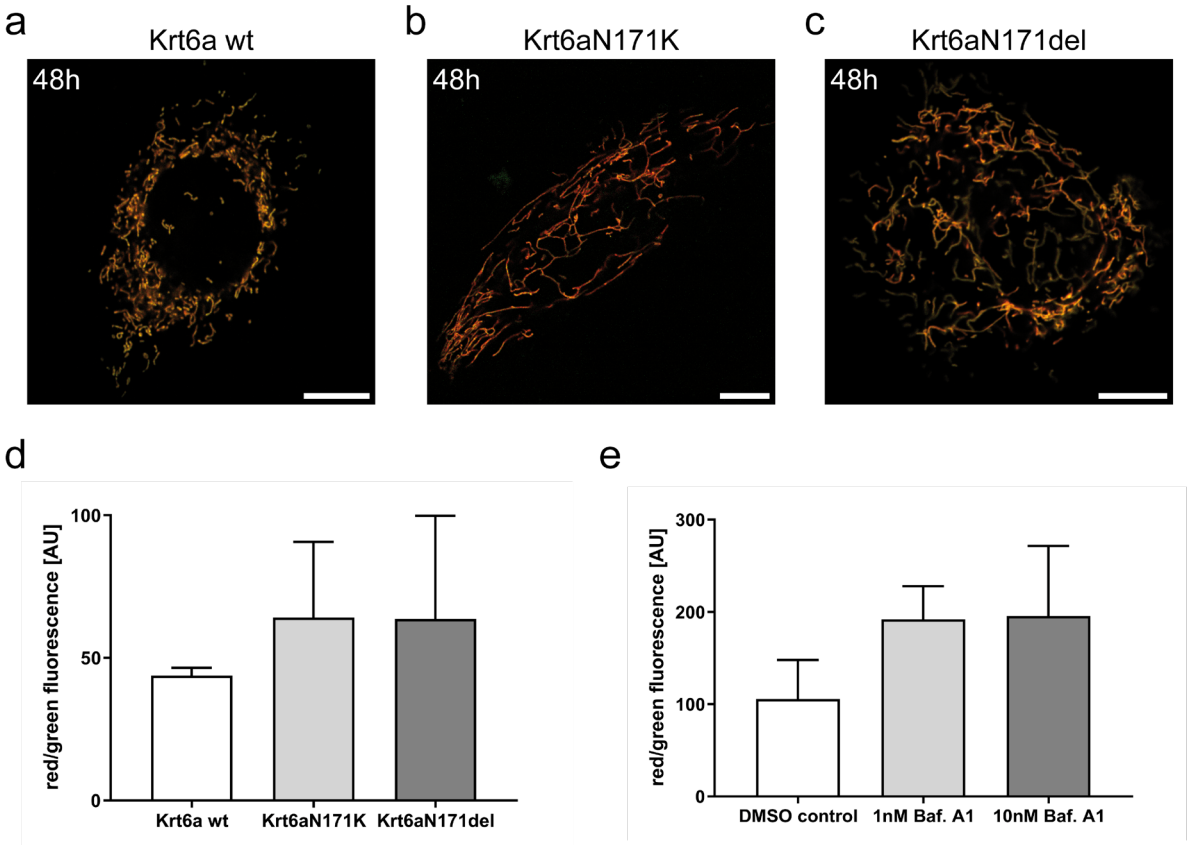

Figure 44 – Deacidification of lysosomes mimics the mitochondria overaging phenotype in wt cells. Proliferating keratinocytes were transfected with MitoTimer, a mitochondrial-targeted dsRed derivative, that switches fluorescence from green to red with increasing time after synthesis. 6 hours after transfection, the cells were incubated with 1 nM of the vacuolar type H^+-ATPase inhibitor Bafilomycin A1 in order to alkalise lysosomes. The cells were fixed after 48 hours of treatment, and 20 images per condition were taken for each of three independent experiments. The micrographs of wt (a), Krt6aN171K (b), and Krt6aN171del (c) show an overlay of the red and green channel (contrast was set individually for each image, as they were taken on different days). Comparisons between groups were performed by one-way ANOVA with Dunnett's post-test (d). Note that no significant differences are present. (e) shows the data of one replicate of wt cells only, with 2 different concentrations of Bafilomycin A1 tested. Note that the treatment leads to a considerable increase of red-to-green fluorescence ratio. Scale bars = 10 µm.

As depicted in Fig. 44 a-c, the red-to-green ratio was shifted towards red in Bafilomycin-treated wt cells, resulting in an orange signal similar to that of both PC cell lines. No significant differences could be observed between all cell lines (43.75±2.761 in wt; 65.14±26.53 in Krt6aN171K; 63.64±36.18 in Krt6aN171del). Furthermore, Fig. 44e shows the results of one replicate of wt cells only, which were treated with DMSO only, 1 nM, and 10 nM Bafilomycin A1. A clear shift towards the red signal is observed for both Bafilomycin A1 concentrations (105.6±42.38 in DMSO control; 191.9±36.03 in 1 nM Bafilomycin A1; 195.6±75.88 in 10 nM Bafilomycin A1). Alterations of cellular morphology were observed for 10 nM; the replicated experiments (Fig. 44 a-d) were thus performed using the lower concentration.

These results indicate that alkalisation of lysosomes induces the same mitochondria overaging phenotype in wt cells, as it is present in the ground state in PC cell lines.

IV. Discussion and Outlook

IV.1 Mutant keratin granules as highly dynamic LLPS condensates

In the first part of this work, a new automated tracking routine was established, which allowed quantification of important parameters of EBS-mutant Krt14R125C granule dynamics, which:

- are formed in the outermost lamellum and disassembled at a distinct transition zone
- grow up to a certain plateau size by incorporation of soluble keratins
- have a limited lifetime
- move towards the cell centre by actomyosin-dependent transport
- in most cases display multiple fusions with other granules during their lifetime
- are formed based on the principles of liquid-liquid phase separation

IV.1.1 Automated mutant keratin granule tracking as a novel screening system

Pharmacological inhibition of nm myosin II has demonstrated that the automated tracking system established in this work is able to generate quantitative measures of the main dynamic features of cytoplasmic protein granules (Fig.45 a). Although it has been already shown in other studies that intermediate filament granules are not just static protein aggregates,[290-292] this study is the first that takes precise quantitative parameters into account. As keratin (granule) dynamics are regulated by a multitude of modulating factors, such as transcriptional control, posttranslational modifications or protein interactions, a concise determination of these factors has not been clarified yet. For example, cell adhesion or mechanical resilience phenotypes highly vary between different EBS-associated mutations.[116,293,294] Also, environmental factors, such as mechanical stress, have been shown to differentially influence mutant keratin network organisation and mechanotransduction.[293,295] Using our tracking routines, a systematic assessment of potential keratin granule-modulating factors, considered either individually or combined, will help to elucidate the complex interplay (Fig. 45 b).

Next to quantitative analysis of keratin granules which are formed due to genetic mutations, it will also be interesting to investigate wt keratin granules appearing during mitosis, apoptosis, increased stress, or phosphatase inhibition[296-298]. Such experiments might shed further light on the formation of keratin granules in either mutant or wild type case. Furthermore, these tools can also be used to quantify the dynamics of other protein aggregation diseases, either involving other intermediate filament classes (e.g. Desminopathies or Alexander disease) or other cytoplasmic proteins (e.g. Parkinson´s or Amyotrophic lateral sclerosis). In order to allow as many researchers as possible to benefit from this work, the established image analysis

protocols have been published (see II.2.5.4). A cooperation of multiple research groups working on different protein aggregation diseases will likely help to further understand details and common features of their pathogeneses and to work on potential new therapeutic options.

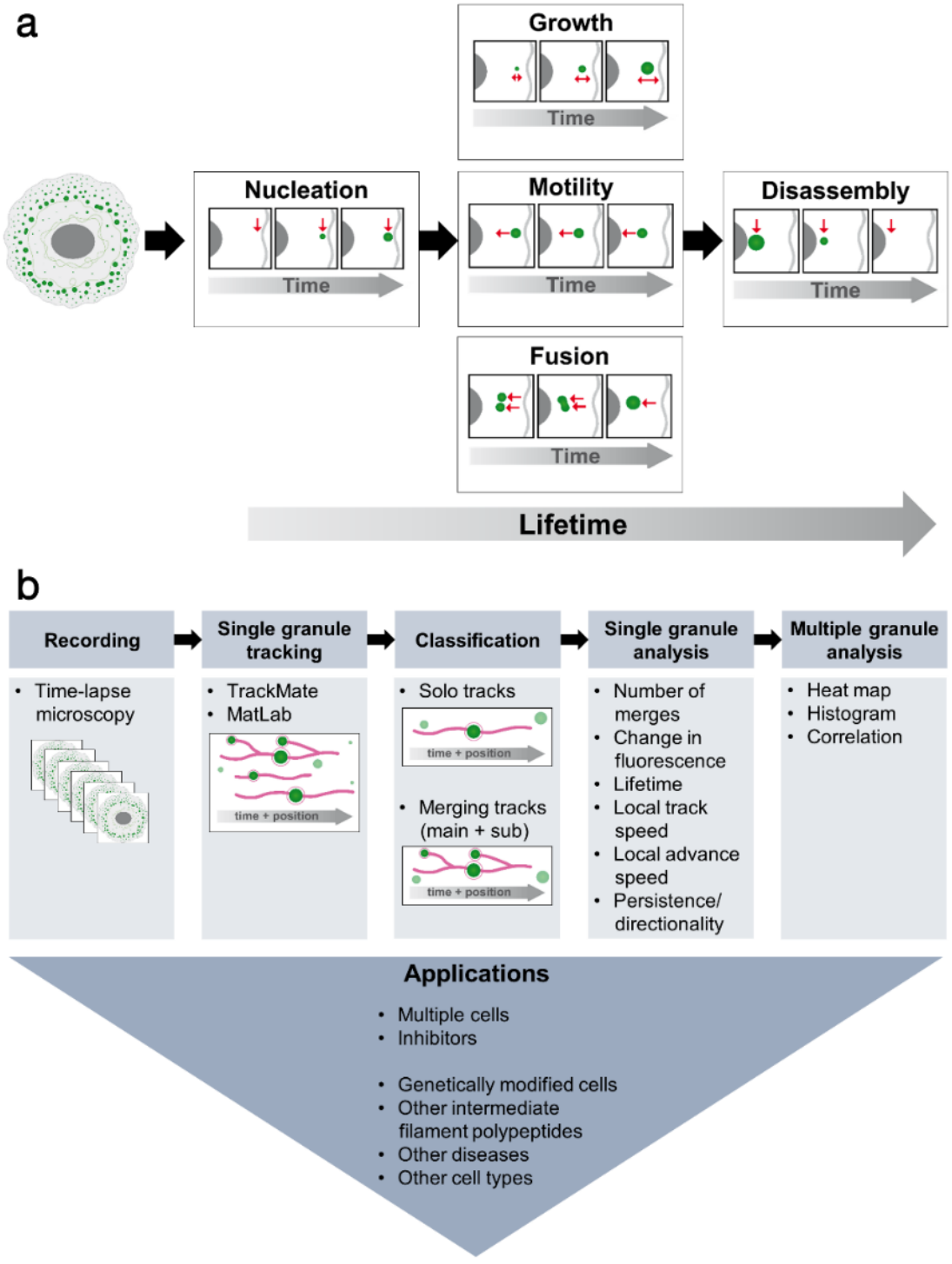

Figure 45 – Scheme of the different keratin granule lifetime stages and workflow to determine them in quantitative terms. The scheme depicts the main characteristics of the mutant keratin granule life cycle: nucleation, growth, motility, fusion, and disassembly (a). The consecutive steps of automated granule analyses and possible further applications are shown in (b). The figure was adapted from [276].

IV.1.2 Comparison of mutant keratin granules and wt keratin filaments

This study has quantified the dynamic properties of mutant keratin granules at single granule resolution. Interestingly, these structures share certain features with healthy keratin filaments,[143] but also show specific distinctions, as discussed in the following sections.

IV.1.2.1 Nascent keratin nucleation

Both wt and mutant keratins nucleate as small precursors from the soluble cytoplasmic keratin pool in the cell periphery. This is in line with *in vitro* studies demonstrating that the early assembly steps of Krt14R125H are functional.[133] In case of wt keratins, it has been shown that nucleation takes place preferentially at desmosomes,[140] hemidesmosomes,[141] and adjacent to focal adhesions.[299] Mutations or knock-out of keratins have been shown to alter all three structures to a certain degree.[116,293,294,300-304] On the contrary, it has been shown that both keratin networks and desmosomes are in principle able to form independently of each other in cultured cells and tissues.[300,302,305] Thus, nucleation of mutant keratin precursors seems to be functional, taking place at the same place and with comparable speed as wt keratins. Apparently, desmosomes, hemidesmosomes, and focal adhesions are not required for the nucleation of intermediate filaments itself. Instead, they might be needed to anchor IF precursors to adhesion structures immediately after their formation. This would prevent that growing filaments move inwards first and have to be transported back to adhesion structures later on if needed at these locations. Future studies are required to clarify the relevance of these structures for keratin nucleation in EBS. They should aim to compare nucleation of both wt and mutant keratins, and both single cells and monolayers should be taken into account to investigate the mutual interactions of keratins and desmosomes.

IV.1.2.2 Directed or indirect transport of mutant keratin granules

The observed retrograde transport via actomyosin is another feature which wt and mutant keratin precursors share with each other.[139,144] The automated quantitative analyses have revealed that pharmacological inhibition of the actin motor protein nm myosin II induces a significant reduction of granule velocity, and minor effects on their directionality (III.1.4). Previous studies have shown that pharmacological disruption of actin filaments inhibited keratin granule movement, in contrast to microtubule inhibition.[39] However, the involvement of actin motor proteins was not clarified. Thus, this study demonstrates that the inward movement of keratin granules does not only rely on actin, but also its motor nm myosin II. However, it has not become clear if mutant keratin granules are transported in a direct or indirect manner. Single granules were observed to move inwards along filopodia-like structures (III.1.3), which

might implicate that an active transport mechanism is possible. In favour of this transport mode are studies that have shown that nm myosin IIA is able to physically associate with keratins 8/18 or keratin 6, with functional implications for cell migration.[159,306]

However, the majority of the granules appeared to be rather pushed inwards by the retrograde flow induced by peripheral actin structures (III.1.3). These movements are in line with observations of brightfield time-lapse recordings which were recorded in parallel with actin, in which the outer lamellipodium shows inward-directed membrane ruffling (not shown). The retrograde actin flow is induced by rapid recycling of actin subunits for subsequent polymerisation,[307] and it is likely that the small keratin granule precursors are driven by this strong inward flow. The latter scenario is also supported by studies which have shown that microtubules are moved towards the cell centre by the treadmilling effect of actin retrograde flow in the outer lamellipodium.[308] Furthermore, the considerable heterogeneity of one slow- and one fast-moving granule fraction in different cells might be the result of cell-dependent differences of actin treadmilling velocity, rather than being due to different active actin transport velocities.

Despite the clear effect of pharmacological nm myosin II inhibition, the movement of mutant keratin granules was only reduced by approximately one third, and not completely abolished. This might be due to the fact that the used myosin inhibitors are known to dissolve transverse actin arcs, but only abolish the retrograde actin flow by approximately 50%.[309-311] This fact further supports the hypothesis that mutant keratin transport in the cell periphery is mainly driven by retrograde actin flow, and not by active transport.

On the other hand, the only partial reduction in granule motility might be due to the involvement of the microtubule system in addition to actin treadmilling. The head domain of keratin 5 is, for example, able to interact with dynein.[312] Also vimentin is moved along microtubules and the assembly of IF networks is relying on kinesin activity.[149] Studies from ~10 years ago have already shown that microtubules are involved in retrograde transport of different intermediate filament particles[148,150,156,157,313] and are supported by a recent study that has shown that keratin filaments are transported along microtubules by the motor protein kinesin.[160]

However, it has to be considered that wild type and mutant keratin precursors might be differentially transported. The kinesin-1-dependent transport seems to be different from the observed mutant keratin granule motility, which is restricted to the outermost cell periphery. Furthermore, it has been suspected that keratin mutations alter the protein conformation in a way that might impair the binding to microtubule-associated proteins.[39]

Thus, further analysis of wt and mutant keratin precursors should aim to determine if they share the same transport mechanisms, or whether there are fundamental differences. Such investigations might shed not only light on the dynamics of mutant intermediate filaments, but also extend the knowledge of the fundamental dynamics of healthy keratins.

IV.1.2.2 Network integration vs. disassembly

The main difference between the two cycles is the integration of wt keratins into the existing filament network on the one hand, and the constant disassembly of mutant granules on the other hand. Interestingly, both events appear to occur at the transition zone between the flat lamellum and the inner, thicker cytoplasm.[143,144] Besides incorporation into the keratin network, wt precursors can also be disassembled into subunits, and be used for another round of assembly once transported back to the cell periphery.[143] In contrast to studies claiming that once formed IF filaments are extremely stable and not disintegrated, a novel study by Tran *et al.* has shown that vimentin filament length reached a plateau >24 hours after assembly *in vitro*, and that from this point on, filament bundles within the network can be disassembled, triggered by fragmentation of individual filaments.[314] However, it has not been solved yet which factors drive keratin disassembly and if disassembly of filaments and precursors is driven by the same mechanisms and should thus be investigated in future studies.

It can be speculated that certain keratin mutations shift the balance of network integration vs. disassembly away from integration and towards disassembly. It might be possible that the keratin mutations induce certain changes within protein structure, for example alternate folding or impaired access of binding sites, and that these changes hamper the integration into the network. Future studies will help to identify the triggers of the shift towards increased disassembly, with posttranslational modifications, especially phosphorylation, being promising candidates (see IV.2.2).

IV.1.2.2 Turnover of keratin granules vs. filaments

Regarding protein turnover, this study has for the first time measured the fluoresce recovery after photobleaching of completely and half bleached mutant keratin granules. Completely bleached granules remarkably display a ~50% recovery 5 minutes after bleaching.

Wild type keratin 13 filaments in single AK13-1 cells on the other hand show a recovery of 8.1% after 10 minutes,[315] and overexpressed Krt5 in single HaCaT cells a recovery of 71% after 18 minutes.[140] Especially if taken into account that keratin turnover in MCF-7 cells seems to be relatively low (observations from our lab) compared to other cell lines, it can be speculated that keratin granules exchange soluble keratin with the cytoplasm faster than wt filaments. As keratin granules most likely represent less ordered structures than filament bundles, a less complicated and thus faster integration of soluble subunits seems reasonable. The different cell lines and conditions used for the different FRAP experiments should however be taken into consideration. Future investigations of the turnover of wt keratins with the same settings as used in this work are necessary to compare absolute values.

Besides keratin granules, it should also be considered that a part of mutant keratins can still build filaments and form the perinuclear cage. These filaments might also contribute to the EBS pathogenesis. Although Krt14R125C filaments display a normal ultrastructure, they lack the typical motion of wt filaments[150,156] and are unusually stiff.[39] If subjected to osmotic stress, these filaments are more fragile,[39] which might be due to altered bundling properties *in vitro* and it is proposed that this results in reduced resilience to deformation.[316]
Thus, as suggested by Werner *et al.*, it is likely that not only keratin granules play a role in EBS pathogenesis, but also filaments that can still be formed.[39] The presence of two mutant keratin structures, granules and filaments, argues for a toxic gain-of-function. However, the authors also show that siRNA-induced downregulation of mutant keratin is able to restore a normal keratin network, and that granule formation is based on the wt to mutant protein ratio.[39] It is therefore very likely that EBS-type keratin mutations cause the typical symptoms due to both a gain-of-function of keratin granules, and also due to a loss-of-function of missing filaments.

To further elucidate the similarities and differences between wt and mutant keratins, future studies should make use of the newly established keratinocyte cell clones overexpressing Krt14R125C (III.2.2) which display a normal cytoplasmic network pattern in ground state. These cell clones might be a useful system to find triggers of granule formation. They could be subjected to pharmacological inhibitors or be transiently transfected to discover if certain kinases etc. induce granule appearance. Besides phosphorylation, the influence of other posttranslational modifications should be investigated. Furthermore, expression levels of different keratins or granule-inducing candidates should be determined.

In summary, our findings extend the knowledge of the details of keratin granule-forming diseases, but they also are of benefit to comprehend normal keratin network dynamics and regulation.

IV.1.3 Pathological relevance of mutant keratin granules

When investigating the pathogenesis of *Epidermolysis bullosa* (*simplex*), the essential question arises, whether the prominent keratin granules analysed in this study actually have pathological relevance. Regarding the presence of mutant keratin granules in cells, Werner *et al.* have shown in electron microscopy that the MCF-7-Krt14R125C-eYFP cells used in this work contain round “aggregated” keratin structures, with a size of ~0.5 µm in the cell periphery.[39] This size approximately matches the size of keratin granules in fluorescence microscopy of this work. Furthermore, keratin granules of comparable size have been observed in an EM study of patient-derived KEB-7 keratinocytes carrying the Krt14R125P

mutation without any fluorescent construct.[317] Interestingly, the mutant keratin granules appear as ring-like structures if stained with keratin antibodies,[317] whereas electron microscopy[39,317] and fluorescence microscopy of fluorophore-tagged overexpressed keratin granules show them as filled structures. This is probably due to a reduced penetration of antibodies, and they are most likely densely filled *in vivo*, according to the EM data. High resolution cryo-electron microscopy may help to identify potential intrinsic sub-structures of keratin granules.

Numerous studies have proven a functional impact of EBS-causing keratin mutations on different cellular functions in cultured cells. For example, KEB-7-Krt14R125P keratinocytes were less resistant to mechanical stretching than wt cells.[317] Furthermore, osmotic shock-induced cell swelling induced deformation of MCF-7-Krt14R125C-eYFP cells.[39] This is in line with other studies showing that disruption of the keratin network softens cells and makes them more susceptible to deformation[113,114,318] while increased IF expression levels stiffens cells.[319] An explanation for the altered mechanical characteristics in EBS is that the mechanical properties of intermediate filaments in general depend on filament length and the assembly into bundles and networks.[320] Thus, the shift from filaments towards granules is likely to affect the mechanical properties of keratin networks and consequently of cells.

Another important functional aspect of EBS-related granule formation is the bidirectional relationship of keratins and adhesion structures (IV.1.3). Cell adhesion is crucial to support mechanical stability of the plasma membrane via desmosomes, hemidesmosomes, ECM, or focal adhesions.[103] Especially desmosomes might be key players in EBS pathogenesis. According to the “rim and spokes” hypothesis developed by Quinlan *et al.*, the keratin cytoskeleton can be morphologically segmented into radial spokes which connect the plasma membrane to the nucleus, and a circumferential rim which is located underneath the plasma membrane and is connected by/to desmosomes.[321] In EBS cells, the circumferential rim is missing, which suggests that a lack of keratin IFs at this location induces stretching of the plasma membrane and consequently its rupture between desmosomes upon mechanical stress.[321] Two different hypotheses, the “fragile network”[39,317] and the “sparse network”[322,323] hypotheses, implicate that the formation of keratin aggregates instead of filaments leads to uncoupling of desmosomes from each other and from the network surrounding the nucleus.[321]

It has been shown in wt mice, that keratinocytes of the *Stratum basale*, which contain the highest amounts of Krt5 and Krt14 within the epidermis, display less desmosomes than those in suprabasal layers.[324,325] In light of these studies, disruption of keratin filaments into granules and the associated impaired desmosomal cell-cell connections are especially crucial in the basal epidermal layer. On the contrary, other keratins such as Krt1 and Krt10 are upregulated in suprabasal layers.[326] Combined with an increased occurrence of desmosomes in these upper layers,[326] it is likely that the suprabasal layers are not severely affected by keratin 5/14 mutations, and that blister formation is thus limited to the basal layer in EBS.[25,28]

Furthermore, several studies have investigated potential therapeutic treatments which aim to reduce keratin granules. Among them is the usage of chemical chaperones to prevent keratin aggregation, which has shown promising first results.[327,328] Clinical studies might yield interesting therapeutic options in the future.
The occurrence of keratin granules, cytolysis and skin blistering is not only observed in cells,[30] but has also been observed in keratin 5 or 14 knockout mice, as well as in transgenic mice expressing mutant keratins.[323,329-333] These animal studies are in favour of the hypothesis that granule formation is a crucial process within EBS pathogenesis.
Due to the relatively low prevalence of *Epidermolysis bullosa* and the burden of taking biopsies, studies on human EB epidermis are limited. Still, a number of studies during the past 40 years have found "aggregated" or "clumped" cytoplasmic structures defined as keratins.[38,334-340] However, these studies must be viewed critically, as they do not include quantitative analyses or include technical flaws. Another aspect that has to be critically considered is the variable size of the clumped structures, which are often larger than the granules observed in cells.

In summary, studies showing "aggregated" keratins *in vitro* and *in vivo*, the functional consequences of keratin mutations, and promising studies aiming to reduce these are in favour of a pathological relevance of mutant keratin granules. Establishing high-end image analysis routines as developed in this work has shown to yield precise and reproducible results. In the future, mutant keratin dynamics should further be investigated in monolayers and epidermal equivalents, as these represent more physiological situations than single cells.

IV.1.4 Implications of mutant keratin granules being LLPS condensates

The concept of liquid-liquid phase separation has emerged during the past ~10 years and is nowadays widely accepted. In principle, it states that the formation of a phase boundary, specifically the dynamic sequestration of molecules by stable concentration differences between the phase condensate and the surrounding cytoplasm, affects different biochemical processes by creating specific confined reaction sites.[341-346] It has been shown that actin and microtubule cytoskeletal dynamics can be modulated by condensates [reviewed in [347]], but it has only been briefly speculated that intermediate filament dynamics might also be shaped by liquid-liquid phase separation (LLPS).[347] Specific low complexity head domains of neurofilaments and desmin have been shown to influence the assembly of these IFs.[348] As LLPS condensates often contain proteins with low-complexity regions,[349] these regions might favour phase separation of intermediate filaments.

The sequestration of molecules into LLPS condensates has shown to concentrate them approximately 1000x compared to cytoplasmic concentrations.[350] Interestingly, the concentration differences stay stable during LLPS, so molecules can still diffuse in and out of the droplet, but not in a range that changes the concentration gradient. In case of keratin granules, this might imply that concentrating mutant keratins in condensates could represent a rescue mechanism, in order to prevent them from fulfilling toxic functions in the cell. On the other hand, structural changes induced by mutations might lead to a compartmentalisation which hinders them from fulfilling their normal functions.

To further investigate the implications of phase separation on keratin granule dynamics, new expression systems such as inducible protein expression, for example using the ProteoTuner system,[351] or CRISPR-Cas knock-in of fluorophores to endogenous proteins should be established. This is important, as the formation of LLPS condensates is highly concentration dependent, and the overexpression of key components of stress granules can induce their formation even without any stress.[352-354] However, as mutant keratin granules are also observed in untransfected patient-derived cells (III.3.1), the overexpression cell line used in this study does not represent a simple overexpression artefact. Future investigations could also focus on other situations, which might favour local concentration peaks and consequently condensation of keratins, such as during mitosis, desmosome clustering, or stress. Specific molecular properties of keratin condensates should be examined for non-overexpressed proteins, such as binding rates or diffusion coefficients, either by fluorescence correlation spectroscopy[355] or by a novel less complicated FRAP method.[356] Also, targeted deformation of mutant keratin granules should be performed in future studies to confirm the random deformation observed in this work, for example by using nanoindenters.

Crucial for the assembly of LLPS condensates is a certain concentration threshold, the so-called critical concentration, which is required to initiate the formation of a condensate.[357] Two different scenarios are conceivable in case of mutant keratin granules. The first one implies that a physiological high critical concentration in the outer lamellum is present, which induces condensation, but a drastic reduction of the concentration in the inner cytoplasm leads to disassembly. The second scenario is very similar, with the exception that it might also be possible that non-physiological increased disassembly at the transition zone results in an increase of the soluble keratin concentration beyond the physiological level, triggering condensation in the lamellum. Measurements of the concentration of soluble endogenous fluorescence-tagged keratins in mutant and wt cells might help to clarify these considerations. Furthermore, it might be examined if keratins are able to condensate also in the inner cytoplasm, by expressing keratins fused to specific localisation sequences of cytoplasmic structures, such as mitochondria or the nucleus.

Regarding the structure of LLPS condensates, it has been shown that they are composed of scaffolds, which are the proteins initially condensating, and clients, which are other proteins which partition into the already formed scaffold.[358] Future investigations should aim to determine if this is also valid for mutant keratin granules, for example by antibody stainings of putative clients. It has been shown that clients can diffuse much more rapidly than scaffolds,[359] a characteristic that might also be investigated by FRAP of potential clients.
Regarding the missing formation of keratin granules *in vitro*,[133] it can be speculated that condensation of mutant keratin offers a rescue mechanism to separate them from the rest of the cell, which might not be needed in a test tube with only keratins present. This is also supported by a study showing that filament formation of Krt8/18 was functional *in vitro*, although the proteins were purified from heat-stressed cells, in which the same keratins form granules.[360] Thus it is likely that external factors such as kinases or actin might be required to form condensates in a cellular environment. The missing evidence of condensate formation *in vitro* speaks consequently not per se against the LLPS phenomenon.

Posttranslational modifications have been shown to alter the valency and intrinsic solubility of key condensate components and may thus regulate the concentration at which condensates assemble.[361] Furthermore, keratin 5 phosphorylated at the head domain was found in EBS keratin granules. The same study also showed that overexpression of a phospho-mimetic variant of mutant keratin 5 disturbs keratin filament formation in murine keratinocytes. Both results indicate a role of phosphorylation within mutant keratin granule formation.[362]

It is possible that phosphorylation of keratins in the inner cytoplasm changes the concentration gradient of unphosphorylated proteins, and thus the unphosphorylated keratin inside the condensate diffuses into the cytoplasm, leading to the disassembly of granules at the distinct transition zone. Furthermore, it can be hypothesised that phosphatases might be present inside granules in the outer lamellum, and the concentration gradient for unphosphorylated keratins might change at the transition zone, leading to diffusion into the cytoplasm. On the other hand, it is also possible that kinases might be either able to enter granules at the transition zone and not before, or that the disassembly of granules would allow kinases to act on the soluble keratins only. Future studies should aim to answer these complicated scenarios, preferably if specific kinase or phosphatase candidates have shown to be promising.

Besides investigation of the details of formation of LLPS condensates, it will also be critical to focus on potential functions that accompany it. It has been shown that LLPS of different molecules can either enhance[363] or suppress[364] biochemical reactions. Furthermore, certain LLPS condensates are able to detect environmental changes[365] or even apply mechanical

forces.[366] One function might be especially important within EBS, in particular the buffering of protein concentrations.[367] The sequestration of mutant keratins inside condensates might either hinder them from fulfilling their physiological functions or prevent potential harmful effects which might happen if they get incorporated into the network. As both the soluble and the condensated state of proteins can represent a physiological situation, the two scenarios are both possible in case of EBS.

Another aspect to be investigated in the future is the possibility that nucleation of wt keratin filament precursors might also be based on LLPS. It might be a potential mechanism to overcome the “critical concentration” required for keratin nucleation in general, for example during keratin nucleation observed at newly forming desmosomes.[140]

In summary, the finding that EBS-mutant keratin granules are LLPS condensates, opens up a novel research field, and future investigations taking this concept into account may extend the knowledge about the dynamics and functions of keratin intermediate filaments.

IV.2 DYRK kinases show no functional effect on mutant keratin granules

Based on a study showing that DYRK3 kinase is able to colocalise with and dissolve multiple LLPS condensates,[281] this work examined if DYRK kinases have an influence on mutant keratin dynamics as well. Transiently overexpressed fluorescence-tagged DYRK proteins were shown to localise in granules highly resembling mutant keratin granules in EBS-patient-derived keratinocytes, and they display similar dynamics (III.2.1). These structures were shown to colocalise with endogenous keratins, but the labelling of endogenous DYRKs was not possible. Despite the promising colocalisation, a functional influence of pharmacological DYRK inhibition on the percentage of granule-positive cells could not be shown (III.2.4).

IV.2.1 Ambivalence of colocalisation of mutant keratin granules and overexpressed DYRK but no effect of pharmacological DYRK inhibition

The contradicting results of the close spatial proximity of keratin granules and overexpressed DYRK kinases on the one hand and on the missing functional consequences of pharmacological DYRK inhibition seem to be paradox. It might be possible that DYRKs do colocalise with mutant keratin granules only if they are highly overexpressed. The colocalisation itself is unambiguous, however, overexpression of DYRK does not reduce the amount or dynamics of keratin granules on short-term observations. On the other hand,

pharmacological inhibition does not increase the number of granule-positive cells, as it was hypothesised. A possible explanation is that DYRK kinases only colocalise with mutant keratin granules in specific situations. One example might be the transient occurrence of granules during reorganisation during cell migration, as it was shown for keratinocytes expressing mutant keratin. Such situations require reorganisation of the keratin network which is probably triggered by posttranslational modifications such as phosphorylation.[162,163] Future investigations may use inducible expression systems to observe if DYRK kinases are able to alter the migration behaviour of keratinocytes expressing EBS-mutant keratins.

Furthermore, future studies should aim to examine novel DYRK antibodies in order to assess the endogenous localisation of the kinase. If colocalisation of mutant keratin and endogenous DYRK protein could be shown, further investigation of a potential functional influence should be considered. Future studies could make use of a recently established cell clone developed in our laboratory, which overexpresses fluorescence-tagged wt Krt5 in EBS-mutant Krt14R125C keratinocytes and shows nearly 100% of granule-positive cells (not shown). Cells which in addition transiently overexpress DYRK might be quantitatively analysed with regard to granular keratin content. Kinase-dead DYRK variants are already available in our laboratory and could be used to examine if the kinase activity itself is crucial to dissolve granules.

Overall, the results regarding a potential influence of DYRK kinases on mutant keratin granules remain ambivalent, and future investigations are required to unravel the inconsistencies.

IV.2.2 Kinases as potential drivers of EBS-mutant keratin granule dynamics

Despite the fact that the specific influence of DYRK kinases on mutant keratin granule dynamics could not be proven in this work, a variety of other studies argues for a general influence of kinases on EBS-mutant keratins. Multiple studies have shown that hyperphosphorylation in a pathological sense induces reorganisation of intermediate filaments and aggregate formation.[368-370] Other posttranslational modifications (PTMs) also haven an influence on keratin polymerisation,[117,296,298] but phosphorylation is the main responsible PTM.[103] By promotion of keratin solubility by serine or threonine phosphorylation,[117] the equilibrium of soluble vs. filamentous keratin is fine-tuned.[164,292,371,372] Furthermore, subunit exchange of keratin filaments is likely also regulated by phosphorylation.[164,373,374] It is suggested that kinases are preferably targeting depolymerised keratin subunits, i.e. soluble keratin.[375] With regards to the details on mutant keratin granule dynamics from this work, it is likely that EBS mutations may shift the balance towards soluble keratin, which is hypothesised to be the main component of the mutant granules. In favour of this argument are studies suggesting that phosphorylation hampers the lateral alignment of keratin tetramers into ULFs,[105] and possibly also the subsequent longitudinal annealing.[296] An additional

phosphorylation site due to an EBS-related Krt5 mutation[376] is supposed to induce structural alterations which likely interfere with the lateral association.[377-380] These studies support the pathological relevance of mutation-induced conformational protein changes, which in turn can have a large impact on keratin network dynamics.

Another interesting aspect is the influence of phosphorylation on protein degradation. One hypothesis claims that increased keratin phosphorylation might induce sumoylation and ubiquitination, ultimately leading to protein degradation.[117] The other possibility might be that increased phosphorylation protect keratins against ubiquitin-mediated degradation,[296,381] or rather keeping aberrantly folded keratins in an inactive state.[296]

Furthermore, keratin phosphorylation is widely accepted to function as a “phosphate sponge”, i.e. buffering excessive kinase activity[117,118,296,382] and thus influencing important kinase signalling pathways.[296] It would be interesting to investigate whether the different EBS-causing mutations might influence this important keratin function.

Regarding the function of phosphorylation in cell migration, contradicting results have been obtained. On the one hand, Krt8 phosphorylation promotes the migration in cells originating from pancreas or intestine.[383] However, in oral squamous carcinoma cells, it decreases cell migration.[384] In the context of EBS patient-derived keratinocyte cell lines, it has been shown that these cells migrate faster in scratch wound healing assays,[385] demonstrating a migration-promoting effect in EBS cells. As the frequent blister formation in EBS requires functional wound healing, cell migration is important within the pathogenesis. Interestingly, it has been shown for neurofilaments that phosphorylation events can be performed differentially in different regions of the cell.[386] It can thus be speculated that a compartmentalisation of PTMs might have a larger influence in polarised migrating keratinocytes than in resident cells. This in turn would imply that EBS mutations might lead to altered phosphorylation and thus impaired wound healing. However, studies on wound healing are very limited in the context of *Epidermolysis bullosa*,[387] but some have indeed shown that wound healing is delayed in the epidermis of junctional and dystrophic EB of respective knock-out models.[388,389] A fascinating study has recently demonstrated that healing of sub-epidermal blisters is facilitated not by interfollicular stem cells, but by junctional hair follicle stem cells.[389] This finding offers a new opportunity to investigate and possibly also target wound healing in *Epidermolysis bullosa*.

In light of the limited studies on specific effects of phosphorylation in the context of EBS, our automated tracking system offers a way to systematically investigate the potential influence of phosphorylation on mutant keratin granule dynamics. Such systematic analyses are necessary, because one phosphorylation site can be targeted by multiple kinases.[390] In summary, detailed future investigations are required to elucidate the proposed impact of keratin phosphorylation within EBS pathogenesis,[168,376] and to clarify whether these PTMs positively or negatively influence disease progression.[117]

IV.3 Disturbed mitophagy and autolysosomal recycling in *Pachyonychia congenita*

The second part of this work addressed the influence of *Pachyonychia congenita* keratin mutations on mitochondrial quality control. The initial experiment investigated whether mitochondrial disturbances occur in PC keratinocytes. It revealed that PC cells contain increased amounts of overaged mitochondria. As schematically depicted in Fig. 46, investigation of the mitophagy process further elucidated that PC keratinocytes:

- contain reduced contact sites between mitochondria and ER
- are able to correctly label defective mitochondria for mitophagy
- show perturbed mitochondrial clearance
- accumulate autolysosomes
- contain functionally defective lysosomes

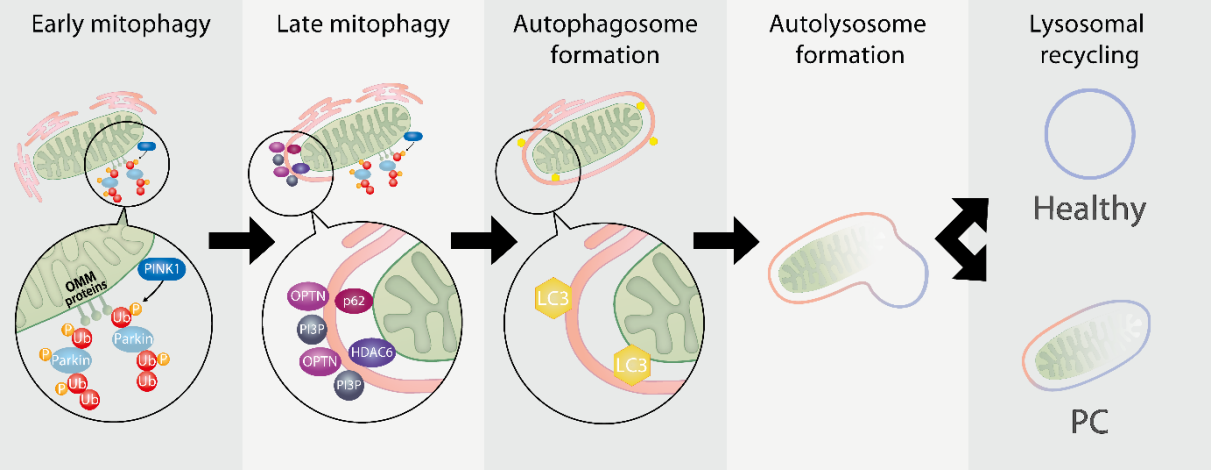

Figure 46 – The mitophagy pathway in *Pachyonychia congenita* keratinocytes. The scheme depicts the consecutive steps of mitophagy for healthy and PC patient-derived keratinocytes. Early mitophagy, characterised by accumulation of PINK1 and polyubiquitin chains on outer mitochondrial membrane (OMM) proteins, is functional in both healthy and PC cells. Late mitophagy, marked by connecting defective mitochondria to the autophagosomal membrane by adaptor proteins such as p62 and HDAC6, is also not disturbed in PC. Engulfment of mitochondria by the autophagosome via LC-3 is functional as well. Subsequent fusion of autophagosomes and lysosomes into autolysosomes is not disturbed in PC keratinocytes. However, an accumulation of autolysosomes together with reduced lysosomal function in PC keratinocytes indicates dysfunctional autolysosomal reformation or recycling.

IV.3.1 Effects of PC-mutant keratins on the integrity of mitochondria

Several studies have shown that intermediate filament mutations cause mitochondrial impairments (see I.11). Thus, this work concentrated on one important aspect of mitochondrial integrity, i.e. the removal of defective organelles by macro-autophagy.

One important factor influencing mitochondrial integrity is their distribution/localisation, as they must be present at locations of increased energy demands. It has been proposed that the absence of intermediate filaments decreases the cellular viscosity, and thus possibly organelle localisation,[103] which might also be true for mutant keratins. Mitochondria are also required at specific contact sites with other organelles. One of these contact sites is the mitochondria-associated membrane (MAM), representing a distribution centre for lipids and calcium.[206-208] Keratin mutations inducing an altered localisation of mitochondria might consequently alter the contact sites beween the two organelles and thus impair MAM functions. For example, EBS-associated mutations[391] and keratin 8 knock-out[202] lead to a more peripheral mitochondrial distribution. Mutations in desmin furthermore lead to a disturbed mitochondria-ER distance in particular.[392] These studies are in line with the observations from this work.

It has recently been shown that MAMs can be sources of autophagosomal membranes such as omegasomes[257,259,393] which might imply functional consequences for autophagosome formation. However, this work has shown evidence that the formation of autophagosomes is functional in PC. Thus, despite altered MAM contacts, they are probably still able to contribute to autophagosome formation or PC keratinocytes use other sources of autophagosomal membranes .

A deeper look into autophagosome biogenesis did demonstrate that MAMs may create a specialised lipid raft platform.[394-396] In particular, one element of these lipid rafts, GD3 ganglioside, was shown to interact with early autophagosome formation proteins, and this interaction was shown to be functionally important for autophagosome formation.[394] Interestingly, GD3 has been shown to interact with both actin and microtubule cytoskeletal elements.[397,398] A possible interaction of GD3 with intermediate filaments might be investigated in future studies.

Besides their role in autophagosome formation, MAMs have also been shown to be important to transfer lipids between ER and mitochondria.[399] Keratins might be important for this transfer, as knockout of all type I or type II keratins in mice leads not only to epidermal thickening and mitochondrial dispositioning in the granular layer, but also to an increase of the mitochondrial lipid cardiolipin.[215] The authors of this study have consequently hypothesised that keratins presumably have an effect on ER-mitochondria trafficking, in particular on lipid distribution.[215] This is supported by other investigations that have shown that mouse models displaying mitochondrial dysfunction show defects in skin architecture and barrier function.[400,401] Based on this knowledge, it could be speculated that in PC keratinocytes, omegasomes can still be formed originating from MAMs, but that they lack specific (lipid) contents which are crucial for mitochondrial removal in autolysosomes.

Apart from lipid trafficking, MAM sites are also responsible for calcium transfer from the ER to mitochondria.[221] As intracellular calcium activates autophagy by mTORC1 inhibition,

disturbances of MAMs and a resulting increase of cytoplasmic calcium[402] might modify the calcium-dependent epidermal differentiation. This would also explain why the autolysosomal accumulation is only seen after differentiation in PC keratinocytes. One particular study has shown that remarkably, most of the cytoplasmic free calcium is derived from intracellular ER or Golgi repositories, instead of being originated from extracellular calcium.[403] This supports the hypothesis that keratin mutations might disturb the MAM-regulated intracellular calcium shuttling, and thus cause differentiation defects.

In summary, this work has shown that mutations in keratin 6a alter the mitochondria-ER contact sites and potentially influence mitochondrial integrity, potentially by disrupting the lipid and/or calcium handling of mitochondria.

IV.3.3 A putative role of keratins in autolysosomal recycling/maturation

This work has discovered that mitochondrial removal via mitophagy is severely impaired in PC-patient-derived keratinocytes, though the underlying cause seems to be a disturbance within lysosomal recycling.

The *de novo* formation of lysosomes does not appear to be affected, as lysosomes are in general present and are able to fuse with autophagosomes upon induction of mitophagy. Furthermore, first follow-up experiments gave hints that markers of lysosomal biogenesis are not affected in PC (unpublished results from this laboratory).

In favour of a more downstream influence of intermediate filaments, multiple studies have shown interactions of lysosomes and different intermediate filaments. For example, GFAP and vimentin influence the motility and positioning of lysosomes,[404] which is supported by studies showing that distribution and acidification of lysosomes are disturbed in vimentin-null cells, as well as trafficking of the lysosomal proteins LAMP-1 and LAMP-2.[178] Direct interactions between vimentin and the lysosomal membrane trafficking-related protein Rab9[191] have also been revealed, as well as with the adaptor protein AP-3, which for example influences lysosomal pH and zinc uptake.[178] Lysosomes support degradation, signalling, and mitochondrial metabolism, all of which are crucial for functional differentiation of the epidermis.[405] Disturbances of IF-lysosome interactions within the epidermis are thus a putative key player within skin disorder pathogeneses.

A lysosomal pH of ~4.5-4.7[406,407] is crucial for lysosomal function, i.e. for activation of cathepsins and other lysosomal hydrolases/proteases or for lysosome-autophagosome fusion.[408,409,410] The lysosomal pH is in general quite stable, but it is controversial if a different subcellular localisation of lysosomes or different cellular states, such as cell division or migration, have an influence on lysosomal function and pH.[408] The relevance of lysosomal

function, which largely relies on the correct pH, is underlined by defective lysosomes in lysosomal storage disorders,[411] neurodegenerative diseases such as Alzheimer´s,[412] or mitochondrial disorders.[413] Interestingly, the dysfunction of lysosomes seems to cause mitochondrial defects in many lysosomal storage disorders.[414-418] Pharmacological reduction of lysosome pH by chloroquine was demonstrated to slow down the autophagosome-lysosome fusion.[419] Live-cell experiments should be conducted in the future to clarify if a delayed fusion of the two organelles contributes to the observed phenotype.

The Magic Red® Cathepsin B assay revealed decreased lysosomal function in PC and Bafilomycin A1 treatment of wt cells recreated the mitochondrial overaging phenotype. Both experiments clearly point towards a disturbed lysosomal pH. However, the lysosomal pH of wt and PC keratinocytes should be examined directly in future studies, for example via ratiometric lysosomal pH biosensors.[420,421,408] Transfection, imaging, and analysis of these sensors in wt vs. PC cells represents a feasible way to determine if pH alterations are present in PC.

Artificial acidification of lysosomes could furthermore determine whether re-acidification of lysosomes ameliorates the PC phenotype. Restoration of the lysosomal acidity in lipotoxicity-burdened pancreatic beta cells has been shown to restore mitochondrial function,[422] indicating that mitochondrial dysfunction is downstream of lysosomal disturbances. Supportive of this hypothesis is pharmacological acidification by the phosphodiesterase 3 inhibitor Cilostazol, which reduced amyloid beta burden in mouse models of Alzheimer´s.[423]

As *de novo* lysosome biogenesis does not seem to be the cause of dysfunctional mitophagy in PC, the recently discovered process of autolysosomal reformation (ALR) moves into focus. It represents the process during which the lysosomal compartments of autolysosomes are recycled after degradation of the autolysosomal cargo. The distinction between autophagosomal and lysosomal proteins is important for cellular efficiency, as both components can be recycled instead of being formed anew. Autophagosomal membranes have very recently been shown to be assorted by the “recycler” complex.[424] Lysosomal proteins on the other hand apparently contain sorting signals in their cytosolic tails, to which AP adaptor proteins can bind and consequently ensure correct sorting.[425] An initial step of ALR has been shown to involve the conversion of specific phospholipids such as PI4P by PIP5K1B kinase, resulting in $PI(4,5)P_2$-enriched domains.[426] These phospholipids are important to anchor clathrin to the autolysosomal surface, which canonically plays an important role during the formation of coated vesicles.[427] Subsequently, clathrin induces the formation of small membrane buds.[427] Next, empty tubules are extruded from the autolysosomes,[266] driven by the microtubule motor protein KIF5B.[267] After reaching a certain size, dynamin 2 severs the

tubules, which are released into the cytoplasm as “proto-lysosomes”.[428] *In vitro* reconstitution of this tubulation process is however not possible with addition of PI(4,5)P_2, clathrin and KIF5B only, which indicates that additional adaptor proteins are necessary.[429] Until now, it has not been shown if ALR occurs during selective autophagy such as mitophagy,[429] but it is extremely likely that selective autophagy also requires recycling of lysosomes in order to function in an efficient way. It would make sense to use the same highly regulated recycling system for both autophagy systems, and this study suggests that ALR is required within mitophagy.

The next step within ALR is the maturation of proto-lysosomes in order to be recycled into functional lysosomes, with re-acidification being essential. It is suggested that this maturation depends on *de novo* protein synthesis,[426] but apart from this, the process is mostly unknown.[429] The canonical phenotype of ALR-deficiency consists of enlarged autolysosomes,[266] which is not observed in PC keratinocytes. Thus, it is plausible that ALR tubulation itself is functional in PC and instead re-acidification of proto-lysosomes might be disturbed.

One important regulator of lysosomal reformation is mTORC1, which is able to initiate proto-lysosome tubulation.[426,430] The stress-upregulated ALR is relying on mTORC1, and its pharmacological inhibition by rapamycin/Sirolimus can block lysosomal reformation.[266,405] However, rapamycin treatment is also able to induce autophagy. This is likely due to a feedback mechanism which prevents disproportionate autophagy.[431] Rapamycin was tested as a potential PC treatment in human keratinocytes and was shown to block Krt6a expression, and to improve symptoms in three patients if taken orally.[66] However, the diversity of mTORC1 functions is a risk, and only one additional case study has been published yet which used topical Sirolimus in two PC patients, but markedly ameliorated the symptoms.[432]

Remarkably, treatments which alkalinise lysosomes also modulate mTORC1 signalling.[433] However, re-acidification of lysosomes is not able to reverse mTORC1 signalling once it is initiated [434] and it has been hypothesised that a correct lysosomal pH is only required to induce, but not maintain mTORC1 activity.[408] In line with this hypothesis, it has been demonstrated that the activity of mTORC1 is fluctuating in correspondence to the autophagic cycle.[266] Hyperactive mTORC1 activity was linked to a defective epidermal barrier in the scaling skin disorder psoriasis.[435,436] Despite its multifactorial nature, mTORC1 activity might be investigated in the context of defective lysosomal recycling in PC.

Furthermore, starvation and thus increased cellular energy demands are drivers of mTORC1 activation.[437] Nuclear translocation of the ”master lysosomal transcription factor” TFEB is induced by mTORC1, and it upregulates v-ATPase, which is important for lysosome acidification and the expression of lysosome biogenesis genes.[438] Although TFEB translocation does not require lysosome acidification,[408] nuclear translocation of this important transcription factor might be investigated in future studies.

If an organelle encounters increased stress levels, severe cellular consequences can often only be prevented by removing the affected organelle.[439] However, cells have to discriminate between acute and chronic stress. If acute stress would immediately lead to elimination of mitochondria, the cell would quickly run out of energy. Thus, it has been hypothesised that cells prefer to transiently shut down mitophagy by inhibiting both lysosomal function and autophagosome formation.[439] If mitochondria are on the other hand chronically disturbed, for example due to respiratory chain deficiencies, it ultimately results in calcium accumulation in lysosomes, as well as loss-of-function of lysosome acidity and hydrolysis.[413] It has been demonstrated that *de novo* lysosome biogenesis, for example via TFEB activation, is taking place under acute, but not chronic mitochondrial stress.[440] In line with this are experiments that have shown that chronic mitochondrial respiratory chain deficiencies impair a cell´s ability to trigger lysosome biogenesis.[413] Considering these findings, it seems possible that PC-related keratin mutations induce rather chronic than acute mitochondrial stress, which in turn can lead to long-term lysosome deficiency. In line with this hypothesis are studies showing that dysfunctional lysosomes interfere with transcriptional programmes which in turn reduce biogenesis and function of mitochondria as a protection mechanism.[439] Underlying could be a bidirectional influence: mitochondrial dysfunction (induced by keratin mutations) triggers increased mitophagy, but lysosomal disturbances could prevent that these mitochondria are properly removed, which in turn would further diminish the mitochondrial pool and thereby potentially increase the burden of remaining functional mitochondria. Consequently, a negative feedback loop of mitochondrial and lysosomal malfunction could prevent mitochondrial removal during epidermal differentiation in PC.

Another aspect of lysosomal function could further impair the differentiation of keratin-mutant epidermis. In particular, lysosomes are able to retain calcium,[441] and it has been shown that calcium homeostasis is disturbed in lysosomal storage disorders, combined with a mitochondrial calcium overload.[442] These malfunctions have been demonstrated to contribute to increased mitochondrial fragmentation and decrease of mitochondrial function.[443] Remarkably, mutations of a Golgi calcium importer cause Hailey-Hailey disease,[5] also called benign familiar chronic pemphigus, which manifests in suprabasal skin blisters.[444] Underlying are increased cytoplasmic calcium concentrations which impair the cells´ ability to respond to extracellular calcium.[5] These studies hint at a link between lysosomes, calcium, and epidermal defects, which might also be the case in PC. Thus it might be speculated that lysosomal dysfunction in PC keratinocytes could ultimately disturb cellular calcium homeostasis, which in turn might cause or aggravate the differentiation phenotype in *Pachyonychia congenita*.

IV.3.4 Mutant keratins as drivers of disturbed epidermal differentiation in *Pachyonychia congenita*

Autophagy plays a crucial role during epidermal differentiation. This view is supported by observations in mice lacking the key autophagy protein Atg-7, which do not survive >24 hours after birth. If skin of these mice is grafted on immunodeficient mice, they show an increase in hyperkeratosis and a decreased expression of cornified envelope/keratinisation proteins.[17] Excessive hyperkeratosis, as it is encountered in PC, implicates that epidermal differentiation is not abolished. Instead, this work indicates that the differentiation process is delayed due to the dysfunctional autophagy of mitochondria. Consequently, suprabasal layers of the epidermis may accumulate, which fail to differentiate fast enough to maintain a normal epidermal thickness.

The formation of the highly specialised corneocytes is ultimately functional in PC, represented by the thick palmoplantar calluses. However, if the differentiation process takes longer, the final steps which are required for shedding of the outer layer, might not be triggered early enough, resulting in the thickened epidermis. This work has shown that mitophagy is impaired, but also that the underlying cause is most likely an autolysosomal reformation defect. This implies that most likely not only the specific autophagy of mitochondria is disturbed, but that other organelles can also not be removed properly during epidermal differentiation. A putative disruption of macroautophagy in general seems reasonable in light of the severe hyperkeratosis in PC.

Pachyonychia congenita-causing keratin 6a mutations were shown to cause mitophagy defects and disturb lysosomal function, probably by reducing the acidification of recycled lysosomes. The important question to be answered in the future is how exactly keratins are able to mediate these dysfunctions. According to a review article from this laboratory, three options of keratin-mitochondria interactions are possible.[445] The first option is direct binding of keratins to mitochondria. As direct binding to mitochondria has been shown for other intermediate filaments such as vimentin (reviewed in [445]) or desmin,[496] it is likely that keratins are also able to bind to mitochondria, either directly or via potential linkers such as trichoplein or plectin.[445] (In)direct binding of the two cellular components could for example influence mitochondrial localisation, which in turn might have consequences for their functions.

The second option is that keratin intermediate filaments spatially confine mitochondria.[445] One potential function would be that keratins physically organise the correct distance between mitochondria and endoplasmic reticulum or other organelles. As discussed earlier, disruption of these contacts can have severe functional consequences. Among them, disruption of calcium shuttling/handling represents a possible mechanism which might be disturbed if mutant keratins cannot maintain important inter-organelle contact sites. This in turn might have drastic consequences for the calcium-regulated epidermal differentiation.

The third potential interplay is bidirectional signalling between keratins and mitochondria.[445] This work indicates that bidirectional signalling obviously also occurs between mitochondria and lysosomes, and also keratins and lysosomes, which might result in detrimental feedback loops. Possibly, altered lipid or zinc distributions induced by keratin defects could disturb important signalling events between different organelles.

The impaired lysosomal dysfunction shown in this work, probably due to dysfunctional lysosomal recycling, adds a new potential function of keratins, in particular within proto-lysosome tubulation or their subsequent maturation. However, future studies are required to narrow down at which exact step the keratin mutations induce alterations.

Overall, this work has elucidated that mitophagy and autolysosome recycling/maturation are dysfunctional in *Pachyonychia congenita*-derived patient keratinocytes. These defects may lead to a prolonged differentiation process, resulting in pathological hyperkeratosis of the epidermis.

V. References

1. Proksch E, Brandner JM, Jensen JM. The skin: an indispensable barrier. Exp Dermatol. 2008;17(12):1063-1072.
2. Elias PM. The skin barrier as an innate immune element. Semin Immunopathol. 2007;29(1):3-14.
3. McGrath JA, Pope FM. Anatomy and Organization of Human Skin. In Burns T; Breathnach S; Cox N; Griffiths C Rook's Textbook of Dermatology (7th ed) Blackwell Publishing p 4190. 2004.
4. Simpson CL, Patel DM, Green KJ. Deconstructing the skin: cytoarchitectural determinants of epidermal morphogenesis. Nat Rev Mol Cell Biol. 2011;12(9):565-580.
5. Rinnerthaler M, Streubel MK, Bischof J, et al. Skin aging, gene expression and calcium. Exp Gerontol. 2015;68:59-65.
6. Moll R, Divo M, Langbein L. The human keratins: biology and pathology. Histochem Cell Biol. 2008;129(6):705-733.
7. Eckhart L, Lippens S, Tschachler E, et al. Cell death by cornification. Biochim Biophys Acta. 2013;1833(12):3471-3480.
8. Kypriotou M, Huber M, Hohl D. The human epidermal differentiation complex: cornified envelope precursors, S100 proteins and the 'fused genes' family. Exp Dermatol. 2012;21(9):643-649.
9. Candi E, Schmidt R, Melino G. The cornified envelope: a model of cell death in the skin. Nat Rev Mol Cell Biol. 2005;6(4):328-340.
10. Fuchs E. Epidermal differentiation: the bare essentials. J Cell Biol. 1990;111(6 Pt 2):2807-2814.
11. Ishida-Yamamoto A, Igawa S, Kishibe M, et al. Clinical and molecular implications of structural changes to desmosomes and corneodesmosomes. J Dermatol. 2018;45(4):385-389.
12. Ishida-Yamamoto A, Igawa S. The biology and regulation of corneodesmosomes. Cell Tissue Res. 2015;360(3):477-482.
13. Brandner JM. Importance of Tight Junctions in Relation to Skin Barrier Function. Curr Probl Dermatol. 2016;49:27-37.
14. Costanzo A, Fausti F, Spallone G, et al. Programmed cell death in the skin. Int J Dev Biol. 2015;59(1-3):73-78.
15. Akinduro O, Sully K, Patel A, et al. Constitutive Autophagy and Nucleophagy during Epidermal Differentiation. J Invest Dermatol. 2016;136(7):1460-1470.
16. Yu T, Zuber J, Li J. Targeting autophagy in skin diseases. J Mol Med (Berl). 2015;93(1):31-38.
17. Yoshihara N, Ueno T, Takagi A, et al. The significant role of autophagy in the granular layer in normal skin differentiation and hair growth. Arch Dermatol Res. 2015;307(2):159-169.
18. Lee HM, Shin DM, Yuk JM, et al. Autophagy negatively regulates keratinocyte inflammatory responses via scaffolding protein p62/SQSTM1. J Immunol. 2011;186(2):1248-1258.
19. Menon GK, Grayson S, Elias PM. Ionic calcium reservoirs in mammalian epidermis: ultrastructural localization by ion-capture cytochemistry. J Invest Dermatol. 1985;84(6):508-512.
20. Menon GK, Elias PM. Ultrastructural localization of calcium in psoriatic and normal human epidermis. Arch Dermatol. 1991;127(1):57-63.
21. Elias P, Ahn S, Brown B, et al. Origin of the epidermal calcium gradient: regulation by barrier status and role of active vs passive mechanisms. J Invest Dermatol. 2002;119(6):1269-1274.
22. Omary MB. "IF-pathies": a broad spectrum of intermediate filament-associated diseases. J Clin Invest. 2009;119(7):1756-1762.
23. Toivola DM, Boor P, Alam C, et al. Keratins in health and disease. Curr Opin Cell Biol. 2015;32:73-81.
24. Bonifas JM, Rothman AL, Epstein EH, Jr. Epidermolysis bullosa simplex: evidence in two families for keratin gene abnormalities. Science. 1991;254(5035):1202-1205.
25. Coulombe PA, Hutton ME, Letai A, et al. Point mutations in human keratin 14 genes of epidermolysis bullosa simplex patients: genetic and functional analyses. Cell. 1991;66(6):1301-1311.
26. Fuchs E. The cytoskeleton and disease: genetic disorders of intermediate filaments. Annu Rev Genet. 1996;30:197-231.
27. Has C, Bauer JW, Bodemer C, et al. Consensus reclassification of inherited epidermolysis bullosa and other disorders with skin fragility. Br J Dermatol. 2020;183(4):614-627.
28. Fine JD, Eady RA, Bauer EA, et al. The classification of inherited epidermolysis bullosa (EB): Report of the Third International Consensus Meeting on Diagnosis and Classification of EB. J Am Acad Dermatol. 2008;58(6):931-950.
29. Vassar R, Coulombe PA, Degenstein L, et al. Mutant keratin expression in transgenic mice causes marked abnormalities resembling a human genetic skin disease. Cell. 1991;64(2):365-380.
30. Coulombe PA, Kerns ML, Fuchs E. Epidermolysis bullosa simplex: a paradigm for disorders of tissue fragility. J Clin Invest. 2009;119(7):1784-1793.
31. Haneke E, Anton-Lamprecht I. Ultrastructure of blister formation in epidermolysis bullosa hereditaria: V. Epidermolysis bullosa simplex localisata type Weber-Cockayne. J Invest Dermatol. 1982;78(3):219-223.
32. Fine JD, Eady RA, Bauer EA, et al. Revised classification system for inherited epidermolysis bullosa: Report of the Second International Consensus Meeting on diagnosis and classification of epidermolysis bullosa. J Am Acad Dermatol. 2000;42(6):1051-1066.
33. Cooper TW, Bauer, E.A., Briggaman, R.A. The mechanobullous diseases (epidermolysis bullosa). In Fitzpatrick's dermatology in general medicine 3rd edition TB Fitzpatrick, et al, editors McGraw-Hill New York, New York, USA 610–626. 1987.

34. Coulombe PA, Fuchs E. Epidermolysis bullosa simplex. Semin Dermatol. 1993;12(3):173-190.
35. Horn HM, Tidman MJ. The clinical spectrum of epidermolysis bullosa simplex. Br J Dermatol. 2000;142(3):468-472.
36. Coulombe PA, Hutton ME, Vassar R, et al. A function for keratins and a common thread among different types of epidermolysis bullosa simplex diseases. J Cell Biol. 1991;115(6):1661-1674.
37. Fuchs E, Esteves RA, Coulombe PA. Transgenic mice expressing a mutant keratin 10 gene reveal the likely genetic basis for epidermolytic hyperkeratosis. Proc Natl Acad Sci U S A. 1992;89(15):6906-6910.
38. Anton-Lamprecht I, Schnyder UW. Epidermolysis bullosa herpetiformis Dowling-Meara. Report of a case and pathomorphogenesis. Dermatologica. 1982;164(4):221-235.
39. Werner NS, Windoffer R, Strnad P, et al. Epidermolysis bullosa simplex-type mutations alter the dynamics of the keratin cytoskeleton and reveal a contribution of actin to the transport of keratin subunits. Mol Biol Cell. 2004;15(3):990-1002.
40. Ross CA, Poirier MA. Protein aggregation and neurodegenerative disease. Nat Med. 2004;10 Suppl:S10-17.
41. Langan SM, Williams HC. A systematic review of randomized controlled trials of treatments for inherited forms of epidermolysis bullosa. Clin Exp Dermatol. 2009;34(1):20-25.
42. Hou PC, Wang HT, Abhee S, et al. Investigational Treatments for Epidermolysis Bullosa. Am J Clin Dermatol. 2021;22(6):801-817.
43. Gurevich I, Agarwal P, Zhang P, et al. In vivo topical gene therapy for recessive dystrophic epidermolysis bullosa: a phase 1 and 2 trial. Nat Med. 2022.
44. Chung HJ, Uitto J. Type VII collagen: the anchoring fibril protein at fault in dystrophic epidermolysis bullosa. Dermatol Clin. 2010;28(1):93-105.
45. Zieman AG, Coulombe PA. Pathophysiology of pachyonychia congenita-associated palmoplantar keratoderma: New insight into skin epithelial homeostasis and avenues for treatment. Br J Dermatol. 2019.
46. Project PC. PC data of the International PC Research Registry (IPCRR) [Available from: https://www.pachyonychia.org/pc-data/.
47. Franklin J. Pachyonychia Congenita (Jadassohn and Lewandowski). Proc R Soc Med. 1939;32(4):263-265.
48. Jackson AD, Lawler SD. Pachyonychia congenita; a report of six cases in one family, with a note on linkage data. Ann Eugen. 1951;16(2):142-146.
49. Leachman SA, Kaspar RL, Fleckman P, et al. Clinical and pathological features of pachyonychia congenita. J Investig Dermatol Symp Proc. 2005;10(1):3-17.
50. McLean WH, Rugg EL, Lunny DP, et al. Keratin 16 and keratin 17 mutations cause pachyonychia congenita. Nat Genet. 1995;9(3):273-278.
51. Smith FJ, Jonkman MF, van Goor H, et al. A mutation in human keratin K6b produces a phenocopy of the K17 disorder pachyonychia congenita type 2. Hum Mol Genet. 1998;7(7):1143-1148.
52. Bowden PE, Haley JL, Kansky A, et al. Mutation of a type II keratin gene (K6a) in pachyonychia congenita. Nat Genet. 1995;10(3):363-365.
53. Lin MT, Levy ML, Bowden PE, et al. Identification of sporadic mutations in the helix initiation motif of keratin 6 in two pachyonychia congenita patients: further evidence for a mutational hot spot. Exp Dermatol. 1999;8(2):115-119.
54. Goldberg I, Fruchter D, Meilick A, et al. Best treatment practices for pachyonychia congenita. J Eur Acad Dermatol Venereol. 2014;28(3):279-285.
55. Chen J, Roop DR. Mouse models in preclinical studies for pachyonychia congenita. J Investig Dermatol Symp Proc. 2005;10(1):37-46.
56. Lessard JC, Coulombe PA. Keratin 16-null mice develop palmoplantar keratoderma, a hallmark feature of pachyonychia congenita and related disorders. J Invest Dermatol. 2012;132(5):1384-1391.
57. Wong P, Domergue R, Coulombe PA. Overcoming functional redundancy to elicit pachyonychia congenita-like nail lesions in transgenic mice. Mol Cell Biol. 2005;25(1):197-205.
58. Tong X, Coulombe PA. A novel mouse type I intermediate filament gene, keratin 17n (K17n), exhibits preferred expression in nail tissue. J Invest Dermatol. 2004;122(4):965-970.
59. Lessard JC, Pina-Paz S, Rotty JD, et al. Keratin 16 regulates innate immunity in response to epidermal barrier breach. Proc Natl Acad Sci U S A. 2013;110(48):19537-19542.
60. Kerns ML, Hakim JM, Lu RG, et al. Oxidative stress and dysfunctional NRF2 underlie pachyonychia congenita phenotypes. J Clin Invest. 2016;126(6):2356-2366.
61. Zieman AG, Poll BG, Ma J, et al. Altered keratinocyte differentiation is an early driver of keratin mutation-based palmoplantar keratoderma. Hum Mol Genet. 2019;28(13):2255-2270.
62. Quigley DA, Kandyba E, Huang P, et al. Gene Expression Architecture of Mouse Dorsal and Tail Skin Reveals Functional Differences in Inflammation and Cancer. Cell Rep. 2016;16(4):1153-1165.
63. Leachman SA, Hickerson RP, Schwartz ME, et al. First-in-human mutation-targeted siRNA phase Ib trial of an inherited skin disorder. Mol Ther. 2010;18(2):442-446.
64. Leachman SA, Hickerson RP, Hull PR, et al. Therapeutic siRNAs for dominant genetic skin disorders including pachyonychia congenita. J Dermatol Sci. 2008;51(3):151-157.
65. Hickerson RP, Smith FJ, Reeves RE, et al. Single-nucleotide-specific siRNA targeting in a dominant-negative skin model. J Invest Dermatol. 2008;128(3):594-605.
66. Hickerson RP, Leake D, Pho LN, et al. Rapamycin selectively inhibits expression of an inducible keratin (K6a) in human keratinocytes and improves symptoms in pachyonychia congenita patients. J Dermatol Sci. 2009;56(2):82-88.
67. Zhao Y, Gartner U, Smith FJ, et al. Statins downregulate K6a promoter activity: a possible therapeutic avenue for pachyonychia congenita. J Invest Dermatol. 2011;131(5):1045-1052.

68. Kerns ML, DePianto D, Dinkova-Kostova AT, et al. Reprogramming of keratin biosynthesis by sulforaphane restores skin integrity in epidermolysis bullosa simplex. Proc Natl Acad Sci U S A. 2007;104(36):14460-14465.
69. Kerns ML, Guss L, Fahey J, et al. Randomized, split-body, single-blinded clinical trial of topical broccoli sprout extract: Assessing the feasibility of its use in keratin-based disorders. J Am Acad Dermatol. 2017;76(3):449-453 e441.
70. Ledbetter MC, Porter KR. A "Microtubule" in Plant Cell Fine Structure. J Cell Biol. 1963;19(1):239-250.
71. Goldman RD, Follett EA. The structure of the major cell processes of isolated BHK21 fibroblasts. Exp Cell Res. 1969;57(2):263-276.
72. Goodson HV, Jonasson EM. Microtubules and Microtubule-Associated Proteins. Cold Spring Harb Perspect Biol. 2018;10(6).
73. Hohmann T, Dehghani F. The Cytoskeleton-A Complex Interacting Meshwork. Cells. 2019;8(4).
74. Pernier J, Montaville P, Carlier M-F. Actin Assembly Dynamics and Its Regulation in Motile and Morphogenic Processes. In: Bradshaww RA, Stahl PD, editors. Encyclopedia of Cell Biology. 2. 1 ed. Amsterdam: Elsevier Inc.; 2016. p. 548-568.
75. Holmes KC, Popp D, Gebhard W, et al. Atomic model of the actin filament. Nature. 1990;347(6288):44-49.
76. Moseley JB, Goode BL. The yeast actin cytoskeleton: from cellular function to biochemical mechanism. Microbiol Mol Biol Rev. 2006;70(3):605-645.
77. Pollard TD. Regulation of actin filament assembly by Arp2/3 complex and formins. Annu Rev Biophys Biomol Struct. 2007;36:451-477.
78. Fowler WE, Aebi U. A consistent picture of the actin filament related to the orientation of the actin molecule. J Cell Biol. 1983;97(1):264-269.
79. Lauffenburger DA, Horwitz AF. Cell migration: a physically integrated molecular process. Cell. 1996;84(3):359-369.
80. Pollard TD, Cooper JA. Actin, a central player in cell shape and movement. Science. 2009;326(5957):1208-1212.
81. Bugyi B, Carlier MF. Control of actin filament treadmilling in cell motility. Annu Rev Biophys. 2010;39:449-470.
82. Salbreux G, Charras G, Paluch E. Actin cortex mechanics and cellular morphogenesis. Trends Cell Biol. 2012;22(10):536-545.
83. Heisenberg CP, Bellaiche Y. Forces in tissue morphogenesis and patterning. Cell. 2013;153(5):948-962.
84. Svitkina TM, Borisy GG. Arp2/3 complex and actin depolymerizing factor/cofilin in dendritic organization and treadmilling of actin filament array in lamellipodia. J Cell Biol. 1999;145(5):1009-1026.
85. Xu K, Babcock HP, Zhuang X. Dual-objective STORM reveals three-dimensional filament organization in the actin cytoskeleton. Nat Methods. 2012;9(2):185-188.
86. Vicente-Manzanares M, Ma X, Adelstein RS, et al. Non-muscle myosin II takes centre stage in cell adhesion and migration. Nat Rev Mol Cell Biol. 2009;10(11):778-790.
87. Vallotton P, Gupton SL, Waterman-Storer CM, et al. Simultaneous mapping of filamentous actin flow and turnover in migrating cells by quantitative fluorescent speckle microscopy. Proc Natl Acad Sci U S A. 2004;101(26):9660-9665.
88. Vignjevic D, Peloquin J, Borisy GG. In vitro assembly of filopodia-like bundles. Methods Enzymol. 2006;406:727-739.
89. Naumanen P, Lappalainen P, Hotulainen P. Mechanisms of actin stress fibre assembly. J Microsc. 2008;231(3):446-454.
90. Sjoblom B, Salmazo A, Djinovic-Carugo K. Alpha-actinin structure and regulation. Cell Mol Life Sci. 2008;65(17):2688-2701.
91. Eghiaian F, Rigato A, Scheuring S. Structural, mechanical, and dynamical variability of the actin cortex in living cells. Biophys J. 2015;108(6):1330-1340.
92. Lock JG, Wehrle-Haller B, Stromblad S. Cell-matrix adhesion complexes: master control machinery of cell migration. Semin Cancer Biol. 2008;18(1):65-76.
93. Clausen MP, Colin-York H, Schneider F, et al. Dissecting the actin cortex density and membrane-cortex distance in living cells by super-resolution microscopy. J Phys D Appl Phys. 2017;50(6):064002.
94. Spector I, Shochet NR, Kashman Y, et al. Latrunculins: novel marine toxins that disrupt microfilament organization in cultured cells. Science. 1983;219(4584):493-495.
95. Cooper JA. Effects of cytochalasin and phalloidin on actin. J Cell Biol. 1987;105(4):1473-1478.
96. Holzinger A. Jasplakinolide. An actin-specific reagent that promotes actin polymerization. Methods Mol Biol. 2001;161:109-120.
97. Nolen BJ, Tomasevic N, Russell A, et al. Characterization of two classes of small molecule inhibitors of Arp2/3 complex. Nature. 2009;460(7258):1031-1034.
98. Hetrick B, Han MS, Helgeson LA, et al. Small molecules CK-666 and CK-869 inhibit actin-related protein 2/3 complex by blocking an activating conformational change. Chem Biol. 2013;20(5):701-712.
99. Leung DW, Morgan DM, Rosen MK. Biochemical properties and inhibitors of (N-)WASP. Methods Enzymol. 2006;406:281-296.
100. Rizvi SA, Neidt EM, Cui J, et al. Identification and characterization of a small molecule inhibitor of formin-mediated actin assembly. Chem Biol. 2009;16(11):1158-1168.
101. Leube RE, Schwarz N. Intermediate Filaments. In: Bradshaw RA, Stahl PD, editors. Encyclopedia of Cell Biology. 2. 1 ed. Amsterdam: Elsevier inc.; 2016. p. 569-578.
102. Herrmann H, Strelkov SV. History and phylogeny of intermediate filaments: now in insects. BMC Biol. 2011;9:16.

103. Etienne-Manneville S. Cytoplasmic Intermediate Filaments in Cell Biology. Annu Rev Cell Dev Biol. 2018;34:1-28.
104. Coulombe PA, Wong P. Cytoplasmic intermediate filaments revealed as dynamic and multipurpose scaffolds. Nat Cell Biol. 2004;6(8):699-706.
105. Herrmann H, Strelkov SV, Burkhard P, et al. Intermediate filaments: primary determinants of cell architecture and plasticity. J Clin Invest. 2009;119(7):1772-1783.
106. Bannasch P, Zerban H, Mayer D. The cytoskeleton in tumor cells. Pathol Res Pract. 1982;175(2-3):196-211.
107. Toivola DM, Tao GZ, Habtezion A, et al. Cellular integrity plus: organelle-related and protein-targeting functions of intermediate filaments. Trends Cell Biol. 2005;15(11):608-617.
108. Pekny M, Lane EB. Intermediate filaments and stress. Exp Cell Res. 2007;313(10):2244-2254.
109. Magin TM, Vijayaraj P, Leube RE. Structural and regulatory functions of keratins. Exp Cell Res. 2007;313(10):2021-2032.
110. Kim S, Coulombe PA. Intermediate filament scaffolds fulfill mechanical, organizational, and signaling functions in the cytoplasm. Genes Dev. 2007;21(13):1581-1597.
111. dos Santos G, Rogel MR, Baker MA, et al. Vimentin regulates activation of the NLRP3 inflammasome. Nat Commun. 2015;6:6574.
112. Sequeira I, Watt FM. The role of keratins in modulating carcinogenesis via communication with cells of the immune system. Cell Stress. 2019;3(4):136-138.
113. Ramms L, Fabris G, Windoffer R, et al. Keratins as the main component for the mechanical integrity of keratinocytes. Proc Natl Acad Sci U S A. 2013;110(46):18513-18518.
114. Seltmann K, Fritsch AW, Kas JA, et al. Keratins significantly contribute to cell stiffness and impact invasive behavior. Proc Natl Acad Sci U S A. 2013;110(46):18507-18512.
115. Ridge KM, Linz L, Flitney FW, et al. Keratin 8 phosphorylation by protein kinase C delta regulates shear stress-mediated disassembly of keratin intermediate filaments in alveolar epithelial cells. J Biol Chem. 2005;280(34):30400-30405.
116. Homberg M, Ramms L, Schwarz N, et al. Distinct Impact of Two Keratin Mutations Causing Epidermolysis Bullosa Simplex on Keratinocyte Adhesion and Stiffness. J Invest Dermatol. 2015;135(10):2437-2445.
117. Snider NT, Omary MB. Post-translational modifications of intermediate filament proteins: mechanisms and functions. Nat Rev Mol Cell Biol. 2014;15(3):163-177.
118. Ku NO, Omary MB. A disease- and phosphorylation-related nonmechanical function for keratin 8. J Cell Biol. 2006;174(1):115-125.
119. Lai YK, Lee WC, Chen KD. Vimentin serves as a phosphate sink during the apparent activation of protein kinases by okadaic acid in mammalian cells. J Cell Biochem. 1993;53(2):161-168.
120. DePianto D, Coulombe PA. Intermediate filaments and tissue repair. Exp Cell Res. 2004;301(1):68-76.
121. Ivaska J, Pallari HM, Nevo J, et al. Novel functions of vimentin in cell adhesion, migration, and signaling. Exp Cell Res. 2007;313(10):2050-2062.
122. Chung BM, Rotty JD, Coulombe PA. Networking galore: intermediate filaments and cell migration. Curr Opin Cell Biol. 2013;25(5):600-612.
123. Styers ML, Kowalczyk AP, Faundez V. Intermediate filaments and vesicular membrane traffic: the odd couple's first dance? Traffic. 2005;6(5):359-365.
124. Fountoulakis M, Soumaka E, Rapti K, et al. Alterations in the heart mitochondrial proteome in a desmin null heart failure model. J Mol Cell Cardiol. 2005;38(3):461-474.
125. Capetanaki Y. Desmin cytoskeleton: a potential regulator of muscle mitochondrial behavior and function. Trends Cardiovasc Med. 2002;12(8):339-348.
126. Milner DJ, Mavroidis M, Weisleder N, et al. Desmin cytoskeleton linked to muscle mitochondrial distribution and respiratory function. J Cell Biol. 2000;150(6):1283-1298.
127. Fay N, Pante N. The intermediate filament network protein, vimentin, is required for parvoviral infection. Virology. 2013;444(1-2):181-190.
128. Liem RK, Messing A. Dysfunctions of neuronal and glial intermediate filaments in disease. J Clin Invest. 2009;119(7):1814-1824.
129. Clemen CS, Herrmann H, Strelkov SV, et al. Desminopathies: pathology and mechanisms. Acta Neuropathol. 2013;125(1):47-75.
130. Chou YH, Flitney FW, Chang L, et al. The motility and dynamic properties of intermediate filaments and their constituent proteins. Exp Cell Res. 2007;313(10):2236-2243.
131. Haines RL, Lane EB. Keratins and disease at a glance. J Cell Sci. 2012;125(Pt 17):3923-3928.
132. Quinlan RA, Schiller DL, Hatzfeld M, et al. Patterns of expression and organization of cytokeratin intermediate filaments. Ann N Y Acad Sci. 1985;455:282-306.
133. Herrmann H, Wedig T, Porter RM, et al. Characterization of early assembly intermediates of recombinant human keratins. J Struct Biol. 2002;137(1-2):82-96.
134. Soellner P, Quinlan RA, Franke WW. Identification of a distinct soluble subunit of an intermediate filament protein: tetrameric vimentin from living cells. Proc Natl Acad Sci U S A. 1985;82(23):7929-7933.
135. Chou CF, Riopel CL, Rott LS, et al. A significant soluble keratin fraction in 'simple' epithelial cells. Lack of an apparent phosphorylation and glycosylation role in keratin solubility. J Cell Sci. 1993;105 (Pt 2):433-444.
136. Bachant JB, Klymkowsky MW. A nontetrameric species is the major soluble form of keratin in Xenopus oocytes and rabbit reticulocyte lysates. J Cell Biol. 1996;132(1-2):153-165.
137. Chou YH, Helfand BT, Goldman RD. New horizons in cytoskeletal dynamics: transport of intermediate filaments along microtubule tracks. Curr Opin Cell Biol. 2001;13(1):106-109.

138. Martys JL, Ho CL, Liem RK, et al. Intermediate filaments in motion: observations of intermediate filaments in cells using green fluorescent protein-vimentin. Mol Biol Cell. 1999;10(5):1289-1295.
139. Windoffer R, Kolsch A, Woll S, et al. Focal adhesions are hotspots for keratin filament precursor formation. J Cell Biol. 2006;173(3):341-348.
140. Moch M, Schwarz N, Windoffer R, et al. The keratin-desmosome scaffold: pivotal role of desmosomes for keratin network morphogenesis. Cell Mol Life Sci. 2020;77(3):543-558.
141. Moch M, Leube RE. Hemidesmosome-Related Keratin Filament Bundling and Nucleation. Int J Mol Sci. 2021;22(4).
142. Miller RK, Vikstrom K, Goldman RD. Keratin incorporation into intermediate filament networks is a rapid process. J Cell Biol. 1991;113(4):843-855.
143. Kolsch A, Windoffer R, Wurflinger T, et al. The keratin-filament cycle of assembly and disassembly. J Cell Sci. 2010;123(Pt 13):2266-2272.
144. Windoffer R, Beil M, Magin TM, et al. Cytoskeleton in motion: the dynamics of keratin intermediate filaments in epithelia. J Cell Biol. 2011;194(5):669-678.
145. Coulombe PA, Bousquet O, Ma L, et al. The 'ins' and 'outs' of intermediate filament organization. Trends Cell Biol. 2000;10(10):420-428.
146. Moch M, Herberich G, Aach T, et al. Measuring the regulation of keratin filament network dynamics. Proc Natl Acad Sci U S A. 2013;110(26):10664-10669.
147. Robert A, Herrmann H, Davidson MW, et al. Microtubule-dependent transport of vimentin filament precursors is regulated by actin and by the concerted action of Rho- and p21-activated kinases. FASEB J. 2014;28(7):2879-2890.
148. Hookway C, Ding L, Davidson MW, et al. Microtubule-dependent transport and dynamics of vimentin intermediate filaments. Mol Biol Cell. 2015;26(9):1675-1686.
149. Prahlad V, Yoon M, Moir RD, et al. Rapid movements of vimentin on microtubule tracks: kinesin-dependent assembly of intermediate filament networks. J Cell Biol. 1998;143(1):159-170.
150. Yoon M, Moir RD, Prahlad V, et al. Motile properties of vimentin intermediate filament networks in living cells. J Cell Biol. 1998;143(1):147-157.
151. Gyoeva FK, Gelfand VI. Coalignment of vimentin intermediate filaments with microtubules depends on kinesin. Nature. 1991;353(6343):445-448.
152. Ho CL, Martys JL, Mikhailov A, et al. Novel features of intermediate filament dynamics revealed by green fluorescent protein chimeras. J Cell Sci. 1998;111 (Pt 13):1767-1778.
153. Kreitzer G, Liao G, Gundersen GG. Detyrosination of tubulin regulates the interaction of intermediate filaments with microtubules in vivo via a kinesin-dependent mechanism. Mol Biol Cell. 1999;10(4):1105-1118.
154. Helfand BT, Mikami A, Vallee RB, et al. A requirement for cytoplasmic dynein and dynactin in intermediate filament network assembly and organization. J Cell Biol. 2002;157(5):795-806.
155. Yoon KH, Yoon M, Moir RD, et al. Insights into the dynamic properties of keratin intermediate filaments in living epithelial cells. J Cell Biol. 2001;153(3):503-516.
156. Windoffer R, Leube RE. Detection of cytokeratin dynamics by time-lapse fluorescence microscopy in living cells. J Cell Sci. 1999;112 (Pt 24):4521-4534.
157. Windoffer R, Leube RE. De novo formation of cytokeratin filament networks originates from the cell cortex in A-431 cells. Cell Motil Cytoskeleton. 2001;50(1):33-44.
158. Gregor M, Osmanagic-Myers S, Burgstaller G, et al. Mechanosensing through focal adhesion-anchored intermediate filaments. FASEB J. 2014;28(2):715-729.
159. Kwan R, Chen L, Looi K, et al. PKC412 normalizes mutation-related keratin filament disruption and hepatic injury in mice by promoting keratin-myosin binding. Hepatology. 2015;62(6):1858-1869.
160. Robert A, Tian P, Adam SA, et al. Kinesin-dependent transport of keratin filaments: a unified mechanism for intermediate filament transport. FASEB J. 2018:fj201800604R.
161. Liovic M, Mogensen MM, Prescott AR, et al. Observation of keratin particles showing fast bidirectional movement colocalized with microtubules. J Cell Sci. 2003;116(Pt 8):1417-1427.
162. Omary MB, Ku NO, Tao GZ, et al. "Heads and tails" of intermediate filament phosphorylation: multiple sites and functional insights. Trends Biochem Sci. 2006;31(7):383-394.
163. Tao GZ, Toivola DM, Zhou Q, et al. Protein phosphatase-2A associates with and dephosphorylates keratin 8 after hyposmotic stress in a site- and cell-specific manner. J Cell Sci. 2006;119(Pt 7):1425-1432.
164. Woll S, Windoffer R, Leube RE. p38 MAPK-dependent shaping of the keratin cytoskeleton in cultured cells. J Cell Biol. 2007;177(5):795-807.
165. Zatloukal K, French SW, Stumptner C, et al. From Mallory to Mallory-Denk bodies: what, how and why? Exp Cell Res. 2007;313(10):2033-2049.
166. Yoneda K, Furukawa T, Zheng YJ, et al. An autocrine/paracrine loop linking keratin 14 aggregates to tumor necrosis factor alpha-mediated cytotoxicity in a keratinocyte model of epidermolysis bullosa simplex. J Biol Chem. 2004;279(8):7296-7303.
167. Loffek S, Woll S, Hohfeld J, et al. The ubiquitin ligase CHIP/STUB1 targets mutant keratins for degradation. Hum Mutat. 2010;31(4):466-476.
168. Chamcheu JC, Navsaria H, Pihl-Lundin I, et al. Chemical chaperones protect epidermolysis bullosa simplex keratinocytes from heat stress-induced keratin aggregation: involvement of heat shock proteins and MAP kinases. J Invest Dermatol. 2011;131(8):1684-1691.
169. Hutchison CJ, Worman HJ. A-type lamins: guardians of the soma? Nat Cell Biol. 2004;6(11):1062-1067.
170. Goldman R, Goldman A, Green K, et al. Intermediate filaments: possible functions as cytoskeletal connecting links between the nucleus and the cell surface. Ann N Y Acad Sci. 1985;455:1-17.

171. Sarria AJ, Lieber JG, Nordeen SK, et al. The presence or absence of a vimentin-type intermediate filament network affects the shape of the nucleus in human SW-13 cells. J Cell Sci. 1994;107 (Pt 6):1593-1607.
172. Shah SB, Davis J, Weisleder N, et al. Structural and functional roles of desmin in mouse skeletal muscle during passive deformation. Biophys J. 2004;86(5):2993-3008.
173. Reichelt J, Magin TM. Hyperproliferation, induction of c-Myc and 14-3-3sigma, but no cell fragility in keratin-10-null mice. J Cell Sci. 2002;115(Pt 13):2639-2650.
174. Toivola DM, Nieminen MI, Hesse M, et al. Disturbances in hepatic cell-cycle regulation in mice with assembly-deficient keratins 8/18. Hepatology. 2001;34(6):1174-1183.
175. Gao Y, Sztul E. A novel interaction of the Golgi complex with the vimentin intermediate filament cytoskeleton. J Cell Biol. 2001;152(5):877-894.
176. Gillard BK, Clement R, Colucci-Guyon E, et al. Decreased synthesis of glycosphingolipids in cells lacking vimentin intermediate filaments. Exp Cell Res. 1998;242(2):561-572.
177. Lieber JG, Evans RM. Disruption of the vimentin intermediate filament system during adipose conversion of 3T3-L1 cells inhibits lipid droplet accumulation. J Cell Sci. 1996;109 (Pt 13):3047-3058.
178. Styers ML, Salazar G, Love R, et al. The endo-lysosomal sorting machinery interacts with the intermediate filament cytoskeleton. Mol Biol Cell. 2004;15(12):5369-5382.
179. Robinson MS. Adaptable adaptors for coated vesicles. Trends Cell Biol. 2004;14(4):167-174.
180. Salazar G, Love R, Styers ML, et al. AP-3-dependent mechanisms control the targeting of a chloride channel (ClC-3) in neuronal and non-neuronal cells. J Biol Chem. 2004;279(24):25430-25439.
181. Bucci C, Bakke O, Progida C. Charcot-Marie-Tooth disease and intracellular traffic. Prog Neurobiol. 2012;99(3):191-225.
182. Zhao C, Takita J, Tanaka Y, et al. Charcot-Marie-Tooth disease type 2A caused by mutation in a microtubule motor KIF1Bbeta. Cell. 2001;105(5):587-597.
183. Tanaka Y, Hirokawa N. Mouse models of Charcot-Marie-Tooth disease. Trends Genet. 2002;18(12):S39-44.
184. Verhoeven K, De Jonghe P, Coen K, et al. Mutations in the small GTP-ase late endosomal protein RAB7 cause Charcot-Marie-Tooth type 2B neuropathy. Am J Hum Genet. 2003;72(3):722-727.
185. Abati E, Manini A, Velardo D, et al. Clinical and genetic features of a cohort of patients with MFN2-related neuropathy. Sci Rep. 2022;12(1):6181.
186. Bhuin T, Roy JK. Rab proteins: the key regulators of intracellular vesicle transport. Exp Cell Res. 2014;328(1):1-19.
187. Mruk DD, Lau AS, Sarkar O, et al. Rab4A GTPase catenin interactions are involved in cell junction dynamics in the testis. J Androl. 2007;28(5):742-754.
188. McCaffrey MW, Bielli A, Cantalupo G, et al. Rab4 affects both recycling and degradative endosomal trafficking. FEBS Lett. 2001;495(1-2):21-30.
189. Kurzchalia TV, Gorvel JP, Dupree P, et al. Interactions of rab5 with cytosolic proteins. J Biol Chem. 1992;267(26):18419-18423.
190. Cogli L, Progida C, Bramato R, et al. Vimentin phosphorylation and assembly are regulated by the small GTPase Rab7a. Biochim Biophys Acta. 2013;1833(6):1283-1293.
191. Walter M, Chen FW, Tamari F, et al. Endosomal lipid accumulation in NPC1 leads to inhibition of PKC, hypophosphorylation of vimentin and Rab9 entrapment. Biol Cell. 2009;101(3):141-152.
192. Margiotta A, Bucci C. Role of Intermediate Filaments in Vesicular Traffic. Cells. 2016;5(2).
193. Summerhayes IC, Wong D, Chen LB. Effect of microtubules and intermediate filaments on mitochondrial distribution. J Cell Sci. 1983;61:87-105.
194. Shen J, Zhang JH, Xiao H, et al. Mitochondria are transported along microtubules in membrane nanotubes to rescue distressed cardiomyocytes from apoptosis. Cell Death Dis. 2018;9(2):81.
195. Melkov A, Abdu U. Regulation of long-distance transport of mitochondria along microtubules. Cell Mol Life Sci. 2018;75(2):163-176.
196. Lopez-Domenech G, Covill-Cooke C, Ivankovic D, et al. Miro proteins coordinate microtubule- and actin-dependent mitochondrial transport and distribution. EMBO J. 2018.
197. Moore AS, Holzbaur ELF. Mitochondrial-cytoskeletal interactions: dynamic associations that facilitate network function and remodeling. Curr Opin Physiol. 2018;3:94-100.
198. Tang HL, Lung HL, Wu KC, et al. Vimentin supports mitochondrial morphology and organization. Biochem J. 2008;410(1):141-146.
199. Almahbobi G, Williams LJ, Han XG, et al. Binding of lipid droplets and mitochondria to intermediate filaments in rat Leydig cells. J Reprod Fertil. 1993;98(1):209-217.
200. Collier NC, Sheetz MP, Schlesinger MJ. Concomitant changes in mitochondria and intermediate filaments during heat shock and recovery of chicken embryo fibroblasts. J Cell Biochem. 1993;52(3):297-307.
201. Tolstonog GV, Belichenko-Weitzmann IV, Lu JP, et al. Spontaneously immortalized mouse embryo fibroblasts: growth behavior of wild-type and vimentin-deficient cells in relation to mitochondrial structure and activity. DNA Cell Biol. 2005;24(11):680-709.
202. Tao GZ, Looi KS, Toivola DM, et al. Keratins modulate the shape and function of hepatocyte mitochondria: a mechanism for protection from apoptosis. J Cell Sci. 2009;122(Pt 21):3851-3855.
203. Silvander JSG, Kvarnstrom SM, Kumari-Ilieva A, et al. Keratins regulate beta-cell mitochondrial morphology, motility, and homeostasis. FASEB J. 2017;31(10):4578-4587.
204. Uttam J, Hutton E, Coulombe PA, et al. The genetic basis of epidermolysis bullosa simplex with mottled pigmentation. Proc Natl Acad Sci U S A. 1996;93(17):9079-9084.
205. Chan YM, Yu QC, LeBlanc-Straceski J, et al. Mutations in the non-helical linker segment L1-2 of keratin 5 in patients with Weber-Cockayne epidermolysis bullosa simplex. J Cell Sci. 1994;107 (Pt 4):765-774.

206. Achleitner G, Gaigg B, Krasser A, et al. Association between the endoplasmic reticulum and mitochondria of yeast facilitates interorganelle transport of phospholipids through membrane contact. Eur J Biochem. 1999;264(2):545-553.
207. Filippin L, Magalhaes PJ, Di Benedetto G, et al. Stable interactions between mitochondria and endoplasmic reticulum allow rapid accumulation of calcium in a subpopulation of mitochondria. J Biol Chem. 2003;278(40):39224-39234.
208. Szabadkai G, Bianchi K, Varnai P, et al. Chaperone-mediated coupling of endoplasmic reticulum and mitochondrial Ca2+ channels. J Cell Biol. 2006;175(6):901-911.
209. Vance JE. MAM (mitochondria-associated membranes) in mammalian cells: lipids and beyond. Biochim Biophys Acta. 2014;1841(4):595-609.
210. Nekrasova OE, Mendez MG, Chernoivanenko IS, et al. Vimentin intermediate filaments modulate the motility of mitochondria. Mol Biol Cell. 2011;22(13):2282-2289.
211. Matveeva EA, Venkova LS, Chernoivanenko IS, et al. Vimentin is involved in regulation of mitochondrial motility and membrane potential by Rac1. Biol Open. 2015;4(10):1290-1297.
212. Lowery J, Jain N, Kuczmarski ER, et al. Abnormal intermediate filament organization alters mitochondrial motility in giant axonal neuropathy fibroblasts. Mol Biol Cell. 2016;27(4):608-616.
213. Israeli E, Dryanovski DI, Schumacker PT, et al. Intermediate filament aggregates cause mitochondrial dysmotility and increase energy demands in giant axonal neuropathy. Hum Mol Genet. 2016;25(11):2143-2157.
214. Straube-West K, Loomis PA, Opal P, et al. Alterations in neural intermediate filament organization: functional implications and the induction of pathological changes related to motor neuron disease. J Cell Sci. 1996;109 (Pt 9):2319-2329.
215. Kumar V, Bouameur JE, Bar J, et al. A keratin scaffold regulates epidermal barrier formation, mitochondrial lipid composition, and activity. J Cell Biol. 2015;211(5):1057-1075.
216. Kostareva A, Sjoberg G, Bruton J, et al. Mice expressing L345P mutant desmin exhibit morphological and functional changes of skeletal and cardiac mitochondria. J Muscle Res Cell Motil. 2008;29(1):25-36.
217. Smolina N, Bruton J, Sjoberg G, et al. Aggregate-prone desmin mutations impair mitochondrial calcium uptake in primary myotubes. Cell Calcium. 2014;56(4):269-275.
218. Zhu L, Ling S, Yu XD, et al. Modulation of mitochondrial Ca(2+) homeostasis by Bcl-2. J Biol Chem. 1999;274(47):33267-33273.
219. McCormack JG, Denton RM. Intracellular calcium ions and intramitochondrial Ca2+ in the regulation of energy metabolism in mammalian tissues. Proc Nutr Soc. 1990;49(1):57-75.
220. Cardenas C, Miller RA, Smith I, et al. Essential regulation of cell bioenergetics by constitutive InsP3 receptor Ca2+ transfer to mitochondria. Cell. 2010;142(2):270-283.
221. Rizzuto R, Pinton P, Carrington W, et al. Close contacts with the endoplasmic reticulum as determinants of mitochondrial Ca2+ responses. Science. 1998;280(5370):1763-1766.
222. Nishizawa M, Izawa I, Inoko A, et al. Identification of trichoplein, a novel keratin filament-binding protein. J Cell Sci. 2005;118(Pt 5):1081-1090.
223. Cerqua C, Anesti V, Pyakurel A, et al. Trichoplein/mitostatin regulates endoplasmic reticulum-mitochondria juxtaposition. EMBO Rep. 2010;11(11):854-860.
224. Vance JE. Newly made phosphatidylserine and phosphatidylethanolamine are preferentially translocated between rat liver mitochondria and endoplasmic reticulum. J Biol Chem. 1991;266(1):89-97.
225. Zhong Q, Gohil VM, Ma L, et al. Absence of cardiolipin results in temperature sensitivity, respiratory defects, and mitochondrial DNA instability independent of pet56. J Biol Chem. 2004;279(31):32294-32300.
226. DeVay RM, Dominguez-Ramirez L, Lackner LL, et al. Coassembly of Mgm1 isoforms requires cardiolipin and mediates mitochondrial inner membrane fusion. J Cell Biol. 2009;186(6):793-803.
227. Vakifahmetoglu-Norberg H, Ouchida AT, Norberg E. The role of mitochondria in metabolism and cell death. Biochem Biophys Res Commun. 2017;482(3):426-431.
228. Kiriyama Y, Nochi H. Intra- and Intercellular Quality Control Mechanisms of Mitochondria. Cells. 2017;7(1).
229. Ni HM, Williams JA, Ding WX. Mitochondrial dynamics and mitochondrial quality control. Redox Biol. 2015;4:6-13.
230. Unoki M, Nakamura Y. Growth-suppressive effects of BPOZ and EGR2, two genes involved in the PTEN signaling pathway. Oncogene. 2001;20(33):4457-4465.
231. Youle RJ, Narendra DP. Mechanisms of mitophagy. Nat Rev Mol Cell Biol. 2011;12(1):9-14.
232. Okatsu K, Oka T, Iguchi M, et al. PINK1 autophosphorylation upon membrane potential dissipation is essential for Parkin recruitment to damaged mitochondria. Nat Commun. 2012;3:1016.
233. Voigt A, Berlemann LA, Winklhofer KF. The mitochondrial kinase PINK1: functions beyond mitophagy. J Neurochem. 2016;139 Suppl 1:232-239.
234. Fiesel FC, Ando M, Hudec R, et al. (Patho-)physiological relevance of PINK1-dependent ubiquitin phosphorylation. EMBO Rep. 2015;16(9):1114-1130.
235. Narendra DP, Jin SM, Tanaka A, et al. PINK1 is selectively stabilized on impaired mitochondria to activate Parkin. PLoS Biol. 2010;8(1):e1000298.
236. Geisler S, Holmstrom KM, Skujat D, et al. PINK1/Parkin-mediated mitophagy is dependent on VDAC1 and p62/SQSTM1. Nat Cell Biol. 2010;12(2):119-131.
237. Shiba K, Arai T, Sato S, et al. Parkin stabilizes PINK1 through direct interaction. Biochem Biophys Res Commun. 2009;383(3):331-335.
238. Um JW, Stichel-Gunkel C, Lubbert H, et al. Molecular interaction between parkin and PINK1 in mammalian neuronal cells. Mol Cell Neurosci. 2009;40(4):421-432.

239. Kim Y, Park J, Kim S, et al. PINK1 controls mitochondrial localization of Parkin through direct phosphorylation. Biochem Biophys Res Commun. 2008;377(3):975-980.
240. Sha D, Chin LS, Li L. Phosphorylation of parkin by Parkinson disease-linked kinase PINK1 activates parkin E3 ligase function and NF-kappaB signaling. Hum Mol Genet. 2010;19(2):352-363.
241. Yamano K, Matsuda N, Tanaka K. The ubiquitin signal and autophagy: an orchestrated dance leading to mitochondrial degradation. EMBO Rep. 2016;17(3):300-316.
242. Matsuda N, Sato S, Shiba K, et al. PINK1 stabilized by mitochondrial depolarization recruits Parkin to damaged mitochondria and activates latent Parkin for mitophagy. J Cell Biol. 2010;189(2):211-221.
243. Jin SM, Lazarou M, Wang C, et al. Mitochondrial membrane potential regulates PINK1 import and proteolytic destabilization by PARL. J Cell Biol. 2010;191(5):933-942.
244. Gegg ME, Cooper JM, Chau KY, et al. Mitofusin 1 and mitofusin 2 are ubiquitinated in a PINK1/parkin-dependent manner upon induction of mitophagy. Hum Mol Genet. 2010;19(24):4861-4870.
245. Tanaka A, Cleland MM, Xu S, et al. Proteasome and p97 mediate mitophagy and degradation of mitofusins induced by Parkin. J Cell Biol. 2010;191(7):1367-1380.
246. Pankiv S, Clausen TH, Lamark T, et al. p62/SQSTM1 binds directly to Atg8/LC3 to facilitate degradation of ubiquitinated protein aggregates by autophagy. J Biol Chem. 2007;282(33):24131-24145.
247. Ding WX, Ni HM, Li M, et al. Nix is critical to two distinct phases of mitophagy, reactive oxygen species-mediated autophagy induction and Parkin-ubiquitin-p62-mediated mitochondrial priming. J Biol Chem. 2010;285(36):27879-27890.
248. Lee JY, Nagano Y, Taylor JP, et al. Disease-causing mutations in parkin impair mitochondrial ubiquitination, aggregation, and HDAC6-dependent mitophagy. J Cell Biol. 2010;189(4):671-679.
249. Okatsu K, Saisho K, Shimanuki M, et al. p62/SQSTM1 cooperates with Parkin for perinuclear clustering of depolarized mitochondria. Genes Cells. 2010;15(8):887-900.
250. Narendra D, Kane LA, Hauser DN, et al. p62/SQSTM1 is required for Parkin-induced mitochondrial clustering but not mitophagy; VDAC1 is dispensable for both. Autophagy. 2010;6(8):1090-1106.
251. Heo JM, Ordureau A, Paulo JA, et al. The PINK1-PARKIN Mitochondrial Ubiquitylation Pathway Drives a Program of OPTN/NDP52 Recruitment and TBK1 Activation to Promote Mitophagy. Mol Cell. 2015;60(1):7-20.
252. Wong YC, Holzbaur EL. Optineurin is an autophagy receptor for damaged mitochondria in parkin-mediated mitophagy that is disrupted by an ALS-linked mutation. Proc Natl Acad Sci U S A. 2014;111(42):E4439-4448.
253. . !!! INVALID CITATION !!! {}.
254. Klionsky DJ, Cregg JM, Dunn WA, Jr., et al. A unified nomenclature for yeast autophagy-related genes. Dev Cell. 2003;5(4):539-545.
255. Nakatogawa H, Ichimura Y, Ohsumi Y. Atg8, a ubiquitin-like protein required for autophagosome formation, mediates membrane tethering and hemifusion. Cell. 2007;130(1):165-178.
256. Noda NN, Ohsumi Y, Inagaki F. Atg8-family interacting motif crucial for selective autophagy. FEBS Lett. 2010;584(7):1379-1385.
257. Axe EL, Walker SA, Manifava M, et al. Autophagosome formation from membrane compartments enriched in phosphatidylinositol 3-phosphate and dynamically connected to the endoplasmic reticulum. J Cell Biol. 2008;182(4):685-701.
258. Roberts R, Ktistakis NT. Omegasomes: PI3P platforms that manufacture autophagosomes. Essays Biochem. 2013;55:17-27.
259. Hamasaki M, Furuta N, Matsuda A, et al. Autophagosomes form at ER-mitochondria contact sites. Nature. 2013;495(7441):389-393.
260. Huang Y, Yang P, Chen H, et al. A "Lamellar structure" contributes to autophagosome biogenesis and mitophagy in zebrafish hepatocytes. Fish Shellfish Immunol. 2018.
261. Uemura T, Yamamoto M, Kametaka A, et al. A cluster of thin tubular structures mediates transformation of the endoplasmic reticulum to autophagic isolation membrane. Mol Cell Biol. 2014;34(9):1695-1706.
262. Gelmetti V, De Rosa P, Torosantucci L, et al. PINK1 and BECN1 relocalize at mitochondria-associated membranes during mitophagy and promote ER-mitochondria tethering and autophagosome formation. Autophagy. 2017;13(4):654-669.
263. Kim I, Rodriguez-Enriquez S, Lemasters JJ. Selective degradation of mitochondria by mitophagy. Arch Biochem Biophys. 2007;462(2):245-253.
264. Kuchitsu Y, Homma Y, Fujita N, et al. Rab7 knockout unveils regulated autolysosome maturation induced by glutamine starvation. J Cell Sci. 2018;131(7).
265. Matsuda N. Phospho-ubiquitin: upending the PINK-Parkin-ubiquitin cascade. J Biochem. 2016;159(4):379-385.
266. Yu L, McPhee CK, Zheng L, et al. Termination of autophagy and reformation of lysosomes regulated by mTOR. Nature. 2010;465(7300):942-946.
267. Du W, Su QP, Chen Y, et al. Kinesin 1 Drives Autolysosome Tubulation. Dev Cell. 2016;37(4):326-336.
268. Kepiro M, Varkuti BH, Vegner L, et al. para-Nitroblebbistatin, the non-cytotoxic and photostable myosin II inhibitor. Angew Chem Int Ed Engl. 2014;53(31):8211-8215.
269. Rauscher AA, Gyimesi M, Kovacs M, et al. Targeting Myosin by Blebbistatin Derivatives: Optimization and Pharmacological Potential. Trends Biochem Sci. 2018;43(9):700-713.
270. Diecke FP, Wen Q, Iserovich P, et al. Regulation of Na-K-2Cl cotransport in cultured bovine corneal endothelial cells. Exp Eye Res. 2005;80(6):777-785.
271. Cui WJ, Liu Y, Zhou XL, et al. Myosin light chain kinase is responsible for high proliferative ability of breast cancer cells via anti-apoptosis involving p38 pathway. Acta Pharmacol Sin. 2010;31(6):725-732.

272. Kimura S, Noda T, Yoshimori T. Dissection of the autophagosome maturation process by a novel reporter protein, tandem fluorescent-tagged LC3. Autophagy. 2007;3(5):452-460.
273. Tinevez JY, Perry N, Schindelin J, et al. TrackMate: An open and extensible platform for single-particle tracking. Methods. 2017;115:80-90.
274. Tarantino N, Tinevez JY, Crowell EF, et al. TNF and IL-1 exhibit distinct ubiquitin requirements for inducing NEMO-IKK supramolecular structures. J Cell Biol. 2014;204(2):231-245.
275. Wilcoxon F. Individual comparisons of grouped data by ranking methods. J Econ Entomol. 1946;39:269.
276. Lehmann SM, Leube RE, Windoffer R. Growth, lifetime, directional movement and myosin-dependent motility of mutant keratin granules in cultured cells. Sci Rep. 2021;11(1):2379.
277. Qian H, Sheetz MP, Elson EL. Single particle tracking. Analysis of diffusion and flow in two-dimensional systems. Biophys J. 1991;60(4):910-921.
278. Saitoh M, Ishikawa T, Matsushima S, et al. Selective inhibition of catalytic activity of smooth muscle myosin light chain kinase. J Biol Chem. 1987;262(16):7796-7801.
279. Hyman AA, Weber CA, Julicher F. Liquid-liquid phase separation in biology. Annu Rev Cell Dev Biol. 2014;30:39-58.
280. Brangwynne CP, Eckmann CR, Courson DS, et al. Germline P granules are liquid droplets that localize by controlled dissolution/condensation. Science. 2009;324(5935):1729-1732.
281. Rai AK, Chen JX, Selbach M, et al. Kinase-controlled phase transition of membraneless organelles in mitosis. Nature. 2018;559(7713):211-216.
282. Friedl P, Wolf K. Plasticity of cell migration: a multiscale tuning model. J Cell Biol. 2010;188(1):11-19.
283. Welch MD. Cell migration, freshly squeezed. Cell. 2015;160(4):581-582.
284. Gottlieb RA, Stotland A. MitoTimer: a novel protein for monitoring mitochondrial turnover in the heart. J Mol Med (Berl). 2015;93(3):271-278.
285. Lehmann SM, Leube RE, Schwarz N. Keratin 6a mutations lead to impaired mitochondrial quality control. Br J Dermatol. 2019.
286. Korge BP, Krieg T. The molecular basis for inherited bullous diseases. J Mol Med (Berl). 1996;74(2):59-70.
287. Iwata A, Riley BE, Johnston JA, et al. HDAC6 and microtubules are required for autophagic degradation of aggregated huntingtin. J Biol Chem. 2005;280(48):40282-40292.
288. Lee JY, Koga H, Kawaguchi Y, et al. HDAC6 controls autophagosome maturation essential for ubiquitin-selective quality-control autophagy. EMBO J. 2010;29(5):969-980.
289. Kabeya Y, Mizushima N, Ueno T, et al. LC3, a mammalian homologue of yeast Apg8p, is localized in autophagosome membranes after processing. EMBO J. 2000;19(21):5720-5728.
290. Chou YH, Goldman RD. Intermediate filaments on the move. J Cell Biol. 2000;150(3):F101-106.
291. Strnad P, Windoffer R, Leube RE. In vivo detection of cytokeratin filament network breakdown in cells treated with the phosphatase inhibitor okadaic acid. Cell Tissue Res. 2001;306(2):277-293.
292. Strnad P, Windoffer R, Leube RE. Induction of rapid and reversible cytokeratin filament network remodeling by inhibition of tyrosine phosphatases. J Cell Sci. 2002;115(Pt 21):4133-4148.
293. Fujiwara S, Deguchi S, Magin TM. Disease-associated keratin mutations reduce traction forces and compromise adhesion and collective migration. J Cell Sci. 2020.
294. Liovic M, D'Alessandro M, Tomic-Canic M, et al. Severe keratin 5 and 14 mutations induce down-regulation of junction proteins in keratinocytes. Exp Cell Res. 2009;315(17):2995-3003.
295. D'Alessandro M, Russell D, Morley SM, et al. Keratin mutations of epidermolysis bullosa simplex alter the kinetics of stress response to osmotic shock. J Cell Sci. 2002;115(Pt 22):4341-4351.
296. Sawant MS, Leube RE. Consequences of Keratin Phosphorylation for Cytoskeletal Organization and Epithelial Functions. Int Rev Cell Mol Biol. 2017;330:171-225.
297. Schutte B, Henfling M, Kolgen W, et al. Keratin 8/18 breakdown and reorganization during apoptosis. Exp Cell Res. 2004;297(1):11-26.
298. Loschke F, Seltmann K, Bouameur JE, et al. Regulation of keratin network organization. Curr Opin Cell Biol. 2015;32:56-64.
299. Leube RE, Moch M, Windoffer R. Intermediate filaments and the regulation of focal adhesion. Curr Opin Cell Biol. 2015;32:13-20.
300. Kroger C, Loschke F, Schwarz N, et al. Keratins control intercellular adhesion involving PKC-alpha-mediated desmoplakin phosphorylation. J Cell Biol. 2013;201(5):681-692.
301. Gallicano GI, Kouklis P, Bauer C, et al. Desmoplakin is required early in development for assembly of desmosomes and cytoskeletal linkage. J Cell Biol. 1998;143(7):2009-2022.
302. Vasioukhin V, Bowers E, Bauer C, et al. Desmoplakin is essential in epidermal sheet formation. Nat Cell Biol. 2001;3(12):1076-1085.
303. McMillan JR, McGrath JA, Tidman MJ, et al. Hemidesmosomes show abnormal association with the keratin filament network in junctional forms of epidermolysis bullosa. J Invest Dermatol. 1998;110(2):132-137.
304. Seltmann K, Cheng F, Wiche G, et al. Keratins Stabilize Hemidesmosomes through Regulation of beta4-Integrin Turnover. J Invest Dermatol. 2015;135(6):1609-1620.
305. Bar J, Kumar V, Roth W, et al. Skin fragility and impaired desmosomal adhesion in mice lacking all keratins. J Invest Dermatol. 2014;134(4):1012-1022.
306. Wang F, Chen S, Liu HB, et al. Keratin 6 regulates collective keratinocyte migration by altering cell-cell and cell-matrix adhesion. J Cell Biol. 2018;217(12):4314-4330.
307. Amann KJ, Pollard TD. The Arp2/3 complex nucleates actin filament branches from the sides of pre-existing filaments. Nat Cell Biol. 2001;3(3):306-310.

308. Waterman-Storer CM, Salmon ED. Actomyosin-based retrograde flow of microtubules in the lamella of migrating epithelial cells influences microtubule dynamic instability and turnover and is associated with microtubule breakage and treadmilling. J Cell Biol. 1997;139(2):417-434.
309. Medeiros NA, Burnette DT, Forscher P. Myosin II functions in actin-bundle turnover in neuronal growth cones. Nat Cell Biol. 2006;8(3):215-226.
310. Nobezawa D, Ikeda SI, Wada E, et al. Directional Transport of a Bead Bound to Lamellipodial Surface Is Driven by Actin Polymerization. Biomed Res Int. 2017;2017:7804251.
311. Yi J, Wu XS, Crites T, et al. Actin retrograde flow and actomyosin II arc contraction drive receptor cluster dynamics at the immunological synapse in Jurkat T cells. Mol Biol Cell. 2012;23(5):834-852.
312. Byers HR, Maheshwary S, Amodeo DM, et al. Role of cytoplasmic dynein in perinuclear aggregation of phagocytosed melanosomes and supranuclear melanin cap formation in human keratinocytes. J Invest Dermatol. 2003;121(4):813-820.
313. Yuan A, Rao MV, Veeranna, et al. Neurofilaments and Neurofilament Proteins in Health and Disease. Cold Spring Harb Perspect Biol. 2017;9(4).
314. Tran QD, Sorichetti V, Pehau-Arnaudet G, et al. Vimentin intermediate filament assembly is a reversible process. bioRxiv. 2022:2022.2003.2019.484978.
315. Schwarz N, Moch M, Windoffer R, et al. Multidimensional Monitoring of Keratin Intermediate Filaments in Cultured Cells and Tissues. Methods Enzymol. 2016;568:59-83.
316. Ma L, Yamada S, Wirtz D, et al. A 'hot-spot' mutation alters the mechanical properties of keratin filament networks. Nat Cell Biol. 2001;3(5):503-506.
317. Russell D, Andrews PD, James J, et al. Mechanical stress induces profound remodelling of keratin filaments and cell junctions in epidermolysis bullosa simplex keratinocytes. J Cell Sci. 2004;117(Pt 22):5233-5243.
318. Sivaramakrishnan S, DeGiulio JV, Lorand L, et al. Micromechanical properties of keratin intermediate filament networks. Proc Natl Acad Sci U S A. 2008;105(3):889-894.
319. Lu YB, Iandiev I, Hollborn M, et al. Reactive glial cells: increased stiffness correlates with increased intermediate filament expression. FASEB J. 2011;25(2):624-631.
320. Koster S, Weitz DA, Goldman RD, et al. Intermediate filament mechanics in vitro and in the cell: from coiled coils to filaments, fibers and networks. Curr Opin Cell Biol. 2015;32:82-91.
321. Quinlan RA, Schwarz N, Windoffer R, et al. A rim-and-spoke hypothesis to explain the biomechanical roles for cytoplasmic intermediate filament networks. J Cell Sci. 2017;130(20):3437-3445.
322. Beriault DR, Haddad O, McCuaig JV, et al. The mechanical behavior of mutant K14-R125P keratin bundles and networks in NEB-1 keratinocytes. PLoS One. 2012;7(2):e31320.
323. Peters B, Kirfel J, Bussow H, et al. Complete cytolysis and neonatal lethality in keratin 5 knockout mice reveal its fundamental role in skin integrity and in epidermolysis bullosa simplex. Mol Biol Cell. 2001;12(6):1775-1789.
324. Drochmans P, Freudenstein C, Wanson JC, et al. Structure and biochemical composition of desmosomes and tonofilaments isolated from calf muzzle epidermis. J Cell Biol. 1978;79(2 Pt 1):427-443.
325. Hibbs RG, Clark WH, Jr. Electron microscope studies of the human epidermis; the cell boundaries and topography of the stratum malpighii. J Biophys Biochem Cytol. 1959;6(1):71-76.
326. Pieperhoff S, Borrmann C, Grund C, et al. The area composita of adhering junctions connecting heart muscle cells of vertebrates. VII. The different types of lateral junctions between the special cardiomyocytes of the conduction system of ovine and bovine hearts. Eur J Cell Biol. 2010;89(5):365-378.
327. Chamcheu JC, Siddiqui IA, Mukhtar H. Chemical chaperone therapy, a new strategy for genetic skin fragility disorders. Exp Dermatol. 2016;25(3):183-184.
328. Bchetnia M, Lacroix J, Farez T, et al. Reduction in keratin aggregates in epidermolysis bullosa simplex keratinocytes after pretreatment with trimethylamine N-oxide. Exp Dermatol. 2016;25(3):229-230.
329. Lloyd C, Yu QC, Cheng J, et al. The basal keratin network of stratified squamous epithelia: defining K15 function in the absence of K14. J Cell Biol. 1995;129(5):1329-1344.
330. Arin MJ, Roop DR. Inducible mouse models for inherited skin diseases: implications for skin gene therapy. Cells Tissues Organs. 2004;177(3):160-168.
331. Magin TM, Hesse M, Meier-Bornheim R, et al. Developing mouse models to study intermediate filament function. Methods Cell Biol. 2004;78:65-94.
332. Arin MJ, Oji V, Emmert S, et al. Expanding the keratin mutation database: novel and recurrent mutations and genotype-phenotype correlations in 28 patients with epidermolytic ichthyosis. Br J Dermatol. 2011;164(2):442-447.
333. Bouameur JE, Magin TM. Lessons from Animal Models of Cytoplasmic Intermediate Filament Proteins. Subcell Biochem. 2017;82:171-230.
334. Smith LT. Ultrastructural findings in epidermolysis bullosa. Arch Dermatol. 1993;129(12):1578-1584.
335. Shemanko CS, Mellerio JE, Tidman MJ, et al. Severe palmo-plantar hyperkeratosis in Dowling-Meara epidermolysis bullosa simplex caused by a mutation in the keratin 14 gene (KRT14). J Invest Dermatol. 1998;111(5):893-895.
336. Eady RA, Dopping-Hepenstal PJ. Transmission electron microscopy for the diagnosis of epidermolysis bullosa. Dermatol Clin. 2010;28(2):211-222, vii.
337. Rossi S, Castiglia D, Pisaneschi E, et al. Immunofluorescence mapping, electron microscopy and genetics in the diagnosis and sub-classification of inherited epidermolysis bullosa: a single-centre retrospective comparative study of 87 cases with long-term follow-up. J Eur Acad Dermatol Venereol. 2021;35(4):1007-1016.

338. Jaunzems AE, Woods AE, Staples A. Electron microscopy and morphometry enhances differentiation of epidermolysis bullosa subtypes. With normal values for 24 parameters in skin. Arch Dermatol Res. 1997;289(11):631-639.
339. Shinkuma S, McMillan JR, Shimizu H. Ultrastructure and molecular pathogenesis of epidermolysis bullosa. Clin Dermatol. 2011;29(4):412-419.
340. Niemi KM, Kero M, Kanerva L, et al. Epidermolysis bullosa simplex. A new histologic subgroup. Arch Dermatol. 1983;119(2):138-141.
341. Moon SL, Morisaki T, Khong A, et al. Multicolour single-molecule tracking of mRNA interactions with RNP granules. Nat Cell Biol. 2019;21(2):162-168.
342. Lyon AS, Peeples WB, Rosen MK. A framework for understanding the functions of biomolecular condensates across scales. Nat Rev Mol Cell Biol. 2021;22(3):215-235.
343. Saha S, Weber CA, Nousch M, et al. Polar Positioning of Phase-Separated Liquid Compartments in Cells Regulated by an mRNA Competition Mechanism. Cell. 2016;166(6):1572-1584 e1516.
344. Guillen-Boixet J, Kopach A, Holehouse AS, et al. RNA-Induced Conformational Switching and Clustering of G3BP Drive Stress Granule Assembly by Condensation. Cell. 2020;181(2):346-361 e317.
345. Sanders DW, Kedersha N, Lee DSW, et al. Competing Protein-RNA Interaction Networks Control Multiphase Intracellular Organization. Cell. 2020;181(2):306-324 e328.
346. Yang P, Mathieu C, Kolaitis RM, et al. G3BP1 Is a Tunable Switch that Triggers Phase Separation to Assemble Stress Granules. Cell. 2020;181(2):325-345 e328.
347. Wiegand T, Hyman AA. Drops and fibers - how biomolecular condensates and cytoskeletal filaments influence each other. Emerg Top Life Sci. 2020;4(3):247-261.
348. Zhou X, Lin Y, Kato M, et al. Transiently structured head domains control intermediate filament assembly. Proc Natl Acad Sci U S A. 2021;118(8).
349. Martin EW, Mittag T. Relationship of Sequence and Phase Separation in Protein Low-Complexity Regions. Biochemistry. 2018;57(17):2478-2487.
350. Alberti S, Hyman AA. Biomolecular condensates at the nexus of cellular stress, protein aggregation disease and ageing. Nat Rev Mol Cell Biol. 2021;22(3):196-213.
351. Haugwitz M, Nourzaie O, Gandlur S, et al. ProteoTuner: a novel system with rapid kinetics enables reversible control of protein levels in cells and organisms. Biotechniques. 2008;44(3):432-433.
352. Tourriere H, Chebli K, Zekri L, et al. The RasGAP-associated endoribonuclease G3BP assembles stress granules. J Cell Biol. 2003;160(6):823-831.
353. Wilczynska A, Aigueperse C, Kress M, et al. The translational regulator CPEB1 provides a link between dcp1 bodies and stress granules. J Cell Sci. 2005;118(Pt 5):981-992.
354. Gilks N, Kedersha N, Ayodele M, et al. Stress granule assembly is mediated by prion-like aggregation of TIA-1. Mol Biol Cell. 2004;15(12):5383-5398.
355. Ries J, Schwille P. Fluorescence correlation spectroscopy. Bioessays. 2012;34(5):361-368.
356. Hubatsch L, Jawerth LM, Love C, et al. Quantitative theory for the diffusive dynamics of liquid condensates. Elife. 2021;10.
357. Shin Y, Brangwynne CP. Liquid phase condensation in cell physiology and disease. Science. 2017;357(6357).
358. Banani SF, Lee HO, Hyman AA, et al. Biomolecular condensates: organizers of cellular biochemistry. Nat Rev Mol Cell Biol. 2017;18(5):285-298.
359. Gao Z, Zhang W, Chang R, et al. Liquid-Liquid Phase Separation: Unraveling the Enigma of Biomolecular Condensates in Microbial Cells. Front Microbiol. 2021;12:751880.
360. Liao J, Lowthert LA, Omary MB. Heat stress or rotavirus infection of human epithelial cells generates a distinct hyperphosphorylated form of keratin 8. Exp Cell Res. 1995;219(2):348-357.
361. Snead WT, Gladfelter AS. The Control Centers of Biomolecular Phase Separation: How Membrane Surfaces, PTMs, and Active Processes Regulate Condensation. Mol Cell. 2019;76(2):295-305.
362. Sawant M, Schwarz N, Windoffer R, et al. Threonine 150 phosphorylation of keratin 5 is linked to EBS and regulates filament assembly and cell viability. J Invest Dermatol. 2017.
363. Case LB, Zhang X, Ditlev JA, et al. Stoichiometry controls activity of phase-separated clusters of actin signaling proteins. Science. 2019;363(6431):1093-1097.
364. Franzmann TM, Jahnel M, Pozniakovsky A, et al. Phase separation of a yeast prion protein promotes cellular fitness. Science. 2018;359(6371).
365. Riback JA, Katanski CD, Kear-Scott JL, et al. Stress-Triggered Phase Separation Is an Adaptive, Evolutionarily Tuned Response. Cell. 2017;168(6):1028-1040 e1019.
366. Shin Y, Chang YC, Lee DSW, et al. Liquid Nuclear Condensates Mechanically Sense and Restructure the Genome. Cell. 2018;175(6):1481-1491 e1413.
367. Klosin A, Oltsch F, Harmon T, et al. Phase separation provides a mechanism to reduce noise in cells. Science. 2020;367(6476):464-468.
368. Omary MB, Ku NO, Strnad P, et al. Toward unraveling the complexity of simple epithelial keratins in human disease. J Clin Invest. 2009;119(7):1794-1805.
369. Toivola DM, Ku NO, Resurreccion EZ, et al. Keratin 8 and 18 hyperphosphorylation is a marker of progression of human liver disease. Hepatology. 2004;40(2):459-466.
370. Strnad P, Paschke S, Jang KH, et al. Keratins: markers and modulators of liver disease. Curr Opin Gastroenterol. 2012;28(3):209-216.
371. Feng L, Zhou X, Liao J, et al. Pervanadate-mediated tyrosine phosphorylation of keratins 8 and 19 via a p38 mitogen-activated protein kinase-dependent pathway. J Cell Sci. 1999;112 (Pt 13):2081-2090.

372. Zhou X, Liao J, Hu L, et al. Characterization of the major physiologic phosphorylation site of human keratin 19 and its role in filament organization. J Biol Chem. 1999;274(18):12861-12866.
373. Hyder CL, Pallari HM, Kochin V, et al. Providing cellular signposts--post-translational modifications of intermediate filaments. FEBS Lett. 2008;582(14):2140-2148.
374. Sivaramakrishnan S, Schneider JL, Sitikov A, et al. Shear stress induced reorganization of the keratin intermediate filament network requires phosphorylation by protein kinase C zeta. Mol Biol Cell. 2009;20(11):2755-2765.
375. He T, Stepulak A, Holmstrom TH, et al. The intermediate filament protein keratin 8 is a novel cytoplasmic substrate for c-Jun N-terminal kinase. J Biol Chem. 2002;277(13):10767-10774.
376. Chan YM, Yu QC, Fine JD, et al. The genetic basis of Weber-Cockayne epidermolysis bullosa simplex. Proc Natl Acad Sci U S A. 1993;90(15):7414-7418.
377. Chipev CC, Korge BP, Markova N, et al. A leucine----proline mutation in the H1 subdomain of keratin 1 causes epidermolytic hyperkeratosis. Cell. 1992;70(5):821-828.
378. Parry DA, Steinert PM. Intermediate filament structure. Curr Opin Cell Biol. 1992;4(1):94-98.
379. Steinert PM. Organization of coiled-coil molecules in native mouse keratin 1/keratin 10 intermediate filaments: evidence for alternating rows of antiparallel in-register and antiparallel staggered molecules. J Struct Biol. 1991;107(2):157-174.
380. Steinert PM. Analysis of the mechanism of assembly of mouse keratin 1/keratin 10 intermediate filaments in vitro suggests that intermediate filaments are built from multiple oligomeric units rather than a unique tetrameric building block. J Struct Biol. 1991;107(2):175-188.
381. Jiang S, Zhao L, Lu Y, et al. Piwil2 inhibits keratin 8 degradation through promoting p38-induced phosphorylation to resist Fas-mediated apoptosis. Mol Cell Biol. 2014;34(21):3928-3938.
382. Fortier AM, Riopel K, Desaulniers M, et al. Novel insights into changes in biochemical properties of keratins 8 and 18 in griseofulvin-induced toxic liver injury. Exp Mol Pathol. 2010;89(2):117-125.
383. Busch T, Armacki M, Eiseler T, et al. Keratin 8 phosphorylation regulates keratin reorganization and migration of epithelial tumor cells. J Cell Sci. 2012;125(Pt 9):2148-2159.
384. Alam H, Gangadaran P, Bhate AV, et al. Loss of keratin 8 phosphorylation leads to increased tumor progression and correlates with clinico-pathological parameters of OSCC patients. PLoS One. 2011;6(11):e27767.
385. Morley SM, D'Alessandro M, Sexton C, et al. Generation and characterization of epidermolysis bullosa simplex cell lines: scratch assays show faster migration with disruptive keratin mutations. Br J Dermatol. 2003;149(1):46-58.
386. Binukumar BK, Shukla V, Amin ND, et al. Topographic regulation of neuronal intermediate filaments by phosphorylation, role of peptidyl-prolyl isomerase 1: significance in neurodegeneration. Histochem Cell Biol. 2013;140(1):23-32.
387. Natsuga K, Shinkuma S, Hsu CK, et al. Current topics in Epidermolysis bullosa: Pathophysiology and therapeutic challenges. J Dermatol Sci. 2021;104(3):164-176.
388. Liu N, Matsumura H, Kato T, et al. Stem cell competition orchestrates skin homeostasis and ageing. Nature. 2019;568(7752):344-350.
389. Fujimura Y, Watanabe M, Ohno K, et al. Hair follicle stem cell progeny heal blisters while pausing skin development. EMBO Rep. 2021;22(7):e50882.
390. Steinert PM. The dynamic phosphorylation of the human intermediate filament keratin 1 chain. J Biol Chem. 1988;263(26):13333-13339.
391. Vetter A, Jahn K, Bouameur JE, et al. Epidermolysis Bullosa Simplex keratinocytes show disturbed mitochondrial positioning and activity. J Invest Dermatol. 2020.
392. Diokmetzidou A, Soumaka E, Kloukina I, et al. Desmin and alphaB-crystallin interplay in the maintenance of mitochondrial homeostasis and cardiomyocyte survival. J Cell Sci. 2016;129(20):3705-3720.
393. Hailey DW, Rambold AS, Satpute-Krishnan P, et al. Mitochondria supply membranes for autophagosome biogenesis during starvation. Cell. 2010;141(4):656-667.
394. Garofalo T, Matarrese P, Manganelli V, et al. Evidence for the involvement of lipid rafts localized at the ER-mitochondria associated membranes in autophagosome formation. Autophagy. 2016;12(6):917-935.
395. Garofalo T, Giammarioli AM, Misasi R, et al. Lipid microdomains contribute to apoptosis-associated modifications of mitochondria in T cells. Cell Death Differ. 2005;12(11):1378-1389.
396. Browman DT, Resek ME, Zajchowski LD, et al. Erlin-1 and erlin-2 are novel members of the prohibitin family of proteins that define lipid-raft-like domains of the ER. J Cell Sci. 2006;119(Pt 15):3149-3160.
397. Giammarioli AM, Garofalo T, Sorice M, et al. GD3 glycosphingolipid contributes to Fas-mediated apoptosis via association with ezrin cytoskeletal protein. FEBS Lett. 2001;506(1):45-50.
398. Sorice M, Matarrese P, Tinari A, et al. Raft component GD3 associates with tubulin following CD95/Fas ligation. FASEB J. 2009;23(10):3298-3308.
399. Levine T. Short-range intracellular trafficking of small molecules across endoplasmic reticulum junctions. Trends Cell Biol. 2004;14(9):483-490.
400. Baris OR, Klose A, Kloepper JE, et al. The mitochondrial electron transport chain is dispensable for proliferation and differentiation of epidermal progenitor cells. Stem Cells. 2011;29(9):1459-1468.
401. Hamanaka RB, Glasauer A, Hoover P, et al. Mitochondrial reactive oxygen species promote epidermal differentiation and hair follicle development. Sci Signal. 2013;6(261):ra8.
402. Cardenas C, Foskett JK. Mitochondrial Ca(2+) signals in autophagy. Cell Calcium. 2012;52(1):44-51.
403. Celli A, Sanchez S, Behne M, et al. The epidermal Ca(2+) gradient: Measurement using the phasor representation of fluorescent lifetime imaging. Biophys J. 2010;98(5):911-921.

404. Kouloumenta A, Mavroidis M, Capetanaki Y. Proper perinuclear localization of the TRIM-like protein myospryn requires its binding partner desmin. J Biol Chem. 2007;282(48):35211-35221.
405. Monteleon CL, Agnihotri T, Dahal A, et al. Lysosomes Support the Degradation, Signaling, and Mitochondrial Metabolism Necessary for Human Epidermal Differentiation. J Invest Dermatol. 2018.
406. Casey JR, Grinstein S, Orlowski J. Sensors and regulators of intracellular pH. Nat Rev Mol Cell Biol. 2010;11(1):50-61.
407. Ohkuma S. Use of fluorescein isothiocyanate-dextran to measure proton pumping in lysosomes and related organelles. Methods Enzymol. 1989;174:131-154.
408. Ponsford AH, Ryan TA, Raimondi A, et al. Live imaging of intra-lysosome pH in cell lines and primary neuronal culture using a novel genetically encoded biosensor. Autophagy. 2021;17(6):1500-1518.
409. Kawai A, Uchiyama H, Takano S, et al. Autophagosome-lysosome fusion depends on the pH in acidic compartments in CHO cells. Autophagy. 2007;3(2):154-157.
410. Yamamoto A, Tagawa Y, Yoshimori T, et al. Bafilomycin A1 prevents maturation of autophagic vacuoles by inhibiting fusion between autophagosomes and lysosomes in rat hepatoma cell line, H-4-II-E cells. Cell Struct Funct. 1998;23(1):33-42.
411. Bagh MB, Peng S, Chandra G, et al. Misrouting of v-ATPase subunit V0a1 dysregulates lysosomal acidification in a neurodegenerative lysosomal storage disease model. Nat Commun. 2017;8:14612.
412. Wolfe DM, Lee JH, Kumar A, et al. Autophagy failure in Alzheimer's disease and the role of defective lysosomal acidification. Eur J Neurosci. 2013;37(12):1949-1961.
413. Fernandez-Mosquera L, Yambire KF, Couto R, et al. Mitochondrial respiratory chain deficiency inhibits lysosomal hydrolysis. Autophagy. 2019;15(9):1572-1591.
414. Osellame LD, Rahim AA, Hargreaves IP, et al. Mitochondria and quality control defects in a mouse model of Gaucher disease--links to Parkinson's disease. Cell Metab. 2013;17(6):941-953.
415. Yambire KF, Fernandez-Mosquera L, Steinfeld R, et al. Mitochondrial biogenesis is transcriptionally repressed in lysosomal lipid storage diseases. Elife. 2019;8.
416. Nilsson MI, MacNeil LG, Kitaoka Y, et al. Combined aerobic exercise and enzyme replacement therapy rejuvenates the mitochondrial-lysosomal axis and alleviates autophagic blockage in Pompe disease. Free Radic Biol Med. 2015;87:98-112.
417. Pshezhetsky AV. Lysosomal storage of heparan sulfate causes mitochondrial defects, altered autophagy, and neuronal death in the mouse model of mucopolysaccharidosis III type C. Autophagy. 2016;12(6):1059-1060.
418. Norambuena A, Wallrabe H, Cao R, et al. A novel lysosome-to-mitochondria signaling pathway disrupted by amyloid-beta oligomers. EMBO J. 2018;37(22).
419. Mauthe M, Orhon I, Rocchi C, et al. Chloroquine inhibits autophagic flux by decreasing autophagosome-lysosome fusion. Autophagy. 2018;14(8):1435-1455.
420. Chin MY, Patwardhan AR, Ang KH, et al. Genetically Encoded, pH-Sensitive mTFP1 Biosensor for Probing Lysosomal pH. ACS Sens. 2021;6(6):2168-2180.
421. Chin MY, Ang KH, Davies J, et al. Phenotypic Screening Using High-Content Imaging to Identify Lysosomal pH Modulators in a Neuronal Cell Model. ACS Chem Neurosci. 2022.
422. Trudeau KM, Colby AH, Zeng J, et al. Lysosome acidification by photoactivated nanoparticles restores autophagy under lipotoxicity. J Cell Biol. 2016;214(1):25-34.
423. Kim HN, Seo BR, Kim H, et al. Cilostazol restores autophagy flux in bafilomycin A1-treated, cultured cortical astrocytes through lysosomal reacidification: roles of PKA, zinc and metallothionein 3. Sci Rep. 2020;10(1):9175.
424. Zhou C, Wu Z, Du W, et al. Recycling of autophagosomal components from autolysosomes by the recycler complex. Nat Cell Biol. 2022.
425. Braulke T, Bonifacino JS. Sorting of lysosomal proteins. Biochim Biophys Acta. 2009;1793(4):605-614.
426. Chen Y, Yu L. Autophagic lysosome reformation. Exp Cell Res. 2013;319(2):142-146.
427. Rong Y, Liu M, Ma L, et al. Clathrin and phosphatidylinositol-4,5-bisphosphate regulate autophagic lysosome reformation. Nat Cell Biol. 2012;14(9):924-934.
428. Schulze RJ, Weller SG, Schroeder B, et al. Lipid droplet breakdown requires dynamin 2 for vesiculation of autolysosomal tubules in hepatocytes. J Cell Biol. 2013;203(2):315-326.
429. Chen Y, Yu L. Development of Research into Autophagic Lysosome Reformation. Mol Cells. 2018;41(1):45-49.
430. Munson MJ, Allen GF, Toth R, et al. mTOR activates the VPS34-UVRAG complex to regulate autolysosomal tubulation and cell survival. EMBO J. 2015;34(17):2272-2290.
431. Zhang J, Zhou W, Lin J, et al. Autophagic lysosomal reformation depends on mTOR reactivation in H2O2-induced autophagy. Int J Biochem Cell Biol. 2016;70:76-81.
432. Teng JMC, Bartholomew FB, Patel V, et al. Novel treatment of painful plantar keratoderma in pachyonychia congenita using topical sirolimus. Clin Exp Dermatol. 2018.
433. Lawrence RE, Zoncu R. The lysosome as a cellular centre for signalling, metabolism and quality control. Nat Cell Biol. 2019;21(2):133-142.
434. Senturk M, Lin G, Zuo Z, et al. Ubiquilins regulate autophagic flux through mTOR signalling and lysosomal acidification. Nat Cell Biol. 2019;21(3):384-396.
435. Buerger C, Malisiewicz B, Eiser A, et al. Mammalian target of rapamycin and its downstream signalling components are activated in psoriatic skin. Br J Dermatol. 2013;169(1):156-159.
436. Kjellerup RB, Iversen L, Kragballe K, et al. The expression and phosphorylation of eukaryotic initiation factor 4E are increased in lesional psoriatic skin. Br J Dermatol. 2009;161(5):1059-1066.

437. Sengupta S, Peterson TR, Sabatini DM. Regulation of the mTOR complex 1 pathway by nutrients, growth factors, and stress. Mol Cell. 2010;40(2):310-322.
438. Zhang W, Bai J, Hang K, et al. Role of Lysosomal Acidification Dysfunction in Mesenchymal Stem Cell Senescence. Front Cell Dev Biol. 2022;10:817877.
439. Deus CM, Yambire KF, Oliveira PJ, et al. Mitochondria-Lysosome Crosstalk: From Physiology to Neurodegeneration. Trends Mol Med. 2020;26(1):71-88.
440. Fernandez-Mosquera L, Diogo CV, Yambire KF, et al. Acute and chronic mitochondrial respiratory chain deficiency differentially regulate lysosomal biogenesis. Sci Rep. 2017;7:45076.
441. Perera RM, Zoncu R. The Lysosome as a Regulatory Hub. Annu Rev Cell Dev Biol. 2016;32:223-253.
442. Lim JA, Li L, Kakhlon O, et al. Defects in calcium homeostasis and mitochondria can be reversed in Pompe disease. Autophagy. 2015;11(2):385-402.
443. Cereghetti GM, Stangherlin A, Martins de Brito O, et al. Dephosphorylation by calcineurin regulates translocation of Drp1 to mitochondria. Proc Natl Acad Sci U S A. 2008;105(41):15803-15808.
444. Hernandez-Perez E. Familial benign chronic pemphigus. Cutis. 1987;39(1):75-77.
445. Schwarz N, Leube RE. Intermediate Filaments as Organizers of Cellular Space: How They Affect Mitochondrial Structure and Function. Cells. 2016;5(3).

VI. Abbreviations

ADP	Adenosine diphosphate
AGPAT5	1-acyl-sn-glycerol-3-phosphate acyltransferase epsilon 5
ALR	Autophagic lysosome reformation
ANOVA	Analysis of variance
APS	Ammonium persulfate
ATG	Autophagy-related genes
ATP	Adenosine triphosphate
AU	Airy units
bp	Base pairs
Ca^{2+}	Calcium
CCCP	Cyanide m-chlorophenylhydrazone
cDNA	Complementary DNA
CE	Cornified envelope
cm^2	Cubic centimetre
CMT	Charcot-Marie-Tooth
CO_2	Carbon dioxide
DFCP1	Double FYVE-containing protein 1
DIC	Differential interference contrast
DMSO	Dimethylsulfoxid
DNA	Deoxyribonucleic acid
EB	*Epidermolysis bullosa*
EBS	*Epidermolysis bullosa simplex*
ECL	Enhanced Chemiluminescence
E. coli	*Escherichia coli*
EGFP	Enhanced green fluorescent protein
EYFP	Enhanced yellow fluorescent protein
ER	Endoplasmic reticulum
FBS	Fetal bovine serum
Fig.	Figure
FRAP	Fluorescence recovery after photobleaching
g	Standard gravity
GAPDH	Glyceraldehyde 3-phosphate dehydrogenase
GFP	Green fluorescent protein
h	Hour
HF	High fidelity
hKC	Human Keratinocytes
HRP	Horseradish peroxidase
Hsp	Heat shock protein
IF	Intermediate filament
Ig	Immunoglobulin
IMM	Inner mitochondrial membrane
kDa	Kilodalton
KIF	Keratin intermediate filament
Krt	Keratin
l	Litre
LC3	MAP1LC3A; Microtubule-associated protein 1 light chain 3 alpha
LLPS	Liquid-liquid phase separation
LSM	Laser scanning microscope
M	Mol per litre
MAM	Mitochondria-associated membrane
MFN	Mitofusin
Mg^{2+}	Magnesium
min	Minute
mg	Milligram

mM	Millimolar
ml	Millilitre
mRNA	Messenger RNA
MSD	Mean square displacement
mtDNA	Mitochondrial DNA
MTS	Mitochondrial targeting sequence
N	Normality
n	number
N.A.	Numerical aperture
nDNA	Nuclear DNA
NF	Neurofilament
nm	Nanometre
Nm myosin	Non-muscle myosin
OMM	Outer mitochondrial membrane
P	Phosphate
PAGE	Polyacrylamide-gel-electrophoresis
PARL	Presenilin associated rhomboid like
PBS	Phosphate buffered saline
PC	*Pachyonychia congenita*
PCR	Polymerase chain reaction
PFA	Paraformaldehyde
PI3K	Phosphoinositide kinase 3
PI3P	Phosphatidylinositol-3-phosphate
PINK1	PTEN-induced kinase 1
PPK	Palmoplantar keratoderma
PTEN	Phosphatase and tensin homolog
PVDF	Polyvinylidene difluoride
Px	Pixel
qPCR	Quantitative polymerase chain reaction
RFP	Red fluorescent protein
RNA	Ribonucleic acid
ROI	Region of interest
RT	Room temperature
s	Second
SD	Standard deviation
SDS	Sodium dodecyl sulphate
Ser	Serine
shRNA	Short hairpin RNA
t	Time
TBST	Tris buffered saline plus Tween-20
TEMED	Tetramethylethylendiamine
TIM23	Translocase of inner membrane 23
Thr	Threonine
TOM	Translocase of outer membrane
Tris	Tris-(hydroxymethyl)-Aminomethan
U	Unit
ULF	Unit-length filaments
VDAC	Voltage-dependent anion channel
WB	Western-Blot
wt	Wild type
°C	Degree Celsius
µg	Microgram
µl	Microliter
µm	Micrometre
µM	Micromolar
% (v/v)	Percent by volume
% (w/v)	Percent by weight

VII. List of Figures

VIII. List of Tables

IX. List of Movies

Movie 01. Time-lapse fluorescence recording of eYFP-K14R125C in a MCF-7 cell.
Shown is an inverse projection view of 5 focal planes, which cover most of the keratin granule signal. Recording frequency: 3 frames/min. Corresponding Fig. 9 shows the still image recorded at time point 0 min.

Movie 02. Automated image analysis intermediate steps projected onto a time-lapse fluorescence recording of eYFP-K14R125C in a MCF-7 cell.
(A) Image analyses of the time-lapse fluorescence recording depicted in Movie 01 (original representation). The four quadrants illustrate different stages of image documentation and analysis as described in corresponding Fig. 9.
(B) The segment is a magnification of (A) (see boxed area in Fig. 9), showing the original recordings, the derived tracks of detected granules (magenta circles), the number of granule merging events (colour-coded), and the speed of keratin granules along individual tracks for each time point (colour-coded). Further information is provided in corresponding Fig. 9.

Movie 03. Image analyses of time-lapse fluorescence recording of eYFP-K14R125C in an MCF-7 cell (recording frequency: 3 frames/min). The track of a single, non-fusing granule is highlighted in green (see the corresponding still in Fig. 14c as inverse representation). Magenta circles highlight granules from other tracks.

Movie 04. Image analyses of time-lapse fluorescence recording of eYFP-K14R125C in an MCF-7 cell (recording frequency: 3 frames/min). The tracks of three fusing granules are encircled in green. Magenta circles show granules from other tracks.

Movie 05. Analysis of fluorescence intensity alterations in a single granule that was tracked in a time-lapse fluorescence recording of eYFP-K14R125C in MCF-7 cell (corresponding Movie 03). The fluorescence intensity was measured in a single, non-fusing granule moving along the track highlighted in magenta at top (see also corresponding Fig. 14c).

Movie 06. (A) Analysis of track speed, (B) analysis of advance speed, and (C) analysis of advance speed to track speed ratios of a single granule that is monitored in a time-lapse fluorescence recording of eYFP-K14R125C in an MCF-7 cell (corresponding Movie 03). The values were determined for a single, non-fusing granule moving along the track which is highlighted in magenta at top (see also corresponding Fig. 16m-o).

Movie 07. Fluorescence recording of eYFP-K14R125C in an MCF-7 cell. Shown is an inverse projection view of 6 focal planes with a total height of 3.44 µm. The cell was incubated in normal medium for 10 min and subsequently medium was replaced with medium containing 20 µM para-nitroblebbistatin until 26 min 20 s. (see quantification of multiple treated cells in Fig. 20).

Movie 08. Fluorescence recording of eYFP-K14R125C and mCherry-non-muscle myosin IIB in an MCF-7 cell. Projection view of 3 focal planes with a total height of 1.0 µm for 4 min 45 s.

Movie 09. Fluorescence recording of eYFP-K14R125C mCherry-non-muscle myosin IIB in an MCF-7 cell. Projection view of 4 focal planes with a total height of 1.5 µm (recording frequency: 3 frames/min). The cell was incubated in normal medium for 7 min and subsequently medium was replaced with medium containing 20 µM para-nitroblebbistatin and imaged for another 25 min 40 s. The keratin track speed was reduced by 24.6% in the treated cell (see corresponding Fig. 22a-b).

Movie 10. Fluorescence recording of eYFP-K14R125C and LifeAct-RFP in an MCF-7 cell. Projection view of 4 focal planes with a total height of 1.5 µm (recording frequency: 3 frames/min). The cell was incubated in normal medium for 7 min and subsequently medium was replaced with medium containing 20 µM para-nitroblebbistatin and imaged for another 25 min 40 s. Keratin granule track speed was reduced by 27.8% in the treated cell (see corresponding Fig. 22c-d).

X. Appendix

X.1 Zusammenfassung

Die Haut stellt eine der wichtigsten Barrieren des Körpers dar. Ihre äußerste Schicht, die Epidermis, besteht hauptsächlich aus differenzierenden Keratinozyten. Die Integrität der Epidermis wird zu einem großen Teil durch das Keratin-Intermediärfilament-Zytoskelett gewährleistet. Die Bedeutung dieses Netzwerks wird durch eine Reihe von Keratinmutationen untermauert, die Krankheiten wie *Epidermolysis bullosa simplex* (EBS) oder *Pachyonychia congenita* (PC) verursachen, welche durch Keratin 5/14- bzw. Keratin 6/16/17-Mutationen ausgelöst werden. EBS ist charakterisiert durch traumabedingte Blasenbildung, die auf die Zytolyse von Keratinozyten in der basalen Schicht der Epidermis zurückzuführen ist und die auf einer Strukturveränderung des Keratinnetzwerks beruht. Statt des Zytoplasma-durchspannenden filamentösen Netzwerks entstehen periphere Keratin-Granula. PC-Patienten hingegen zeigen eine Verdickung der Epidermis mit extremer Hyperkeratose an bestimmten Hautarealen, z. B. an den Fußsohlen.

Ziel dieser Arbeit war es, Einblick in die verschiedenen Pathogenesen zu gewinnen, um zum einen durch Etablierung und Anwendung neu entwickelter Bildanalysewerkzeuge mutierte EBS-Keratin-Granula quantitativ zu beschreiben, und um zum anderen zu klären, ob die Autophagie von Mitochondrien, welche einen wesentlichen Schritt innerhalb der epidermalen Differenzierung darstellt, bei PC gestört ist.

Mit Hilfe von Lebendzellmikroskopie von Epithelzellen, die Fluorophor-markiertes, mutiertes Keratin stabil überexprimieren, wurde eine automatisierte Tracking-Routine entwickelt. Sie ermöglichte eine detaillierte quantitative Analyse verschiedener dynamischer Parameter der mutierten Keratin-Granula. Insbesondere konnte gezeigt werden, dass die Granula zunächst im äußersten Lamellum der Epithelzellen gebildet werden. Anschließend wachsen sie bis zum Erreichen eines Plateaus und werden konstitutiv mit einer Geschwindigkeit von etwa 0,5 µm/min nach innen transportiert. Die meisten Keratin-Granula fusionieren mehrfach miteinander, bevor sie sich an der Grenze zwischen dem Lamellum und dem inneren Zytoplasma rasch auflösen. Ihr Transport ähnelt stark dem Aktin-Transport, und es konnte gezeigt werden, dass eine pharmakologische Hemmung des Aktin-Motorproteins non-muscle Myosin II ihre gerichtete Motilität deutlich verringert. Fluoreszenz-Bleich-Experimente zeigten weiterhin, dass die Granula lösliche Keratine schnell mit dem Zytoplasma und innerhalb der Granula selbst austauschen. Die Bildung von EBS-assoziierten Keratin-Granula beruht demzufolge auf dem Prinzip der Flüssig-Flüssig-Phasentrennung.

Als nächstes wurde die Kinase DYRK untersucht, basierend auf ihrer Fähigkeit, verschiedene Flüssig-Phasen-Kondensate aufzulösen. Obwohl eine deutliche Kolokalisierung verschiedener überexprimierter DYRK-Isoformen und mutierter Keratin-Granula in Patienten-Keratinozyten gezeigt werden konnte, führte die pharmakologische Hemmung dieser Kinasen nicht zu einer Änderung des Prozentsatzes der Granula-positiven Zellen in verschiedenen Wildtyp-Keratinozyten-Zellklonen, die Fluorophor-markierte mutierte Keratine stabil überexprimieren.

Im zweiten Teil dieser Arbeit wurden funktionelle Auswirkungen der mutierten Keratine auf die mitochondriale Integrität untersucht. Im Hinblick auf Makroautophagie von Mitochondrien wurde das mitochondriale Alter mit Hilfe eines Fluoreszenzreporters bestimmt. Es zeigte sich, dass PC-Zellen erhöhte Mengen an überalterten Mitochondrien enthalten, was bei EBS nicht der Fall war. Außerdem zeigte sich, dass die Kontaktstellen zwischen Mitochondrien und dem endoplasmatischen Retikulum in PC reduziert sind. Die Expression von frühen Mitophagie-Markern war nicht verändert, jedoch war der Abbau von Mitochondrien in PC-Keratinozyten stark beeinträchtigt. Obwohl die Keratinozyten in der Lage sind, Autolysosomen zu bilden, wurde gezeigt, dass sich diese Strukturen in PC stark anreichern. Die Analyse der Funktion von Lysosomen ergab eine verringerte enzymatische Kapazität, und der Phänotyp der Mitochondrien-Überalterung konnte durch pH-Veränderungen in Wildtyp-Zellen nachgeahmt werden. Daraus lässt sich schließen, dass der Prozess des autolysosomalen Recyclings, der im Anschluss an die Makroautophagie unerlässlich ist, in PC gestört ist, was zu einer beeinträchtigten Mitophagie führt.

Insgesamt wurden im Rahmen dieser Arbeit neue Bildanalysewerkzeuge entwickelt, die eine detaillierte Quantifizierung der Dynamik mutierter Keratine ermöglichen, und es wurde entdeckt, dass mutierte Keratine die Mitophagie und das autolysosomale Recycling in PC-Keratinozyten modulieren.

X.2 Vector maps

X.2.1 Vector #2383: Krt14R125C-eYFP_Cbh_T2A_Puro

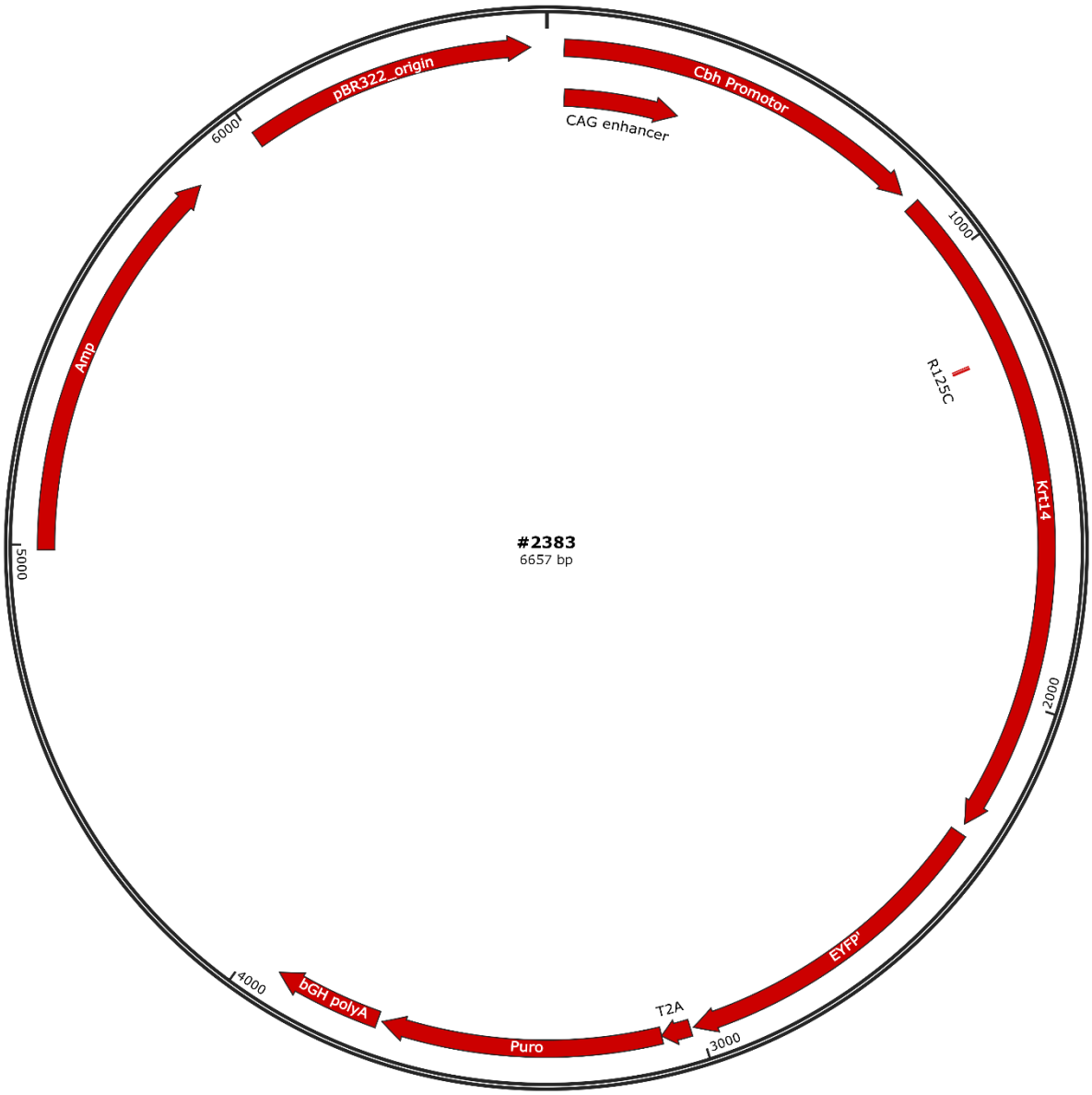

X.2.2 Vector #2400: Krt14R125C-mCerulean_Cbh_T2A_Puro

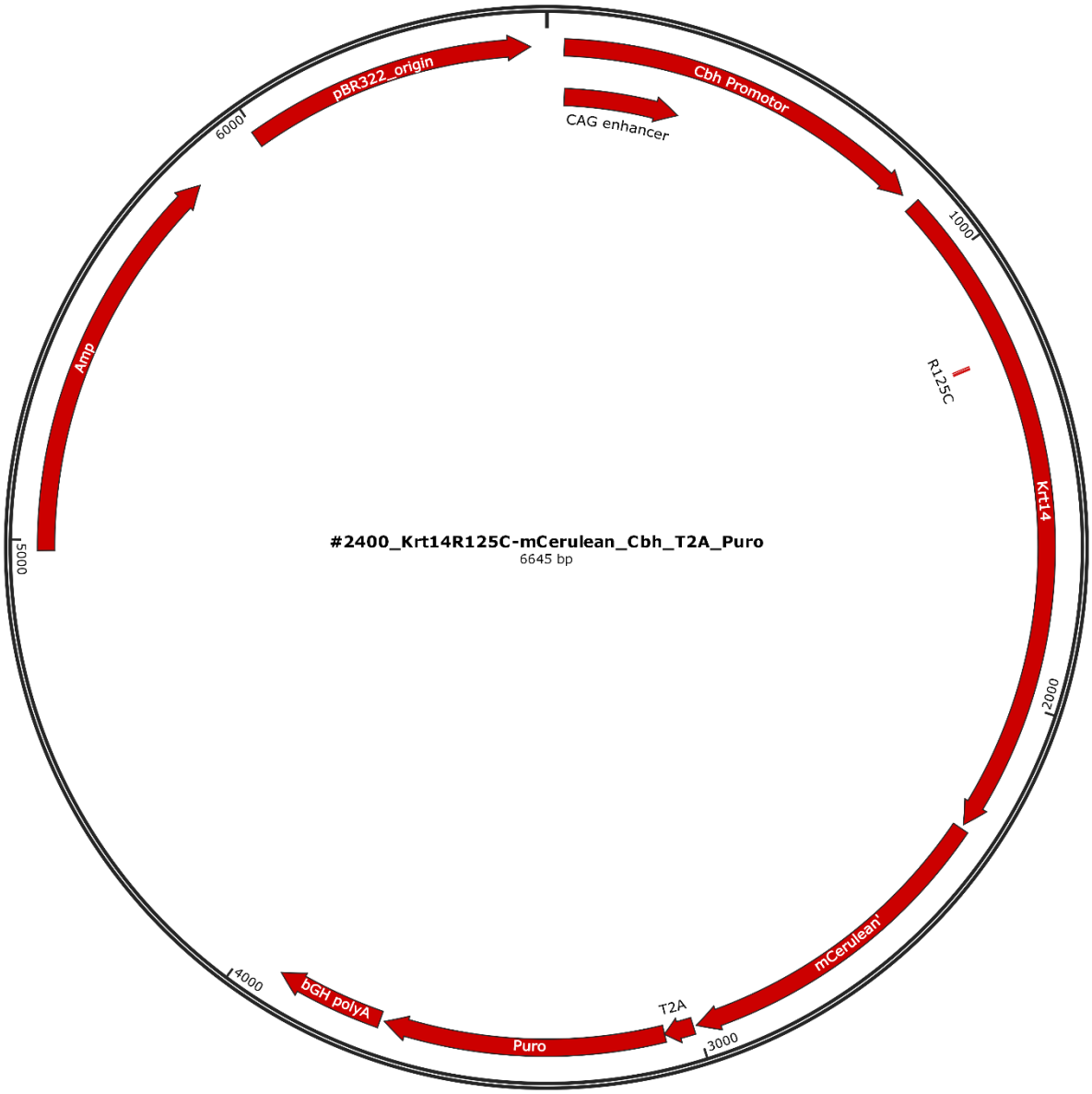

X.3 Author contribution of published scientific papers

X.3.1 Growth, lifetime, directional movement and myosin-dependent motility of mutant keratin granules in cultured cells.

Lehmann, S. M. (S.M.L.) , Leube, R. E. (R.E.L.) & Windoffer, R. (R.W.)

Sci Rep 11, 2379, doi:10.1038/s41598-021-81542-8 (2021).

Conceptualization: R.W., R.E.L., S.M.L.; data curation: R.W., S.M.L.; formal analysis: R.W., S.M.L.; funding acquisition: R.E.L., R.W.; investigation: S.M.L.; Methodology: R.W.; project administration: R.W., R.E.L.; resources: R.E.L., R.W.; software: R.W.; supervision: R.E.L., R.W.; validation: R.W.; visualization: S.M.L., R.W.; writing-original draft preparation: S.M.L., R.E.L.; writing—review and editing: S.M.L., R.E.L., R.W.

X.3.2 Keratin 6a mutations lead to impaired mitochondrial quality control.

Lehmann S (S.M.L), Leube RE (R.E.L) , Schwarz N (N.S.)

Br J Dermatol. 2019 Apr 20. doi: 10.1111/bjd.18014.

Conceptualization: N.S., S.M.L.; data curation: S.M.L., N.S., formal analysis: S.M.L., N.S. funding acquisition: R.E.L., N.S.; investigation: S.M.L.; Methodology: N.S., S.L.; project administration: N.S.; resources: R.E.L., N.S.; supervision: N.S., R.E.L.; visualization: S.M.L. writing-original draft preparation: N.S., S.M.L..; writing-review and editing: N.S., S.M.L., R.E.L.

X.3.3 Expression profile of pattern recognition receptors in skeletal muscle of SOD1((G93A)) amyotrophic lateral sclerosis (ALS) mice and sporadic ALS patients.

Lehmann S (S.L.), Esch E (E.E.), Hartmann P (P.H.), Goswami A (A.G.), Nikolin S (S.N.), Weis J (J.W), Beyer C (C.B.), and Johann S (S.J.)

Neuropathol Appl Neurobiol. 2018;44(6):606-27.

S.L. and E.E. performed the H&E stains, immunohistochemistry and western blot analysis of human control and sALS samples. S.L. and E.E. also executed immunostaining and Western blotting for NLRP1, NLRC4, AIM2, IL18 and B8H10 in SOD1(G93A) mouse samples. P.H. performed western blot analysis and immunohistochemistry for NLRP3, ASC, caspase 1 and

IL1b for the SOD1(G93A) mouse samples. P.H. and S.J performed mRNA extraction, cDNA synthesis and realtime PCR analysis. S.J and S.L performed DNA extraction and copy number analysis. S.J. was responsible for animal experiments and tissue collection from SOD1(G93A) mice. S.L., E.E. and S.J. wrote the manuscript. Skeletal muscle biopsies of control and sALS cases were sampled and processed by S.N, J.W. and A.G. S.J. raised the hypothesis and designed the experiments. Statistics was carried out by S.J, S.L., E.E and P.H. The entire project was supervised by S.J. and C.B.

X.4 Affidavit/Eidesstattliche Erklärung

Ich, Sonja Maria Lehmann,

erkläre hiermit, dass diese Dissertation und die darin dargelegten Inhalte die eigenen sind und selbstständig, als Ergebnis der eigenen originären Forschung, generiert wurden.

Hiermit erkläre ich an Eides statt

1. Diese Arbeit wurde vollständig oder größtenteils in der Phase als Doktorand dieser Fakultät und Universität angefertigt;

2. Sofern irgendein Bestandteil dieser Dissertation zuvor für einen akademischen Abschluss oder eine andere Qualifikation an dieser oder einer anderen Institution verwendet wurde, wurde dies klar angezeigt;

3. Wenn immer andere eigene- oder Veröffentlichungen Dritter herangezogen wurden, wurden diese klar benannt;

4. Wenn aus anderen eigenen- oder Veröffentlichungen Dritter zitiert wurde, wurde stets die Quelle hierfür angegeben. Diese Dissertation ist vollständig meine eigene Arbeit, mit der Ausnahme solcher Zitate;

5. Alle wesentlichen Quellen von Unterstützung wurden benannt;

6. Wenn immer ein Teil dieser Dissertation auf der Zusammenarbeit mit anderen basiert, wurde von mir klar gekennzeichnet, was von anderen und was von mir selbst erarbeitet wurde;

7. Ein Teil oder Teile dieser Arbeit wurden zuvor veröffentlicht und zwar wie aufgeführt in: Publications

Aachen, den 14.07.2022

S. Lehmann

XI. Acknowledgements

Im Folgenden möchte ich mich herzlich bei all den Menschen bedanken, die mir bei der Erstellung dieser Dissertation und während meiner Zeit als Doktorandin im MOCA eine große Hilfe waren:

Ein besonderer Dank gilt Prof. Dr. Rudolf Leube für die Vergabe des Promotionsthemas, seine stets offene Tür, sowie für die Begeisterung jederzeit zum Mikroskop zu eilen und sich die neueste Aufnahme anzusehen.

Ein herzlicher Dank geht an Prof. Geraldine Zimmer-Bensch und Prof. Dr. Marc Spehr für die Betreuung meiner Dissertation als weitere Gutachter.

Prof. Dr. Reinhard Windoffer danke ich für die Einarbeitung am Mikroskop, die Kreativität und Geduld beim Erarbeiten der Bildanalysetools und all die wissenschaftlichen Diskussionen.

Dr. Nicole Schwarz danke ich von ganzem Herzen für die weiterführende Betreuung nach meiner Masterarbeit, ihre große Motivation für das Mitochondrien-Projekt, die Bereitschaft mir bei neuen Ideen freie Hand zu lassen, sowie für Freundschaft in allen Lebenslagen.

Dr. Marcin Moch danke ich für eine wunderbare gemeinsam verbrachte Bürozeit im Halbdunklen („Igitt, Licht!“), für die unermüdliche Hilfe am Mikroskop, jedes „klar, komm mit“ bei einer Frage, beste Beratung bei der Anschaffung neuer technischer Geräte und seine Freundschaft.

Dr. Sebastian Kant danke ich für all die Hilfe am ApoTome, das Einspringen als Ersatz-Betreuer am Anfang der Doktorandenzeit, sowie für die Freundschaft mit ihm und seiner Familie.

Prof. Dr. Irmgard Classen-Linke danke ich für ihr stets offenes Ohr und dafür, auch nach der offiziellen Zeit weiterhin mit großer Motivation für das MOCA und das Graduiertenkolleg da zu sein.

Dr. Jacopo Di Russo danke ich für die Zweitbetreuung innerhalb des Graduiertenkollegs.

Weiterhin danke ich Anna Sternberg, Jana Schieren, Joana Ahlburg, Nadieh Kuijpers (mit Suki), Dr. Anne Pora, Dr. Mugdha Sawant, Dr. Richard Coch, Paula Frohn und allen weiteren medizinischen Doktorand:innen für all die laborspezifischen Diskussionen und für ihre Freundschaft während und nach unser gemeinsam verbrachten Doktorandenzeit.

Sabina Hennes-Mades danke ich herzlich für die Einarbeitung und Hilfe in der Zellkultur; Ursula Wilhelm und Christiane Jaeschke für die Einarbeitung und Hilfe in der Molekularbiologie; Laura Koenigs für die Hilfe bei Klonierungen und unsere Freundschaft; Sabine Eisner für die Elektronenmikroskopie; Adam Breitscheidel für die Hilfe mit Illustrator; Markus Paul für technische Hilfe und seine wunderbare „Markus-Art“; Justus Schwarzott für IT-Unterstützung; und natürlich Elke Broekmeulen und Marina Lürkens-Weber dafür, die besten „MOCA-Mamas“ zu sein.

Ein großer Dank gilt allen weiteren MOCAs für die angenehme Arbeitsatmosphäre und für die gute Zusammenarbeit bei der Lehre.

Dr. Nicole Schwarz, Prof. Dr. Rudolf Leube und Dr. Richard Coch danke ich im Besonderen für das Korrekturlesen der Dissertation.

Ein weiterer Dank gilt Prof. Dr. Walter Becker für die Kooperation und Bereitstellung von Materialien bezüglich des DYRK-Kinase Projekts.

Ein besonderer Dank gilt meiner lieben Freundin Stefanie Trinh für die Freundschaft in allen Lebenslagen und lebensrettende gemeinsame Pausen, sowie meiner Familie in Aachen, Bonn, Remscheid, und Katzhütte für Unterstützung und ein stets offenes Ohr während der letzten Jahre – besonders dem weltbesten Bruder!

Meinem Freund Richard Coch danke ich von ganzem Herzen für sämtliche nach Feierabend geführten Diskussionen über meine Arbeit und all die anderen spannenden Themen, und dafür immer für mich da zu sein, wenn ich ihn brauche!

Zuletzt danke ich meinen Großeltern und meinem Vater für alles was sie für mich getan haben, um mir mein Studium zu ermöglichen, sowie meiner Mutter für 30 Jahre Hingabe, Liebe und Unterstützung bei allem was ich in meinem Leben vorhabe – du hast mir alles gegeben was ich brauche!